

THE SCALED-UP SYNTHESIS OF NANOSTRUCTURED ULTRA-  
HIGH-TEMPERATURE CERAMICS AND RESISTANCE SINTERING  
OF TANTALUM CARBIDE NANOPOWDERS AND COMPOSITES

BY

JAMES P. KELLY

A THESIS

SUBMITTED TO THE FACULTY OF

ALFRED UNIVERSITY

IN PARTIAL FULFILLMENT OF THE REQUIREMENTS  
FOR THE DEGREE OF

DOCTOR OF PHILOSOPHY

IN

CERAMICS

ALFRED, NEW YORK

FEBRUARY, 2013

Alfred University theses are copyright protected and may be used for education or personal research only. Reproduction or distribution in any format is prohibited without written permission from the author.

THE SCALED-UP SYNTHESIS OF NANOSTRUCTURED ULTRA-HIGH-  
TEMPERATURE CERAMICS AND RESISTANCE SINTERING OF  
TANTALUM CARBIDE NANOPOWDERS AND COMPOSITES

BY

JAMES P. KELLY

B.S. ALFRED UNIVERSITY (2006)  
M.S. ALFRED UNIVERSITY (2009)

SIGNATURE OF AUTHOR

APPROVED BY \_\_\_\_\_ (SIGNATURE ON FILE)  
OLIVIA A. GRAEVE, ADVISOR

\_\_\_\_\_  
(SIGNATURE ON FILE)  
LINDA E. JONES, ADVISORY COMMITTEE

\_\_\_\_\_  
(SIGNATURE ON FILE)  
WILLIAM M. CARTY, ADVISORY COMMITTEE

\_\_\_\_\_  
(SIGNATURE ON FILE)  
GEOFFREY M. BOWERS, ADVISORY COMMITTEE

\_\_\_\_\_  
(SIGNATURE ON FILE)  
CHAIR, ORAL THESIS DEFENSE

ACCEPTED BY \_\_\_\_\_ (SIGNATURE ON FILE)  
DOREEN D. EDWARDS, DEAN  
KAZUO INAMORI SCHOOL OF ENGINEERING

ACCEPTED BY \_\_\_\_\_ (SIGNATURE ON FILE)  
NANCY J. EVANGELISTA, ASSOCIATE PROVOST  
FOR GRADUATE AND PROFESSIONAL PROGRAMS  
ALFRED UNIVERSITY

## ACKNOWLEDGMENTS

I would like to thank my thesis advisor, Dr. Olivia Graeve, for providing me with a professional experience that allowed me to advance my education, increase my interest in non-oxide ceramics, and have moral and financial support through a contract with the National Science Foundation. I would like to thank Dr. Graeve for going above and beyond when it came to presenting me with opportunity. I also want to acknowledge my coworkers who provided assistance: Braeden Clark, Ryan Grohsmeyer, Daniel Davies, Alex Turner, and Robert Locker. Gerald Wynick and Swavek Zdzieszynski assisted with SEM and XRD characterization.

I would like to thank my committee members, Drs. Linda Jones, William Carty, and Geoffrey Bowers. I first met Dr. Jones in an undergraduate sophomore class. She probably did not know at the time that I believe she is one of the most influential educators I have been honored to learn from. Dr. Carty has been consistent, serving as my advisor or committee member for my B.S., M.S., and Ph.D. degrees. I requested he be included with good reason. I have always had a deep appreciation for his knowledge, the methodologies he employs in research, and his attention to details. I first met Dr. Bowers at the start of my Ph.D. when I requested to have a chemist on the team. The insights Dr. Bowers provided in our meetings inspired creative thinking and have been invaluable for moving the research forward.

Dr. William Hall deserves special recognition. In addition to serving on my committee temporarily, it was Dr. Hall who provided support when I needed it most. As a sophomore student, I was questioning my career choice and his encouragement and suggestions have been invaluable for making the choice to explore my options, but ultimately remain in my field of study and being glad that I did.

I would like to thank my family and friends for being supportive while I continued my education. It hasn't always been easy and even the smallest gestures have been so meaningful to me. Thank you for pushing me to be my best professionally and personally. I pledge to do my best improving further.

## PREFACE

The following thesis is written in a publication style format. Each chapter is intended to be coherent without reading the other chapters unless otherwise referenced, although a connection between the chapters also exists and is outlined here. Some information is repeated because it is relevant in more than one chapter. The thesis is not formatted for a specific publication. Instead it is formatted according to the requirements of Kazuo Inamori School of Engineering at Alfred University, but broken into segments that are adaptable into a format suitable for a specific destination. After the organization of the chapters is described, the remainder of the preface will address the broader impacts of this research.

Chapters one and two are written for adapting into a book chapter, but separated because of the difference in content: chapter one consists entirely of a literature review and serves as a general introduction to the thesis while chapter two contains a literature review and experimental work. The literature review in chapter two is specifically relevant to the experimental work, as is done for the remaining chapters. The reference to the book chapter that is now in press is: O.A. Graeve and J.P. Kelly, "High Temperature Materials Processing," in *High Temperature Materials and Mechanisms*. Edited by Y. Bar-Cohen. Taylor and Francis Group, Boca Raton, FL, 2013.

Chapter one contains a general introduction to ultra-high temperature ceramics (UHTCs). There is a focus on the thermal management concept for next-generation space re-entry vehicles and high-mach aircraft, which has been a major driving force for recent UHTC development, and the property requirements for these applications. The oxidation behavior is one of the primary limiting behaviors for UHTC composites and is discussed in detail, including the approaches for improving the oxidation behavior. Addition of TaC to UHTC composites is one approach for improved oxidation resistance and is the connection to studying TaC.

A broad demonstration of the synthesis technique used for this thesis is provided in chapter two. The work was produced after chapters three and four, but placed prior to in this document because it begins to define the criteria for the successful production of

non-oxide nanopowders (including borides, carbides, and nitrides among other materials) by the solvothermal synthesis method and is broader in scope than the subsequent chapters. The technique is suitable for highly exothermic reactions, but other considerations are necessary to determine whether the nanopowders can be made by self-propagating behavior or require sustained temperature to complete the reaction. The chapter is finished by suggesting the potential to use the solvothermal synthesis technique for hundreds of other systems. General guidelines for using the technique successfully are included.

Chapter three represents the first demonstration of producing  $\text{LaB}_6$  and TaC by the solvothermal synthesis technique. An alternative method for initiating solvothermal reactions that produce  $\text{LaB}_6$  is introduced that requires no external energy input and the process is scaled up to produce larger quantities of TaC powder (up to 50 grams). This chapter is based on a communication published in the Journal of the American Ceramic Society: J.P. Kelly, R. Kanakala, and O.A. Graeve, "A Solvothermal Approach for the Preparation of Nanostructured Carbide and Boride Ultra-high Temperature Ceramics," *J. Am. Ceram. Soc.*, **93** [10] 3035-8 (2010).

The fourth chapter presents further analysis of the solvothermal synthesis process for making TaC nanopowders. A factorial experimental design without replication is used to analyze the powder characteristics. Visual trends are established for changes in reactant concentrations or type of reductant metal that represent the degree of dilution, magnitude of the chemical gradients, and reaction temperature. A  $2^3$  factorial design with replication is used to corroborate the results with statistical analyses of the variation. The benefit of a factorial experimental design is that it allows for analysis of interactions between the factors being studied that might not otherwise be apparent. The results demonstrate some level of process control via chemical gradient induced and thermal induced diffusion of carbon into tantalum particles. Reaction temperature to control TaC characteristics is highlighted. The experiments outlined in this chapter were used to establish the synthesis conditions that were used in the subsequent sintering studies presented in chapters five, six, seven, and eight. Chapter four is based on a published article: J.P. Kelly and O.A. Graeve, "Statistical Experimental Design Approach for the

Solvothermal Synthesis of Nanostructured Tantalum Carbide Powders,” *J. Am. Ceram. Soc.*, **94** [6] 1706-15 (2011).

Some of the details for the preliminary resistance sintering trials of TaC powders prepared by the solvothermal synthesis method are not included in this thesis, but can be found as a conference proceedings publication: B.M. Clark, J.P. Kelly, and O.A. Graeve, “Exploring the Synthesis Parameters and Spark Plasma Sintering of Tantalum Carbide Powders Prepared by Solvothermal Synthesis,” *Mater. Res. Soc. Symp. Proc.*, **1373**, 7-17 (2012). This paper highlights the need for adequate post-synthesis processing to remove LiOH from the TaC powders.

Chapter five is based on a conference proceedings paper: B.M. Clark, J.P. Kelly, and O.A. Graeve, “Recent Advances on Bulk Tantalum Carbide Produced by Solvothermal Synthesis and Spark Plasma Sintering,” *Mater. Res. Soc. Symp. Proc.*, submitted (2012). The chapter addresses the post-synthesis processing necessary to consolidate TaC using resistance sintering, including removal of LiOH from the TaC powders. The resistance sintering behavior of the powders was investigated by interrupting the sintering cycle at intermediate temperatures, quenching to room temperature, and characterizing the compacts. A Ta<sub>2</sub>O<sub>5</sub> phase develops at relatively low temperatures and is then removed at intermediate temperatures, followed by sintering of TaC. The final sintering temperature and carbon additions to the powders influence the microstructural development of TaC, particularly with respect to porosity. Chapters six and seven explore these two variables in more detail and have not been submitted for publication before submission of this thesis.

The effect of sintering temperature on densification, grain growth, and microstructural development is presented in chapter six. Grain growth as a result of dwelling at the temperatures studied is small relative to grain growth during heating. Likewise, the density is not greatly affected by the dwell temperatures studied. However, there is a distinct transition in the microstructure above a critical temperature that corresponds to the development of a second pore population at the interfaces between TaC grains in addition to porosity at triple points. The development of pores at the grain interfaces is accompanied by the loss of carbon from TaC, which should be avoided for producing high quality TaC.

Chapters five and six indicate that the amount of free carbon in the powders is important for removing the Ta<sub>2</sub>O<sub>5</sub> impurity phase from TaC. The free carbon content is investigated for a sintering temperature that is below the critical temperature established in chapter six for avoiding carbon loss from TaC and presented in chapter seven. The optimum conditions resulted in obtaining densities that are at the upper end of those obtained in literature without the use of extreme heating or pressure conditions. High density is important for obtaining good mechanical behavior. Grain growth was unaffected by the differences in free carbon content.

Nanostructured TaC compacts were not obtained because of simultaneous grain growth that accompanies densification. The focus of chapter eight is using additives to control grain growth, specifically additions of WC and ZrC. The original hypothesis was that additives in solid solution with TaC would affect the activation energy for carbon diffusion, depending on relative size difference between the transition metals, and that the differences in carbon diffusivity would influence densification and grain growth. Some conditions enhanced or inhibited grain growth and are discussed. Decreasing grain size can have a positive impact on the mechanical behavior of TaC. The details of this chapter will not be submitted for publication prior to the submission of the thesis.

Chapter nine is the last chapter and is included as a replacement for a future work section that is often included in a thesis. The chapter outlines hypotheses concerning microstructural control of TaC with a focus on nanostructuring and extending the hypotheses to other transition metal UHTCs. The hypotheses developed for TaC is supported by the work presented in chapter eight and what is already known about TaC. Examples from the literature are also provided to provide support for extending the hypotheses to other systems. The chapter is the basis for a white paper that was submitted in response to Special Notice 13-SN-0001, a special program announcement for the Office of Naval Research who will be providing unclassified grants on the topic after reviewing full proposals.

While chapter nine presents future research originating from the work done for this thesis, the individual chapters highlight future work as well. More specifically, studies that would benefit the analysis of each chapter are often included in the conclusion and discussed in the results and discussion sections of the chapter.

Melting temperatures for non-oxide ceramics are reported throughout this thesis. It is important to realize that melting temperatures are difficult to define for these materials. In many cases, the compounds will decompose via sublimation before melting and the decomposition behavior depends on the composition, temperature, and environment. For example, TaC is known to vaporize either congruently or incongruently well below the reported melting temperature in a vacuum environment and the vaporization rate follows an Arrhenius temperature dependence, but has relatively low vaporization rates. Such behavior complicates the determination of melting temperatures, although evidence of melting behavior is found in the literature.

Some of the figures in this thesis are best represented in color. Others do not require, but benefit from having color. Overall, there are 45 figures in this thesis that contain color. For the benefit of those with impairment of color perception, each of these figures contain the words “With color” inside parentheses after the figure caption to aid in seeking help to interpret these images if it is necessary or desired.

The overall goal of this research is to develop processes for the scaled-up manufacturing of nanostructured ceramics for ultra-high temperature applications. Such applications might include leading edge materials for spacecraft and aircraft, propulsion technologies, and refractories for energy production or metal processing.

The broader impacts of this thesis are best evaluated by considering the grand challenges for engineering, a list of fourteen achievable and sustainable subjects of great importance to society put together by a diverse committee of experts. This thesis is directly or indirectly related to some of the subject areas while not closely related to others. The list is published by the National Academy of Engineering at the request of the National Science Foundation and is reproduced here in the order given and described in more detail at [www.engineeringchallenges.org](http://www.engineeringchallenges.org):

- (i) Make solar energy economical
- (ii) Provide energy from fusion
- (iii) Develop carbon sequestration methods
- (iv) Manage the nitrogen cycle
- (v) Provide access to clean water
- (vi) Restore and improve urban infrastructure
- (vii) Advance health informatics
- (viii) Engineer better medicines
- (ix) Reverse-engineer the brain

- (x) Prevent nuclear terror
- (xi) Secure cyberspace
- (xii) Enhance virtual reality
- (xiii) Advance personal learning
- (xiv) Engineer the tools of scientific discovery

The following thesis is directly applicable to topics (ii), (x), and (xiv). The connection between the thesis and these topics is the development of advanced structural materials for shielding technologies. There is also an indirect connection to topics (i), (iii), (iv), and (viii). Most of the remaining topics are focused towards improved knowledge, management of information, and integrated systems than they are material based needs. The direct and indirect connections to these grand challenges will be discussed in more detail. The topics will be underlined in the text to provide emphasis.

Engineering the tools of scientific discovery should be the most obvious broader impact derived from reading this thesis. Part of this engineering challenge is described by first asking the question, “How will engineering help us explore the universe?” There are several approaches, including studying the tiny fundamental building blocks of all matter as well as the large scale study of the cosmos. Chapter one describes advanced aerospace concepts that contribute to the latter by assisting the development of thermal protection systems and propulsion systems. Exploring frontiers of science requires materials that exceed current limitations. This thesis explores materials for overcoming thermal limitations. The concept of asteroid mining is an idea that currently seems like science fiction, or not economical at least, but may someday become a reality as technology and needs mature.

Energy from fusion would also benefit from advanced thermal shielding technology. Some of the materials discussed in this thesis are candidate materials for Gen IV nuclear fission reactors because of the low neutron capture cross section, thermal stability, and neutron-induced damage tolerance. Fast flying neutrons will be generated during fusion reactions that will interact with the walls of the reaction vessel. The interaction will generate heat and potentially create structural defects that weaken the wall materials. Therefore the vessel must be made with materials that can withstand heat and survive structural weakening for extended periods of time, similar to the materials that are being developed for next-generation fission reactors.

Shielding technologies can also be used to aid the prevention of nuclear terror. Current challenges include detecting, securing, deactivating, and tracking nuclear materials and devices. Pulses of neutrons or high energy X-rays interact with nuclear materials to produce  $\gamma$ -rays, which can be easily detected and used to monitor imports and exports in ports for example. Scanners for this technology should be equipped to shield both the source and signals as a result of the irradiation. Similar materials as those described for fission and fusion chambers above can be expected to be of interest. General defense capabilities could also benefit from this thesis. Propulsion systems operating at higher temperatures and generating faster speeds can provide greater opportunity to intercept attacks.

Making solar energy economical and providing energy from fusion are of similar scope and part of a broader issue of energy production. Both can be considered solutions to minimizing the environmental impact of energy production, which is also intimately connected to developing carbon sequestration methods, by reducing greenhouse gases rather than sequestering them. The specific appeal of these two energy sources compared to other forms of energy harvesting techniques is the vast availability of the energy source. The challenges of making solar energy economical include improving the efficiency and storing the energy once it is converted.

Limitations of current solar cell technology can be overcome by using nanotechnology. However, the use of nanotechnology complicates fabrication and increases costs. New technology to produce and fabricate devices incorporating nanotechnology is needed. Self-assembly of atoms, molecules, and particles are promising methods for producing ordered nanoarrays that could facilitate such technology. Part of this process would require the use of suitable templates, or surfaces that control the self-assembly behavior, but also provide function within the device. Two-dimensional materials are a form of nanotechnology that may prove to be suitable templates. Much attention is received from graphene and boron nitride as two-dimensional materials and to some extent they are tailorable. Recently, a family of two-dimensional materials called MXenes has been demonstrated. Chapter nine of this thesis is a precursor to understanding two-dimensional structure within a three-dimensional structure for diverse chemistries beyond more traditional layered ceramics, which may

ultimately be exfoliated into two-dimensional materials that can be useful templates for self-assembly.

Group IV-VI transition metal carbides, like TaC, are known to have catalytic activity for hydrogenation, dehydrogenation, dehydrogenolysis, hydrodenitrogenation, oxidation, and isomerization reactions. The catalytic activity approaches, and sometimes exceeds, that of the more expensive group VIII metal catalyst for certain reactions. Lower catalytic activity can be offset by the cost reduction for some reactions. These types of reactions can be used as a substitute for carbon sequestration. Rather than trap and store carbon dioxide, it could be converted to fuels and other useful compounds, including liquids that are more manageable than gaseous carbon dioxide. Likewise, such reactions could be useful for denitrification, to balance the nitrogen cycle. These types of reactions can also be used for engineering medicines. Thus materials in this study are of interest as catalysts or for catalyst supports. The development of high surface area nanopowders is particularly important for catalysis. The prospect of two-dimensional materials described previously could also become important.

Several potential impacts of this thesis for the grand challenges of engineering have been described. However, this list fails to fully encompass all of the potential usefulness. Defining the benefits of this thesis is also complicated by the broad potential applicability to many material systems. For example, some of the nitrides studied in chapter two are of interest for microelectronics. The BN studied in chapter two has a structure that is thought to be a more suitable precursor to forming cubic BN, a potential material for applications requiring ultra hardness. Perhaps those reading this thesis will find alternate ways to exploit these materials in beneficial ways.

# TABLE OF CONTENTS

	<b>Page</b>
Acknowledgments .....	iii
Preface .....	iv
Table of contents.....	xii
List of Tables .....	xv
List of Figures.....	xvii
Abstract.....	xxvi
<b>CHAPTER 1: INTRODUCTION.....</b>	<b>1</b>
A. Ultra-High Temperature Ceramics .....	1
1. Applications .....	4
2. Property and Characteristic Requirements.....	11
1. Testing of Ultra-High Temperature Ceramics .....	12
B. Oxidation of Ultra-High Temperature Ceramics .....	15
1. Protective Oxidation Scales .....	17
2. Methodologies of Improving the MB <sub>2</sub> /SiC Oxidation Scale .....	21
C. Tantalum Carbide .....	26
1. Properties and Characteristics of Tantalum Carbide.....	28
2. Tantalum Carbide Synthesis .....	35
3. Sintering .....	37
References.....	45
<b>CHAPTER 2: SYNTHESIS OF NANOSTRUCTURED TRANSITION METAL BORIDE, CARBIDE, AND NITRIDE POWDERS PRODUCED BY SOLVOTHERMAL SYNTHESIS.....</b>	<b>63</b>
A. Introduction.....	63
B. Experimental Procedures .....	67
C. Results and Discussion .....	71
1. Borides .....	71
2. Carbides .....	74
D. Nitrides.....	76
1. Analysis of TaB <sub>2</sub> , ZrC, HfC, and BN.....	79
2. Potential of the Solvothermal Synthesis Technique .....	86
E. Conclusions.....	88

F. References.....	90
<b>CHAPTER 3: A SOLVOTHERMAL APPROACH FOR THE PREPARATION OF NANOSTRUCTURED CARBIDE AND BORIDE ULTRA-HIGH TEMPERATURE CERAMICS .....</b>	<b>99</b>
A. Introduction.....	99
B. Experimental Procedures .....	100
G. Results and Discussion .....	102
H. Conclusions.....	108
I. References.....	110
<b>CHAPTER 4: STATISTICAL EXPERIMENTAL DESIGN APPROACH TO THE SOLVOTHERMAL SYNTHESIS OF NANOSTRUCTURED TANTALUM CARBIDE POWDERS .....</b>	<b>112</b>
A. Introduction.....	112
B. Experimental Procedures .....	114
1. Experimental Methodologies .....	114
2. Data Analysis .....	118
C. Results and Discussion .....	120
1. Phase Development.....	120
2. Crystallite and Particle Size .....	126
3. Surface Characteristics.....	132
4. Evaluating Trends using Analysis of Variance.....	133
D. Conclusions.....	136
E. References.....	138
<b>CHAPTER 5: RESISTANCE SINTERING OF TANTALUM CARBIDE NANOPOWDERS PRODUCED BY SOLVOTHERMAL SYNTHESIS.....</b>	<b>141</b>
A. Introduction.....	141
B. Experimental Procedures .....	142
C. Results and Discussion .....	143
D. Conclusions.....	155
E. References.....	157
<b>CHAPTER 6: THE EFFECT OF SINTERING TEMPERATURE ON CARBON VOLATILITY DURING RESISTANCE SINTERING OF TANTALUM CARBIDE NANOPOWDERS PRODUCED BY SOLVOTHERMAL SYNTHESIS .....</b>	<b>160</b>
A. Introduction.....	160
B. Experimental Procedures .....	162
C. Results and Discussion .....	163

D. Conclusions.....	172
E. References.....	174
<b>CHAPTER 7: OBTAINING HIGH DENSITY TANTALUM CARBIDE COMPACTS VIA RESISTANCE SINTERING OF NANOPOWDERS PRODUCED BY THE SOLVOTHERMAL SYNTHESIS METHOD.....</b>	<b>177</b>
A. Introduction.....	177
B. Experimental Procedures.....	178
C. Results and Discussion.....	179
D. Conclusions.....	188
E. References.....	190
<b>CHAPTER 8: THE EFFECT OF TUNGSTEN CARBIDE AND ZIRCONIUM CARBIDE ADDITIONS ON THE DENSIFICATION AND GRAIN GROWTH OF TANTALUM CARBIDE.....</b>	<b>195</b>
A. Introduction.....	195
B. Experimental Procedures.....	197
C. Results and Discussion.....	199
D. Conclusions.....	211
References.....	213
<b>CHAPTER 9: CONTROL OF MICROSTRUCTURAL DEVELOPMENT IN ULTRA-HIGH TEMPERATURE CERAMICS.....</b>	<b>217</b>
A. Introduction.....	217
B. TaC-Based Composites.....	219
C. MB <sub>2</sub> -Based Composites.....	223
D. Other UHTC Systems.....	225
E. Summary.....	227
F. References.....	229

## LIST OF TABLES

	Page
Table 1 – I. Melting Temperatures of UHTCs <sup>[16,20]</sup> .....	3
Table 1 – II. Critical Properties and Characteristics for UHTC Analysis and Design <sup>[2]</sup> .....	12
Table 1 – III. Selection of ground-based testing of UHTCs (adapted from Corral <sup>[54]</sup> ).....	14
Table 1 – IV. Average Thermal Expansion Coefficients of TaC from Jun and Shaffer <sup>[132]</sup> .....	30
Table 1 – V. Advantages and Disadvantages of TaC Synthesis Techniques .....	38
Table 1 – VI. Density (% $\rho_{th}$ ), Grain Size (G), Powder Type, Applied Pressure (P), and Temperature (T) used to Sinter Nearly Stoichiometric (or Unreported) TaC by Different Sintering Methods .....	39
Table 2 – I. Melting Temperatures ( $T_m$ ) and Adiabatic Flame Temperature ( $T_{ad}$ ) by Reaction from the Compound Constituents of Selected Ultra-High Temperature Ceramics <sup>[14-15]</sup> .....	64
Table 2 – II. Balanced Solvothermal Synthesis Reactions of Various Ultra-High Temperature Ceramics .....	68
Table 2 – III. Supplier Information for Raw Materials .....	68
Table 2 – IV. Reactant Amounts used to Produce Boride, Carbide, and Nitride Powders.....	69
Table 2 – V. Crystallite Sizes of TaB <sub>2</sub> , HfC, ZrC, and BN Measured by X-Ray Diffraction Line Broadening ( $d_{XRD}$ ) and Calculated from Density/Surface Area Measurements ( $d_{CALC}$ ).....	80
Table 2 – VI. Compounds Synthesized by Self-Propagating High-Temperature Synthesis. Adapted from Moore and Feng. <sup>[27]</sup> .....	87
Table 4 – I. Analysis of Variance (ANOVA) Summary Containing F-statistics, Rejection or Acceptance of the Null Hypothesis Stating No Significant	

Contribution for a 10% Confidence Interval, Highlighting for Comparisons to  
Prior Discussion, and the Estimated Probability (P) of a Type I Error..... 135

Table 9 – I. Compositions of TaC-Based Composites with WC, ZrC, and carbon Added.  
..... 198

# LIST OF FIGURES

	Page
Figure 1 - 1. Arbitrarily drawn trajectories that could be expected for blunt leading edge vehicles (trajectory 1) and sharp leading edge vehicles (trajectory 2) for space re-entry.....	6
Figure 1 - 2. Large angle of attack (AOA) for (a) blunt leading edge (BLE) and optimum AOA for (b) sharp leading edge (SLE) designs. (c) Lift-to-drag is optimum at a critical AOA, and decreases for higher AOA.....	6
Figure 1 - 3. Various schemes for sharp leading edges that incorporate ultra-high temperature ceramics (grey phase).....	8
Figure 1 - 4. Thermal management concept of UHTC sharp leading edges demonstrating heat dissipation by heat transport to cooler regions via high thermal conductivity (K) and radiation to the atmosphere via high emissivity ( $\epsilon$ ) (adapted from Squire <i>et al.</i> <sup>[2]</sup> ).....	9
Figure 1 - 5. (a) Model temperature distribution in a simulated re-entry trajectory for a ZrB <sub>2</sub> nose cone reaching speeds near Mach 8 and (b) the effect of thermal conductivity and emissivity on the tip temperature. (Dotted lines are pseudo contours demonstrating the increasing importance of emissivity at low thermal conductivities/higher temperatures. Adapted from Savino <i>et al.</i> <sup>[38]</sup> ). (With color).....	10
Figure 1 - 6. Differences in stream characteristics generated by subsonic and supersonic flows (adapted from Marschall and Fletcher. <sup>[68]</sup> ).....	15
Figure 1 - 7. Typical oxide scale of ZrB <sub>2</sub> /SiC or HfB <sub>2</sub> /SiC UHTC after (a) furnace oxidation and (b)/(c) arc-jet testing (features include (I) glass layer, (II) oxide sub-scale, (III) SiC depleted layer, and (IV) bulk UHTC. Images reproduced from Levine <i>et al.</i> and Monteverede <i>et al.</i> ). <sup>[48,85]</sup> .....	18
Figure 1 - 8. Vapor pressure of B <sub>2</sub> O <sub>3</sub> , SiO <sub>2</sub> , and ZrO <sub>2</sub> as a function of temperature (P = 1 atm). Dotted lines correspond to temperatures where vapor pressures exceed 0.01 Pa (adapted from Zhang <i>et al.</i> <sup>[39]</sup> ). (With color).....	22
Figure 1 - 9. (a) ZrB <sub>2</sub> -SiC and (b) ZrB <sub>2</sub> -SiC-LaB <sub>6</sub> compacts after oxyacetylene torch testing for 600 sec, reaching temperature of ~2673 K and (c) surface and (d) cross-section analysis of the ZrB <sub>2</sub> -SiC-LaB <sub>6</sub> , indicating a dense outer surface	

is responsible for advanced ablation resistance (Images reproduced from Zhang <i>et al.</i> <sup>[90]</sup> ). (With color).....	23
Figure 1 - 10. Oxidation scale thickness of HfB <sub>2</sub> -20SiC samples with (a) large grain size and (b) small grain size as well HfB <sub>2</sub> -10SiC-5TaSi <sub>2</sub> samples with (c) large and (d) small grain sizes after arc-jet testing (Images reproduced from Gasch <i>et al.</i> <sup>[13]</sup> ). (With color).....	25
Figure 1 - 11. Ta-C phase diagram (adapted from Gusev <i>et al.</i> <sup>[98]</sup> ). Single-phase fields are labeled and abbreviated, two-phase fields are labeled with the phase abbreviations, and a box surrounds the label if the label is outside of the phase field. An “x” denotes possible carbon sub-stoichiometry. (With color).....	26
Figure 1 - 12. (a) Molecular orbital diagram demonstrating the reconfiguration of tantalum and carbon electron states in the TaC ground state (adapted from Krechkivska and Morse <sup>[102]</sup> ) and (b) the approximate density of states about the Fermi energy for TaC (adapted from Sahnoun <i>et al.</i> <sup>[103]</sup> ). (With color).....	27
Figure 1 - 13. Variation in TaC density with carbon content (14.5 g/cm <sup>3</sup> describes the density of TaC <sub>0.88-1.00</sub> . Adapted from Bowman <sup>[112]</sup> ). (With color).....	29
Figure 1 - 14. Specific heat of TaC from 1200-2500 K, (adapted from Samsonov <sup>[101]</sup> ).....	31
Figure 1 - 15. Elastic moduli of TaC with porosity. (With color).....	32
Figure 1 - 16. Summary of TaC fracture strength found in the literature as a function of density. The black dotted line is an exponential fit to the data. The red dotted lines are arbitrary exponential functions demonstrating the range of values reported. (With color).....	34
Figure 1 - 17. (a) Density and (b) grain sizes of TaC sintered at temperatures from 1073-1923 K and pressures from 1.5-4.5 GPa (dotted lines correspond to temperature of maximum density. Adapted from Yohe and Ruoff. <sup>[125]</sup> ) (With color).....	41
Figure 1 - 18. Microstructures observed by pressureless sintering of TaC at 2573 K, (a) Powder B with a particle size of 360 nm and (b) Powder C with a particle size of 250 nm (adapted from Liu <i>et al.</i> <sup>[121]</sup> ). (With color).....	42
Figure 1 - 19. Microstructural differences observed for (a) TaC and (b) TaC <sub>0.7</sub> (adapted from Hackett <i>et al.</i> <sup>[129]</sup> ). .....	43

Figure 2 - 1.	Powder X-ray diffraction patterns and phase identification for the attempted (a) TaB <sub>2</sub> , (b) HfB <sub>2</sub> , and (c) ZrB <sub>2</sub> synthesis. (With color).....	72
Figure 2 - 2.	Powder X-ray diffraction patterns and phase identification for the attempted (a) ZrC and (b) HfC. (With color).....	75
Figure 2 - 3.	Powder X-ray diffraction patterns for (a) TaC containing residual tantalum and (b) the same TaC after heat treating at 873 K for 3 hours in argon to reduce the tantalum phase. (With color).....	76
Figure 2 - 4.	Powder X-ray diffraction patterns and phase identification for the attempted (a) TaN, (b) HfN, (c) ZrN, and (d) BN. (With color) .....	77
Figure 2 - 5.	Particle size distributions of TaB <sub>2</sub> , ZrC, HfC, and BN measured by dynamic light scattering (average sizes are given in the legend). (With color)	81
Figure 2 - 6.	Back-scattered electron image of (a) TaB <sub>2</sub> , (b) ZrC, (c) HfC, and (d) BN powders.....	82
Figure 2 - 7.	Secondary electron image of BN powders, highlighting a few examples of bright edges that could correspond to whisker or platelet morphologies. (With color).....	83
Figure 2 - 8.	Thermogravimetric analysis of TaB <sub>2</sub> , HfC, ZrC, and BN powders. (With color).....	85
Figure 3 - 1.	Images of the self-propagating solvothermal synthesis reaction, followed by cooling, for the synthesis of TaC. Images are taken every two seconds for 30 sec after ignition (t = 0 s). (With color).....	103
Figure 3 - 2.	X-ray diffraction patterns for 3-g TaC and LaB <sub>6</sub> powders after washing. (With color).....	105
Figure 3 - 3.	Particle size distributions for TaC and LaB <sub>6</sub> powders. Average particle sizes are given in the legend. (With color) .....	106
Figure 3 - 4.	Back-scattered electron image of TaC powders.....	107

Figure 3 - 5.	Back-scattered electron images of (a) thermally-ignited LaB <sub>6</sub> and (b) chemically-ignited LaB <sub>6</sub> .	108
Figure 4 - 1.	Experimental design space for the 48 experiments of the 4×4×3 full factorial design. The experiments are represented by intersecting lines. Red lines contain all experimental space, blue dotted lines are drawn for the interior of the outer surfaces of the design space, purple lines are drawn for space extending into the interior of the design space. (With color).	115
Figure 4 - 2.	Powder X-ray diffraction patterns demonstrating the effects of (a) reductant type, (b) carbon stoichiometry, and (c) reductant stoichiometry on TaC phase development for solvothermal synthesis. (With color).	121
Figure 4 - 3.	Qualitative phase analysis according to the reductant type, carbon stoichiometry, and reductant stoichiometry.	123
Figure 4 - 4.	Compound stoichiometry of TaC, C/Ta, according to reductant type (a) lithium and (b) calcium, carbon stoichiometry, and reductant stoichiometry. Actual data is superimposed onto the plot.	125
Figure 4 - 5.	Crystallite sizes of TaC determined by XRD, according to reductant type (a) lithium and (b) calcium, carbon stoichiometry, and reductant stoichiometry. Actual data is superimposed onto the plot.	126
Figure 4 - 6.	Specific surface area of TaC, according to reductant type (a) lithium and (b) calcium, carbon stoichiometry, and reductant stoichiometry. Actual data is superimposed onto the plot.	128
Figure 4 - 7.	Comparison of the average crystallite sizes of TaC measured by powder X-ray diffraction ( $d_{XRD}$ ) versus calculation from specific surface area and density measurements ( $d_{CALC}$ ) assuming a spherical morphology. Black circles are lithium data, red squares are calcium data, perfect correlation is given as a solid line and 45% deviation from perfect correlation is given as dotted lines. (With color).	129
Figure 4 - 8.	Average particle size of TaC according to reductant type (a) lithium and (b) calcium, carbon stoichiometry, and reductant stoichiometry. Actual data is superimposed onto the plot.	130
Figure 4 - 9.	Figure of merit of TaC powders according to reductant type (a) lithium and (b) calcium, carbon stoichiometry, and reductant stoichiometry. Actual data is superimposed onto the plot.	131

Figure 4 - 10. Percent weight loss of tantalum carbide powders up to 400°C in air according to (a) lithium and (b) calcium, carbon stoichiometry, and reductant stoichiometry. Actual data is superimposed onto the plot. ....	133
Figure 5 - 1. Phase analysis for powder XRD patterns for oxidized (a) as-synthesized powders, (b) powders after two nitric acid washing cycles, and (c) powders after nine water washes. ....	144
Figure 5 - 2. (a) Displacement rate curve for a resistance sintered TaC at 2323 K. Dotted lines in this curve are cut-off temperatures, held for 30 s, for the sintering of secondary specimens used to generate the XRD patterns given in (b)-(e). The XRD patterns correspond to specimens sintered to temperatures of (b) 1073 K, (c) 1373 K, (d) 1773 K, and (e) 2223 K. ....	146
Figure 5 - 3. (a) Back-scattered electron image and (b) secondary electron image of the fracture surface for a specimen that was sintered at 1073 K using resistance sintering. An impurity phase is circled. (With color). ....	148
Figure 5 - 4. (a) Back-scattered electron image and (b) secondary electron image of the fracture surface for a specimen that was sintered at 1773 K using resistance sintering. Heterogeneous distribution of Ta <sub>2</sub> O <sub>5</sub> impurity phase is demonstrated by red circle. (With color) ....	149
Figure 5 - 5. Back-scattered electron images of fracture surfaces for specimens sintered at (a) 2223 K and (b) 2323 K for 30 sec by resistance sintering. Phase of lower average atomic number at grain boundaries are highlighted. (With color). ....	150
Figure 5 - 6. Secondary electron images of specimens from powders containing (a) zero, (b) three, (c) five, and (d) six weight percent addition of carbon and sintered at 2473 K for 10 min by resistance sintering. ....	151
Figure 5 - 7. (a) Back-scattered electron image and (b) secondary electron image of TaC with six percent carbon added and sintered at 2473 K for 10 min by resistance sintering. ....	152
Figure 5 - 8. Back-scattered electron images of TaC specimens with three percent carbon added and sintered at 2473 K for 10 min by resistance sintering and using heating rates of (a) 200 K/min, (b) 300 K/min, and (c)/(d) 400 K/min. ....	154

Figure 5 - 9. (a) Back-scattered electron image and (b) secondary electron images for TaC specimens with three percent carbon added sintered using a heating rate of 400 K/min, a dwell temperature of 2123 K, and a dwell time of 10 min.....	155
Figure 6 - 1. (a) Displacement and displacement rate during resistance sintering of tantalum carbide as a function of temperature and (b) displacement as a function of time at different sintering temperatures. (With color).....	163
Figure 6 - 2. Secondary electron micrographs of TaC and produced by resistance sintering at (a) 1973 K, (b) 2173 K, (c) 2233 K, and (d) 2373 K. ....	165
Figure 6 - 3. Average grain sizes (with fitted line) of TaC sintered by resistance sintering of nanopowders produced by solvothermal synthesis. (With color).....	166
Figure 6 - 4. Total, closed, and open porosity of TaC sintered at various temperatures and calculated by the immersion technique. (With color) .....	167
Figure 6 - 5. (a) Back-scattered electron image and (b) secondary electron image of an inclusion leading to Type I pore generation at high temperature. (With color).....	168
Figure 6 - 6. (a) Back-scattered electron image and (b) secondary electron image demonstrating inclusions of higher average atomic number (AAN) or similar AAN that could lead to Type II pore generation. ....	169
Figure 6 - 7 Lattice parameter of tantalum carbide after resistance sintering at different temperatures. The scale to the right corresponds to the carbon stoichiometry from Bowman. <sup>[32]</sup> (With color).....	171
Figure 7 - 1. (a) Ram displacement during the resistance sintering of TaC/C mixtures as a function of temperature and (b) the data presented again using truncated scales. (With color).....	180
Figure 7 - 2. Secondary electron images of samples (a) T250, (b) T275, (c) T300, (d) T325, and (e) T350. (f) Optical images of the TaC samples with different free carbon contents. ....	181

Figure 7 - 3.	The average grain sizes and plus or minus one standard deviation measured for TaC as a function of carbon additions after resistance sintering at 2173 K for 10 min with an applied pressure of 50 MPa. (With color).....	182
Figure 7 - 4.	Apparent specific gravity (ASG) and bulk density of TaC/C mixtures sintered via resistance sintering at 2173 K for 10 min and with an applied pressure of 50 MPa. (With color) .....	183
Figure 7 - 5.	Lattice parameters and corresponding carbon stoichiometry of TaC with different carbon additions. (With color) .....	185
Figure 7 - 6.	(a) Backscattered electron image of T350 demonstrating a “melted” TaC grain. (b) Secondary electron image of TaC grain “melted” around a carbon nanotube. <sup>[36]</sup> (With color).....	187
Figure 7 - 7.	(a) Oxide segregation at grain boundary following 2673 K reheat treatment. <sup>[52]</sup> (b) Decohesive grain boundaries observed after creep testing at 1500°C/60 MPa for 60-70 hours, followed by 50%HF-50%HNO <sub>3</sub> etching. <sup>[53]</sup> .....	188
Figure 8 - 1.	(a) Ram displacement and displacement rate for TaC-WC composites during resistance sintering. (b) The ram displacement is provided again with a truncated scale and with the onset temperature, T <sub>o</sub> , for densification of TaC without WC. (With color).....	200
Figure 8 - 2.	(a) Ram displacement and displacement rate for TaC-ZrC composites during resistance sintering. (b) The ram displacement is provided again with a truncated scale and with the onset temperature, T <sub>o</sub> , for densification of TaC without WC. (With color).....	201
Figure 8 - 3.	X-ray diffraction patterns for tantalum carbide-based composites having tungsten carbide or zirconium carbide additions. (With color) .....	202
Figure 8 - 4.	Secondary electron images of samples (a) W001, (b) W010, (c) W100, (d) W200, (e) W300, and (f) W300 (lower magnification). .....	203
Figure 8 - 5.	Secondary electron images of samples (a) Z001, (b) Z010, (c) Z100, (d) Z200, (e) Z300, and (f) a back-scattered electron image of Z300. ....	205
Figure 8 - 6.	Lattice parameters of (a) binary cubic monocarbides, derived from literature, and of (b) (W,Ta)C <sub>0.98</sub> composites based on mole percentages and using Vegard’s law. <sup>[44-47]</sup> (With color).....	206

Figure 8 - 7. Images of TaC grain boundary and sub-grain boundary structures: (a) Seven TaC grains containing sub-grain boundaries, (b) a single grain boundary with sub-grain boundaries intersecting, and (c) a replica of dislocation etch pits making up a sub-grain boundary. <sup>[47]</sup> .....	208
Figure 8 - 8. (a) Experimental and predicted lattice parameters for (Zr,Ta)C <sub>0.98</sub> composites based on mole percentages and Vegard's law and (b) provided again with a truncated scale. (With color) .....	208
Figure 8 - 9. (a) Back-scattered electron image of the fracture surface of sample Z300 and energy dispersive spectra of (b) region B, (c) region C, and region D. Circled regions are clusters of (Zr,Ta)C grains. (With color).....	210
Figure 8 - 10. Predicted lattice parameter of TaC-HfC composites, including experimental data points from the literature. <sup>[43,47]</sup> (With color) .....	211
Figure 9 - 1. (a) Oxide scale features of MB <sub>2</sub> /SiC composite, (b) microstructure of the nanolamellar Ta <sub>4</sub> C <sub>3</sub> phase, and (c)/(d) reduced oxide scale thickness with decreased grain size. <sup>[1,2,7]</sup> (With color) .....	218
Figure 9 - 2. (a) TaC, (b) TaC-WC composite, (c) and TaC-ZrC composite sintered by resistance sintering with the same parameters. (d) Proposed nanostructuring schemes include nanolammelar structuring with stacking faults with a second phase to pin grain growth and solid solutions that remove stacking faults. (With color).....	220
Figure 9 - 3. Microstrucutral comparison of fully dense (a) TaC and (b) TaC-1%B <sub>4</sub> C and partially dense (c) TaC and (b) TaC-1%B <sub>4</sub> C. Fully dense samples are prepared using similar conditions and partially dense samples are produced using similar conditions (reproduced from Bakshi <i>et al.</i> ). <sup>[17]</sup> .....	222
Figure 9 - 4. Microstructural comparison of HfB <sub>2</sub> -based composites prepared by resistance sintering and demonstrating refinement in microstructure by substitution of TaSi <sub>2</sub> for SiC (reproduced from Gasch and Johnson). <sup>[7]</sup> .....	224
Figure 9 - 5. Microstructural comparison of (a) 90TiB <sub>2</sub> -10TaC and (b) 80TiB <sub>2</sub> -20TaC (adapted from Shvab and Egorov). <sup>[30]</sup> .....	226
Figure 9 - 7. Microstructural comparison of (a) TiC <sub>0.8</sub> N <sub>0.2</sub> and (b) TiN <sub>0.8</sub> C <sub>0.2</sub> compositions (adapted from Urbonaite <i>et al.</i> ). <sup>[16]</sup> .....	227



## ABSTRACT

Ultra-high temperature ceramics (UHTCs) are a unique class of materials with the potential to withstand harsh environments due to covalent bonding, which gives these materials high melting temperatures, although decomposition temperatures should also be considered. For example, the melting temperature of TaC is near 4000 K, but may vaporize at lower temperatures. The high melting temperatures also make them difficult to process without high pressures and temperatures and to achieve dense ceramics with a nanostructure. Such materials however are appealing for aerospace technologies. The ability to generate high density compacts and maintain a nanostructure could allow for unprecedented control and improvement to the mechanical properties.

The goal of this work is to develop processes for the synthesis and consolidation of nanostructured UHTCs. A self-propagating solvothermal synthesis technique for making UHTC nanopowders is presented. The technique is fast, scalable, and requires minimal external energy input. Synthesis of transition metal boride, carbide, and nitride powders is demonstrated. TaC is synthesized using a range of synthesis conditions and characterized to determine the fundamental mechanisms controlling the nanopowder characteristics. Discussion on purification of the powders is also presented.

The sintering of TaC nanopowders produced by the solvothermal synthesis method is performed by resistance sintering. The effects of temperature, heating rate, and dwell time on densification and grain growth is presented. Adequate powder processing, carbon content, volatilization, and additives are found to be critical factors affecting the densification, microstructure, and grain growth.

The optimal range of carbon addition for minimizing oxygen content is determined. WC and ZrC are evaluated as additives for reducing grain growth of TaC. Secondary phases and/or solid solutions are capable of suppressing grain growth. A unified approach to solid solution chemistries to control the densification, microstructure, and properties of UHTCs in general is presented. This work has important consequences on advancing the properties of UHTCs.



## **CHAPTER 1: INTRODUCTION**

Ultra-high temperature ceramics (UHTCs) are a class of materials capable of withstanding harsh environments. The key characteristic is a material having a high melting temperature, but the remaining properties distinguish UHTC materials. Unlike most ceramics, which are insulators, UHTCs have metallic like properties and characteristics as well. Although UHTCs can withstand high temperature, it is the ability to conduct heat away from a hot zone (i.e. high thermal conductivity) that makes them suitable for advanced thermal protection systems. Ultimately, much work is still required for obtaining a suitable combination of properties/characteristics designed for specific applications.

UHTCs are primarily limited by the formation (or lack of formation) of protective oxide scales on their surfaces following degradation. The general approach for obtaining a suitable oxide scale is via design of composite materials. The current understanding of the oxide scale formation mechanisms is guiding the design of new composite UHTC materials that may result in improved performance of UHTCs. Tantalum containing compounds, such as TaC for example, have been identified as a promising additive for improving the oxidation resistance of UHTC composites.

Any modification to UHTC composite chemistry should be studied from two perspectives. The actual composite needs to be tested rigorously. Applications for UHTCs require characterization up to potential operating temperatures in both simulated operating environments and in actual operating environments. However, it is also useful to know how the individual components of a UHTC behave in the absence of other components. The combination of the two perspectives provides insight for how components will interact during processing and application.

### **A. Ultra-High Temperature Ceramics**

Ultra-high temperature ceramics (UHTCs) are designed for ultra-high temperature applications. Therefore, they should have high melting temperatures. Some researchers choose to define UHTCs by their melting temperatures, citing temperatures greater than

values ranging from 2773-3273 K.<sup>[1-3]</sup> The lower end of this range includes oxide ceramics, which are not typically considered UHTC materials. Other researchers consider that UHTCs must be able to function at operating temperatures greater than values ranging from 2073 to 2773 K.<sup>[1,4-7]</sup> Many of the materials classified as UHTCs cannot withstand prolonged exposure at these temperatures if the atmosphere is oxidizing. Another way of defining UHTCs is by application (such as materials for hypersonic flight, space re-entry vehicles, or rocket propulsion).<sup>[1,5,8-10]</sup> However, this definition overlooks the fact that these materials have the potential to be replacement materials for applications that typically do not require UHTC materials.

UHTCs are defined as borides, carbides, nitrides, and silicides with melting temperatures above 2000 K in this work. This includes group IV-VI compounds and covalently bonded metalloid compounds. One group III boride has also been included (LaB<sub>6</sub>). It is important to stress that the temperature limit is lower than typically reported for UHTC materials, but is necessary to include materials that have been included as additives in UHTC composites to improve the high temperature behavior. For example, SiC has a lower melting temperature than ZrB<sub>2</sub> and HfB<sub>2</sub>, but is an additive used to improve the oxidation resistance of these materials at high temperatures.<sup>[11-12]</sup> AlN and disilicide compounds having even lower melting temperatures (closer to 2000 K) can also provide improved behavior at high temperatures.<sup>[13-15]</sup> A partial list of materials commonly researched as UHTCs is provided in Table 1-I. In general, the melting temperatures are highest for the respective carbide and decreases in the order of boride, nitride, and silicide. As UHTC composites are designed to withstand the harsh conditions of multiple applications and ranges of conditions, it may become necessary to continue to modify the definition of UHTC materials.

The group IV-VI carbides and nitrides can be considered interstitial carbides and nitrides.<sup>[17]</sup> In these interstitial compounds, the electronegativity difference between the two elements is large. The size of the carbon and nitrogen are small enough to fit in the interstitial site of the metal lattice. The bonding is metallic, giving rise to high electrical and thermal conductivities, but also covalent and ionic leading to the refractory and brittle nature of the compounds. The bonding of group IV-VI diborides is similarly mixed.<sup>[18-19]</sup> The presence of boron-boron, metal-boron, and metal-metal bonds results in

covalent, a mixture of covalent and ionic (< 8% ionic), and predominantly metallic types of bonding, respectively. It is these materials that are most interesting for advanced thermal protection systems because of their ability to withstand extreme heat and dissipate that heat by quickly conducting it away and emit it back to the atmosphere.

Table 1 – I. Melting Temperatures of UHTCs<sup>[16,20]</sup>

<b>Carbides</b>	<b>T<sub>m</sub> (K)</b>	<b>Borides</b>	<b>T<sub>m</sub> (K)</b>	<b>Nitrides</b>	<b>T<sub>m</sub> (K)</b>	<b>Silicides</b>	<b>T<sub>m</sub> (K)</b>
HfC	4100	HfB <sub>2</sub>	3640	HfN	3600	---	---
TaC	4100	TaB <sub>2</sub>	3540	TaN	3220	TaSi <sub>2</sub>	2670
NbC	3770	NbB <sub>2</sub>	3270	NbN	2900	NbSi <sub>2</sub>	2140
VC	3600	VB <sub>2</sub>	2373	VN	2593	VSi <sub>2</sub>	2023
ZrC	3533	ZrB <sub>2</sub>	3270	ZrN	3230	Zr <sub>5</sub> Si <sub>3</sub>	2420
TiC	3210	TiB <sub>2</sub>	3500	TiN	3560	Ti <sub>5</sub> Si <sub>3</sub>	2400
Mo <sub>2</sub> C	2963	MoB	2625	---	---	MoSi <sub>2</sub>	2553
WC	2900	WB	3133	---	---	WSi <sub>2</sub>	2320
SiC	2820	---	---	---	---	---	---
---	---	LaB <sub>6</sub>	2770	---	---	---	---
B <sub>4</sub> C	2720	---	---	BN	3240	---	---
---	---	---	---	AlN	2470	---	---
---	---	---	---	Si <sub>3</sub> N <sub>4</sub>	2170	---	---

UHTC materials such as B<sub>4</sub>C, BN, AlN, and Si<sub>3</sub>N<sub>4</sub> are characterized by low electronegativity, small elemental size differences, and with bonding that is essentially covalent.<sup>[17]</sup> This gives high melting temperature, but a lack of metallic-like properties compared to the interstitial compounds. In addition to the compounds listed in Table 1-I, there are about 240 binary UHTC materials with melting temperatures above 2273 K and at least 130 with melting temperature above 2773 K if oxide, sulfide, and phosphide compounds are also counted.<sup>[21]</sup> The use of oxides, sulfides, and phosphides are not as well studied as UHTC components. These materials can be added to UHTC compositions to optimize high temperature properties and behavior.

Research on UHTCs is being fueled by the need for the next generation of advanced thermal protection systems for the aerospace and aviation industries. Such applications include, but are not limited to, sharp leading edge structures on space re-entry vehicles, hypersonic aircraft and missiles, and structural materials for rocket propulsion technologies. These applications require a unique combination of thermomechanical and electrical properties. To fully realize the potential of UHTC composites for these applications, a rigorous development and testing program is necessary. More specific details concerning these applications and property requirements leading to the identification of base materials for UHTC composites and the required testing of these materials will be described herein.

## **1. Applications**

Non-oxide ceramics have been known for nearly 200 years, but most applications are more recent. Their use as UHTCs in aviation has been pursued in the 1960's and early 70's by industry, primarily for the United States Air Force.<sup>[22-29]</sup> A review of the status at the beginning of the 1970's is provided by Fenter.<sup>[30]</sup> Given the military implications of the research, it is uncertain how much information has been released and what is left in secrecy. Beyond the controlled dissemination of this early information, UHTC publications were essentially dormant for decades and begins to appear again in the late 1990's.<sup>[12]</sup>

In the 1990's the National Aeronautics and Space Administration (NASA) would renew interest in UHTC research with the development of sharp UHTC leading edge components and testing of such components in real hypersonic flight conditions.<sup>[31-34]</sup> Overall, the emerging technology has the potential to reduce cost, increase reliability, increase operability, and improve safety of cargo- and crew-carrying launch vehicles when compared to the Space Shuttle, for example.<sup>[35-36]</sup> The tests indicated the need for improved processing to obtain more suitable microstructures and properties as well as a need to improve modeling to predict the in-flight conditions.

The design of the recently retired Space Shuttle by NASA consisted of a blunt nose and blunt leading edge wing configuration (~10 cm radius of curvature at the wing tip).<sup>[2]</sup> The first commercial spacecraft to provide transport to the International Space Station, the Dragon capsule developed by Space Exploration Technologies Corporation,

also relies on blunt features. The nose and wing leading edges experience the greatest deal of aerodynamic heating. The blunt configuration in conjunction with a high angle of attack upon space re-entry are used to limit the aerodynamic heating of these structures and allow for the use of thermal protection systems made from carbon/carbon or carbon/SiC composite materials.<sup>[37-38]</sup>

For example, a trajectory using a high angle of attack (AOA) is given in Figure 1-1. A steep trajectory into the earth's atmosphere with a high angle of attack is beneficial for reducing the exposed temperature of the spacecraft, but specific disadvantages of using blunt features include: limited maneuverability, limited re-entry points, ocean aborts on take-off, electromagnetic interference that causes communications blackouts, and high propulsion requirements to balance the high drag.<sup>[31]</sup> A design incorporating sharp features (having radius of curvature of several millimeters instead of centimeters) can overcome many of these disadvantages.<sup>[1-19,21-36,39-42]</sup> Such vehicles can fly at optimum angles of attack with high lift-to-drag ratios, which improves maneuverability. This concept is depicted in Figure 1-2. Vehicles with sharp leading edges are capable of flying similar re-entry trajectories as blunt designs, but they can also follow more gentle trajectories (trajectory 2 in Figure 1-1 for example) because of the improved gliding capabilities. Gentle trajectories improve safety by allowing re-entry at any point into the atmosphere and providing greater abort options.

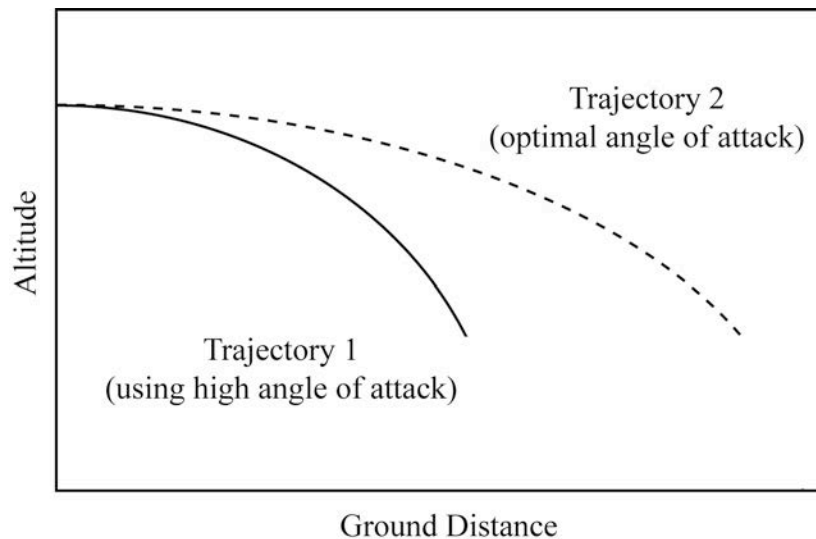


Figure 1 - 1. Arbitrarily drawn trajectories that could be expected for blunt leading edge vehicles (trajectory 1) and sharp leading edge vehicles (trajectory 2) for space re-entry.

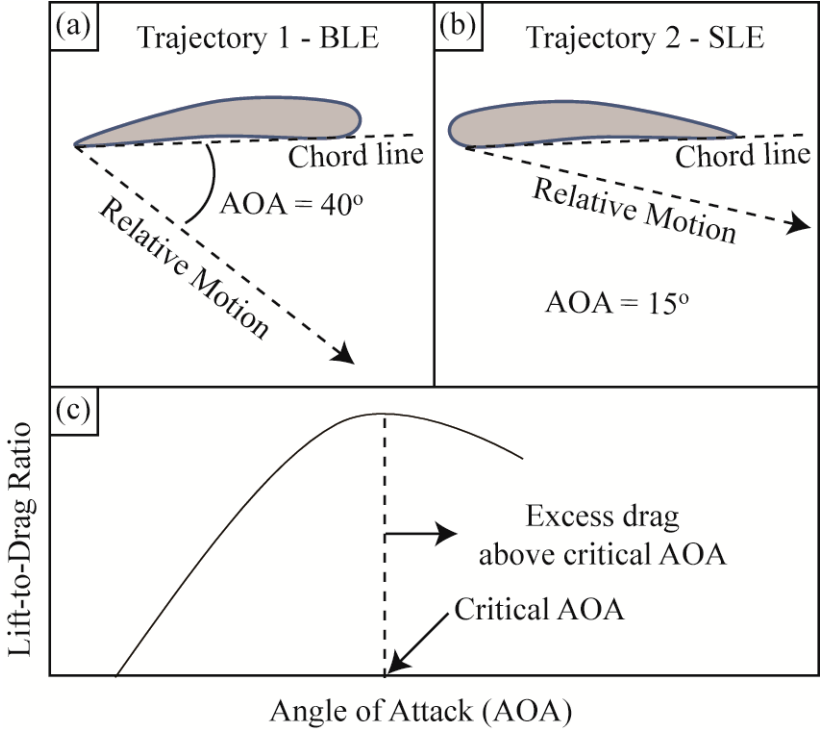


Figure 1 - 2. Large angle of attack (AOA) for (a) blunt leading edge (BLE) and optimum AOA for (b) sharp leading edge (SLE) designs. (c) Lift-to-drag is optimum at a critical AOA, and decreases for higher AOA.

The lack of excess drag to reduce aerodynamic heating implies that the leading edges will be subjected to higher temperature. Furthermore, the reduced curvature of the wing leading edge contributes to a greater amount of aerodynamic heating.<sup>[3,37]</sup> The combined effects result in exposure temperatures that can be in excess of 2073 K, the single-use temperature of currently used carbon/carbon or carbon/SiC composite materials.<sup>[42-48]</sup> The demands of designs that incorporate sharp leading edges will require advanced materials to withstand these temperatures, especially for having multiple-use capabilities.

There are three schemes proposed in the literature for the advanced thermal protection system necessary to enable sharp leading edge components for high-mach aircraft and spacecraft.<sup>[1-2,5,47,50-56]</sup> The three schemes are depicted in Figure 1-3. All schemes would consist of a sharp leading edge having a radius of curvature of a few to

several millimeters and length of several centimeters. The first scheme consists of dispersing UHTC phase(s) into a traditional carbon/carbon or carbon/SiC composite matrix. The major advantage to this scheme is that the matrix phase has already been engineered to meet many of the demanding requirements, such as the mechanical properties for example. The well-established processing of the matrix phase only requires that an understanding of the interactions between the dispersed phase and the matrix phase be established and engineered. Although also an advantage, the major drawback to this scheme is that the continuous matrix will still dominate the behavior. For example, the poor ablation resistance and oxidation behavior when temperatures exceed 2073 K can degrade the interconnected matrix too rapidly.

The second scheme is to form thick UHTC coatings on carbon/carbon or carbon/SiC composites. The advantages of this scheme are similar to the first scheme since the bulk interior of the component is established technology. This scheme would utilize the least amount of UHTC material, reducing the excess weight associated with the relatively high density materials and reducing the overall cost associated with the high cost of processing UHTC materials. Part refurbishment could be as simple as removal and reapplication of the coating materials, followed by the necessary quality checks. The major disadvantage of this scheme is that if the coating cracks or is removed by damage/spalling, the part will become unprotected and result in large material removal of the underlying thermal protection system that cannot withstand the harsh conditions of re-entry. This scenario is reminiscent of the Space Shuttle Columbia disaster in 2003.

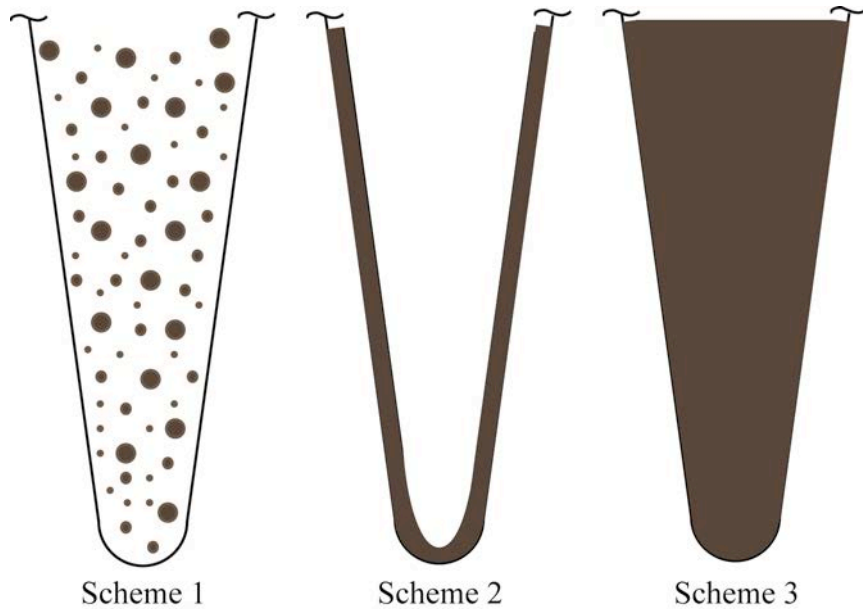


Figure 1 - 3. Various schemes for sharp leading edges that incorporate ultra-high temperature ceramics (grey phase).

The third scheme in Figure 1-3 is the most promising sharp-leading edge concept, a sharp leading edge consisting entirely of a UHTC matrix. The advantage of this configuration is not only the capability to withstand high temperatures, but also the capability to dissipate the heat. The thermal management concept of this scheme is given in Figure 1-4. A high heat flux at the tip of the leading edge would heat the part locally. An UHTC composite having a high thermal conductivity can rapidly transport the heat to cooler surfaces of the leading edge, where it can be radiated back into the atmosphere for UHTC composites having high emissivity. The heat dissipation method is enabled because the heat flux distribution has an inverse square-root dependence on the distance from the tip.<sup>[3,42]</sup> The thermal equilibrium at the tip is determined by a balance of thermal processes into and out of the tip (i.e. convective heating at the tip, chemical heating at the tip, thermal conduction of heat away, and radiation of heat away).<sup>[42]</sup>

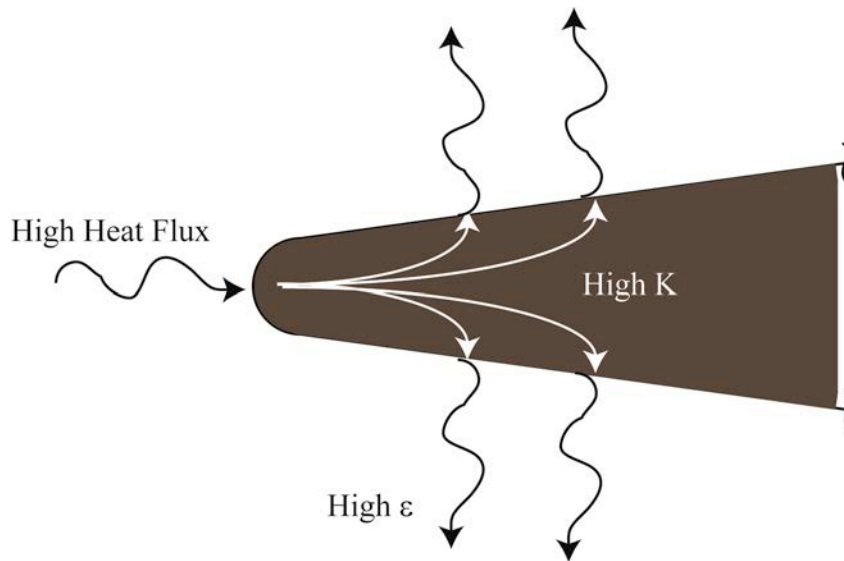


Figure 1 - 4. Thermal management concept of UHTC sharp leading edges demonstrating heat dissipation by heat transport to cooler regions via high thermal conductivity ( $K$ ) and radiation to the atmosphere via high emissivity ( $\epsilon$ ) (adapted from Squire *et al.*<sup>[2]</sup>).

Modeling of the thermal management concept of a UHTC-based sharp leading edge is demonstrated by Savino *et al.*<sup>[39]</sup> In this example the temperature distribution of a sharp cone was simulated for a reference trajectory (sub-orbital re-entry reaching speeds near Mach 8) and using  $ZrB_2$  properties as model parameters. Figure 1-5 gives the temperature distribution in the model component at various times during the simulated re-entry trajectory. The important features are that the tip temperature is the hottest, the temperature is significantly reduced just millimeters away from the tip, and the hottest temperatures are experienced over a short time scale (seconds). Within 10 mm into the bulk of the model, the temperature is approximately 320 K lower at the peak temperature. The maximum temperature is achieved at approximately 60 sec into the re-entry trajectory. Within five seconds from achieving the maximum temperature, the tip temperature has reduced by 200 K. Figure 1-5 also demonstrates that a high thermal conductivity and high emissivity are favorable for reducing the maximum temperature, at the tip of the model. This is exactly why UHTCs are the most promising materials for such an application, particularly zirconium or hafnium diborides as base materials.

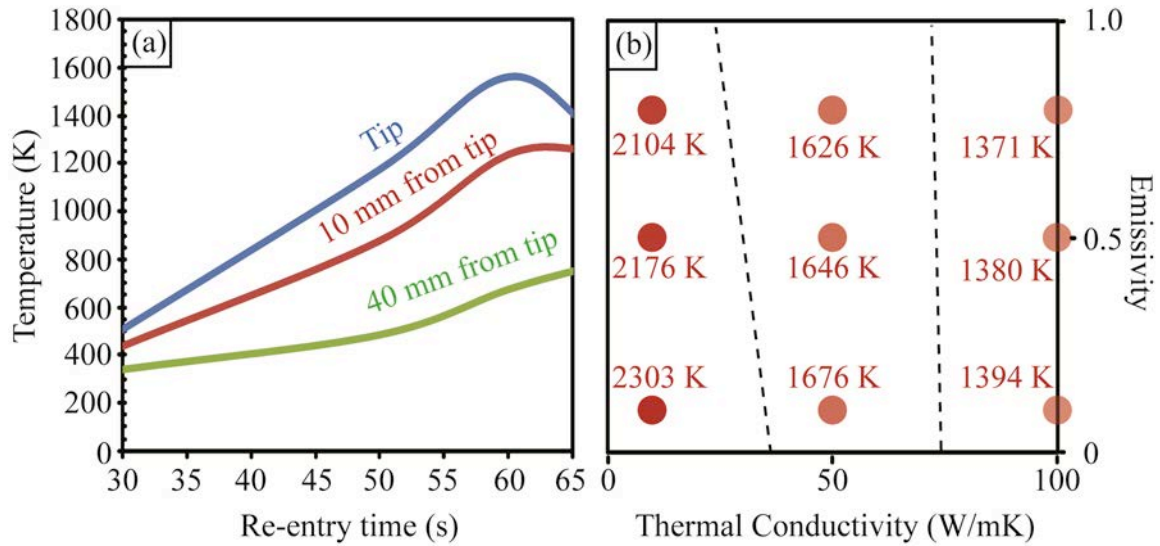


Figure 1 - 5. (a) Model temperature distribution in a simulated re-entry trajectory for a  $ZrB_2$  nose cone reaching speeds near Mach 8 and (b) the effect of thermal conductivity and emissivity on the tip temperature. (Dotted lines are pseudo contours demonstrating the increasing importance of emissivity at low thermal conductivities/higher temperatures. Adapted from Savino *et al.*<sup>[39]</sup>). (With color)

It is worth noting that the initial modeling and testing by NASA resulted in actual temperatures 41-121% lower than expected from modeling.<sup>[31]</sup> More recent modeling and ground-based testing are in good agreement.<sup>[3,57-58]</sup> Squire and Marschall discuss the essential material properties that are necessary to produce accurate models and highlight the importance of accuracy and uncertainty in the property measurements.<sup>[2]</sup> The temperature dependence of all relevant properties are desirable, but are especially critical for thermal conductivity, specific heat, emissivity, tensile modulus, and the thermal expansion coefficient. Measurements of thermal conductivity and emissivity can vary dramatically with temperature, chemistry, and with processing.<sup>[3,59]</sup> Therefore, there is a basic research need to understand the fundamental interplay between processing and properties of a wide range of UHTC compounds and composites.

In addition to space re-entry applications, UHTCs have many other potential uses that supplement the benefit of developing these materials.<sup>[3,12,58,60-68]</sup> In addition to spacecraft, UHTC materials could enable hypersonic aircraft as well, but the UHTCs need to be able to withstand extreme conditions for a more extended period of time compared to space re-entry (minutes to hours compared to seconds). For either

spacecraft or aircraft, UHTC materials could provide benefits for the propulsion systems. For example, by allowing a convectively cooled combustion chamber wall to approach temperatures of 3000 K, propulsion efficiency can be enhanced by up to 50%. Kinetic intercept missiles capable of travelling at greater speeds and with greater propulsion efficiency would greatly benefit national defense capabilities as well. Transition metal carbide UHTCs are also attractive for high-temperature nuclear power generation. UHTCs are currently applied in a variety of applications such as engines, plasma-arc electrodes, crucibles, cutting tools, and wear-resistant coatings.

## **2. Property and Characteristic Requirements**

There is an immediate need to develop and test UHTC compounds and composites. Not only will this increase the certainty of material properties and therefore the confidence of designers, but it will also facilitate the development of multi-scale modeling necessary for UHTC implementation. Multi-scale modeling will be critical for shortening the development time of UHTCs, leading to improvements of existing UHTC properties and the development of new UHTC composites. The modeling of the thermal and mechanical responses to simulated environments typical of laboratory testing as well as the application is necessary. It is crucial to understand the differences between laboratory testing environments and actual conditions and how this affects UHTC behavior to corroborate how modeled and actual behavior during laboratory tests applies to the predictability of performance during application. This is extremely important because actual test environment opportunities are rare, often impractical, and expensive.<sup>[2]</sup>

The development of analytical performance models for the thermomechanical response of UHTCs will require extensive knowledge of UHTC properties, either determined experimentally or verified experimentally.<sup>[2]</sup> It will also be important to know many of these properties as a function of temperature, up to the application temperatures. A slightly more challenging aspect to consider is the development of surface oxidation scales (discussed later), which develop *in situ*. It may be difficult to incorporate the formation of the surface scales and the phase interactions into models that will predict actual behavior, but doing so will require the properties of the scale phases and an understanding of the scale development.

Table 1-II lists the important properties and characteristics that are necessary for developing adequate models of UHTC performance. The physical, thermal, mechanical, and surface properties are used in fundamental equations for computational fluid dynamic calculations. The other properties and characteristics are important support information to help track processing related variances. In reporting properties, it is best to use standardized techniques with well-established uncertainty, or else it is necessary to establish uncertainty of the technique for newly established methods. Most of the properties and characteristics will need to be known as a function of environment and temperature, up to UHTC operating temperatures if possible. It may be necessary to estimate some high-temperature properties.

### 1. Testing of Ultra-High Temperature Ceramics

It is a great challenge to test UHTCs. It becomes increasingly difficult, costly, and sometimes implausible to design equipment for performing characterization at UHTC operating temperatures short of testing components in an actual application environment. The ability to test UHTCs extensively is a major contributing factor to the slow pace of development of UHTC materials. Development of UHTCs is expedited by modeling, but will still require experimental verification to provide confidence in the models. Testing the properties of UHTCs to develop the models and using them to predict behavior are also challenging. Testing performance of UHTCs is the focus of this section.

Table 1 – II. Critical Properties and Characteristics for UHTC Analysis and Design<sup>[2]</sup>

Physical Properties	Density, coefficient of thermal expansion
Thermal Properties	Specific heat, thermal conductivity
Mechanical Properties	Tensile modulus, poisson's ratio
Surface Properties	Total hemispherical emissivity, catalytic efficiency, surface roughness
Other	Melting/eutectic temperatures, microstructural details (phases, lattice parameters, grain sizes, pore sizes,

	distributions), fracture strengths, thermal shock resistance, oxidation behavior/kinetics
Considerations	Standard techniques, error/uncertainty, environment, report processing history/characterization, temperature, reactions at elevated temperatures, anisotropy

There are a variety of testing options currently available for UHTC development. A summary of the ground-based testing facilities has been provided in a review by Corral and is summarized in Table 1-III.<sup>[54]</sup> None of these techniques provides all the hypersonic environmental conditions of actual test flights, but rather serve as screening tests for further development, where low cost testing in a high-temperature furnace or an oxyacetylene torch test can be used to test samples prior to more expensive testing, such as Arcjet testing for example.

The list of techniques given in Table 1-III does not completely summarize efforts to test UHTCs. Plasmatron facilities in general, rather than just arc-jet testing, have also been used to evaluate UHTCs, for example.<sup>[26,69-71]</sup> An inductively coupled plasma (ICP) design produces a stream free of metal contaminants such as copper that can be found in arc-jet flows. Such metal contaminants could influence the chemical processes during the test. However, because of the difficulties in managing high pressures with an ICP design, it is usually used to generate subsonic flows whereas arc-jet facilities can produce supersonic flows. The difference in stream flow behavior can significantly affect the thermochemical state of the gas interacting with the test specimen, specifically because of the formation of a shock wave generated for supersonic flow. The differences in flow characteristics are summarized in Figure 1-6. Careful considerations can allow the establishment of similar boundary layer edge compositions for the two techniques. Although potentially useful from a materials science perspective, the gas composition at the sample surface is not currently accessible experimentally and would require modeling.

Table 1 – III. Selection of ground-based testing of UHTCs (adapted from Corral<sup>[54]</sup>)

<b>Testing method</b>	<b>High-temp furnace</b>	<b>Oxyacetylene torch</b>	<b>Solar</b>	<b>Laser subsonic tunnel</b>	<b>Arcjet</b>
<b>Heating mode</b>	Radiative & convective	Convective	Radiative	Radiative w/ convective cooling	Convective w/ some radiative
<b>Maximum temperature</b>	~2273 K	>2273 K	>2873 K	~2773 K	>2473 K
<b>Heat flux</b>	N/A	>150 W/cm <sup>2</sup>	250-800 W/cm <sup>2</sup>	>250 W/cm <sup>2</sup>	>250 W/cm <sup>2</sup>
<b>Oxygen flux</b>	Poor	Poor	Fair	Good	Excellent
<b>Atomic oxygen</b>	Poor	Poor	Poor	Poor	Excellent
<b>Shear flow</b>	N/A	Some <sup>56</sup>	N/A	Fair	Excellent

Not all plasmatron facilities are created equal. For example, the United States Air Force arc-jet facilities are used to simulate aero-heating for ballistic atmospheric trajectories, while the National Aeronautics and Space Administration arc-jet facilities simulate low pressure trajectories of upper atmosphere/planetary reentry.<sup>[70,72]</sup> Understanding the test environments and interactions with materials is an ongoing effort and it usually involves computational fluid dynamics that require adequate characterization of the part being tested (see previous section). Other considerations beyond those given in Table 1-III include heating rate, modes of ablation, atmospheric gradients, and gas pressures to name a few.

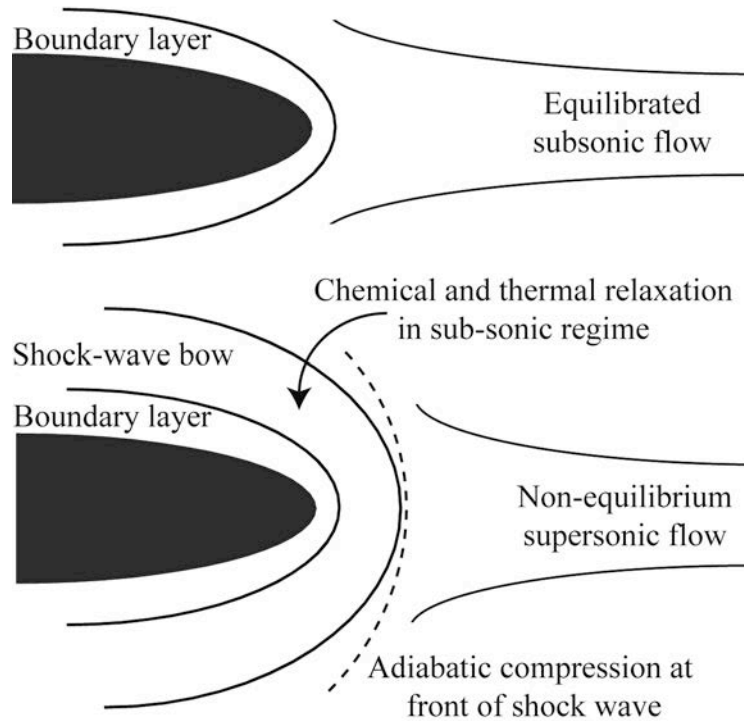


Figure 1 - 6. Differences in stream characteristics generated by subsonic and supersonic flows (adapted from Marschall and Fletcher.<sup>[69]</sup>).

Simulated environments related to propulsion technology are also available. A combustion environment has been simulated using a high-pressure burner rig.<sup>[74]</sup> Such a design is capable of testing at temperatures up to at least 1450°C, pressures of at least 15 atmospheres, gas velocities of at least 30 m/s, and lean and rich fuel-to-air ratios. In general, testing actual combustion environments for propulsion systems is not as difficult as re-entry testing and is something that can be reproduced in ground-based facilities.

## B. Oxidation of Ultra-High Temperature Ceramics

The major limitation of all non-oxide ceramics, and therefore important UHTC materials, is the tendency to oxidize in the presence of oxidizers (primarily oxygen or water) at elevated temperature. In addition to the higher thermal conductivity and relatively low density of  $ZrB_2$ , it was early recognized as one of the more oxidation resistant UHTC non-oxide compounds. These combined factors make  $ZrB_2$  a good candidate as a base UHTC material. Indeed,  $ZrB_2$  and  $HfB_2$  UHTCs represent the most

studied candidate materials for next generation thermal protection systems of space re-entry vehicles and high mach aircraft.

Studying and understanding the oxide scales that form on the surfaces of UHTCs (and interact with the UHTC bulk) is arguably the most important feature for understanding UHTC limitations and guiding the design of UHTC compositions. There are two ways to design such materials: development of a fully protective oxide scale or the development of a partially protective oxide scale for which ablation can be suitably controlled.

In order for a UHTC utilizing application relying on a fully protective oxide scale to be realized, it must be demonstrated that the oxide scale is protective in the atmospheric conditions of the application and through the entire application time. The oxidation scale must slow or eliminate further oxidation to be considered protective, never leading to an accelerated, or active, oxidation condition in which the scale and underlying material are being rapidly removed from the UHTC surface. Maintaining a protective oxide scale provides safety and reliability that is desirable of a UHTC component.

The development of a partially protective oxide scale is more complex, but can be beneficial. In this case, the protective oxide scale should be fully protective at low and moderate temperatures. However, in the most extreme heating conditions, controlled ablation of the material can contribute to the heat removal processes by carrying it away with the gases formed during decomposition. Ablative cooling is the currently used heat shielding technology. If UHTCs are to be used in ablative conditions, then sufficient understanding and control over the ablation behavior is necessary and there should be a demonstrated advantage over using traditional ablative materials.

To reduce costs and further promote the use of UHTCs for advanced thermal protection systems, reusability is another key aspect. From this perspective, a fully protective oxide scale is more beneficial than a partially protective oxide scale relying on ablation. To be as economically advantageous as possible, a protective scale must be able to withstand thermal cycling without losing integrity or at least require minimal refurbishment costs and time compared to already established technology. Baseline analyses of this type are provided in the literature.<sup>[36]</sup>

## 1. Protective Oxidation Scales

The generally improved oxidation resistance of the transition metal diborides versus the respective carbides or nitrides can be attributed to their oxidation products. While carbides and nitrides form a metal oxide solid and gases such as  $\text{CO}_x$  and  $\text{NO}_x$ , the borides tend to form a metal oxide solid and  $\text{B}_2\text{O}_3$  liquid when oxidation is initiated.<sup>[54]</sup> The liquid phase preferentially developed on the surfaces is an oxygen diffusion barrier for further oxidation reactions. The oxide scale is protective up to temperatures of  $1000^\circ\text{C}$ , above which volatilization of the  $\text{B}_2\text{O}_3$  liquid is rapid and no longer able to function as a protective layer on the surface.<sup>[12]</sup>

$\text{SiC}$  and  $\text{Si}_3\text{N}_4$  are notable exceptions of UHTC materials known to have excellent oxidation resistance compared to  $\text{ZrB}_2$  or  $\text{HfB}_2$  at elevated temperature (above the active to passive transition temperature).<sup>[74]</sup> This can be attributed to a protective  $\text{SiO}_2$  layer that develops on the surface of these materials at high temperature. The transition metal diboride/ $\text{SiC}$  system (primarily  $\text{ZrB}_2$  or  $\text{HfB}_2$ ) represents the most studied UHTC system and are the current benchmark for UHTC studies.<sup>[3-4,7,10-12,14,40,46,49,58-60,67,75-88]</sup>

$\text{ZrB}_2$  or  $\text{HfB}_2$  with 15-30% by volume  $\text{SiC}$  is found to have exceptional oxidation resistance. The oxidation of the diboride forms liquid  $\text{B}_2\text{O}_3$  that provides oxidation protection at low temperatures, a borosilicate liquid that provides oxidation protection at intermediate temperatures, a silicate liquid that provides oxidation protection at high temperature, and a refractory oxide layer that can provide oxidation protection at ultra-high temperatures. This is an oversimplification of the complex oxidation processes, but provides the framework for understanding the improved oxidation resistance of these composites. The development of the oxidation scale is highly dependent on the composition and thermal history.

The  $\text{ZrB}_2/\text{SiC}$  and  $\text{HfB}_2/\text{SiC}$  UHTC materials tend to have excellent ablation resistance at ultra-high temperature compared to  $\text{SiC}$  because the presence of a porous refractory oxide layer. The porous oxide layer provides a rigid structural framework that helps maintain the liquid within the capillaries rather than being rapidly removed from the surface via shear flow.

The typical microstructure of the  $\text{ZrB}_2/\text{SiC}$  or  $\text{HfB}_2/\text{SiC}$  UHTC oxidation layer after high temperature exposure is provided in Figure 1-7. Comparisons between Figure

1-7a and Figure 1-7b demonstrates that the same features can be observed using completely different tests (see Table 1-III). Comparing Figure 1-7b and Figure 1-7c, which are images of the same part, but in different regions, demonstrate that the environmental conditions influence the configuration of the oxide scale. More specifically, Figure 1-7b is an image of a region subjected to lower shear stress and lower temperature than Figure 1-7c. The oxidation scale is more compact and retains a higher amount of silicate at the low stress/temperature condition.

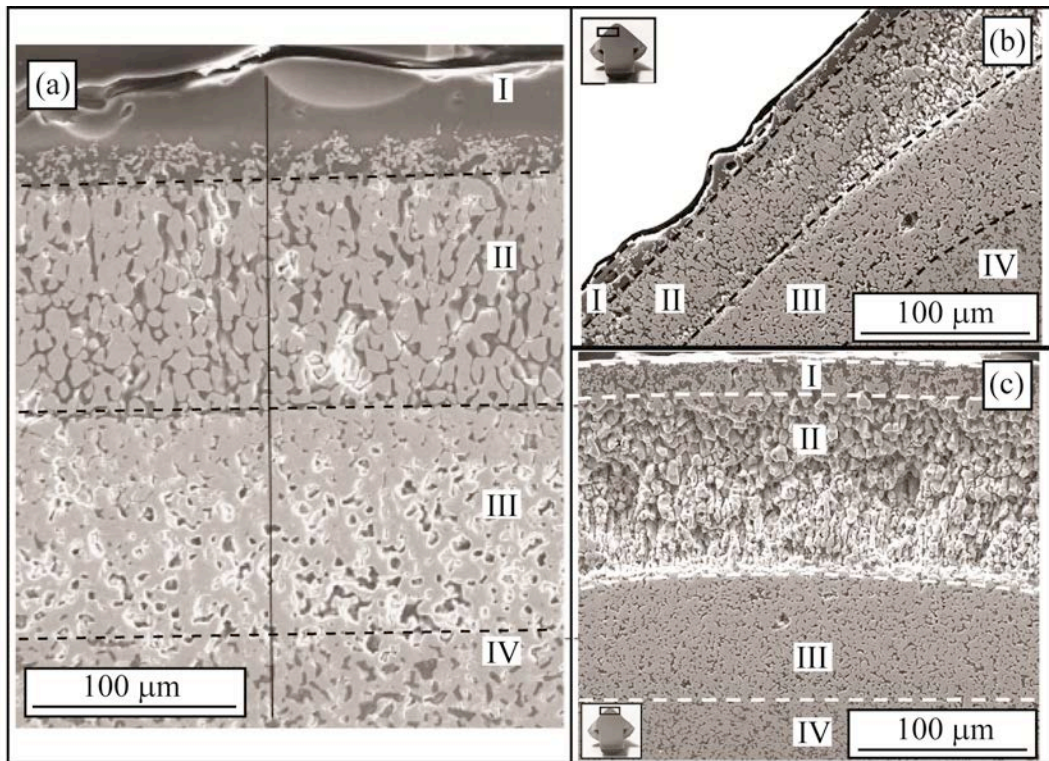


Figure 1 - 7. Typical oxide scale of  $ZrB_2/SiC$  or  $HfB_2/SiC$  UHTC after (a) furnace oxidation and (b)/(c) arc-jet testing (features include (I) glass layer, (II) oxide sub-scale, (III) SiC depleted layer, and (IV) bulk UHTC. Images reproduced from Levine *et al.* and Monteverede *et al.*).<sup>[49,86]</sup>

Figure 1-7 includes typical observations of  $ZrB_2/SiC$  or  $HfB_2/SiC$  after high temperature exposure: a glassy silicate layer, an oxide sub-layer, a SiC depletion layer, and the bulk ceramic. Besides the bulk ceramic, all of these features are not always observed depending on the thermal history. It is important to understand how each of these layers form, how they can be influenced by interacting with other layers, and processes that occur within these layers. A review is given by Eakins.<sup>[10]</sup>

The SiC depletion layer is a result of active oxidation. Active oxidation can be activated in different ways. If the temperature is high enough to cause oxidation, but low enough that a protective liquid layer does not form a complete diffusion barrier, then active oxidation occurs via loss of CO. It can also be activated by low pressures, which facilitates volatilization of SiO gas. High temperatures have a similar effect of increasing SiO volatility and may induce active oxidation. Active oxidation can be observed above ~1600-1700°C even in the presence of a protective liquid layer.

It is thought that oxygen mobility through the porous oxide sub-layer can influence the active oxidation of SiC just below and therefore the development of the depletion layer. The amount of SiC also influences the depletion layer. The depletion layer thickness decreases with initial increases in silicon carbide, but then thickens for larger SiC content. Optimum SiC content is suggested: enough to form sufficient SiO<sub>2</sub> for oxidation protection, but not enough that SiC becomes interconnected to form direct pathways for active oxidation (i.e. must be below the percolation threshold).

The typically porous oxide sub-layer is a result of ZrB<sub>2</sub> or HfB<sub>2</sub> oxidation resulting in ZrO<sub>2</sub> or HfO<sub>2</sub> formation, respectively. Nodular or columnar grains can be observed. Columnar grains are usually attributed to outgassing to the surface caused by oxidation of material within or below this sub-layer and are aligned with the direction of gas or liquid transport to the surface (i.e. perpendicular to surface). If the gas evolution is forceful enough, it can dislodge oxide grains into the glassy layer above or remove the grains from the material completely in the absence of a protective silicate layer. This will depend on how much gas is being produced, the gas pressure, the morphology of the oxide grains, and the interconnectedness of the porous oxide structure.

Depending on the composition and temperature, the oxide sub-layer may contain a silicate liquid within the pores. In general the silicate liquids do not wet ZrO<sub>2</sub>. Non-wetting behavior and chemistry variation of the liquid on the surface compared to the chemistry beneath the surface are both driving forces for liquid transport to the surface. If there is an insufficient amount of liquid, from insufficient SiC content or due to material removal, then the oxide sub-scale will typically be porous. Oxygen transport through the oxide layer, which can influence active oxidation of silicon carbide beneath this layer, is influenced by the presence or filling of porosity and the defect structure of

the oxide. Phase transformations of the oxide must also be considered and is particularly relevant to thermal cycling.

The outer glassy layer may or may not be present. If present, then the composition, morphology, and behavior can vary dramatically depending on the thermal history. The composition varies dramatically as a function of temperature and location. Higher temperatures cause preferred volatilization of  $B_2O_3$  and increase the viscosity of the glassy melt, which is generally beneficial. Since  $B_2O_3$  is removed from the surface, the chemistry beneath the surface can vary and is a driving force for transport of the glassy liquid phase to the surface.

The non-wetting behavior of the liquid phase in contact with  $ZrO_2$  is another driving force for liquid transport to the surface. Longer exposure times without high volatilization rates will result in thicker glassy layers due to this transport process. This occurs in sub-sonic conditions more so than hypersonic conditions. The presence or lack of aerodynamic forces, in conjunction with the morphology and composition of the oxidation scale influences the ability to retain glassy liquids and how thick the glassy layer is by how easily the liquid is transported to and removed from the surface. The glassy layer can also contain oxide particles, loosened and carried by gas transport and liquid convection cells or by dissolution/precipitation processes. Sufficient oxide particles in the glassy phase, extending from the surface to the oxide sub-layer, can provide an oxidation pathway to the bulk UHTC material.

The protective liquid glass layer may be depleted at temperatures for which the volatility rate of the glassy melt is greater than the rate of formation from its constituents. A silicate liquid itself becomes increasingly volatile with temperature, but active oxidation of SiC at high temperatures reduces the rate of  $SiO_2$  formation via the direct formation of SiO gas as well. Therefore the net removal of the glassy liquid layer is relevant at progressively higher temperatures. The time for complete removal of the liquid is going to depend on the specific temperature. The time will decrease with increasing temperature. This removal process is important because dramatic temperature increase of the UHTCs occur at high temperatures in the absence of the protective liquid and will limit the exposure times at a given temperature.<sup>[69]</sup>

## 2. Methodologies of Improving the MB<sub>2</sub>/SiC Oxidation Scale

The typical features in a ZrB<sub>2</sub>/SiC or HfB<sub>2</sub>/SiC oxidation scale are a silicate outer layer, a porous oxide scale (often containing the glassy phase within the pores), and a SiC depletion layer between the oxide sub-scale and the UHTC bulk. Further details concerning the oxide scale have been provided in the previous section. Based on the features of the oxidation scale, Eakins *et al.* have identified five potential methods for improving oxidation resistance: eliminating porosity in the oxide scale, formation of refractory oxide phases, using alternatives besides SiC to produce SiO<sub>2</sub>, preventing polymorphic phase transformation of the oxide, and increasing viscosity of the liquid phase.<sup>[10]</sup>

The evaporation rate of an oxide is closely related to the vapor pressure of that oxide. The vapor pressures of B<sub>2</sub>O<sub>3</sub>, SiO<sub>2</sub>, and ZrO<sub>2</sub> at ambient pressure are given in Figure 1-8 as a function of temperature. Assuming that reasonable oxidation protection is provided for a liquid oxide with vapor pressures less than 0.01 Pa, B<sub>2</sub>O<sub>3</sub> and SiO<sub>2</sub> would provide oxidation protection up to 1273 K and ~1873-1973 K, respectively. This is in good agreement with literature.<sup>[10,12]</sup> Using this assumption suggests that ZrO<sub>2</sub> could provide oxidation protection up to temperatures of 2373-2473 K, increasing the potential operating temperature by more than 400 K.

Although a simple estimate based on vapor pressure suggests ZrO<sub>2</sub> can protect UHTCs up to 2373 K, the ZrO<sub>2</sub> sub-scale developed from the oxidation of ZrB<sub>2</sub> based UHTCs is typically porous, rendering it non-protective in the absence of the liquid phase to fill the pores at high temperatures. If the microstructure of the ZrO<sub>2</sub> sub-scale was dense, the oxidation resistance at ultra-high temperatures could be improved. Zhang and co-workers provide evidence that tungsten in a ZrO<sub>2</sub> sub-scale allows for liquid phase sintering of ZrO<sub>2</sub> grains at 1773 K.<sup>[89-90]</sup> Although benefits to low temperature oxidation behavior is enhanced there is no indication about how such a liquid might affect the behavior at ultra-high temperatures, but it seems likely that the integrity of the sub-oxide scale would become limited, possibly melting completely at high temperatures. If the sub-oxide scale was to melt, the ablation resistance would be decreased because of the inability to withstand high shear forces that would remove the liquid and expose fresh surfaces at the tip of a leading edge.

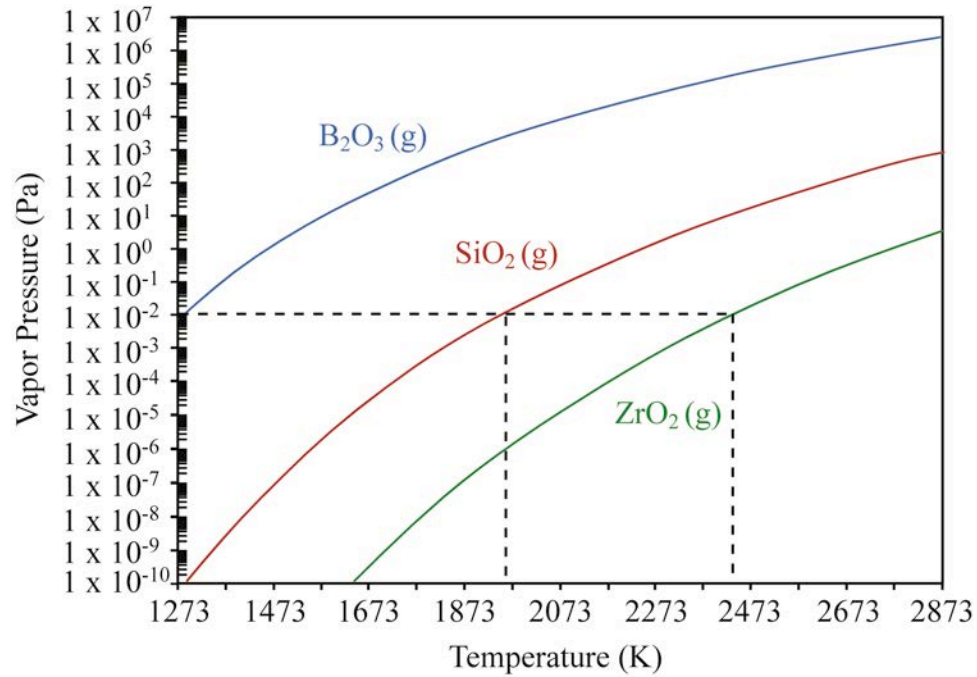


Figure 1 - 8. Vapor pressure of B<sub>2</sub>O<sub>3</sub>, SiO<sub>2</sub>, and ZrO<sub>2</sub> as a function of temperature (P = 1 atm). Dotted lines correspond to temperatures where vapor pressures exceed 0.01 Pa (adapted from Zhang *et al.*<sup>[40]</sup>). (With color)

Rather than use liquid phase sintering to obtain a dense refractory oxide scale, other researchers have used additives based on rare earth elements, particularly those containing lanthanum, to obtain high density refractory oxide scales.<sup>[93]</sup> This type of oxide scale, having superior oxidation/ablation resistance, is demonstrated in Figure 1-9. The weight gain after testing an 80ZrB<sub>2</sub>-20SiC UHTC composite for 600 sec at ~2673 K was 3.1% compared to 0.2% for a 70ZrB<sub>2</sub>-20SiC-10LaB<sub>6</sub> UHTC composite. Phase analysis indicated that the oxide scale in Figure 1-9 contained monoclinic ZrO<sub>2</sub>, tetragonal ZrO<sub>2</sub>, La<sub>2</sub>O<sub>3</sub>, and La<sub>2</sub>Zr<sub>2</sub>O<sub>7</sub>. The benefit of the formed oxide scale is three-fold: the outermost layer was of high density providing excellent oxidation behavior in the absence of a substantial amount silicate phase, the formation of the monoclinic phase upon cooling is partially suppressed reducing the impact of the phase transformation that is accompanied by a large volume change when thermally cycling, and the La<sub>2</sub>Zr<sub>2</sub>O<sub>7</sub> phase has a suitably high melting temperature. The rare earth zirconates (RE<sub>2</sub>Zr<sub>2</sub>O<sub>7</sub> compounds) all have melting temperatures in excess of ~2573 K. Optimization of these

types of compositions and full characterization over a wide temperature range has yet to be undertaken.

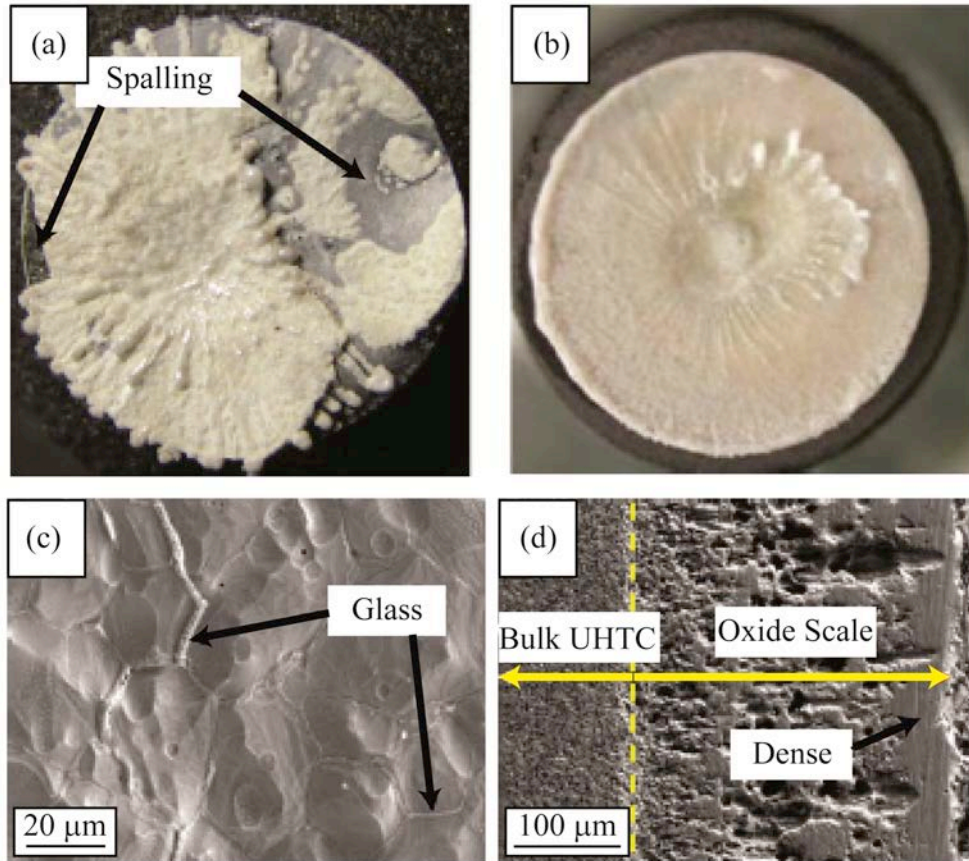


Figure 1 - 9. (a) ZrB<sub>2</sub>-SiC and (b) ZrB<sub>2</sub>-SiC-LaB<sub>6</sub> compacts after oxyacetylene torch testing for 600 sec, reaching temperature of ~2673 K and (c) surface and (d) cross-section analysis of the ZrB<sub>2</sub>-SiC-LaB<sub>6</sub>, indicating a dense outer surface is responsible for advanced ablation resistance (Images reproduced from Zhang *et al.*<sup>[91]</sup>). (With color)

The approaches to improving oxidation resistance so far have relied on the formation of a dense oxide scale. One disadvantage to this approach is that the self-healing effect of having a liquid phase redistribute over a surface if the scale ruptures is lost. There are a few requirements necessary to increase the temperature limits for a design consisting of a porous oxide-scale filled with a liquid phase at operating temperatures. The first requirement is that oxygen diffusion through both the liquid phase and the solid oxide phase should be limited, to prevent oxidation of the underlying bulk material. A second requirement is that the polymorphic phase transformations that

can lead to cracking should be eliminated to prevent failures caused by thermal cycling. A third requirement is that wicking to the surface and subsequent vaporization of the liquid phase should be limited.

The polymorphic phase transformation of  $ZrO_2$  from tetragonal at higher temperatures to monoclinic at lower temperatures can be a source for oxide scale failure during thermal cycling due to the large associated volume changes. For low temperature applications, the phase transformation to the monoclinic phase can be suppressed with stabilizing cations such as magnesium, calcium, or yttrium. However, these cations are lost from the  $ZrO_2$  lattice at high temperatures and they promote oxygen diffusion via formation of oxygen vacancies. Tantalum can also substitute into the  $ZrO_2$  lattice to stabilize the tetragonal phase. The tantalum can be retained at high temperatures and can hinder oxygen diffusion through the oxide scale by eliminating oxygen vacancies because of the higher valence of tantalum compared to zirconium.

The addition of tantalum-containing compounds to  $ZrB_2$ -SiC UHTC composites addresses all three of the previously defined requirements for improving oxidation resistance of a solid/liquid type of protective scale. Diffusivity of oxygen through the liquid phase is indirectly proportional to the viscosity of the liquid.<sup>[92]</sup> The viscosity of borate and silicate glasses can be increased by the addition of various transition metals to improve the oxidation resistance.<sup>[39,93-96]</sup> The improved oxidation resistance is believed to relate to higher liquid viscosity resulting from a higher liquidus temperature and phase immiscibility of the liquid. The conclusion is based on the observation that improvement in oxidation is found to correlate well with cation field strength of the added compound and immiscibility also increases with increasing field strength. The phase separation was observed with electron microscopy. Relatively small additions (~3 volume percent) are recommended. Higher amounts degrade oxidation performance caused by dissolution of  $ZrO_2$  and subsequent  $ZrO_2$  dendrite precipitation.

However, the mechanism for improved oxidation resistance has not been determined exclusively and further research is needed. Smaller particle sizes in the oxide scale, as a result of solid solution oxidation, have also been attributed to improved oxidation resistance in addition to the liquid immiscibility theory.<sup>[95]</sup> It is thought that the finer capillaries in the oxide scale can retain the liquid better. Many of the studies

mentioned thus far have completely neglected grain size in their analysis. Gasch *et al.* have determined that in the absence of chemical variation, grain sizes in the microstructure had a significant impact on the total thickness of the oxide layers and therefore oxidation resistance (see Figure 1-10 for example).<sup>[13]</sup> Resistance sintering can be used to obtain smaller grain sizes than the more traditional hot pressing approach to sintering.<sup>[13,79,97-98]</sup> The advantage of the resistance sintering technique is the excellent heating efficiency and rapid heating rates that can be obtained compared to the hot pressing technique. No advantage was observed if using the same exact heating profile. No advantage is reported in other cases, but the sintering parameters often vary dramatically in these reports.

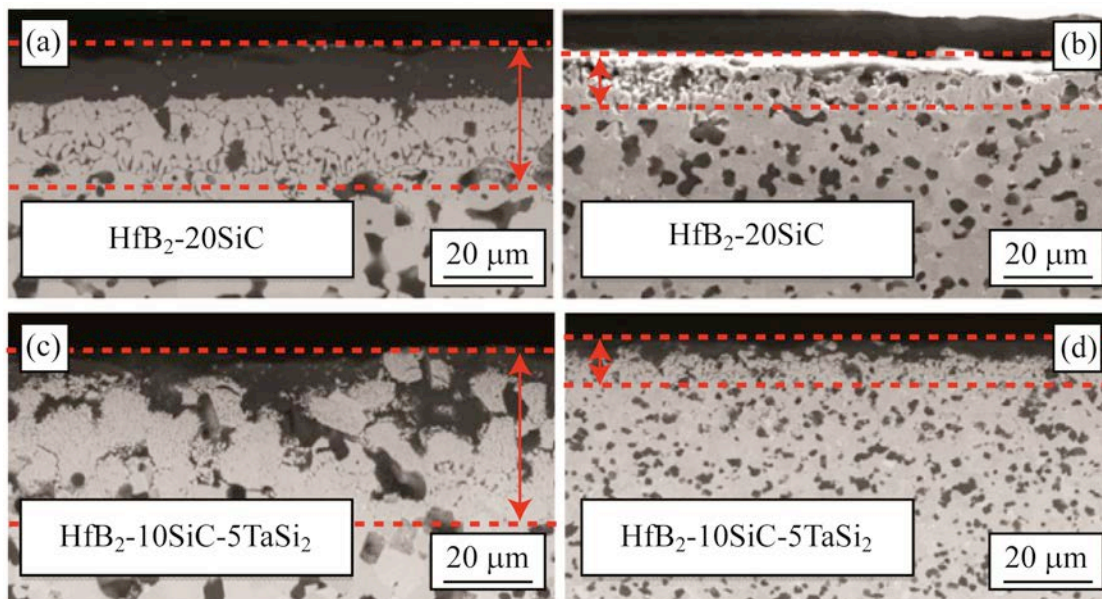


Figure 1 - 10. Oxidation scale thickness of  $\text{HfB}_2\text{-20SiC}$  samples with (a) large grain size and (b) small grain size as well  $\text{HfB}_2\text{-10SiC-5TaSi}_2$  samples with (c) large and (d) small grain sizes after arc-jet testing (Images reproduced from Gasch *et al.*<sup>[13]</sup>). (With color)

In addition to decoupling effects like liquid immiscibility and microstructure refinement, high temperature and ultra-high temperature behavior also needs to be established. Most of the current studies focus on relatively mild temperatures for UHTCs (1273-1873 K). For example, the effect of possible  $\text{Ta}_2\text{O}_5\text{-ZrO}_2$  eutectics on the oxide scale integrity should be established as a function of composition and temperature, which could become particularly important at progressively higher temperatures.

### C. Tantalum Carbide

Tantalum carbide is a potential additive to UHTC composite materials. It is useful to understand tantalum carbide itself to understand how it will interact with other UHTC components and how it will contribute to UHTC performance. The bonding and structure of tantalum carbide phases can be used to describe many of its properties and characteristics. The most recent Ta-C phase diagram is given in Figure 1-11. The three primary tantalum carbide phases of interest are the  $TaC_{1-x}$  monocarbide phase, the  $Ta_2C_{1-x}$  semicarbide phase, and an intermediate  $\zeta$ - $Ta_4C_{3-x}$  phase. Other interesting features within these phases include ordered defect structures and stacking faults.

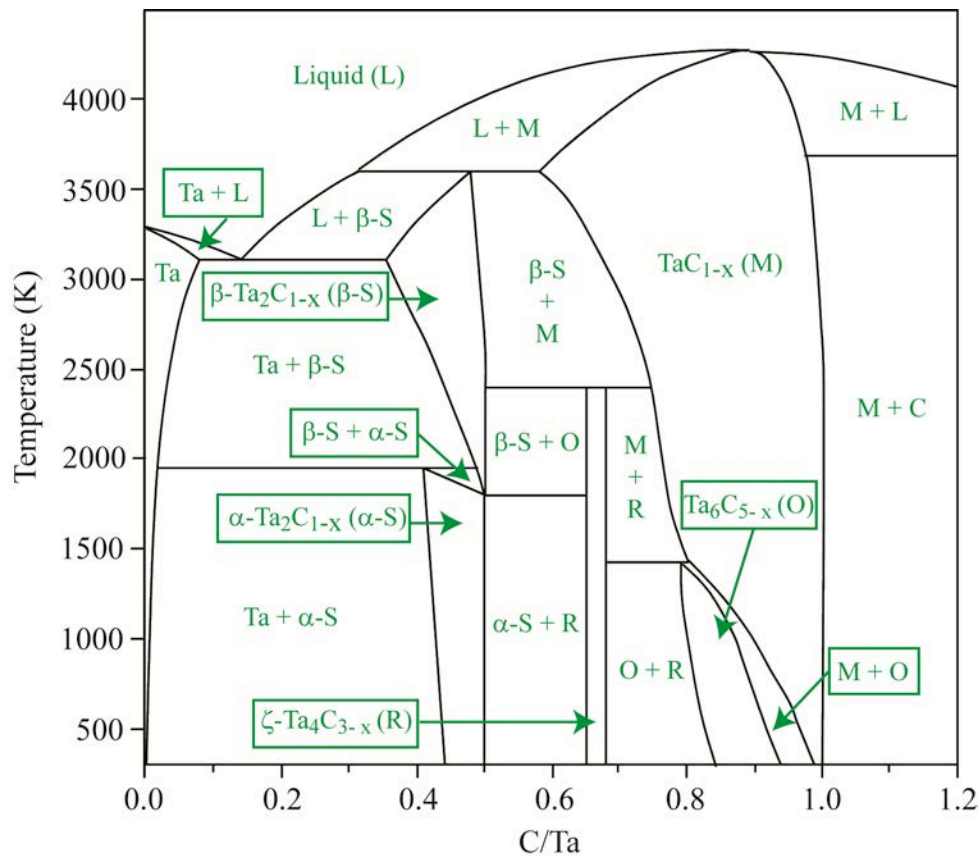


Figure 1 - 11. Ta-C phase diagram (adapted from Gusev *et al.*<sup>[99]</sup>). Single-phase fields are labeled and abbreviated, two-phase fields are labeled with the phase abbreviations, and a box surrounds the label if the label is outside of the phase field. An “x” denotes possible carbon sub-stoichiometry. (With color)

The  $TaC_{1-x}$  monocarbide phase (TaC) is of primary interest due to its large compositional range and higher melting temperature. The monocarbide phase has a rock salt structure. The compound is considered an interstitial carbide because the FCC-

arranged carbon lattice practically fits into the interstitial sites of the FCC-arranged tantalum atoms. The bonding is mixed covalent, metallic, and ionic. Early views considered the primary bonding in tantalum carbide to be metallic.<sup>[100]</sup> Later developments consider tantalum carbide as primarily covalent due to the carbon p-orbital and tantalum d-orbital interaction, slight metallic bonding arising from an extra tantalum d-orbital electron that does not participate in the covalent bond, and a small proportion of ionic bonding arising from a slight net transfer of charge from the tantalum atoms to the carbon atoms.<sup>[101-102]</sup> A more detailed description of the nine valence electrons making up the ground state have been reported recently and consists of a  $1\sigma^2 2\sigma^2 1\pi^4 3\sigma^1$  electron configuration.<sup>[103]</sup> The molecular orbital diagram and density of states relevant to bonding for stoichiometric TaC are given in Figure 1-12.

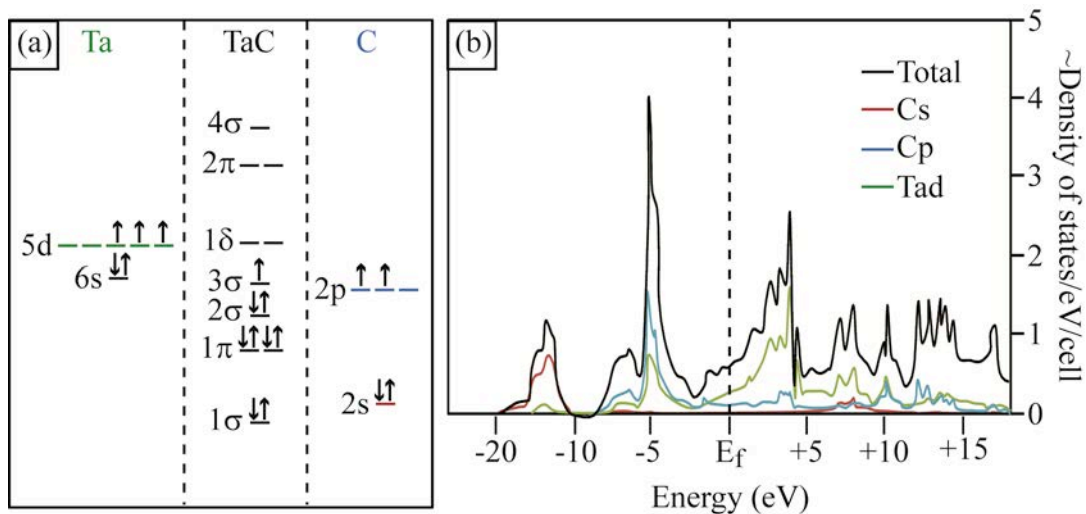


Figure 1 - 12. (a) Molecular orbital diagram demonstrating the reconfiguration of tantalum and carbon electron states in the TaC ground state (adapted from Krechivska and Morse<sup>[103]</sup>) and (b) the approximate density of states about the Fermi energy for TaC (adapted from Sahnoun *et al.*<sup>[104]</sup>). (With color)

The TaC phase is capable of accommodating a wide range of carbon substoichiometry. To achieve stoichiometries approaching TaC<sub>1.0</sub>, excess carbon may be necessary, or found in the product.<sup>[100,105]</sup> The typical single-phase compositional range is considered to be from approximately TaC<sub>0.8</sub> to TaC. Below this compositional range, the ζ-Ta<sub>4</sub>C<sub>3-x</sub> (Ta<sub>4</sub>C<sub>3</sub>) phase is in equilibrium with TaC. If vacancy ordering is taken into consideration, an effect that is inherently difficult to characterize, then the compositional

range of single-phase TaC is essentially non-existent at low temperature and is demonstrated by the phase diagram in Figure 1-11.

At temperatures below 1773 K, vacancy ordering can result in formation of the  $\text{Ta}_6\text{C}_{5-x}$  ( $\text{Ta}_6\text{C}_5$ ) phase.<sup>[106-112]</sup> Noticeable effects of this phase on magnetic susceptibility, neutron diffraction data, and heat capacity have been observed over the  $\text{TaC}_{0.8}$  to  $\text{TaC}_{0.9}$  compositional range. The ordering is efficient in that it requires cooling rates above 2000 K/min to prevent, but inefficient in that complete ordering is not observed even for cooling rates as low as 0.16 K/min. Carbon sub-stoichiometry in the TaC phase can be evaluated by determination of the lattice parameters using diffraction techniques. The relationship between the lattice parameter and the sub-stoichiometry is given by  $C/\text{Ta} = 6.398a - 17.516$ .<sup>[113]</sup> Some deviations in lattice parameter due to vacancy ordering have also been reported. The equation for describing the lattice parameter for this circumstance has been described by the second-order polynomial equation  $a(C/\text{Ta}) = a_0 + a_1(C/\text{Ta}) + a_2(C/\text{Ta})^2$ , where  $a(C/\text{Ta})$  is the lattice parameter in nm,  $a_0 = 0.42131$ ,  $a_1 = 0.03417$ , and  $a_2 = -0.00992$ .<sup>[108]</sup>

Other defects in TaC include dislocations and stacking faults.<sup>[100,114-119]</sup> The dislocations dissociate into Shockley partials bounding a stacking fault. The faulted regions are believed to be of similar composition and structure as the  $\text{Ta}_2\text{C}_{1-x}$  ( $\text{Ta}_2\text{C}$ ) phase, having a hexagonal type of structure. With decreasing carbon content, the density of stacking faults increases and presumably results in the formation of the  $\text{Ta}_4\text{C}_3$  structure. The  $\text{Ta}_4\text{C}_3$  phase is an intermediate structure between the FCC TaC and HCP  $\text{Ta}_2\text{C}$  structures with alternating layers of FCC and HCP sequencing (i.e. a material with a 50% stacking fault density). However, a simple blend of FCC and HCP lattices to produce the  $\text{Ta}_4\text{C}_3$  is an over simplification. The formation of shortened Ta-Ta bonds between tantalum atoms neighboring the  $\{111\}$  plane where missing carbon atoms concentrate results in a distinct energy state approximately 2 eV below  $E_f$ .<sup>[120]</sup> Similar types of relaxation have been observed on terminated (001) surfaces, which form new bonds along the surface.<sup>[101]</sup>

## 1. Properties and Characteristics of Tantalum Carbide

The discussion in this section will be limited to those properties and characteristics given in Table 1-II. Many of these properties and characteristics of TaC

can be understood in terms of the bonding and structure of TaC, including the defect structures and microstructure.

The density of TaC is typically reported as  $14.5 \text{ g/cm}^3$ .<sup>[121-127]</sup> Higher density values, ranging from  $14.6\text{-}14.7 \text{ g/cm}^3$  have also been reported.<sup>[121,128-129]</sup> The discrepancy is best explained by an increase in density with a decrease in carbon stoichiometry.<sup>[130-131]</sup> In Bowman's early work, the lattice parameter was used to determine the theoretical density as a function of the TaC carbon content. These results are demonstrated in Figure 1-13, which indicate that  $14.5 \text{ g/cm}^3$  accurately describes the theoretical density when the carbon stoichiometry exceeds roughly  $\text{TaC}_{0.88}$ . Lower densities could result from impurity phases, such as an oxide phase or free carbon.

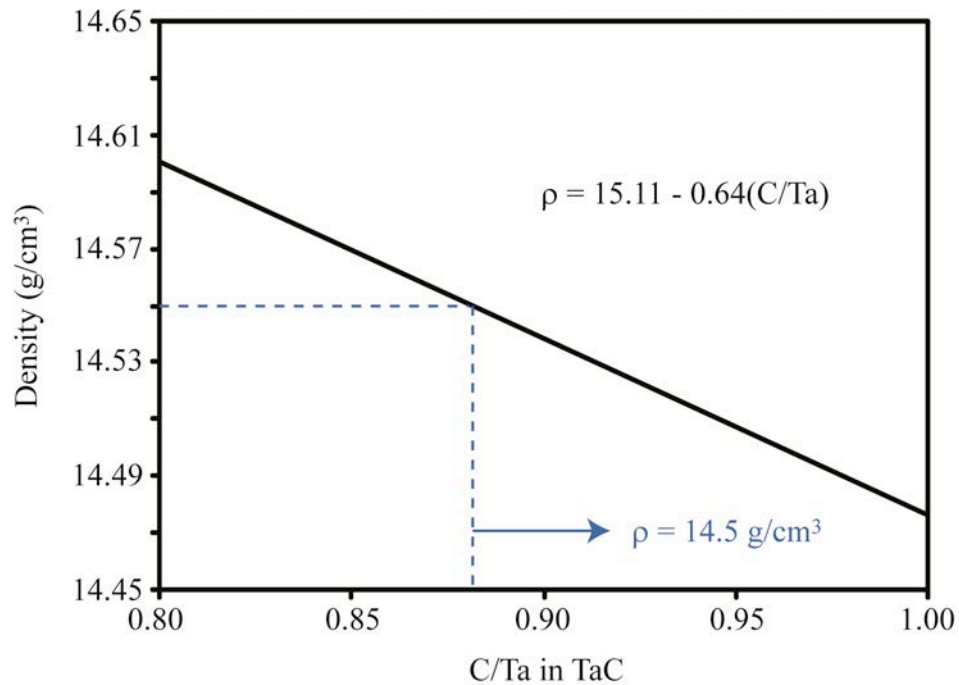


Figure 1 - 13. Variation in TaC density with carbon content ( $14.5 \text{ g/cm}^3$  describes the density of  $\text{TaC}_{0.88-1.00}$ ).<sup>[113]</sup> (With color)

The linear coefficient of thermal expansion for approximately stoichiometric TaC up to 2873 K was investigated and compared to other work available in the early 1970's by the Carborundum Company under a contract for the Navy.<sup>[132]</sup> The results from this work are compiled in Table 1-IV. The thermal expansion coefficient is decreased with decreasing carbon content, passes through a minimum, and then increases again.<sup>[102,133]</sup> Anomalous data was sometimes reported near 2273 K for ascending temperature and was

attributed to further specimen densification.<sup>[134-135]</sup> Another possible explanation for anomalous behavior at higher temperatures is the incongruent vaporization of TaC.<sup>[136-137]</sup> The preferential loss of carbon at higher temperatures lowers the expansion coefficient as the test is being performed. More recent work using neutron powder diffraction resulted in a value of  $6.4 \pm 0.3 \text{ } 10^{-6}/^{\circ}\text{C}$  over the temperature range from room temperature to 686 K is in good agreement for lower temperatures.<sup>[138]</sup>

Table 1 – IV. Average Thermal Expansion Coefficients of TaC from Jun and Shaffer<sup>[132]</sup>

$\alpha \text{ (} 10^{-6}/\text{K)}$	Temperature (K)
6.55	R.T.-1273
7.34	1773
7.86	2273
8.37	2673
8.72	2873

Specific heat measurements of TaC have been studied as a function of the carbon content, carbon ordering, and temperature.<sup>[102,139-140]</sup> When the heat capacity was measured over the temperature range of 1200-2500 K over the compositional range of TaC<sub>0.75</sub> to TaC, a local maximum was found near TaC<sub>0.88</sub>. This is demonstrated in Figure 1-14. The maximum closely corresponds to the depletion of free electrons as carbon stoichiometry is reduced and is a direct consequence of bonding. The decrease in modes for energy storage requires that more energy is necessary to increase temperature. If the ordered Ta<sub>6</sub>C<sub>5</sub> phase forms, then a greater heat capacity can be observed when compared to the disordered TaC<sub>1-x</sub> phase over the composition range of TaC<sub>0.8-0.9</sub> near room temperature. The heat capacity is a complex function of temperature, but seems to increase somewhat linearly from room temperature to 3073 K and then increases exponentially thereafter. It is important to point out that each 1% of free carbon in TaC increases the specific heat by 4.5-5%.

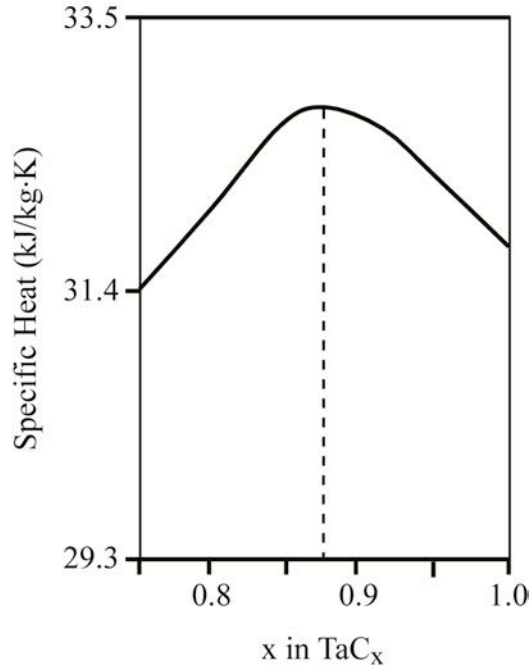


Figure 1 - 14. Specific heat of TaC from 1200-2500 K, (adapted from Samsonov<sup>[102]</sup>).

The thermal conductivity of TaC was investigated by Donald W. Douglas Laboratories of McDonnell-Douglas Astronautics in the late 1960's using an electron beam technique.<sup>[141]</sup> The specimen tested was stoichiometric and the density was 13.87 g/cm<sup>3</sup> or 95.8% of theoretical. The thermal conductivity increased from 31.0 W/m•K at 1200 K to 39.8 W/m•K at 2850 K. The curve was below that of TaC tested by other researchers, but above that of the other researchers' material after being pre-exposed to a temperature dwell at 2756 K. The reason for the discrepancy in the thermal conductivity data associated with the heat soaking was not clear. Increased sintering or grain growth would be expected to increase the thermal conductivity, not lower it. Another study considered the thermal conductivity of nearly stoichiometric TaC deposited onto graphite by gas phase diffusional deposition.<sup>[142]</sup> In this case, the thermal conductivity was 50 W/m•K at 1200 K up to about 63 W/m•K at 2000 K, which was reported to be twice as high as that obtained by hot compaction of powders. The higher values were attributed to a lower contribution of phonon scattering at grain boundaries, although no formal comparison of grain sizes was made. The density of the film prepared by gas diffusional deposition versus specimens sintered by hot compaction were not discussed and could be

another cause because pores in the microstructure could also lower the thermal conductivity.

The Young's modulus has been studied by the sonic resonance technique from room temperature to 1500 K.<sup>[143]</sup> The Young's modulus decreased linearly with both porosity and temperature over the ranges studied. The Poisson's ratio was determined to be 0.21 at room temperature and found to be independent of porosity. As temperature was increased to 1500 K, the Poisson's ratio increased linearly to 0.24. Bukatov *et al.* studied the temperature dependence of the Young's modulus up to temperatures of 2273 K.<sup>[144]</sup> In addition to the linear dependence described in the earlier work, a non-linear decrease is observed beginning at 0.4-0.5 of the melting temperature, assumed to result from thermally activated vacancy formation, with grain boundaries acting as vacancy sources. A plot of Young's modulus versus porosity, with different data points from literature, is given in Figure 1-15 and suggests an intrinsic Young's modulus of 457-545 GPa.<sup>[145-146]</sup> The lower values reported by Bakshi *et al.* are not easily explained.<sup>[128,146]</sup> It is worth noting that they used a different measurement technique.

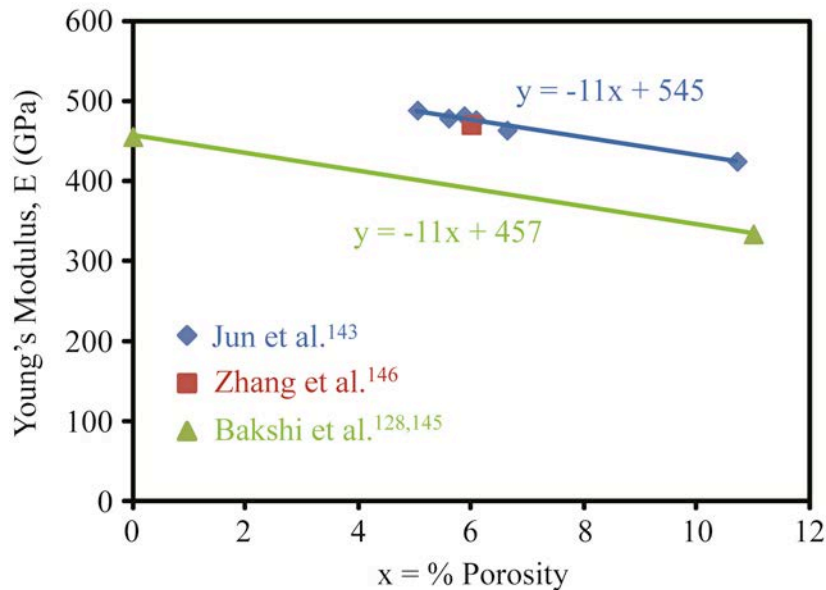


Figure 1 - 15. Elastic moduli of TaC with porosity. (With color)

The total hemispherical emissivity of TaC has been measured from 1200 to 3750 K.<sup>[147]</sup> For initial heating, the total hemispherical emissivity was between 0.5 and 0.6 up to 2100 K. Thereafter, the total hemispherical emissivity varied linearly from 0.44 at

1200 K to 0.54 at 3700 K. These measurements were compared to previous literature, but little data is given concerning the samples so explanation for the results is neglected here. In the same study, the normal spectral emissivity data at 0.65  $\mu\text{m}$  were generally higher and changed linearly from 0.75 at 1200 K to 0.5 at 3700 K compared to the total hemispherical emissivity. Lower values at 0.65  $\mu\text{m}$  were obtained from 1400 to 2000 K by other authors, more comparable to the total hemispherical emissivity.<sup>[148]</sup> The work also discusses a decrease in the spectral emissivity with decreasing carbon content. The total hemispherical emissivity was determined to vary from 0.42 at 1300 K to 0.44 at 3000 K, also requiring an initial heat soak, and is in reasonable agreement with the previously mentioned work.<sup>[149]</sup> An attempt was made to describe the spectral emissivity as a function of temperature and wavelength over the temperature range of 1700 to 3400 K and wavelength range of 0.44 to 1.06  $\mu\text{m}$ .<sup>[150]</sup>

Several researchers have studied the fracture behavior of TaC.<sup>[115,122,130,145,151-156]</sup> The fracture strengths of TaC are highly dependent on the young's modulus and flaw size. Given the brittle fracture behavior of TaC and the difficulty in sintering, microstructural pores are expected to be the strength limiting flaws. Porosity also influences the Young's modulus (see Figure 1-15). Assuming everything else to be equal, the fracture strength would then become indirectly dependent on the density. Such a correlation is demonstrated in Figure 1-16. Based on this concept, the average fracture strength of fully dense TaC is expected to be near 450-500 MPa. However, not all other characteristics are equal and scattering of the data for such an analysis can be attributed to differences in processing resulting in varying carbon stoichiometry and grain size, for example. Most of the fracture strength data has been obtained via flexure testing, although tensile testing has also been used and the test method can make a difference.

Hackett *et al.* demonstrated that the strength was directly correlated with carbon stoichiometry for TaC with similar density ( $\sim 97\%$ ).<sup>[130]</sup> This is despite smaller grain sizes for the sub-stoichiometric samples, which would be expected to increase the fracture strength by reducing flaw sizes. Although partially due to differences in density, Shvab *et al.* demonstrated that fracture strengths were improved from 10 to 40 MPa when starting with an initial average particle size of 24  $\mu\text{m}$  to 60-120 MPa when starting with an initial average particle size of 3.4  $\mu\text{m}$ .<sup>[153]</sup> The fracture strength was further improved

to 230-430 MPa by starting with an initial average particle size of 170 nm. It seems reasonable to assume that starting with a smaller average particle size results in smaller average grain sizes and therefore smaller flaws and higher fracture strengths. However, because density varied, the flaw population can be expected to vary significantly. Liu *et al.* made the general conclusion that grain size has an impact for samples with similar densities.<sup>[122]</sup> Bakshi *et al.* report slightly lower fracture strengths for fully dense TaC with an average grain size of 5.6  $\mu\text{m}$  compared to a fully dense TaC with 4.9  $\mu\text{m}$  grains, but the results are within experimental error. The grain size is similar in this case. A systematic investigation of grain size is lacking, but one could expect that fully dense TaC with small grain sizes would at least approach the upper limit in Figure 1-16, near 700 MPa, by reducing flaw sizes. When TaC was sintered with 15 volume % TaSi<sub>2</sub> or MoSi<sub>2</sub> as a sintering aid, densities between 96-97% were achieved, grain size was limited to 1.2-2.5  $\mu\text{m}$ , and fracture strengths were as high as 1091 MPa.<sup>[157]</sup>

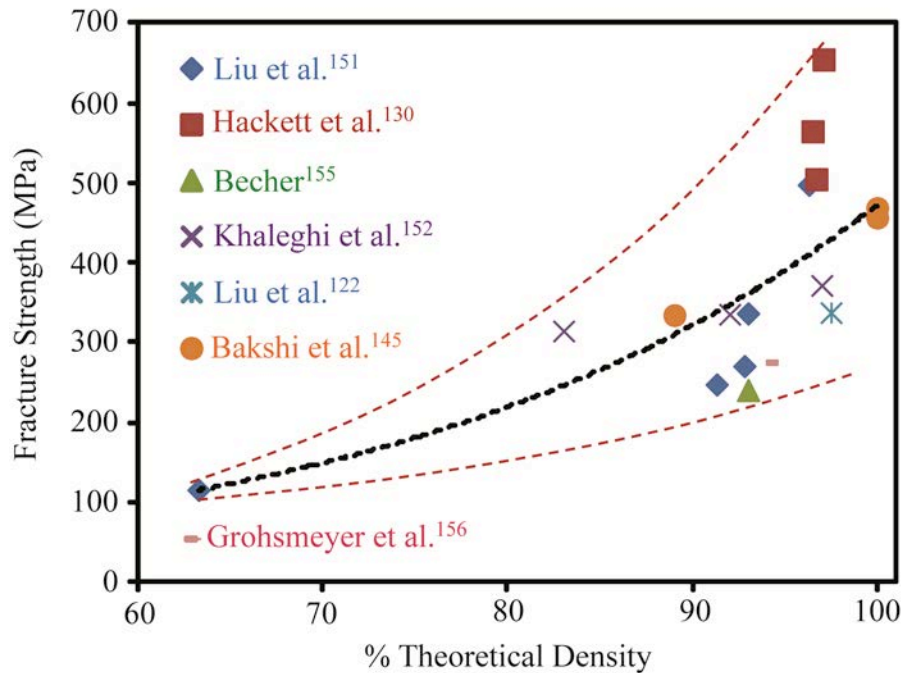


Figure 1 - 16. Summary of TaC fracture strength found in the literature as a function of density. The black dotted line is an exponential fit to the data. The red dotted lines are arbitrary exponential functions demonstrating the range of values reported. (With color)

TaC is typically considered to be brittle, but ductility has been demonstrated at room temperature under sharp diamond indentation.<sup>[114,118]</sup> Slip occurs within the  $\langle 100 \rangle / \{ 111 \}$  system, accomplished mainly by the motion of  $\frac{a}{2} \langle 011 \rangle$  edge dislocation glide. This is similar to the behavior of face-centered cubic (FCC) metals and is attributed to the FCC tantalum lattice. However, unlike pure FCC metals, bulk plastic deformation is prevented by the interstitial carbon resulting in Suzuki hardening.<sup>[116]</sup> Plastic deformation requires overcoming the Suzuki hardening mechanism via carbon diffusion, which becomes appreciable only at higher temperatures. Bulk plastic deformation has been observed at temperatures as low as 1553 K.<sup>[114,155]</sup> The transition temperature from brittle-to-ductile behavior is decreased for low strain rates and substoichiometry, which facilitate carbon diffusion and plastic flow in the absence of brittle failure. Grain-boundary sliding, controlled by dislocation climb, is another deformation mechanism that is activated at higher temperatures. Smaller grain sizes are expected to influence the transition temperature via the grain-boundary sliding mechanism.

Given the low fracture toughness of the monocarbide TaC phase ( $3\text{-}5 \text{ MPa}\cdot\text{m}^{0.5}$ ), the thermal shock resistance is not expected to be exceptional.<sup>[130]</sup> However, the  $\zeta\text{-Ta}_4\text{C}_3$  phase has excellent fracture toughness, as high as  $13 \text{ MPa}\cdot\text{m}^{0.5}$  approaching that of carbon/SiC composites. The low toughness/thermal shock problem can also be overcome by part design. A functionally-graded microstructure, achieved either by fiber reinforcement or compositional grading, has been used for these purposes.<sup>[158-161]</sup>

TaC does not have good oxidation resistance.<sup>[156,162-166]</sup> Oxidation of the monocarbide phase results in a direct transformation to a porous, non-protective  $\text{Ta}_2\text{O}_5$  oxidation layer. The  $\text{Ta}_2\text{C}$  phase is slightly more oxidation resistant, perhaps due to the intermediate oxycarbide phase that forms prior to the  $\text{Ta}_2\text{O}_5$  phase. For high temperature applications in oxidizing atmospheres, composites with engineered oxide scales having superior oxidation resistance will be necessary, like those discussed in a previous section.

## 2. Tantalum Carbide Synthesis

Joly described the synthesis of TaC in 1876 by heating a mixture of  $\text{Ta}_2\text{O}_5$ , tantalite, carbon and  $\text{NaHCO}_3$  at 1773 K.<sup>[167]</sup> Since then, the reduction of an oxide and carburization or direct carburization of tantalum metal at elevated temperatures (even well above 1773 K) using solid carbon or hydrocarbon gases has been used by many

researchers.<sup>[168-178]</sup> Due to the high processing temperatures and nature of the precursors, the particle sizes achieved by this method are relatively large. The amount of oxygen due to a surface oxide layer is typically small because of the low surface area. Reactions have been performed at temperatures as low as 973 K by using more reactive precursors to form nanoparticles, but a reaction above 1773 K is favored for producing powders with low oxygen and free carbon contents. If highly reactive precursors and low temperatures are used, oxygen content will likely be higher and purification may be necessary. Residual carbon to reduce the oxygen during subsequent processing (i.e. sintering) is actually favorable for small particle sizes with high oxygen content.

The reaction between tantalum and carbon to form TaC is a highly exothermic reaction.<sup>[16,179]</sup> This makes the synthesis of TaC by self-propagating high-temperature synthesis (SHS) possible, which many researchers have used.<sup>[180-181]</sup> This technique benefits from a small initial particle size and a high green density compact. Simultaneous pressure application and/or electromagnetic field assistance have been applied to improve the combustion wave propagation, completion of reaction for enhanced phase purity, and higher densities during simultaneous sintering. Secondary additives producing gases and liquids during the reaction are also used and can affect the final product density and composition, but add complexity to the reactions. The primary disadvantage of this technique is the lack of process control after the reaction is initiated. Limited control of temperature has been achieved by diluting the reactants with the final product to reduce temperature or performing the synthesis at elevated temperatures to increase the reaction temperature.

Gas-phase reactions have been used to synthesize TaC.<sup>[186-196]</sup> This is typically a low-temperature synthesis method that utilizes vapors of tantalum chloride compounds and hydrocarbons in hydrogen/argon gas streams, although direct vaporization of tantalum metal has also been applied. Precursors are typically more expensive, but the technique is particularly useful for applying dense coatings and is one of the few techniques capable of providing unique fiber/whisker morphologies with transition metal catalysts. High purities can be difficult to achieve. Products will often contain a mixture of the monocarbide phase, sub-carbide phase, tantalum metal, and/or carbon residuals.

TaC has been synthesized by precipitation in molten salts and metals with and without electromagnetic field assistance.<sup>[197-199]</sup> Dense coatings, powders, and nanofibers have been made by this method. A unique sub-class of SHS synthesis known as solid-state metathesis (SSM) reactions is in this category and has been applied to produce TaC.<sup>[200-201]</sup> The premise is to use exchange reactions to form the compound of interest and a co-produced salt. Besides exchange reactions, a secondary mechanism includes reductive recombination, where the precursors are reduced to elemental form followed by reaction from the elements. The reaction is typically self-sustaining if the reaction temperature exceeds the melting temperature of the co-produced salt. The advantage over traditional SHS is that the coproduced salt from the exchange is an effective heat brake applied to the reaction, limiting the maximum reaction temperature to that of the boiling point of the salt. The lower temperatures favor formation of small particles. However, the reactions are not as exothermic and the self-propagating aspect of traditional SHS reactions is limited. For reaction temperatures below the melting point of the co-produced salt, extended times at moderately elevated temperatures may be necessary to complete the reaction. Ma *et al.* experiments with greater complexity of metathesis reactions by suggesting compositions that produce a vapor phase.<sup>[162]</sup>

Other laboratory-scale synthesis techniques involving nanoparticle synthesis have been presented in the literature.<sup>[163,202-204]</sup> However, since these techniques are prepared by special processes, with more hazardous chemicals, and/or for low quantity yields compared to the other techniques, they are not covered in any detail here. Table 1-V summarizes the more common techniques that have been used for the synthesis of TaC and advantages/disadvantages of each.

### **3. Sintering**

The sintering of dense TaC is challenging, summarized by evaluating Table 1-VI. Recently, in 2011, fully dense TaC of high purity has been reported.<sup>[128]</sup> Resistance sintering at temperatures of 2123 K and pressures of 263-363 MPa were used to do this, in comparison with 89% density using an applied pressure of 100 MPa. Yohe and Ruoff report fully dense TaC in 1978 using pressures of 1.5 to 4.5 GPa, but with 12% Ta<sub>2</sub>O<sub>5</sub> as a result of high oxygen content in the powders that were used.<sup>[126]</sup> High density has only been reported for these high pressure sintering studies.

Table 1 – V. Advantages and Disadvantages of TaC Synthesis Techniques

<b>Technique</b>	<b>Advantages</b>	<b>Disadvantages</b>
<b>High Temperature Carburization</b>	Low free carbon content, inexpensive raw materials, large scale production is demonstrated	Energy intensive, large particle sizes
<b>Low Temperature Carburization</b>	Similar to well established high-temperature carburization, can produce small particle sizes	Requires highly reactive precursors, purity, processing time, and particle agglomeration
<b>Self-Propagating High-Temperature Synthesis</b>	Requires only ignition, fast, simultaneous densification possible, self-purifying, large scale production is demonstrated, inexpensive raw materials	Simultaneous densification difficult, reaction temperature results in large and agglomerated particles, phase purity, lack of control, aggregated particles
<b>Gas-Phase Synthesis</b>	Can obtain fiber/whisker morphology, can be used to apply coatings, low processing temperatures, fine particle size achievable, industrial scale feasible	Typically use expensive precursors, high phase purity is difficult to achieve, potentially hazardous gases, possible particle agglomeration/aggregation
<b>Molten Salt/Metal Synthesis</b>	Used to apply coatings, nanopowders or single crystals can be obtained, fiber/whisker morphology possible, relatively low temperatures used	Requires leaching and further chemical purification, requires extended periods of time at intermediate temperatures possibly leading to aggregation
<b>Metathesis Reactions, sub-class of Molten Salt/Metal Synthesis and Self-Propagating High-Temperature Synthesis</b>	Exothermic reactions provide energy, co-produced salt limits temperature and can produce small particle sizes, combines advantages of multiple techniques	Limited exothermicity may require moderate temperatures to be sustained, requires leaching and further chemical purification, precursor limitations, may lead to particle aggregation

Table 1 – VI. Density (%  $\rho_{th}$ ), Grain Size (G), Powder Type, Applied Pressure (P), and Temperature (T) used to Sinter Nearly Stoichiometric (or Unreported) TaC by Different Sintering Methods

<b>Unspecified sintering method</b>					
<b>% <math>\rho_{th}</math></b>	<b>G (<math>\mu\text{m}</math>)</b>	<b>Powders</b>	<b>P (MPa)</b>	<b>T (K)</b>	<b>Reference</b>
97	12	--	--	--	144
<b>Conventional Sintering</b>					
<b>% <math>\rho_{th}</math></b>	<b>G (<math>\mu\text{m}</math>)</b>	<b>Powders</b>	<b>P (MPa)</b>	<b>T (K)</b>	<b>Reference</b>
65-89	0.17-24	Micro and submicro	--	2673-2973	153
91	6	Micro	--	2223	206
60-95	0.1-18	Nano	--	1373-1873	127
81-98	2-12	Micro and submicro	--	2473-2673	122
<b>Hot pressing</b>					
<b>% <math>\rho_{th}</math></b>	<b>G (<math>\mu\text{m}</math>)</b>	<b>Powders</b>	<b>P (MPa)</b>	<b>T (K)</b>	<b>Reference</b>
85	0.8	Submicro	30	2173	121
81-94	0.02-0.31	Nano	1500-4500	1073-1773	126
89-95	--	--	--	3423	132
75-97	1.3-2.8	Micro	30	2173-2673	123
97	57	--	105	2173	114
<b>Induction heated hot pressing</b>					
<b>% <math>\rho_{th}</math></b>	<b>G (<math>\mu\text{m}</math>)</b>	<b>Powders</b>	<b>P (MPa)</b>	<b>T (K)</b>	<b>Reference</b>
< 96	0.03-0.94	Micro and nano	80	1623	205
<b>Resistance heated hot pressing</b>					
<b>% <math>\rho_{th}</math></b>	<b>G (<math>\mu\text{m}</math>)</b>	<b>Powders</b>	<b>P (MPa)</b>	<b>T (K)</b>	<b>Reference</b>
68-97	0.33-9	Micro	30-75	2173-2673	152
89-100	0.56-5.6	Submicro	100-363	2123	128

The detrimental effect of oxygen on sintering was noted in the first sintering report using nanostructured powders having oxygen content  $> 1\%$ .<sup>[127]</sup> It was determined that the removal of oxygen to less than parts per thousand ranges was essential for obtaining high quality TaC of high density. However, the thermal treatments that were necessary to remove the oxygen grew the primary particle sizes from nanostructured to

the sub-micron regime, casting some doubt on the practical interest of using nanopowders with high surface area. They also noted that liquid phases could form at temperatures as low as 1100°C as a result of binary eutectics between the carbide and transition metal impurities such as iron, nickel, cobalt, and chromium. The liquid is wetting, exists intergranularly, and some evidence is provided to suggest that the liquid phase is directly responsible for grain growth for the intermediate sintering temperatures used in the study (1373-1873 K). Furthermore, this is the same temperature at which densification began, hinting that densification was by liquid phase sintering. Despite starting with nanopowders, final average grain sizes were between 2-20  $\mu\text{m}$ . The difficulty achieving full density was attributed to intragranular porosity as a result of the grain growth, but it is difficult to separate out the effects of oxygen and metallic impurities as a cause.

Yohe and Ruoff developed processing procedures to obtain nanopowders from nominally submicron powders and sintered these nanopowders using high pressures (1.5-4.5 GPa) and intermediate-to-high temperatures (1073-1973 K).<sup>[126]</sup> The densities and grain sizes as a function of temperature are demonstrated in Figure 1-17. Densification was complete ranging from 1273-1573 K and depended on pressure. Higher temperatures lowered the density, perhaps by initiating non-densifying sintering mechanisms or by vaporization of impurity phases. When sintered at these temperatures and pressures, sub-micron average grain sizes were achieved. Fully dense specimens were obtained, but only realized after accounting for the oxide content. An oxide content of 11.8%  $\text{Ta}_2\text{O}_5$  was estimated based on oxygen content. Figure 1-17 indicates that a pressure of approximately 3 GPa is necessary for completing densification without grain growth by comparing the appropriate densification and grain growth curves. Densification is complete just below 1373 K, the same temperature at which grain growth is beginning to become evident. A total transition metal impurity content of about 0.6% is reported.

Additions of carbon and  $\text{B}_4\text{C}$  in small quantities have been used to enhance densification by removing oxygen impurities.<sup>[123]</sup> The reactions between these additives and  $\text{Ta}_2\text{O}_5$  produce gaseous species that can be removed prior to intermediate to late stage sintering. The reaction with carbon becomes favorable just above 1373 K while reaction with  $\text{B}_4\text{C}$  is favorable at all temperatures (vaporization of resulting  $\text{B}_2\text{O}_3$  requires

intermediate temperatures). Despite achieving higher densities at lower temperatures, densification was still accompanied by grain growth. In fact, grain growth could be worse despite higher densities indicating that grain growth is not responsible for poor densification. It seems likely that the additives change the sintering mechanism, allowing the use of reduced temperatures.

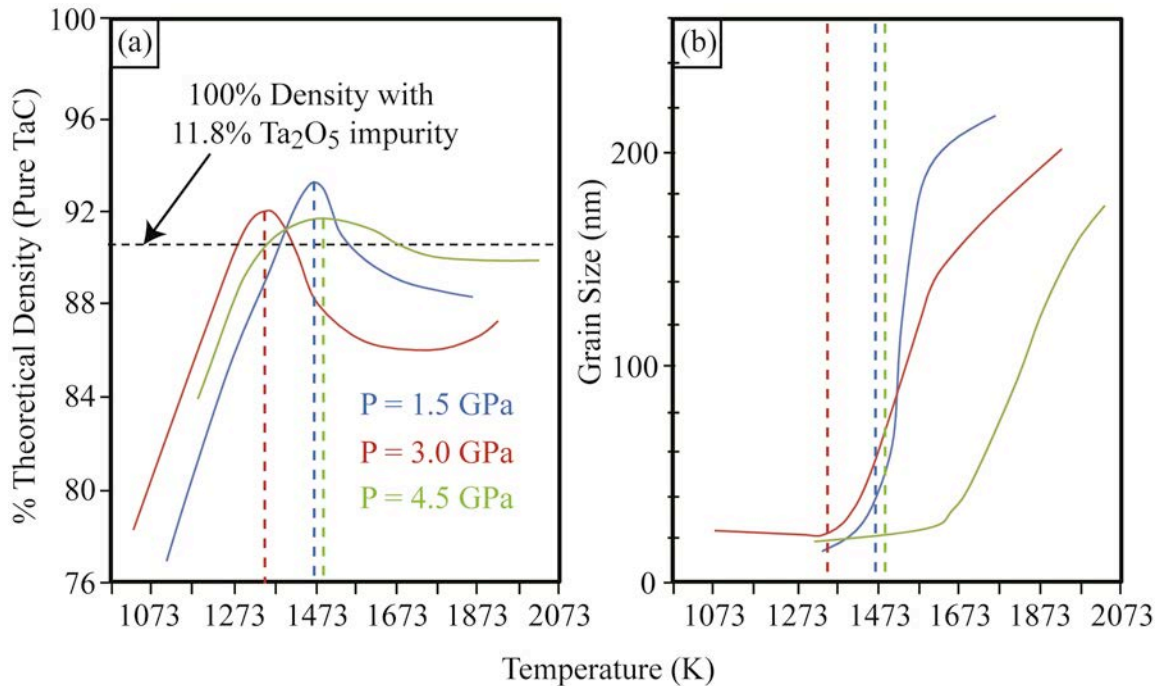


Figure 1 - 17. (a) Density and (b) grain sizes of TaC sintered at temperatures from 1073-1923 K and pressures from 1.5-4.5 GPa (dotted lines correspond to temperature of maximum density. Adapted from Yohe and Ruoff.<sup>[126]</sup>) (With color)

It is interesting to note that the highest density reported in Table 1-VI, besides the high-pressure studies previously discussed, was obtained by a conventional sintering process with no pressure application.<sup>[122]</sup> The key features described for obtaining high density without pressure assistance is a small particle size and a narrow size distribution. Based on the microstructures, it was determined that the narrow particle size distribution prevented grain growth and therefore entrapment of porosity. The microstructures of the sintered specimens using the two different powders, but similar sintering parameters are given in Figure 1-18. Although a smaller grain size (with smaller pore sizes) is observed for the slightly denser sample, the conclusion that was made is questionable for two reasons.

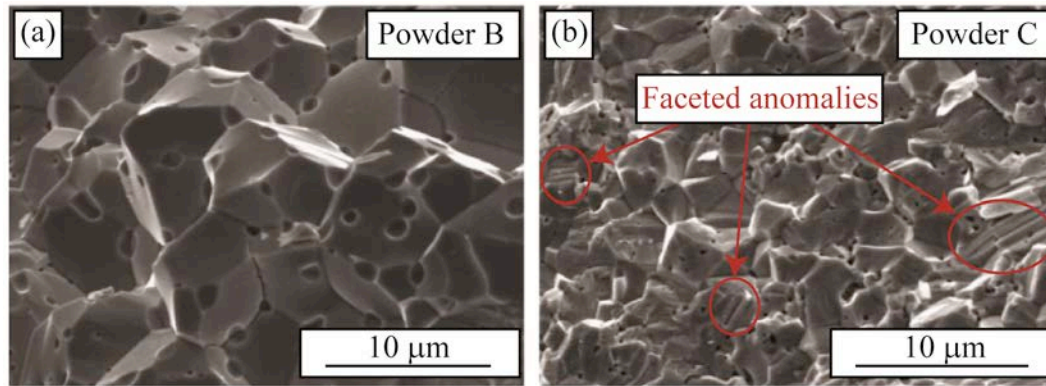


Figure 1 - 18. Microstructures observed by pressureless sintering of TaC at 2573 K, (a) Powder B with a particle size of 360 nm and (b) Powder C with a particle size of 250 nm (images reproduced from Liu *et al.*<sup>[122]</sup>). (With color)

The first reason is that the porosity is primarily at the interfaces between grains without much evidence for intragranular porosity. Other researchers have observed this type of microstructure as well.<sup>[152,207]</sup> Furthermore, the study by Zhang *et al.*, demonstrated that higher densities with the use of additives, to remove oxygen impurities, were obtained even in the presence of more extensive grain growth.<sup>[123]</sup> It seems that grain growth is not the controlling factor for low densities by entrapment of porosity, but that the porosity is controlled by oxygen impurities. Ta<sub>2</sub>O<sub>5</sub> is liquid at typical sintering temperatures and could vaporize, forming pores.

The second observation that makes the argument for their conclusion questionable is the presence of faceted grains in the denser microstructure that is characteristic of the substoichiometric Ta<sub>4</sub>C<sub>3</sub> phase (see Figure 1-19), which has a higher density and could contribute to the slightly higher density that was obtained (see Figure 1-13).<sup>[130,208]</sup> The study by Hackett *et al.* demonstrate that while higher densities were obtained for substoichiometric samples, the % of theoretical was lower.<sup>[130]</sup> Carbon stoichiometry was not characterized for the samples demonstrated in Figure 1-18. Besides the carbon stoichiometry, it is possible that the higher density can be attributed to the process of removing oxygen impurity by reaction of TaC with Ta<sub>2</sub>O<sub>5</sub> to form sub-stoichiometric TaC and gaseous CO by-product. The sample with slightly higher density had 20% more oxygen content.

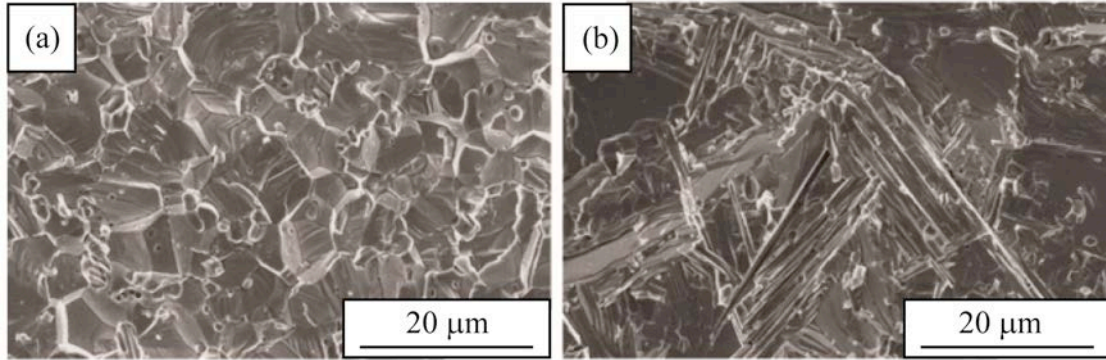


Figure 1 - 19. Microstructural differences observed for (a) TaC and (b) TaC<sub>0.7</sub> (images reproduced from Hackett *et al.*<sup>[130]</sup>).

It seems likely that the slightly different densities between the two powder sets could be attributed to particle size alone, which influences the sintering temperature/densification and impacts oxygen content of the powders. The average particle size of the powder used to produce the denser samples was 250 nm compared to 360 nm for the other powders. Enhanced sintering for smaller particle sizes has been reported by other researchers.<sup>[154,205,207]</sup> Decreasing the particle size apparently changes the mechanism for mass transport, and therefore the sintering mechanism. Sub-micron powders sinter at lower temperatures (~1873 K) with a reaction order indicator of approximately  $n = 1$  during the first stage of sintering, indicating diffusion/viscous flow and grain boundary sliding as the dominant sintering mechanisms. Evidence for viscous flow is given at intermediate temperatures.<sup>[114]</sup> However, coarser micrometer sized powders require higher temperatures to sinter, with a reaction order indicator of near  $n = 3$  and indicating a surface self-diffusion mechanism. The surface diffusion mechanism is a non-densifying mode of sintering that will result in low final density.

A consequence of grain boundary sliding during the initial stage of densification is a sharp increase in grain size in the early stages of sintering (orders of magnitude) with little linear grain growth during isothermal holding, which is observed by multiple researchers.<sup>[153-154,209-212]</sup> Zhang *et al.* gave an alternate explanation for the simultaneous densification and grain growth, corresponding to similar activation energies for these processes.<sup>[123]</sup> The activation energy for grain growth during isothermal holding at temperatures from 2673-2973 K was determined to be 380 kJ/mol, while the activation energy of viscous flow during hot pressing at 16 MPa and 3323 K was determined to be

406 kJ/mol.<sup>[123,153,208]</sup> If viscous flow is the dominant mechanism, then grain growth will be immediately initiated at the onset of densification.

Zhang *et al.* further suggested that the best sintering aids would be those that promote densification below temperatures where rapid grain growth occurs, but that it is unclear which additives would be most effective.<sup>[123]</sup> It has been proposed that the combination of TaB<sub>2</sub> and carbon phases left in the microstructure after reacting TaC and B<sub>4</sub>C inhibited grain growth.<sup>[145-146]</sup> Additions of MoSi<sub>2</sub> did not have an effect on TaC grain growth.<sup>[206]</sup> The form, reactivity, and quantity of excess carbon added to TaC was noted to influence grain growth, thought to be due to excess carbon at the grain boundaries.<sup>[128,207]</sup>

Revisiting the data provided in Table 1-VI and corresponding literature, sub-micron grains are only achieved for samples of low density, before densification is adequate, or for extreme pressure or heating conditions that allow for rapid densification before grain growth can occur significantly.<sup>[126,128,152,205]</sup> It seems reasonable to assume that if nanostructured TaC is to be obtained without the use of extreme heating or pressure conditions, then it will be necessary to find suitable additives to control the microstructural development. Systematic investigations of additives to control microstructural development will be beneficial for designing such systems and may also provide insight to how TaC will interact with other components of UHTC composites.

## References

- [1]. G. Pulci, M. Tului, J. Tirillò, F. Marra, S. Lionetti, and T. Valente, “High Temperature Mechanical Behavior of UHTC Coatings for Thermal Protection of Re-Entry Vehicles,” *J. Therm. Spray Technol.*, **20** [1-2] 139-44 (2011).
- [2]. T.H. Squire and J. Marschall, “Material Property Requirements for Analysis and Design of UHTC Components in Hypersonic Applications,” *J. Eur. Ceram. Soc.*, **30** [11] 2239-51 (2010).
- [3]. R. Savino, M.D.S. Fumo, D. Paterna, A.D. Maso, and F. Monteverde, “Arc-Jet Testing of Ultra-High-Temperature-Ceramics,” *Aerosp. Sci. Technol.*, **14** [3] 178-87 (2010).
- [4]. J. Ramírez-Rico, M.A. Bautista, J. Martínez-Fernández, and M. Singh, “Compressive Strength Degradation in ZrB<sub>2</sub>-Based Ultra-High Temperature Ceramic Composites,” *J. Eur. Ceram. Soc.*, **31** [7] 1345-52 (2011).
- [5]. D.D. Jayaseelan, R.G. de Sá, P. Brown, W.E. Lee, “Reactive Infiltration Processing (RIP) of Ultra-High Temperature Ceramics (UHTC) into Porous C/C Composite Tubes,” *J. Eur. Ceram. Soc.*, **31** [3] 361-8 (2011).
- [6]. F. Yang, X. Zhang, J. Han, and S. Diu, “Analysis of the Mechanical Properties in Short Carbon Fiber-Toughened ZrB<sub>2</sub>-SiC Ultra-High Temperature Ceramics,” *J. Compos. Mater.*, **44** [8] 953-61 (2010).
- [7]. D. Alfano, L. Scattecia, F. Monteverde, E. Bêche, and M. Balat-Pichelin, “Microstructural Characterization of ZrB<sub>2</sub>-SiC Based UHTC Tested in the MESOX Plasma Facility,” *J. Eur. Ceram. Soc.*, **30** [11] 2345-55 (2010).
- [8]. J. Zou, G.-J. Zhang, S.-K. Sun, H.-T. Liu, Y.-M. Kan, J.-X. Liu, and C.-M. Xu, “ZrO<sub>2</sub> Removing Reactions of Groups IV-VI Transition Metal Carbides in ZrB<sub>2</sub> Based Composites,” *J. Eur. Ceram. Soc.*, **31** [3] 421-7 (2011).
- [9]. J.W. Lawson, M.S. Daw, and C.W. Bauschlicher, Jr., “Lattice Thermal Conductivity of Ultra-High Temperature Ceramics ZrB<sub>2</sub> and HfB<sub>2</sub> from Atomistic Simulations,” *J. Appl. Phys.*, **110**, 083507 (2011).
- [10]. E. Eakins, D.D. Jayaseelan, and W.E. Lee, “Toward Oxidation-Resistant ZrB<sub>2</sub>-SiC Ultra High Temperature Ceramics,” *Metall. Mater. Trans. A*, **42** [4] 878-87 (2011).
- [11]. W.G. Fahrenholtz, G.E. Hilmas, A.L. Chamberlain, and J.W. Zimmermann, “Processing and Characterization of ZrB<sub>2</sub>-Based Ultra-High Temperature

- Monolithic and Fibrous Monolithic Ceramics,” *J. Mater. Sci.*, **39** [19] 5951-7 (2004).
- [12]. M.M. Opeka, I.G. Talmy, E.J. Wuchina, J.A. Zaykoski, and S.J. Causey, “Mechanical, Thermal, and Oxidation Properties of Refractory Hafnium and Zirconium Compounds,” *J. Eur. Ceram. Soc.*, **19** [13-14] 2405-14 (1999).
- [13]. M. Gasch and S. Johnson, “Physical Characterization and Arcjet Oxidation of Hafnium-Based Ultra High Temperature Ceramics Fabricated by Hot Pressing and Field-Assisted Sintering,” *J. Eur. Ceram. Soc.*, **30** [11] 2337-44 (2010).
- [14]. X. Zhang, L. Weng, J. Han, S. Meng, and W. Han, “Preparation and Thermal Ablation Behavior of HfB<sub>2</sub>-SiC-Based Ultra-High-Temperature Ceramics Under Severe Heat Conditions,” *Int. J. Appl. Ceram. Technol.*, **6** [2] 134-44 (2009).
- [15]. W.-W. Wu, Z. Wang, G.-J. Zhang, Y.-M. Kan, and P.-L. Wang, “ZrB<sub>2</sub>-MoSi<sub>2</sub> Composites Toughened by Elongated ZrB<sub>2</sub> Grains via Reactive Hot Pressing,” *Scripta Materialia*, **61** [3] 316-19 (2009).
- [16]. A. Varma and J.-P. Lebrat, “Combustion Synthesis of Advanced Materials,” *Chem. Eng. Sci.*, **47** [9-11] 2179-94 (1992).
- [17]. H.O. Pierson, *Handbook of Refractory Carbides and Nitrides: Properties, Characteristics, Processing and Applications*; Ch. 2-6. Noyes Publications, Westwood, 1996.
- [18]. B. Aronsson, T. Lundström, S. Rundqvist, *Borides, Silicides & Phosphides*; Ch. 2-5. Ballantyne and Co. Ltd., Spottiswoode, 1965.
- [19]. P. Vajeeston, P. Ravindran, and R. Asokamani, “Electronic Structure, Bonding, and Ground-State Properties of AlB<sub>2</sub>-Type Transition Metal Diborides,” *Phys. Rev. B.*, **63**, 045115-12 (2001).
- [20]. *Materials Science and Engineering Handbook*, 3<sup>rd</sup> ed., Ch. 4, Edited by J.F. Shackelford and W. Alexander, CRC Press LLC, New York, 2001.
- [21]. R.A. Andrievski, “The State-of-the-Art of High-Melting Point Compounds,” pp. 1-18 in *Materials Science of Carbides, Nitrides, and Borides*. Edited by Y.G. Gogotsi and R.A. Andrievski. Kluwer Academic Publishers, Dordrecht, The Netherlands, 1999.
- [22]. J.B. Berkowitz-Mattuck, “High-Temperature Oxidation, IV. Zirconium and Hafnium Carbides,” *J. Electrochem Soc.*, **114** [10] 1030-33 (1967).

- [23]. W.C. Tripp and H.C. Graham, "Thermogravimetric Study of the Oxidation of  $ZrB_2$  in the Temperature Range of 800° to 1500°C," *J. Electrochem. Soc.*, **118** [7] 1195-9 (1971).
- [24]. L. Kaufman and H. Nesor, "Stability Characterization of Refractory Materials Under High Velocity Atmospheric Flight Conditions," Part III, Volume III: Experimental Results of High Velocity Hot Gas/Cold Wall Tests, Report AFML-TR-69-84, ManLabs, Inc., Cambridge, MA, February 1970.
- [25]. E.V. Clougherty, R.J. Hill, W. H. Rhodes, E.T. Peters, "Research and Development of Refractory Oxidation-Resistant Diborides," Part II, Volume II: Processing and Characterization, Report AFML-TR-68-190, ManLabs, Inc., Cambridge, MA, January 1970.
- [26]. L. Kaufman and H. Nesor, "Stability Characterization of Refractory Materials Under High Velocity Atmospheric Flight Conditions," Part II, Volume I: Facilities and Techniques Employed for Characterization of Candidate Materials, Report AFML-TR-69-84, ManLabs, Inc., Cambridge, MA, December 1969.
- [27]. L. Kaufman and H. Nesor, "Stability Characterization of Refractory Materials Under High Velocity Atmospheric Flight Conditions," Part III, Volume I: Experimental Results of Low Velocity Cold Gas/Hot Wall Tests, Report AFML-TR-69-84, ManLabs, Inc., Cambridge, MA, December 1969.
- [28]. E.V. Clougherty, K.E. Wilkes, and R.P. Tye, "Research and Development of Refractory Oxidation-Resistant Diborides," Part II, Volume V: Thermal, Physical, Electrical and Optical Properties, Report AFML-TR-68-190, ManLabs, Inc., Cambridge, MA, November 1969.
- [29]. E.V. Clougherty, R.L. Pober, L. Kaufman, "Synthesis of Oxidation Resistant Metal Diboride Composites," *Trans. Met. Soc.*, **242**, 1077-82 (1968).
- [30]. J.R. Fenter, "Refractory Borides as Engineering Materials," *SAMPE Quarterly*, **2**, 1-15 (1971).
- [31]. J. Salute, J. Bull, D. Rasky, and D. Keese, "SHARP-B2: Flight Test Objectives, Project Implementation and Initial Results," AIAA Paper 2001-1580, January 2001.
- [32]. P. Kolodziej, J. Bull, J. Salute, and D.L. Keese, "First Flight Demonstration of a Sharp Ultra-High Temperature Ceramic Nosetip," NASA TM 112215, December 1997.
- [33]. J. Bull, P. Kolodziej, J. Salute, and D. Keese, "Design, Instrumentation and Preflight Testing of a Sharp Ultra-High Temperature Ceramic Nosetip," NASA TM-1998-112229, October 1998.

- [34]. J.D. Bull, D.J. Rasky, and C.C. Karika, "Stability Characterization of Diboride Composites Under High Velocity Atmospheric Flight Conditions," *24<sup>th</sup> International SAMPE Technical Conference*, pp. T1092-1106, 1992.
- [35]. U.S. Congress, Office of Technology Assessment, *Affordable Spacecraft: Design and Launch Alternative –Background Paper, OTA-BP-ISC-60* (Washington, DC: U.S. Government Printing Office, January 1990).
- [36]. J.D. Bull, D.J. Rasky, and C.C. Karika, "Stability Characterization of Diboride Composites Under High Velocity Atmospheric Flight Conditions," *24<sup>th</sup> International SAMPE Technical Conference*, pp. T1092-1106, 1992.
- [37]. H.J. Allen and J.Eggers, "A Study of the Motion and Aerodynamic Heating of Ballistic Missiles Entering the Earth's Atmosphere at High Supersonic Speeds," Report NACA-TR-1381, Ames Aeronautical Laboratory, Moffett Field, CA, 1958.
- [38]. M.M. Opeka, I.G. Talmy, and J.A. Zaykoski, "Oxidation-Based Materials Selection for 2000°C Hypersonic Aerosurfaces: Theoretical Considerations and Historical Experience," *J. Mater. Sci.*, **39** [19] 5887-904 (2004).
- [39]. R. Savino, M.D.S Fumo, D. Paterna, and M. Serpico, "Aerothermodynamic Study of UHTC-Based Thermal Protection Systems," *Aerosp. Sci. Technol.*, **9** [2] 151-60 (2005).
- [40]. X. Zhang, P. Hu, J. Han, and S. Meng, "Ablation Behavior of ZrB<sub>2</sub>-SiC Ultra High Temperature Ceramics Under Simulated Atmospheric Re-Entry Conditions," *Composites Sci. Technol.*, **68** [7-8] 1718-26 (2008).
- [41]. M. Tului, G. Marino, and T. Valente, "Plasma Spray Deposition of Ultra High Temperature Ceramics," *Surf. Coat. Technol.*, **201** [5] 2103-8 (2006).
- [42]. R. Monti, M.D.S. Fumo, and R. Savino, "Thermal Shielding of a Re-Entry Vehicle by UHTC materials," *J. Thermophys. Heat Transfer*, **20** [3] 500-06 (2006).
- [43]. K. Upadhyaya, J.M. Yang, and W.P. Hoffman, "Materials for Ultrahigh Temperature Structural Applications," *Am. Ceram. Soc. Bull.*, **58** [12] 51-56 (1997).
- [44]. N. Richet, P. Lespade, P. Goursat, and E. Laborde, "Oxidation Resistance of HfB<sub>2</sub>-SiC Coatings for Protection of Carbon Fiber Based Composites," *Key Eng. Mater.*, **264-268** [TTP] 1047-50 (2004).

- [45]. D.J. Thomas, "Design and Analysis of UHTC Leading Edge Attachment," Report NASA/CR-2002-211505, Ohio Aerospace Institute, Brook Park, Ohio, July 2002.
- [46]. F. Monteverde and L. Scatteia, "Resistance to Thermal Shock and to Oxidation of Metal Diborides-SiC Ceramics for Aerospace Application," *J. Am. Ceram. Soc.*, **90** [4] 1130-8 (2007).
- [47]. Y. Wang, W. Liu, L. Cheng, and L. Zhang, "Preparation and Properties of 2D C/ZrB<sub>2</sub>-SiC Ultra High Temperature Ceramic Composites," *Mater. Sci. Eng. A*, **524** [1-2] 129-33 (2009).
- [48]. W. Li, F. Yang, and D. Fang, "The Temperature-Dependent Fracture Strength Model for Ultra-High Temperature Ceramics," *Acta Mech. Sin.*, **26**, 235-9 (2010).
- [49]. F. Monteverde, R. Savino, M.D.S. Fumo, and A.D. Maso, "Plasma Wind Tunnel Testing of Ultra-High Temperature ZrB<sub>2</sub>-SiC Composites," *J. Eur. Ceram. Soc.*, **30** [11] 2313-21 (2010).
- [50]. H. Hu, Q. Wang, Z. Chen, C. Zhang, Y. Zhang, J. Wang, "Preparation and Characterization of C/SiC-ZrB<sub>2</sub> Composites by Precursor Infiltration and Pyrolysis Process," *Ceram. Int.*, **36** [3] 1011-16 (2010).
- [51]. M. Tului, S. Lionetti, G. Pulci, E. Rocca, T. Valente, and G. Marino, "Effects of Heat Treatments on Oxidation Resistance and Mechanical Properties of Ultra High Temperature Ceramic Coatings," *Surf. Coat. Tech.*, **202** [18] 4394-8 (2008).
- [52]. M. Pavese, P. Fino, C. Badini, A. Ortona, and G. Marino, "HfB<sub>2</sub>/SiC as a Protective Coating for 2D C<sub>f</sub>/SiC Composites: Effect of High Temperature Oxidation on Mechanical Properties," *Surf. Coat. Tech.*, **202** [10] 2059-67 (2008).
- [53]. E.L. Corral and R.E. Loehman, "Ultra-High-Temperature Ceramic Coatings for Oxidation Protection of Carbon-Carbon Composites," *J. Am. Ceram. Soc.*, **91** [5] 1495-1502 (2008).
- [54]. E.L. Corral, "Ultra-High Temperature Ceramic Coatings," *Adv. Mater. Process.*, **166** [10] 30-2 (2008).
- [55]. Y.D. Blum, J. Marschall, D. Hui, and S. Young, "Thick Protective UHTC Coatings for SiC-Based Structures: Process Establishment," *J. Am. Ceram. Soc.*, **91** [5] 1453-60 (2008).
- [56]. S. Tang, J. Deng, S. Wang, W. Liu, and K. Yang, "Ablation Behaviors of Ultra-High Temperature Ceramic Composites," *Mater. Sci. Eng. A*, **465** [1-2] 1-7 (2007).

- [57]. R. Savino, M.D.S. Fumo, L. Silvestroni, and D. Sciti, "Arc-Jet Testing on HfB<sub>2</sub> and HfC-Based Ultra-High Temperature Ceramic Materials," *J. Eur. Ceram. Soc.*, **28** [9] 1899-1907 (2008).
- [58]. F. Monteverde and R. Savino, "Stability of Ultra-High-Temperature ZrB<sub>2</sub>-SiC Ceramics Under Simulated Atmospheric Re-Entry Conditions," *J. Eur. Ceram. Soc.*, **27** [16] 4797-805 (2007).
- [59]. M. Gasch, S. Johnson, and J. Marschall, "Thermal Conductivity Characterization of Hafnium Diboride-Based Ultra-High-Temperature Ceramics," *J. Am. Ceram. Soc.*, **91** [5] 1423-32 (2008).
- [60]. D. Ghosh, G. Subhash, and N. Orlovskaya, "Measurement of Scratch-Induced Residual Stress within SiC Grains in ZrB<sub>2</sub>-SiC Composite Using Micro-Raman Spectroscopy," *Acta Materialia*, **56** [18] 5345-54 (2008).
- [61]. W.G. Fahrenholtz, G.E. Hilmas, I.G. Talmy, and J.A. Zaykoski, "Refractory Diborides of Zirconium and Hafnium," *J. Am. Ceram. Soc.*, **90** [5] 1347-64 (2007).
- [62]. D.M. Van Wie, D.G. Drewry Jr., D.E. King, C.M. Hudson, "They Hypersonic Environment: Required Operating Conditions and Design Challenges," *J. Mater. Sci.*, **39** [19] 5915-24 (2004).
- [63]. T.A. Jackson, D.R. Eklund, and A.J. Fink, "High Speed Propulsion: Performance Advantage of Advanced Materials," *J. Mater. Sci.*, **39** [19] 5905-13 (2004).
- [64]. F. Monteverde, A. Bellosi, and S. Guicciardi, "Processing and Properties of Zirconium Diboride-Based Composites," *J. Eur. Ceram. Soc.*, **22** [3] 279-88 (2002).
- [65]. R. Savino and G. Pezzella, "Numerical Analysis of Supersonic Combustion Ramjet with Upstream Fuel Injection," *Int. J. Numer. Meth. Fluids*, **43** [2] 165-81 (2003).
- [66]. E.T. Curran, "Scramjet Engines: The First Forty Years," *J. Propul. Power*, **17** [6] 1138-48 (2001).
- [67]. D.D. Jayaseelan, H. Jackson, E. Eakins, P. Brown, W.E. Lee, "Laser Modified Microstructures in ZrB<sub>2</sub>, ZrB<sub>2</sub>/SiC and ZrC," *J. Eur. Ceram. Soc.*, **30** [11] 2279-2288 (2010).
- [68]. H.F. Jackson, D.D. Jayaseelan, W.E. Lee, M.J. Reece, F. Inam, D. Manara, C.P. Casoni, F. De Bruycker, and K. Bobridis, "Laser Melting of Spark Plasma-Sintered Zirconium Carbide: Thermophysical Properties of a Generation IV Very

- High-Temperature Reactor Material,” *Int. J. Appl. Ceram. Technol.*, **7** [3] 316-26 (2010).
- [69]. J. Marschall and D.G. Fletcher, “High-Enthalpy Test Environments, Flow Modeling and *in situ* Diagnostics for Characterizing Ultra High Temperature Ceramics,” *J. Eur. Ceram. Soc.*, **30** [11] 2323-2336 (2010).
- [70]. J. Marschall and D.G. Fletcher, “High-Enthalpy Test Environments, Flow Modeling and *in situ* Diagnostics for Characterizing Ultra High Temperature Ceramics,” *J. Eur. Ceram. Soc.*, **30** [11] 2323-2336 (2010).
- [71]. M. Playez, D.G. Fletcher, J. Marschall, W.G. Fahrenholtz, G.E. Hilmas, and S. Zhu, “Optical Emission Spectroscopy during Plasmatron Testing of ZrB<sub>2</sub>-SiC Ultra-High Temperature Ceramic Composites,” *J. Thermophys. Heat Transfer*, **23** [2] 279-85 (2009).
- [72]. R.K. Smith, D.A. Wagner, and J. Cunningham, “A Survey of Current and Future Plasma Arc-Heated Test Facilities for Aerospace and Commercial Applications,” 36<sup>th</sup> Aerospace Sciences Meeting and Exhibit, AIAA Paper 1998-0146, January 1998.
- [73]. R.C. Robinson and J.L. Smialek, “SiC Recession Caused by SiO<sub>2</sub> Scale Volatility under Combustion Conditions: I, Experimental Results and Empirical Model,” *J. Am. Ceram. Soc.*, **82** [7] 1875-25 (1999).
- [74]. W.L. Vaughn and H.G. Maahs, “Active-to-Passive Transition in the Oxidation of Silicon Carbide and Silicon Nitride in Air,” *J. Am. Ceram. Soc.*, **73** [6] 1540-3 (1990).
- [75]. S.J. Lee, E.S. Kang, S.S. Baek, and D.K. Kim, “Reactive Hot Pressing and Oxidation Behavior of Hf-Based Ultra-High-Temperature Ceramics,” *Surf. Rev. Lett.*, **17** [2] 215-21 (2010).
- [76]. P. Hu and Z. Wang, “Flexural Strength and Fracture Behavior of ZrB<sub>2</sub>-SiC Ultra-High Temperature Ceramic Composites at 1800°C,” *J. Eur. Ceram. Soc.*, **30** [4] 1021-26 (2010).
- [77]. P. Hu, X.-H. Zhang, J.-C. Han, X.-G. Luo, and S.-Y. Du, “Effect of Various Additives on the Oxidation Behavior of ZrB<sub>2</sub>-Based Ultra-High-Temperature Ceramics at 1800°C,” *J. Am. Ceram. Soc.*, **93** [2] 345-9 (2010).
- [78]. S. Meng, C. Liu, G. Liu, G. Bai, C. Xu, and W. Xie, “Mechanisms of Material Failure for Fast Heating up at the Center of Ultra High Temperature Ceramic,” *Solid State Sci.*, **12** [4] 527-31 (2010).

- [79]. F. Monteverde, "Ultra-High Temperature HfB<sub>2</sub>-SiC Ceramics Consolidated by Hot-Pressing and Spark Plasma Sintering," *J. Alloys Compd.*, **428** [1-2] 197-205 (2007).
- [80]. S.N. Karlsdottir and J.W. Halloran, "Rapid Oxidation Characterization of Ultra-High Temperature Ceramics," *J. Am. Ceram. Soc.*, **90** [10] 3233-8 (2007).
- [81]. S.S. Hwang, A.L. Vasiliev, and N.P. Padture, "Improved Processing and Oxidation-Resistance of ZrB<sub>2</sub> Ultra-High Temperature Ceramics Containing SiC Nanodispersoids," *Mater. Sci. Eng. A*, **464** [1-2] 216-24 (2007).
- [82]. Y. Yan, Z. Huang, S. Dong, and D. Jiang, "Pressureless Sintering of High-Density ZrB<sub>2</sub>-SiC Ceramic Composites," *J. Am. Ceram. Soc.*, **89** [11] 3589-92 (2006).
- [83]. F. Monteverde, "Progress in the Fabrication of Ultra-High-Temperature Ceramics: "In Situ" Synthesis, Microstructure and Properties of a Reactive Hot-Pressed HfB<sub>2</sub>-SiC Composite," *Composites Sci. Technol.*, **65** [11-12] 1869-79 (2005).
- [84]. M. Gasch, D. Ellerby, E. Irby, S. Beckman, M. Gusman, and S. Johnson, "Processing, Properties and Arc Jet Oxidation of Hafnium Diboride/Silicon Carbide Ultra-High Temperature Ceramics," *J. Mater. Sci.*, **39** [19] 5925-37 (2004).
- [85]. J. Marschall, D.C. Erlich, H. Manning, W. Duppler, E. Ellerby, and M. Gasch, "Microhardness and High-Velocity Impact Resistance of HfB<sub>2</sub>/SiC and ZrB<sub>2</sub>/SiC Composites," *J. Mater. Sci.*, **39** [19] 5959-68 (2004).
- [86]. S.R. Levine, E.J. Opila, M.C. Halbig, J.D. Kiser, M. Singh, and J.A. Salem, "Evaluation of Ultra-High Temperature Ceramics for Aeropropulsion Use," *J. Eur. Ceram. Soc.*, **22** [14-15] 2757-67 (2002).
- [87]. C.R. Wang, J.-M. Yang, and W. Hoffman, "Thermal Stability of Refractory Carbide/Boride Composites," *Mater. Chem. Phys.*, **74** [3] 272-81 (2002).
- [88]. G.-J. Zhang, Z.-Y. Deng, N. Kondo, J.-F. Yang, and T. Ohji, "Reactive Hot Pressing of ZrB<sub>2</sub>-SiC Composites," *J. Am. Ceram. Soc.*, **83** [9] 2330-2 (2000).
- [89]. S.C. Zhang, W.G. Fahrenholtz, and G.E. Hilmas, "Oxidation of ZrB<sub>2</sub> and ZrB<sub>2</sub>-SiC Ceramics with Tungsten Additions," *ECS Trans.*, **16** [44] 137-45 (2009).
- [90]. S.C. Zhang, G.E. Hilmas, and W.G. Fahrenholtz, "Improved Oxidation Resistance of Zirconium Diboride by Tungsten Carbide Additions," *J. Am. Ceram. Soc.*, **91** [11] 3530-5 (2008).

- [91]. X.-H. Zhang, P. Hu, J.-C. Han, L. Xu, and S.-H. Meng, "The Addition of Lanthanum Hexaboride to Zirconium Diboride for Improved Oxidation Resistance," *Scripta Materialia*, **57** [11] 1036-9 (2007).
- [92]. H. Kuhn, H.-D. Försterling, and D.H. Waldeck, *Principles of Physical Chemistry*, 2<sup>nd</sup> ed; p. 429-30. John Wiley & Sons Inc., Hoboken, NJ, 2009.
- [93]. I.G. Talmy, J.A. Zaykoski, M.M. Opeka, and S. Dallek, "Oxidation of ZrB<sub>2</sub> Ceramics Modified with WiC and Group IV-VI Transition Metal Diborides," p. 144-58 in High Temperature Corrosion and Materials Chemistry III. Edited by M. McNallan and E. Opila, The Electrochemical Society, Inc., -Pennington, NJ, 2001.
- [94]. E. Opila, S. Levine, and J. Lorincz, "Oxidation of ZrB<sub>2</sub>- and HfB<sub>2</sub>-Based Ultra-High Temperature Ceramics: Effect of Ta Additions," *J. Mater. Sci.*, **39** [19] 5969-77 (2004).
- [95]. F. Peng, Y. Berta, and R.F. Speyer, "Effect of SiC, TaB<sub>2</sub> and TaSi<sub>2</sub> Additives on the Isothermal Oxidation Resistance of Fully Dense Zirconium Diboride," *J. Mater. Res.*, **24** [5] 1855-67 (2009).
- [96]. I.G. Talmy, J.A. Zaykoski, M.M. Opeka, and A.H. Smith, "Properties of Ceramics in the System ZrB<sub>2</sub>-Ta<sub>5</sub>Si<sub>3</sub>," *J. Mater Res.*, **21** [10] 2593-99 (2006).
- [97]. A. Balbo and D. Sciti, "Spark Plasma Sintering and Hot Pressing of ZrB<sub>2</sub>-MoSi<sub>2</sub> Ultra-High-Temperature Ceramics," *Mater. Sci. Eng. A*, **475** [1-2] 108-12 (2008).
- [98]. X. Zhang, L. Xu, S. Du, C. Liu, J. Han, and W. Han, "Spark Plasma Sintering and Hot Pressing of ZrB<sub>2</sub>-SiC<sub>w</sub> Ultra-High Temperature Ceramics," *J. Alloys and Compd.*, **466** [1-2] 241-5 (2008).
- [99]. A.I. Gusev, A.S. Kurlov, and V.N. Lipatnikov, "Atomic and Vacancy Ordering in Carbide  $\zeta$ -Ta<sub>4</sub>C<sub>3-x</sub> (0.28 ≤ x ≤ 0.4) and Phase Equilibria in the Ta-C System," *J. Solid State Chem.*, **180** [11] 3234-46 (2007).
- [100]. D.J. Rowcliffe and W.J. Warren, "Structure and Properties of Tantalum Carbide Crystals," *J. Mater. Sci.*, **5** [4] 345-50 (1970).
- [101]. D.L. Price, J.M. Wills, and B.R. Cooper, "Linear-Muffin-Tin-Orbital Calculation of TaC(001) Surface Relaxation," *Phys. Rev. B*, **48** [20] 15301-10 (1993).
- [102]. G.V. Samsonov, "How the Defect Content of the Carbon Sublattice Influences the Properties of Refractory Transition-Metal Carbides," *Inorg. Mater.*, **9** [12] 1893-8 (1973).

- [103]. O. Krechkivska and M.D. Morse, "Resonant Two-Photon Ionization Spectroscopy of Jet-Cooled Tantalum Carbide, TaC," *J. Chem. Phys.*, **133**, 054309-1-8 (2010).
- [104]. M. Sahnoun, C. Daul, J.C. Parlebas, C. Demangeat, and M. Driz, "Electronic Structure and Optical Properties of TaC from the First Principles Calculation," *Eur. Phys. J. B*, **44**, 281-6 (2005).
- [105]. N.V. Alekseev, Y.V. Blagoveshchenskii, G.N. Zviadadze, and I.K. Tagirov, "Theory, Production Technology, and Properties of Powders and Fibers," *Sov. Powder. Metall.*, **19** [8] 517-20 (1980).
- [106]. V.N. Lipatnikov and A.A. Rempel, "Formation of the Incommensurate Ordered Phase in TaC<sub>y</sub> Carbide," *JETP Lett.*, **81** [7] 326-30 (2005).
- [107]. A.I. Gusev, A.A. Rempel, and V.N. Lipatnikov, "Heat Capacity of Niobium and Tantalum Carbides NbC<sub>y</sub> and TaC<sub>y</sub> in Disordered and Ordered States below 300 K," *Phys. Stat. Sol. B*, **194**, 467-82 (1996).
- [108]. A.I. Gusev, A.A. Rempel, and V.N. Lipatnikov, "Incommensurate Ordered Phase in Non-Stoichiometric Tantalum Carbide," *J. Phys.: Condens. Matter*, **8** [43] 8277-93 (1996).
- [109]. A.I. Gusev, A.A. Rempel, and V.N. Lipatnikov, "Incommensurate Superlattice and Superconductivity in Tantalum Carbide," *Sov. Phys. Solid State*, **33** [8] 1295-1299 (1991).
- [110]. A.A. Rempel, V.N. Lipatnikov, and A.I. Gusev, "The Superstructure in Nonstoichiometric Tantalum Carbide," *Sov. Phys. Dokl.*, **35** [2] 103-6 (1990).
- [111]. A.I. Gusev, "Atomic Ordering and the Order Parameter Functional Method," *Philos. Mag.*, **60** [3] 307-324 (1989).
- [112]. V.N. Lipatnikov, A.I. Gusev, A.A. Rempel, and G.P. Shveikin, "Effect of a Structural Transition on the Magnetic Susceptibility of Tantalum Carbide," *Sov. Phys. Dokl.*, **32** [12] 988-90 (1987).
- [113]. A.L. Bowman, "The Variation of Lattice Parameter with Carbon Content of Tantalum Carbide," *J. Phys. Chem.*, **65** [9] 1596-8 (1961).
- [114]. C. Kim, G. Gottstein, and D.S. Grummon, "Plastic Flow and Dislocation Structures in Tantalum Carbide: Deformation at Low and Intermediate Homologous Temperatures," *Acta Metall. Mater.*, **42** [7] 2291-2301 (1994).
- [115]. M.A. Khusainov, G.M. Demyshev, and M.M. Myshlyaev, "Mechanical Properties and Structure of Carbide Coatings of Niobium and Tantalum on Graphite," *Russ. Metall.*, [5] 139-42 (1990).

- [116]. M. Hoffman and W.S. Williams, "A Simple Model for the Deformation Behavior of Tantalum Carbide," *J. Am. Ceram. Soc.*, **69** [8] 612-14 (1986).
- [117]. C. Allison, M. Hoffman, and W.S. Williams, "Electron Energy Loss Spectroscopy of Carbon in Dissociated Dislocations in Tantalum Carbide," *J. Appl. Phys.*, **53** [10] 6757-61 (1982).
- [118]. D.J. Rowcliffe and G.E. Hollox, "Hardness Anisotropy, Deformation Mechanisms and Brittle-to-Ductile Transition in Carbides," *J. Mater. Sci.*, **6** [10] 1270-6 (1971).
- [119]. D.J. Rowcliffe and G.E. Hollox, "Plastic Flow and Fracture of Tantalum Carbide and Hafnium Carbide at Low Temperatures," *J. Mater. Sci.*, **6** [10] 1261-9 (1971).
- [120]. O.Y. Khyzhun, E.A. Zhurakovsky, A.K. Sinelnichenko, and V.A. Kolyagin, "Electronic Structure of Tantalum Subcarbides Studied by XPS, XES, and XAS Methods," *J. Electron Spectrosc. Rel. Phenom.*, **82** [3] 179-92 (1996).
- [121]. L. Silvestroni, A. Bellosi, C. Melandri, D. Sciti, J.X. Liu, G.J. Zhang, "Microstructure and Properties of HfC and TaC-Based Ceramics Obtained by Ultrafine Powder," *J. Eur. Ceram. Soc.*, **31** [4] 619-27 (2011).
- [122]. J.-X. Liu, Y.-M. Kan, and G.-J. Zhang, "Pressureless Sintering of Tantalum Carbide Ceramics without Additives," *J. Am. Ceram. Soc.*, **93** [2] 370-73 (2010).
- [123]. X. Zhang, G.E. Hilmas, and W.G. Fahrenholtz, "Hot Pressing of Tantalum Carbide With and Without Sintering Additives," *J. Am. Ceram. Soc.*, **90** [2] 393-401 (2007).
- [124]. R.D. Evans, G.L. Doll, and J.T. Glass, "Mechanical Property Development in Reactively Sputtered Tantalum Carbide/Amorphous Hydrocarbon Thin Films," *J. Mater. Res.*, **21** [6] (2006).
- [125]. S. Urbonaite, M. Johnsson, and G. Svensson, "Synthesis of  $TiC_{1-x}N_x$  and  $TaC_{1-x}N_x$  by Spark Plasma Sintering," *J. Mater. Sci.*, **39**, 1907-11 (2004).
- [126]. W.C. Yohe and A.L. Ruoff, "Ultrafine-Grain Tantalum Carbide by High Pressure Hot Pressing," *Ceram. Bull.*, **57** [12] 1123-30 (1978).
- [127]. J. Sautereau and A. Mocellin, "Sintering Behavior of Ultrafine NbC and TaC Powders," *J. Mater. Sci.*, **9**, 761-71 (1974).
- [128]. S.R. Bakshi, V. Musaramthota, D.A. Virzi, A.K. Keshri, D. Lahiri, V. Singh, S. Seal, and A. Agarwal, "Spark Plasma Sintered Tantalum Carbide-Carbon Nanotube Composite: Effect of Pressure, Carbon Nanotube Length and

- Dispersion Technique on Microstructure and Mechanical Properties,” *Mater. Sci. Eng. A*, **528**, 2538-47 (2011).
- [129]. K. Balani, G. Conzalez, A. Agarwal, R. Hickman, J.S. O’Dell, and S. Seal, “Synthesis, Microstructural Characterization, and Mechanical Property Evaluation of Vacuum Plasma Sprayed Tantalum Carbide,” *J. Am. Ceram. Soc.*, **89** [4] 1419-25 (2006).
- [130]. K. Hackett, S. Verhoef, R.A. Cutler, and D.K. Shetty, “Phase Constitution and Mechanical Properties of Carbides in the Ta-C System,” *J. Am. Ceram. Soc.*, **92** [10] 2404-7 (2009).
- [131]. L. López-de-la-Torre, B. Winkler, J. Schreuer, K. Knorr, and M. Avalos-Borja, “Elastic Properties of Tantalum Carbide (TaC),” *Solid State Commun*, **134**, 245-50 (2005).
- [132]. C.K. Jun and P.T.B. Shaffer, “Thermal Expansion of Niobium Carbide, Hafnium Carbide, and Tantalum Carbide at High Temperatures,” *J. Less-Common Metals*, **24**, 323-7 (1971).
- [133]. R.J. Fries and L.A. Wahman, “Effect of Stoichiometry on the Thermal Expansion of TaC<sub>x</sub>,” *J. Am. Ceram. Soc.*, **50** [9] 475-7 (1967).
- [134]. C.P. Kempter and M.R. Nadler, “Thermal Expansion of Tantalum Monocarbide to 3020°C,” *J. Chem. Phys.*, **43** [5] 1739-42 (1965).
- [135]. B.R. Miccioli and P.T.B. Shaffer, “High Temperature Thermal Expansion Behavior of Refractory Materials: I, Selected Monocarbides and Binary Carbides,” *J. Am. Ceram. Soc.*, **47** [7] 351-6 (1964).
- [136]. C.P. Kempter and M.R. Nadler, “Thermal Decomposition of Niobium and Tantalum Monocarbides,” *J. Chem. Phys.*, **32** [5] 1477-81 (1960).
- [137]. M. Hoch, P.E. Blackburn, D.P. Dingley, and H.L. Johnson, “Heat of Sublimation of Carbon,” *J. Phys. Chem.*, **59** [2] 97-9 (1955).
- [138]. K. Nakamura and M. Yashima, “Crystal Structure of NaCl-Type Transition Metal Monocarbides MC (M = V, Ti, Nb, Ta, Hf, Zr), a Neutron Powder Diffraction Study,” *Mater. Sci. Eng. B*, **148** [1-3] 69-72 (2008).
- [139]. V.N. Lipatnikov, A.A. Rempel, and A.I. Gusev, “Specific Heat of Tantalum Carbide in States with Different Degrees of Order,” *Sov. Phys. Solid State*, **31** [10] 1818-19 (1989).

- [140]. A.E. Sheindlin, I.S. Belevich, and I.G. Kozhevnikov, "Enthalpy and Specific Heat of Tantalum Carbide in the Range of 273-3600 K," *High Temp.*, **10** [3] 581-3 (1973).
- [141]. R.D. Allen, "An Electron Beam Technique for Measuring Thermal Conductivity," *Cer. Bull.*, **48** [6] 614-7 (1969).
- [142]. M.A. Khusainov, G.M. Demyashev, and M.M. Myshlyaev, "Electrophysical Properties and Structure of Niobium and Tantalum Carbide Coatings on Graphite," *Russ. Metall.*, [6] 160-4 (1990).
- [143]. C.K. Jun and P.T.B. Shaffer, "Elastic Moduli of Niobium Carbide and Tantalum Carbide at High Temperature," *J. Less-Common Met.*, **23**, 367-73 (1971).
- [144]. V.G. Bukatov, V.I. Knyazev, O.S. Korostin, and V.M. Baranov, "Temperature Dependence of the Young's Modulus of Metalline Carbides," *Inorganic Mater.*, **11** [2] 310-12 (1975).
- [145]. S.R. Bakshi, V. Musaramthota, D. Lahiri, V. Singh, S. Seal, and A. Agarwal, "Spark Plasma Sintered Tantalum Carbide: Effect of Pressure and Nano-Boron Carbide Addition on Microstructure and Mechanical Properties," *Mater. Sci. Eng. A*, **528**, 1287-95 (2011).
- [146]. X. Zhang, G.E. Hilmas, and W.G. Fahrenholtz, "Densification and Mechanical Properties of TaC-Based Ceramics," *Mater. Sci. Eng. A*, **501**, 37-43 (2009).
- [147]. V.A. Petrov, V.Ya. Chekhovskoi, A.E. Sheindlin, and V.A. Nikolaeva, "Total Hemispherical Emissivity, Spectral Normal Emissivity at a Wavelength 0.65  $\mu\text{m}$ , and Electrical Resistivity of Tantalum Carbide at Very High Temperatures,"
- [148]. W.A. Mackie, P. Carleson, J. Filion, and C.H. Hinrichs, "Normal Spectral Emittance of Crystalline Transition Metal Carbides," *J. Appl. Phys.*, **69** [10] 7236-39 (1991).
- [149]. A.E. Sheindlin, V.A. Petrov, A.N. Vinnikova, and V.A. Nikolaeva, "Integral Normal Emissivity of Tantalum and Hafnium Carbides Over the Temperature Range 1300-3000 K," *High Temp.*, **7** [2] 236-8 (1969).
- [150]. G.I. Danil'yants, A.V. Kirillin, and S.V. Novikov, "Emissivity of Tantalum Carbide at Elevated Temperature," *High Temp.*, **26** [1] 65-9 (1988).
- [151]. L. Liu, F. Ye, and Y. Zhou, "New Route to Densify Tantalum Carbide at 1400°C by Spark Plasma Sintering," *Mater. Sci. Eng. A*, **528**, 4710-14 (2011).
- [152]. E. Khaleghi, Y.-S. Lin, M.A. Meyers, and E.A. Olevsky, "Spark Plasma Sintering of Tantalum Carbide," *Scripta Materialia*, **63**, 577-80 (2010).

- [153]. S.A. Shvab and F.F. Egorov, "Structure and Some Properties of Sintered Tantalum Carbide," *Sov. Powder Metall. Met. Ceram.*, **21** [11] 894-7 (1982).
- [154]. P.S. Kislyi, S.A. Shvab, and F.F. Egorov, "Sintering Kinetics of Tantalum Carbide," *Powder Metall. And Met. Ceram.*, **21** [10] 765-7 (1982).
- [155]. P.F. Becher, "Mechanical Behaviour of Polycrystalline TaC," *J. Mater. Sci.*, **6**, 79-80 (1971).
- [156]. R.J. Grohsmeyer, "Characterization of Thermal, Electrical, Microstructural, and Mechanical Properties of Tantalum Carbide," B.S. Thesis, Alfred University, Alfred, NY (2012).
- [157]. D. Sciti, L. Silvestroni, S. Guicciardi, D.D. Fabbriche, and A. Bellosi, "Processing, Mechanical Properties and Oxidation Behavior of TaC and HfC Composites Containing 15 vol% TaSi<sub>2</sub> or MoSi<sub>2</sub>," *J. Mater. Res.*, **24** [6] 2056-65 (2009).
- [158]. Y. Zhang, C. Zhang, H. Hu, and Y. Zhou, "Preparation and Properties of 20 C/SiC-TaC Composites," *Key Eng. Mater.*, **368-372** [2] 1771-3 (2007).
- [159]. L. Honeycutt III, W.H. Jennings, and C.R. Manning, Jr., "High Temperature Erosion of Tantalum Carbide Composites," *Wear*, **37**, 209-16 (1976).
- [160]. J.C. Fletcher, "Thermal Shock and Erosion Resistant Tantalum Carbide," U.S. Patent 4,067,742, January 1978.
- [161]. C.E. Shulze, The Carborundum Company, "Refractory Body Having High Resistance to Flame Erosion and Thermal Shock," U.S. Patent 3,165,864, January, 1965.
- [162]. J. Ma, Y. Du, M. Wu, and M. Pan, "One Simple Synthesis Route to Nanocrystalline Tantalum Carbide via the Reaction of Tantalum Pentachloride and Sodium Carbonate with Metallic Magnesium," *Mater. Lett.*, **61**, 3658-61 (2007).
- [163]. L. Shi, Y. Gu, L. Chen, Z. Yang, J. Ma, and Y. Qian, "Formation of TaC Nanorods with a Low-Temperature Chemical Route," *Chemistry Lett.*, **33** [12] 1546-7 (2004).
- [164]. M. Johnsson and S. Shimada, "Oxidation of Ta<sub>x</sub>Ti<sub>1-x</sub>C Whiskers Under Formation of Carbon," *J. Mater. Sci. Lett.*, **21**, 955-8 (2002).

- [165]. M. Desmaison-Brut, N. Alexandre, and J. Desmaison, "Comparison of the Oxidation Behavior of Two Dense Hot Isostatically Pressed Tantalum Carbide (TaC and Ta<sub>2</sub>C) Materials," *J. Eur. Ceram. Soc.*, **17**, 1325-34 (1997).
- [166]. É.I. Golovko, L.F. Ochkas, M.S. Koval'chenko, and A.F. Nikityuk, "Oxidation of Tantalum Carbide Alloys," *Poroshkovaya Metallurgiya*, **166** [10] 51-4 (1976).
- [167]. A. Joly, *Compt. Rend. Acad. Sci.*, **82**, 1905 (1876).
- [168]. B.M. Eick and J.P. Youngblood, "Carbothermal Reduction of Metal-Oxide Powders by Synthetic Pitch to Carbide and Nitride Ceramics," *J. Mater. Sci.*, **44**, 1159-71 (2009).
- [169]. P.G. Li, M. Lei, Z.B. Sun, L.Z. Cao, Y.F. Guo, X. Guo, and W.H. Tang, "C<sub>3</sub>N<sub>4</sub> as a Precursor for the Synthesis of NbC, TaC, and WC Nanoparticles," *J. Alloys Compd.*, **430**, 237-40 (2007).
- [170]. H. Xiang, Y. Xu, L. Zhang, and L. Cheng, "Synthesis and Microstructure of Tantalum Carbide and Carbon Composite by Liquid Precursor Route," *Scripta Materialia*, **55**, 339-42 (2006).
- [171]. J.C. Fernandes, F.A.C. Oliveira, B. Granier, J.-M. Badie, L.G. Rosa, and N. Shohoji, "Kinetic Aspects of Reaction Between Tantalum and Carbon Material (Active Carbon or Graphite) Under Solar Radiation Heating," *Solar Energy*, **80**, 1553-60 (2006).
- [172]. D.-H. Kwon, S.-H. Hong, and B.-K. Kim, "Fabrication of Ultrafine TaC Powders by Mechano-Chemical Process," *Mater. Lett.*, **58**, 3863-7 (2004).
- [173]. C. Ciaravino, F.F.P. Medeiros, C.P. De Souza, and M. Roubin, "Elaboration of Mixed Tantalum and Niobium Carbides from Tantalite Mineral (Fe,Mn)(Ta<sub>1-x</sub>Nb<sub>x</sub>)<sub>2</sub>O<sub>6</sub>," *J. Mater. Sci.*, **37**, 2117-23 (2002).
- [174]. Y.-H. Chang, C.-W. Chiu, Y.-C. Chen, C.-C. Wu, C.-P. Tsai, J.-L. Wang, and H.-T. Chiu, "Syntheses of Nano-Sized Cubic Phase Early Transition Metal Carbides From Metal Chlorides and n-Butyllithium," *J. Mater. Chem. Commun.*, **12**, 2189-91 (2002).
- [175]. J. Rodríguez, D. Martínez, L.G. Rosa, J.C. Fernandes, P.M. Amaral, and N. Shohoji, "Photochemical Effects in Carbide Synthesis of d-Group Transition Metals (Ti,Zr; V, Nb, Ta; Cr, Mo, W) in a Solar Furnace at PSA (Platforma Solar de Almería)," *J. Sol. Energ. Eng.*, **123**, 109-16 (2001).
- [176]. H. Preiss, D. Schultze, and P. Klobes, "Formation of NbC and TaC from Gel-Derived Precursors," *J. Eur. Ceram. Soc.*, **17**, 1423-35 (1997).

- [177]. N.A. Hassine, J.G.P. Binner, and T.E. Cross, "Synthesis of Refractory Metal Carbide Powders via Microwave Carbothermal Reduction," *Intl. J. Refractory Met. Hard Mater.*, **13** [6] 353-8 (1995).
- [178]. S.A. Shvab and P.S. Kislyi, "Some Properties of Tantalum Carbide Powder Produced by Synthesis from the Elements," *Sov. Powder Metall. Met. Cer.* **13** [5] 368-70 (1974).
- [179]. J.J. Moore and H.J. Feng, "Combustion Synthesis of Advanced Materials: Part I. Reaction Parameters," *Prog. Mater. Sci.*, **39** [4-5] 243-73 (1995).
- [180]. S.T. Aruna and A.S. Mukasyan, "Combustion Synthesis and Nanomaterials," *Curr. Opin. Solid State Mater. Sci.*, **12**, 44-50 (2008).
- [181]. C.L. Yeh and E.W. Liu, "Combustion Synthesis of Tantalum Carbides TaC and Ta<sub>2</sub>C," *J. Alloys Compd.*, **415**, 66-72 (2006).
- [182]. O.A. Graeve, and Z.A. Munir, "Electric Field Enhanced Synthesis of Nanostructured Tantalum Carbide," *J. Mater. Res.*, **17** [3] 609-13 (2002).
- [183]. H. Xue and Z.A. Munir, "Field-Activated Combustion Synthesis of TaC," *Intl. J. Self-Propag. High-Temp. Synth.*, **5** [3] 229-39 (1996).
- [184]. J.J. Moore and H.J. Feng, "Combustion Synthesis of Advanced Materials: Part II. Classification, Applications and Modelling," *Prog. Mater. Sci.*, **39** [4-5] 275-316 (1995).
- [185]. V.M. Shkiro, G.A. Nersisyan, I.P. Borovinskaya, A.G. Merzhanov, and V.Sh. Shekhtman, "Preparation of Tantalum Carbides by Self-Propagating High-Temperature Synthesis," *Poroshkovaya Metallurgiya*, **196** [4] 14-7 (1979).
- [186]. T. Ishigaki, S.-M. Oh, J.-G. Li, and D.-W. Park, "Controlling the Synthesis of TaC Nanopowders by Injecting Liquid Precursor into RF Induction Plasma," *Sci. Technol. Adv. Mater.*, **6**, 111-118 (2005).
- [187]. Y.-J. Chen, J.-B. Li, Q.-M. Wei, and H.-Z. Zhai, "Preparation of Different Morphology of TaC<sub>x</sub> Whiskers," *Mater. Lett.*, **56**, 279-83 (2002).
- [188]. N. Ahlén, M. Johnsson, A.-K. Larsson, and B. Sundman, "On the Carbothermal Vapour-Liquid-Solid (VLS) Mechanism for TaC, TiC, and Ta<sub>x</sub>Ti<sub>1-x</sub>C Whisker Growth," *J. Eur. Ceram. Soc.*, **20**, 2607-18 (2000).
- [189]. A. Fukunaga, S. Chu, and M.E. McHenry, "Using Carbon Nanotubes for the Synthesis of Transition Metal Carbide Nanoparticles," *J. Mater. Sci. Lett.*, **18**, 431-3 (1999).

- [190]. A. Fukunaga, S. Chu, and M.E. McHenry, "Synthesis, Structure, and Superconducting Properties of Tantalum Carbide Nanorods and Nanoparticles," *J. Mater. Res.*, **13** [9] 2465-71 (1998).
- [191]. M. Johnsson, N. Ahlén, and M. Nygren, "Synthesis and Characterization of Transition Metal Carbide Whiskers," *Key Eng. Mater.*, **132-136**, 201-4 (1997).
- [192]. M. Johnsson and M. Nygren, "Carbothermal Synthesis of TaC Whiskers via a Vapor-Liquid-Solid Growth Mechanism," *J. Mater. Res.*, **12** [9] 2419-27 (1997).
- [193]. M.I. Tatarintseva, N.I. Puzynina, V.N. Kulyukin, and V.N. Arbekov, "Crystallographic and Morphological Features of Carbide Formation in the Ta-C-Cl System," *Inorganic Mater.*, **19** [11] 1630-3 (1983).
- [194]. N.V. Alekseev, Yu.V. Blagoveshchenskii, G.N. Zviadadze, and I.K. Tagirov, "Production of Fine Niobium and Tantalum Carbide Powders," *Soviet Powder Metall. Met. Ceram.*, **19** [8] 517-20 (1980).
- [195]. W. Grossklauss and R.F. Bunshah, "Synthesis and Morphology of Various Carbides in the Ta-C System," *J. Vac. Sci. Technol.*, **12** [4] 811-13 (1975).
- [196]. T. Takahashi and K. Sugiyami, "Fibrous Growth of Tantalum Carbide by A-C Discharge Method," *J. Electrochem. Soc.*, **121** [5] 714-18 (1974).
- [197]. X. Li, A. Westwood, A. Brown, R. Brydson, and B. Rand, "A Convenient, General Synthesis of Carbide Nanofibres via Templated Reactions on Carbon Nanotubes in Molten Salt Media," *Carbon*, **47**, 201-8 (2009).
- [198]. K.H. Stern and S.T. Gadomski, "Electrodeposition of Tantalum Carbide Coatings from Molten Salts," *J. Electrochem. Soc.*, **130** [2] 300-5 (1983).
- [199]. D.A. Robins, *Physical Chemistry of Metallic Solutions and Intermetallic Compounds*, Vol. 2, H.M. Stationery Office, London (1959), pp. 7B/1-10.
- [200]. A.M. Nartowski, I.P. Parkin, M. MacKenzie, A.J. Craven, and I. MacLeod, "Solid State Metathesis Routes to Transition Metal Carbides," *J. Mater. Chem.*, **9**, 1275-81 (1999).
- [201]. E.G. Gillan and R.B. Kaner, "Synthesis of Refractory Ceramics via Rapid Metathesis Reactions between Solid-State Precursors," *Chem. Mater.*, **8**, 333-43 (1996).
- [202]. P.G. Li, M. Lei, and W.H. Tang, "Route to Transition Metal Carbide Nanoparticles through Cyanamide and Metal Oxides," *Mater. Res. Bull.*, **43**, 3621-6 (2008).

- [203]. M. Lei, H.Z. Zhao, H. Yang, B. Song, and W.H. Tang, "Synthesis of Transition Metal Carbide Nanoparticles through Melamine and Metal Oxides," *J. Eur. Ceram. Soc.*, **28**, 1671-7 (2008).
- [204]. J.A. Nelson and M.J. Wagner, "High Surface Area Nanoparticulate Transition Metal Carbides Prepared by Alkalide Reduction," *Chem. Mater.*, **14**, 4460-3 (2002).
- [205]. B.-R. Kim, K.-D. Woo, J.-M. Doh, J.-K. Yoon, and I.-J. Shon, "Mechanical Properties and Rapid Consolidation of Binderless Nanostructured Tantalum Carbide," *Ceram. Intl.*, **35**, 3395-400 (2009).
- [206]. L. Silvestroni and D. Sciti, "Sintering Behavior, Microstructure, and Mechanical Properties: A Comparison among Pressureless Sintered Ultra-Refractory Carbides," *Adv.Mater. Sci. Eng.*, **2010**, 1-11 (2010).
- [207]. I.G. Talmy, J.A. Zaykoski, and M.M. Opeka, "Synthesis, Processing and Properties of TaC-TaB<sub>2</sub>-C Ceramics," *J. Eur. Ceram. Soc.*, **30**, 2253-63 (2010).
- [208]. G.V. Samonov and R.Y. Petrikina, "Sintering of Metals, Carbides, and Oxides by Hot Pressing," *Phys. Sintering*, **2** [3] 1-20 (1970).
- [209]. L. Liu, F. Ye, X. He, and Y. Zhou, "Densification Process of TaC/TaB<sub>2</sub> Composite in Spark Plasma Sintering," *Mater. Chem. Phys.*, **126**, 459-62 (2011).
- [210]. Y.E. Geguzin and Y.I. Klinchuk, "Mechanism and Kinetics of the Initial Stage of Solid-Phase Sintering of Compacts from Powders of Crystalline Solids," *Poroshk. Metall.*, [7] 17-25 (1976).
- [211]. M.F. Ashby and H.A. Verral, "Diffusion-Accommodated Flow and Superplasticity," *Acta Metall.*, **21**, 149-63 (1974).
- [212]. Y.E. Geguzin, "Diffusional Deformation of Porous Crystalline Structures," *Fiz. Tverd. Tela*, **17** [7] 1950-4 (1957).

## CHAPTER 2: SYNTHESIS OF NANOSTRUCTURED TRANSITION METAL BORIDE, CARBIDE, AND NITRIDE POWDERS PRODUCED BY SOLVOTHERMAL SYNTHESIS

### A. Introduction

Non-oxide ceramics are ceramics consisting of a metal bonded with either metalloids or non-metals, other than oxygen, and have become an important class of materials. Non-oxides are rarely found in nature and are sometimes found in meteorites. This rarity ensures that any commercial use of these materials will require synthetic processes.

Bursts of development have occurred depending on a particular need and some non-oxide materials have been developed more than others. For instance,  $\text{Si}_3\text{N}_4$  was a highly pursued material beginning in the 1950's for the use of lightweight ceramics for more efficient engines.<sup>[1-2]</sup> Although an all ceramic engine was never successfully implemented, the intense research efforts to do so have resulted in the development of other important classes of materials (silicon aluminum oxynitrides, other oxynitrides, and oxynitride glasses for example). Overall, the possibility for replacing some engine components with  $\text{Si}_3\text{N}_4$  and introduction of these materials in other suitable markets as processing was developed, tested, and improved.  $\text{Si}_3\text{N}_4$ -based materials are in some ways one of the most well understood advanced ceramic systems as a result of intense development.<sup>[3-5]</sup> Although silicon based non-oxide materials are a great example of successful and widespread commercialization of non-oxide materials, they only represent a small subset of ceramic non-oxide possibilities.

Ultra-high-temperature ceramics (UHTCs) are a particular subclass of non-oxides that had begun to get some attention in the early 1960's to mid 1970's for materials that could be capable of withstanding the harsh environments of space applications.<sup>[6-7]</sup> UHTC research has been substantially expanded in more recent years to meet new technological challenges, particularly as potential candidates for extreme environments associated with hypersonic flight, rocket propulsion, and space re-entry conditions.<sup>[8-11]</sup>

The definition of UHTCs varies, but in general corresponds to ceramics with melting temperatures above ~3000 K for use in high-temperature applications where temperatures may be near the range of 2000-3000 K.<sup>[12]</sup> Some of the transition metal borides, carbides, and nitrides meet this specification and some authors have limited their definition to these materials.<sup>[12-13]</sup> Table 2-I provides a summary of selected compounds demonstrating such high melting temperatures. The high melting temperatures and relatively good thermal-chemical-mechanical stability of these materials is attributed to covalent bonding. Adiabatic flame temperatures are also provided in the table and will be discussed later.

Table 2 – I. Melting Temperatures ( $T_m$ ) and Adiabatic Flame Temperature ( $T_{ad}$ ) by Reaction from the Compound Constituents of Selected Ultra-High Temperature Ceramics<sup>[14-15]</sup>

<b>Carbides</b>	<b><math>T_{ad}</math> (K)</b>	<b><math>T_m</math> (K)</b>	<b>Borides</b>	<b><math>T_{ad}</math> (K)</b>	<b><math>T_m</math> (K)</b>	<b>Nitrides</b>	<b><math>T_{ad}</math> (K)</b>	<b><math>T_m</math> (K)</b>
<b>HfC</b>	3900	4100	<b>HfB<sub>2</sub></b>	3520	3640	<b>HfN</b>	5100	3600
<b>TaC</b>	2700	4100	<b>TaB<sub>2</sub></b>	3370	3540	<b>TaN</b>	3360	3220
<b>ZrC</b>	--	3533	<b>ZrB<sub>2</sub></b>	3310	3270	<b>ZrN</b>	4900	3230
<b>TiC</b>	3210	3210	<b>TiB<sub>2</sub></b>	3190	3500	<b>TiN</b>	4900	3560

Although the melting temperatures of non-oxide UHTCs are high, special care must be considered for realizing the use of these materials at high temperatures without significant decomposition. Virtually all non-oxide ceramics in almost every application environment of interest are in a state of non-equilibrium with the atmosphere and the effective use of the material relies on the characteristics of the degradation processes involved. The most common non-equilibrium condition of interest is the result of being exposed to a chemically oxidizing atmosphere, which has been addressed by many authors not limited to the references provided for examples.<sup>[16-20]</sup> The oxidation resistance is a frequent deficiency in UHTCs, but can be improved with appropriate focus on compositional/composite design to engineer a protective oxidation scale.

The oxidation mechanism for a non-oxide can be classified into active (typically associated with weight and material loss that is continuous) and passive (typically

associated with weight gain with material conversion that slows with time). Active oxidation should be avoided completely for most applications. The typical weight gain associated with passive oxidation is the result of oxide scale formation and the oxidation slows with time because the scale acts as a barrier that limits further oxidation. The oxide scale can also be considered protective or non-protective. Non-protective oxide scales may result when the scale is porous, is not in equilibrium with the atmosphere, and/or cracking of the scale occurs (from physical damage, thermal shock, or stresses from interaction with the non-oxide bulk for example).

The ideal UHTC from a design perspective will balance high melting temperature (to act as the bulk structural support) with a relatively stable oxide scale on the surfaces to protect the bulk from further oxidation at high temperatures. The general approach to this is by designing UHTC composites. The composite should form a dense scale on its surfaces that is as stable as possible with both the UHTC bulk and the atmospheric conditions. The stability of the scale with the UHTC bulk depends on chemical stability, good adhesion, similar thermal expansions to prevent stress development, and low thermal expansion to minimize the risk of thermal shocking the UHTC. The interactions between the oxide scale and the atmosphere should be minimal, requiring that the oxide scale that forms is also highly refractory. However, some lack of refractoriness may be beneficial for “healing” cracks that may form in the scale and will also require a balanced design approach.

One particular issue with exploring UHTC composites is that their high temperatures and stability make them expensive to produce and process, significantly hindering the ability to study them as extensively as would otherwise be possible. As an example, Levine *et al.* report on the study of  $ZrB_2$ , but explicitly state that they did not study  $HfB_2$  because of cost limitations.<sup>[11]</sup> Although computer aided design and modeling will help select appropriate materials for the design of UHTC composite materials, experimental verification and testing is still a necessity. Utilizing nanostructured powders has the potential to reduce sintering temperatures, which could reduce processing costs.

There are several techniques currently utilized for the synthesis of nanostructured non-oxide ceramics.<sup>[21-22]</sup> For obtaining nanostructured non-oxides, the synthesis method

should result in nano-regime crystallite sizes and ideally have low levels of agglomeration, have high phase purity, have high chemical purity (including clean surfaces), and be a well understood and controllable process. An ideal synthesis method for ensuring a low cost would also be energy efficient, fast, scalable, and be able to produce a diverse group of materials (in this case a broad range of UHTCs that can be used for composite development). All of the typical synthesis methods satisfy some of these criteria, but often fall short for a few of the other desired characteristics. New techniques or modifications to currently used techniques that address these issues are desirable.

Table 2-I also demonstrates that these materials having high melting temperatures also have high adiabatic flame temperatures by the stoichiometric reaction between the metal and non-metal. The adiabatic flame temperature is the theoretical temperature that an exothermic reaction will achieve if all of the heat is transferred to the system (reaction products) with no heat loss to the environment and assuming full conversion of the reactants. Realistically heat is also lost to the environment. Highly exothermic reactions having high adiabatic flame temperatures ( $> 2073$  K) are empirically suitable for self-propagating high temperature synthesis (SHS) of materials.<sup>[14]</sup> The high reaction temperature and short reaction time during SHS result in a reaction that approaches adiabatic behavior and therefore reaches a temperature that approaches the adiabatic flame temperature.

A promising and scalable solvothermal synthesis method was recently reported for synthesizing TaC and LaB<sub>6</sub>.<sup>[23-24]</sup> Scalability is important because large-volume production assists in driving costs downward. The solvothermal synthesis of these materials relies on SHS reactions within a melt. The SHS nature of the reaction provides energy efficiency, requiring only a low amount of external energy to ignite the reactants, which also contributes to low synthesis costs. Similar to traditional SHS, the reaction is fast, assisting scalability by allowing for large quantities of powders to be produced rapidly. Similar techniques have been demonstrated in kg-quantities.<sup>[25-27]</sup> The melt reduces grain size, overcoming the difficulty to produce fine powders from traditional SHS. The empirical relationship for the successful synthesis of a material by solvothermal synthesis is expected to be similar to that for the parent SHS technique.

Thus, reactions having adiabatic flame temperatures  $>2073$  K, like many listed in Table 2-I, are good candidates for the solvothermal synthesis method.

By eliminating the use of pressure for solvothermal synthesis, the necessity of an autoclave was eliminated and the reaction could be performed in simpler apparatus. The simpler apparatus is not as costly as an autoclave and the thin walls of the reaction vessel allow for much faster heating and cooling rates when compared to using an autoclave, which helps make the process faster from start to finish and minimizes agglomeration caused by reprecipitation.

The solvothermal process has been used to obtain TaC powders that were nanostructured, phase pure, and had a low level of agglomeration.<sup>[23-24]</sup> Some flexibility in various responses versus processing variables was also demonstrated.<sup>[24]</sup> In fact, the only appealing aspects of an ideal process that were described earlier that have not been studied for this solvothermal synthesis method include chemical purity and demonstrating that a broad range of materials can be synthesized using this method. The primary chemical impurities of non-oxides include carbon or carbon containing impurities, oxygen, metals and halogens. Removal of these impurities from non-oxides is already well studied.<sup>[28]</sup> Therefore, the purpose of this work will be to demonstrate the potential of the solvothermal synthesis method for making a diverse set of UHTC powders and begin to define the criteria that defines the conditions for successful reactions.

It is important to note that the purpose is to demonstrate the synthesis of these materials, not to optimize the synthesis. Some aspects of process optimization have been provided previously.<sup>[24]</sup>

## **B. Experimental Procedures**

Table 2-II, Table 2-III, and Table 2-IV give details about the the non-oxides that were explored, the reaction equation that was used in each instance, the precursor information, and the amounts of reactants that are used to produce a three-gram theoretical yield of powder, except for BN. A one-gram theoretical yield was used for BN because of the low density of the material. The procedure for each of these experiments is similar. All mixing was performed in an argon atmosphere. The compound precursors were weighed out according to the amounts given in Table 2-IV,

which correspond to the reaction equations given in Table 2-II, and hand mixed using a mortar and pestle. This mixture was added to a 95 ml fused-silica test tube. The reductant metal, either lithium or calcium, was weighed out in the amount given in Table 2-IV and added on top of the reactant mixture, but not mixed because the reductant is added in granular form to reduce its reactivity. The test tube was then lightly sealed with a rubber stopper and removed from the argon atmosphere to be ignited underneath a chemical fume hood.

Table 2 – II. Balanced Solvothermal Synthesis Reactions of Various Ultra-High Temperature Ceramics

<b>Compound</b>	<b>Reaction</b>
TaB <sub>2</sub>	$2\text{TaCl}_5 + 8\text{NaBH}_4 + 20\text{Ca} \rightarrow 2\text{TaB}_2 + 4\text{B} + 5\text{CaCl}_2 + 15\text{Ca} + 8\text{Na} + 16\text{H}_2$
HfB <sub>2</sub>	$\text{HfCl}_4 + 6\text{B} + 8\text{Ca} \rightarrow \text{HfB}_2 + 4\text{B} + 2\text{CaCl}_2 + 6\text{Ca}$
ZrB <sub>2</sub>	$\text{ZrCl}_4 + 6\text{B} + 8\text{Ca} \rightarrow \text{ZrB}_2 + 4\text{B} + 2\text{CaCl}_2 + 6\text{Ca}$
HfC	$\text{HfCl}_4 + 3\text{C} + 12\text{Li} \rightarrow \text{HfC} + 2\text{C} + 4\text{LiCl} + 8\text{Li}$
ZrC	$\text{ZrCl}_4 + 3\text{C} + 12\text{Li} \rightarrow \text{ZrC} + 2\text{C} + 4\text{LiCl} + 8\text{Li}$
TaN	$\text{TaCl}_5 + 3\text{NH}_4\text{Cl} + 15\text{Li} \rightarrow \text{TaN} + 2\text{NH}_3 + 8\text{LiCl} + 7\text{Li} + 3\text{H}_2$
HfN	$\text{HfCl}_4 + 3\text{NH}_4\text{Cl} + 24\text{Li} \rightarrow \text{HfN} + 2\text{NH}_3 + 7\text{LiCl} + 17\text{Li} + 3\text{H}_2$
ZrN	$\text{ZrCl}_4 + 3\text{NH}_4\text{Cl} + 12\text{Li} \rightarrow \text{ZrN} + 2\text{NH}_3 + 7\text{LiCl} + 5\text{Li} + 3\text{H}_2$
BN	$\text{NaBH}_4 + 3\text{NH}_4\text{Cl} + 18\text{Li} \rightarrow \text{BN} + 2\text{NH}_3 + 3\text{LiCl} + 15\text{Li} + 3\text{H}_2$

Table 2 – III. Supplier Information for Raw Materials

<b>Reactant</b>	<b>Reactant Information</b>
TaCl <sub>5</sub>	99.8%, Alfa Aesar, Ward Hill, MA
NaB <sub>4</sub> H	98%, Alfa Aesar, Ward Hill, MA
Ca	Granular, 99%, Fisher Scientific, Pittsburgh, PA
HfCl <sub>4</sub>	99.9%, Alfa Aesar, Ward Hill, MA
B	amorphous (submicron), Sigma-Aldrich, St. Louis, MO
ZrCl <sub>4</sub>	98%, Alfa Aesar, Ward Hill, MA
C	Lampblack 101, Degussa, Parsippany, NJ
Li	granular, 99%, Sigma-Aldrich, St. Louis, MO
NH <sub>4</sub> Cl	Fisher Scientific, Pittsburgh, PA

Table 2 – IV. Reactant Amounts used to Produce Boride, Carbide, and Nitride Powders

<b><math>\text{MX}_y</math> Compound</b>	<b>M Precursor (g)</b>	<b>X Precursor (g)</b>	<b>Reductant (g)</b>
TaB <sub>2</sub>	5.30	2.24	5.94 (Ca)
HfB <sub>2</sub>	4.80	0.97	4.81 (Ca)
ZrB <sub>2</sub>	6.20	1.72	8.52 (Ca)
HfC	5.04	0.57	1.31 (Li)
ZrC	6.77	1.05	2.42 (Li)
TaN	5.51	2.47	1.60 (Li)
HfN	4.99	2.50	2.60 (Li)
ZrN	6.64	4.57	2.37 (Li)
BN	1.52	6.47	5.03 (Li)

Prior to igniting, the test tube was rotated at an unspecified angle to mix the granular reductant with the other powder reactants. Once mixed the test-tube stopper was loosened so that it rested on the top and would allow for outgassing. The test tube was lowered into the center of a tube furnace that was held at either 548 K if lithium is used as the reductant or 873 K if calcium was used as the reductant. Once the samples were thoroughly ignited, they were immediately removed from the furnace and allowed to air quench.

After cooling to room temperature, the reaction products were removed from the test tube by adding water, thus forming either LiOH or Ca(OH)<sub>2</sub>, depending on the reductant that was used, to free the reaction products. The contents were emptied into a 250 ml beaker. Additional water was added to the beaker to create a 100 ml suspension, which was magnetically stirred for 1800 s, followed by ultrasonication for 1800 s. All ultrasonication for this work was performed using an ultrasonic cleaner with the perforated tray accessory (Model FS30, Fisher Scientific, Pittsburgh, PA). The ultrasonic cleaner was filled with water until the water level was even with the level of suspension in the 250 ml beaker. All further washing utilizes a similar ultrasonication step. An additional 900 sec of magnetic stirring was performed after ultrasonication. The suspension was centrifuged at  $15,500 \times g$  for 300 sec and decanted to prepare for the powder washing procedures so that the lithium or calcium hydroxide can be removed.

Lithium hydroxide is very soluble in water. Three consecutive water wash cycles were performed for all experiments that used lithium. A water-wash cycle is defined as creating a 100 ml suspension of the powder using deionized water, magnetically stirring for 1800 s, ultrasonicated for 1800 s, magnetically stirring for an additional 900 s, centrifuging the powders at  $15,500 \times g$  for 300 s, and decanting the fluid above the powders. After the three cycles, the powders were left under a fume hood to dry. Powders which contained calcium hydroxide were washed and rinsed according to a procedure that was previously defined.<sup>[24]</sup>

Powder X-ray diffraction (XRD) was performed using a diffractometer (Siemens D5000, Siemens, New York, NY) by scanning from 15 to  $85^\circ 2\theta$  using  $\text{CuK}_\alpha$  radiation, a step size of  $0.04^\circ 2\theta$  and a dwell time of two sec after dispersing the powders on a zero-background holder. Software (Jade 8, Materials Data, Inc., Livermore, CA) was used to qualitatively evaluate the phases present in the powders. Additional analyses were performed on the powders that were close to being optimized. The analysis software was also used to analyze the average crystallite sizes for these samples. The crystallite sizes were determined using the Williamson-Hall technique.<sup>[29]</sup> Previous work, which uses cross-characterization, suggests that this method is accurate within approximately 10% error.<sup>[23]</sup> Since the crystallite size analysis depends on accurate full width at half maximum (FWHM) measurements for the peaks, whole profile fitting was used to help reduce error in the FWHM values.

Specific surface area (SSA) measurements were determined using the Bruauer-Emmett-Teller (BET) method (Tristar 3000, Micromeritics, Norcross, GA) after degassing in argon for 1 day at 423 K. Density measurements were performed by helium pycnometry (AccuPyc II 1340, Micromeritics, Norcross, GA) after drying the powders in an oven at approximately 253 K for 1 hour. The crystallite size was computed from the SSA and density measurements to compare to the crystallite size calculated from the X-ray diffraction data.

Thermogravimetric analysis (TGA) was performed in air using a thermogravimetric analyzer (Q50, TA Instruments, New Castle, DE) by heating from 323 to 1273 K using a heating rate of 5 K/min. This method was used to evaluate weight losses caused by adsorbed molecules, weight gains due to oxidation, and weight losses

associated with elimination of free carbon for example. Physisorbed molecules are typically observed as low temperature weight loss. Oxidation is observed as a weight gain. Free carbon reacts with oxygen at elevated temperatures and manifests as a weight loss as gas is evolved.

Dynamic light scattering (DLS) was performed (Nanotracer<sup>TM</sup> ULTRA, Microtrac, Montgomeryville, PA) after dispersing 0.02 grams of powder in 30 ml of deionized water and allowing the suspension to magnetically stir for one hour, followed by 300 sec of ultrasonication prior to measurement. The DLS measurements were repeated four additional times with 30 sec of ultrasonication between each measurement. Each run consisted of an average of five 30-sec measurements as is recommended by the manufacturer of the instrument and ASTM standard E2490-09.

Scanning electron microscopy (SEM) was performed (FEI<sup>TM</sup> Quanta 200F, FEI Company, Hillsboro, OR) to observe particle characteristics and supplement particle and crystallite size analyses. SEM samples were prepared by dispersing 10 mg of powder into 25 ml of water, magnetically stirring for 1 hr, ultrasonication for 10 min, drop coating onto a silicon wafer, and drying in an oven set at 363 K.

## **C. Results and Discussion**

### **1. Borides**

Figure 2-1 gives the powder X-ray diffraction patterns and the resulting phase analyses for the attempts at synthesizing various diboride powders. Phase-pure TaB<sub>2</sub> was obtained. The breadth of the X-ray diffraction peaks for TaB<sub>2</sub> indicates low crystallinity. Temperatures between 1173-1474 K improved the crystallinity of TaB<sub>2</sub> that had been deposited by chemical vapor deposition and is a process that could be incorporated to improve crystallinity for powders produced by the solvothermal synthesis method.<sup>[30]</sup> There are few reports on bulk TaB<sub>2</sub> powder synthesis. The synthesis trials for HfB<sub>2</sub> and ZrB<sub>2</sub> were not able to yield phase pure powders. In addition to the diboride phases that were desired, monoboride phases, the respective metal phases, and oxide phases were present. Although phase pure powders were not obtained for the latter diborides, valuable information is still obtained.

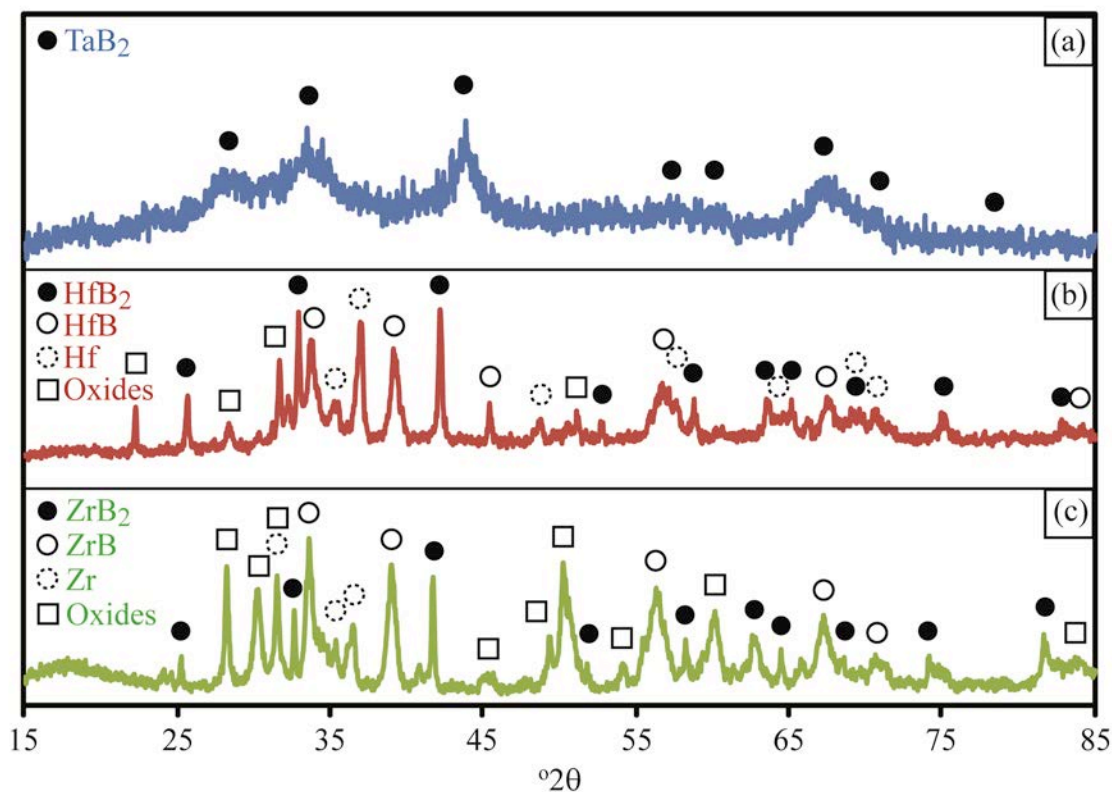


Figure 2 - 1. Powder X-ray diffraction patterns and phase identification for the attempted (a)  $\text{TaB}_2$ , (b)  $\text{HfB}_2$ , and (c)  $\text{ZrB}_2$  synthesis. (With color)

Comparing the three experiments in Figure 2-1 and comparing the precursors for these experiments given in Table 2-II indicate that the boron precursor selection is important. The high phase purity for  $\text{TaB}_2$  is most likely due to the fact that  $\text{NaBH}_4$  was used for the boron source rather than the direct use of boron for the other two experiments. Since  $\text{NaBH}_4$  goes through a decomposition reaction that produces gas, it can be expected to form a high surface area boron source.<sup>[31]</sup> The submicron particle size of the boron would be relatively large with low surface area and therefore less reactive. The evolution and ignition of hydrogen during the decomposition of  $\text{NaBH}_4$  may also be favorable for promoting the reaction. Although some success was achieved forming  $\text{HfB}_2$  and  $\text{ZrB}_2$  from the respective chloride compound and boron, attempts to form these compounds using  $\text{NaBH}_4$  as the boron source produced no diborides (results not included) because ignition and self-propagation of the reaction did not occur.

The synthesis of transition metal diborides has been performed via metathesis reaction between the respective chlorides and  $\text{MgB}_2$ .<sup>[32,33]</sup> A reaction scheme involving

two activation energies, corresponding to two reaction steps, was proposed and supported. The first reaction is the formation of  $\text{MgCl}_2$ , metal particles, and boron particles as intermediates. The second reaction forms the transition metal diboride product via reaction between the metal and boron particles. Both of these reactions have an associated adiabatic flame temperature. The empirical relationship for traditional SHS is still a relevant selection criterion: the adiabatic flame temperature of the second reaction must be sufficiently high ( $>2073$  K), but could not alone explain self-propagating behavior. An additional criterion was developed: the adiabatic flame temperature for the intermediate reaction must exceed the melting temperature of the  $\text{MgCl}_2$  for the reaction to become self-propagating. The presence of a liquid after the intermediate reaction promotes mass transport to allow the initiation and propagation of the second reaction. The concept of the two-step reaction scheme was used to explain why Group IV chlorides were not self-propagating while Group V chlorides were, similar to the observations of this study.

Solvothermal reactions are proposed to be conceptually similar to metathesis reactions and therefore expected to behave similarly.<sup>[23,24]</sup> The difference is the greater complexity of the solvothermal reactions. The ignition of solvothermal synthesis is closely related to the self-ignition temperature of the metal reductant. The transition metal chloride is reduced by the reductant metal forming metal particles and the chloride via a methathesis reaction. The non-metal source may already be particles, may be reduced to non-metal particles by the reductant via a metathesis reaction, or may decompose to form the non-metal particles depending on the precursor. It is proposed that the adiabatic flame temperature of the reaction sequence up to this point determines if the reaction is self-propagating if the adiabatic flame temperature of the subsequent reaction is sufficiently high. If the intermediate adiabatic flame temperature melts any of the intermediate components, including excess reactants and compounds formed by reaction with the environment, or combination of components (i.e. eutectic melting) that promote sufficient mass transport, then the reaction will become self-propagating.

Non-propagating methathesis reactions involving Group IV chlorides and  $\text{MgB}_2$  to form transition metal diborides could be completed by prolonged external heating at temperatures greater than 923 K or by coupling the non-propagating reaction with a self-

propagating reaction.<sup>[33]</sup> The external heat or self-propagating reaction in addition to the non-propagating reaction provides the energy necessary to melt  $\text{MgCl}_2$ , facilitating mass transport to complete the reaction sequence. In another example, phase pure  $\text{HfB}_2$  with an average primary particle size of 25 nm could be formed by reacting  $\text{HfCl}_4$  and excessive  $\text{NaBH}_4$  in an autoclave at 873 K for 12 hours.<sup>[34]</sup> A solvothermal reaction between  $\text{HfCl}_4$ , boron, and magnesium to produce  $\text{HfB}_2$  by prolonged heating produced yields as high as 81% with a mixture of nanometer and micrometer particles.<sup>[35]</sup> Therefore, providing an additional energy input is expected to promote the solvothermal synthesis reactions used in this study as well as promote reactions that are otherwise non-propagating.

Other precursors are available to promote the synthesis of borides. Nanocrystalline  $\text{ZrB}_2$  has been made by diluting an SHS reaction between  $\text{ZrO}_2$ ,  $\text{H}_3\text{BO}_3$ , and magnesium with up to 20 weight percent  $\text{NaCl}$ , for example.<sup>[36]</sup> The reaction was initiated at 943 K and required leaching of an oxide phase in boiling  $\text{HCl}$ , but demonstrates the potential of using  $\text{H}_3\text{BO}_3$  as a boron source. Furthermore, a combination of  $\text{H}_3\text{BO}_3$  and carbon can produce  $\text{B}_4\text{C}$  as a potentially useful reactant path to diboride formation ( $\text{B}_4\text{C}$  could also be used).<sup>[37]</sup> Other alkali borohydrides are also available.

## 2. Carbides

Powder X-ray diffraction patterns for attempts at synthesizing  $\text{HfC}$  and  $\text{ZrC}$ , are given in Figure 2-2. Both experiments resulted in two phases: a major phase of the expected carbide phase and a trace phase of the respective metal. This has been observed in the solvothermal synthesis of  $\text{TaC}$  as well.<sup>[24]</sup> Unpublished results obtained as part of a previous study indicate that improved mixing of the chloride and carbon can eliminate the residual metal phase.<sup>[23]</sup> In addition, trace amounts of metal phase can be eliminated using thermal treatments to homogenize the powders, or may naturally homogenize during sintering processes for example. Similar to  $\text{TaC}$ ,  $\text{ZrC}$  and  $\text{HfC}$  can incorporate a high content of carbon vacancies.<sup>[38-40]</sup> The carbide phases can react with the metal to form sub-stoichiometric carbides and convert the small amounts of residual metal to the sub-stoichiometric carbide phase without destabilizing the carbide phase during the heat treatments. This is demonstrated for  $\text{TaC}$  in Figure 2-3.

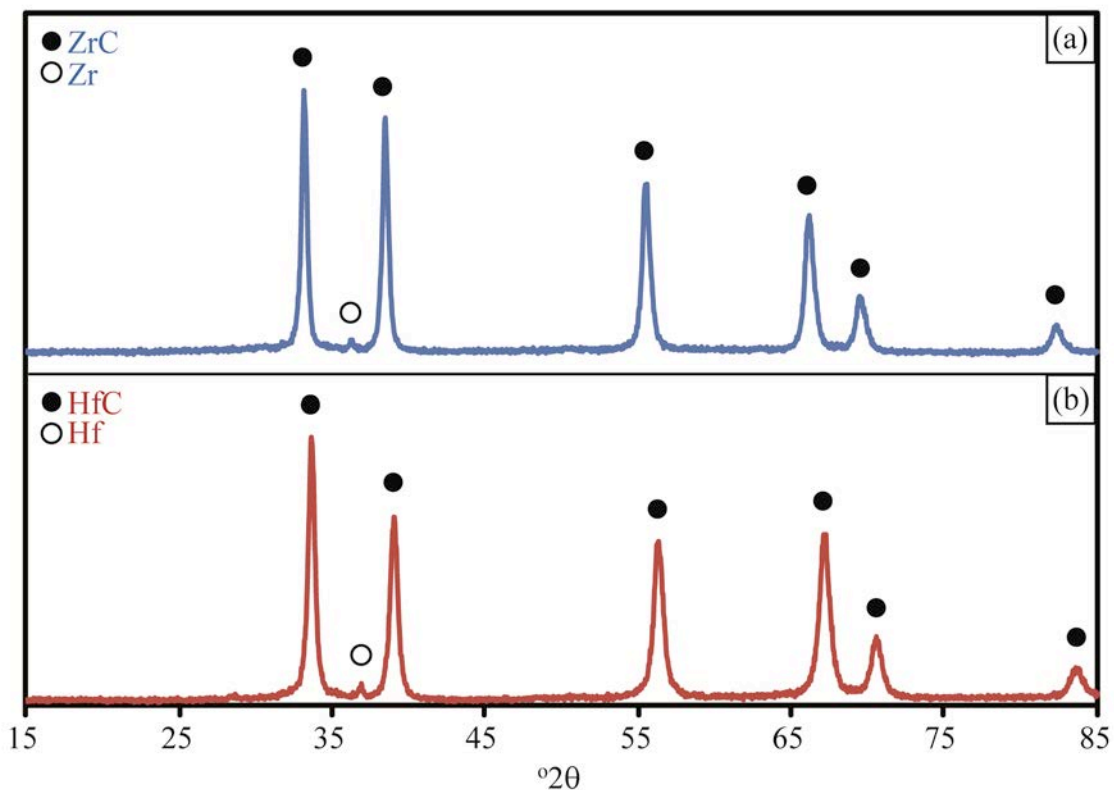


Figure 2 - 2. Powder X-ray diffraction patterns and phase identification for the attempted (a) ZrC and (b) HfC. (With color)

For the carbides attempted by the solvothermal synthesis process, in this work and in previous work, high phase purity is achieved.<sup>[23,24]</sup> In contrast to the boride compounds tested and the boron sources used, high surface area elemental carbon sources are readily available. Lithium was also used as the reactive metal. Lithium and lithium chloride have lower melting and vaporization temperatures than calcium and calcium chloride, which may facilitate self-propagating behavior although a lower reaction temperature overall is obtained.<sup>[24]</sup> The higher success of the carbide phase formation indicates that the formation of carbide phases may be coupled with diboride reactions to initiate self-propagating behavior. If the the reaction is designed so that the carbide phase is promoted only as an intermediate phase, diborides of high phase purity might be obtained this way.<sup>[41]</sup>

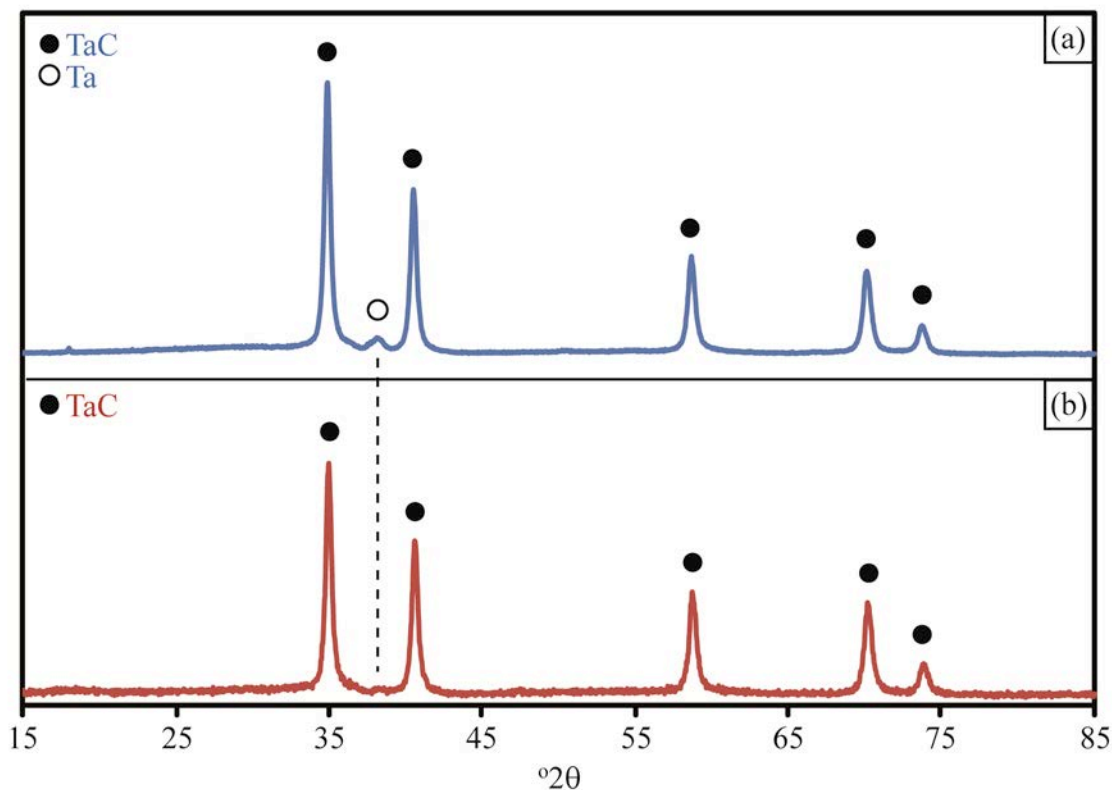


Figure 2 - 3. Powder X-ray diffraction patterns for (a) TaC containing residual tantalum and (b) the same TaC after heat treating at 873 K for 3 hours in argon to reduce the tantalum phase. (With color)

#### D. Nitrides

Forming nitride compounds by self-propagating solvothermal reactions is not as straightforward as borides and carbides because precursor selection is more limited. Elemental nitrogen is a gas and therefore not readily mixed as a reactant by the preparation methods used in this work. To circumvent this, the decomposition of  $\text{NH}_4\text{Cl}$  as a nitrogen source was used. However, the decomposition stills forms a gaseous nitrogen source. It is assumed that boron and carbon dissolve into the reaction melt and react from the melt for solvothermal reactions, which has been proposed before.<sup>[42]</sup> Nitrogen dissolution in the melt can occur as well, but the gas can also escape from the reaction. The  $\text{NH}_4\text{Cl}$  can react with other chloride precursors to form amido and imido complexes and add further complexity.<sup>[43]</sup>

The powder X-ray diffraction patterns for the attempts at forming nitride compounds are given in Figure 2-4. The predominant phase when attempting to synthesize TaN matched the powder diffraction file of a solid solution phase having similar structure to that of cubic TaN, but also containing lithium. This is a reminder that the metal reductants can react with other reactants or products and should be considered in studying the reaction paths and the purity of chemicals produced by the solvothermal method, but is beyond the scope of this work. A similar pattern to the (Li,Ta)N compound can be observed for a nitrogen rich/tantalum deficient compound. Cubic TaN produced by combustion synthesis has been known to contain excess nitrogen.<sup>[44,45]</sup> The cubic TaN is a high temperature and high pressure phase, but is also a metastable phase observed for combustion or low temperature synthesis of nanocrystalline material.<sup>[44-48]</sup> In addition to the (Li,Ta)N phase, phases of tantalum, SiO<sub>2</sub>, silicon, and TaSi<sub>2</sub> were found. The phases containing silicon are contamination from the fused-silica vessel.

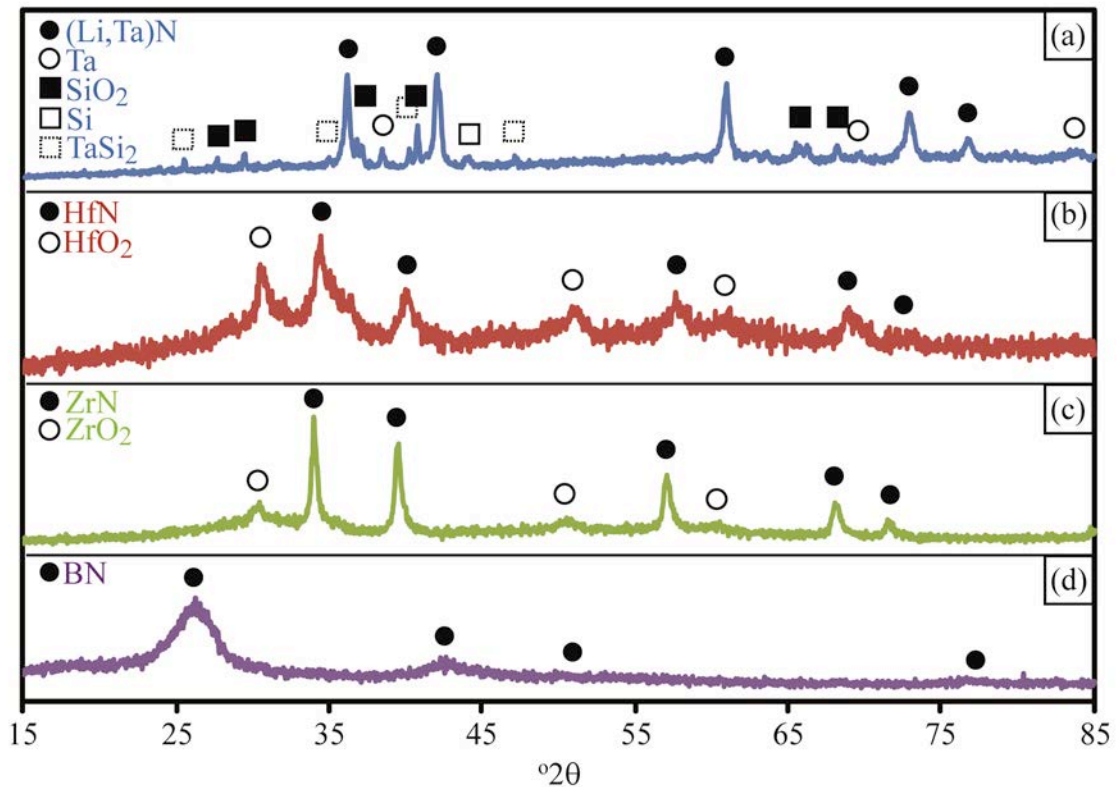


Figure 2 - 4. Powder X-ray diffraction patterns and phase identification for the attempted (a) TaN, (b) HfN, (c) ZrN, and (d) BN. (With color)

The TaN experiment is the first and only experiment in which the sample tube melted locally and formed a hole in the side of the test tube, but the experiment was not repeated to determine if the cause of melting is inherent to the reaction or if there is an alternate explanation. The melting is unlikely inherent to the reaction because it did not happen for any other experiment that used similar precursors. The specific test tube used for the experiment may have been defective, since the melting was only in one location of the test tube, but the experiment will need to be repeated to verify this. The experiment was not reproduced in this work because optimization was not a goal.

The unintended formation of TaSi<sub>2</sub> demonstrates that disilicide compounds can be synthesized by the solvothermal synthesis method as well. Thin films of TaSi<sub>2</sub> have been studied extensively for microelectronic applications.<sup>[49-60]</sup> Likewise, HfN and ZrN are of interest for microelectronic applications.<sup>[61-63]</sup> Reports of bulk TaSi<sub>2</sub> powder synthesis include self-propagating high temperature, mechanochemical, and solid-state metathesis syntheses.<sup>[64-67]</sup> Nanocrystalline TaSi<sub>2</sub> is a potentially useful material for UHTC composites, but is in need of further development.

The results of experiments to form HfN and ZrN in Figure 2-4 are similar. Both resulted in a predominant phase of either HfN or ZrN with a respective oxide phase. The oxide phase could be reduced or eliminated by process optimization, which is beyond the scope of this work. There was slightly less oxide contamination for ZrN synthesis than for HfN synthesis. The cause is unclear and could be due to thermodynamic stability, but looking at the different reaction equations in Table 2-II highlights another possible cause. The reaction to form ZrN utilized less metal reductant and the lower reductant amount could contribute to the better phase conversion to ZrN compared to conversion to HfN as a consequence of the gaseous nature of nitrogen. With less melt, the nitrogen gas can directly react with the other reactants rather than having to dissolve into the melt, where it possibly has low solubility. Direct reaction may be beneficial in this case. This indicates that it may be difficult to produce nitrides of high purity and with fine particle size since the diluent effect of the reductant may also hinder the reaction and favor oxide formation and not enough diluent also favors oxide formation.<sup>[24]</sup> Further optimization is necessary to compete with other methods for synthesizing nanocrystalline transition metal nitrides, which produce powders of higher phase purity.<sup>[68,69]</sup>

The results in Figure 2-4d demonstrate that phase-pure BN was obtained. Although the X-ray diffraction pattern appears to be phase pure, the purity is concluded cautiously. Given the previous difficulties of forming phase-pure nitride powders, mostly due to oxide impurities, it is reasonable to assume that this experiment also resulted in oxide impurities. Boron oxide is a known glass former and would be difficult to detect by X-ray diffraction as a glass phase. There is little-to-no evidence of an amorphous hump in the powder diffraction pattern, however. Boron oxide compounds may be dissolved and removed in the washing procedures. A more detailed study has been performed by another researcher.<sup>[70]</sup> Thermal treatments can be used to crystallize B<sub>2</sub>O<sub>3</sub> to aid in identification of the contaminant, similar to a method that was developed to optimize the removal of LiOH contaminant in TaC powders.<sup>[71]</sup>

The BN formed by this method has a turbostratic structure (t-BN) that is reported by several researchers.<sup>[72-76]</sup> The crystal structure of t-BN is an intermediate structure between that of hexagonal BN and amorphous BN, where the hexagonal rafts are randomly oriented about the c-axis. Intercalation between hexagonal rafts is also possible.<sup>[77-78]</sup> The disorder in t-BN provides a higher reactivity compared to more crystalline forms of BN. For this reason, the use of t-BN is a proposed solution to the sintering difficulties of the higher crystalline forms. It is also thought to be more readily transformed into cubic BN than other crystalline phases, being an intermediate phase in the transformation of rhombohedral BN to cubic BN for example. Intercalation may catalyze (or hinder) the conversion to cubic BN via control of boron, oxygen, and dopant structural defects.<sup>[79-86]</sup>

### **1. Analysis of TaB<sub>2</sub>, ZrC, HfC, and BN**

Experiments for the synthesis of TaB<sub>2</sub>, HfC, ZrC, and BN all produced powders that had excellent phase purity. Therefore, further characterization of these powders was performed to determine the particle sizes and oxidation behavior.

The average primary particle sizes were calculated from X-ray diffraction data. The sizes were also calculated from SSA and density measurements. The results are summarized in Table 2-V. There is relatively good agreement between the average primary particle sizes using the two different techniques for the TaB<sub>2</sub>, ZrC, and HfC powders despite the rudimentary approach of using SSA and density measurements,

which requires an assumption that the particles are spherical. Deviation from spherical shape will affect the accuracy of the calculation. The reasonable agreement between the two techniques indicates that the particles are likely to have equiaxed morphology, but it is impossible to determine if the primary particles are spherical, slightly oblong, or faceted from this analysis. There is a strong disagreement for the BN powders. The disorder in t-BN results in small crystalline domains that do not represent the primary particle size, explaining the small crystallite sizes measured by X-ray diffraction. Electron microscopy will be performed to corroborate these results.

The particle size distributions of the four powders, measured by dynamic light scattering, are given in Figure 2-5. The particle size distributions for the TaB<sub>2</sub>, ZrC, and HfC powders have a narrow primary size distribution between 50 to 200 nm with a small upper-tail size distribution of larger particles up to about a one micrometer, which could be agglomeration or aggregation of smaller particles or a second population of larger particles. An upper-tail distribution caused by aggregation of small particles or consisting of larger particles is a drawback because it can promote grain growth during sintering. TaC with particle sizes less than 200 nm was produced by ultrasonic dispersion, centrifuging, and filtration of powders that originally contained particle sizes in the micrometer range.<sup>[87]</sup> Optimization of the current washing procedure can therefore be used to separate out the larger aggregate sizes from the smaller particles. A dispersion study could be used to address agglomeration of particles. Electron microscopy can provide insight for distinguishing the cause of the upper-tail size distribution and will be presented.

Table 2 – V. Crystallite Sizes of TaB<sub>2</sub>, HfC, ZrC, and BN Measured by X-Ray Diffraction Line Broadening ( $d_{\text{XRD}}$ ) and Calculated from Density/Surface Area Measurements ( $d_{\text{CALC}}$ )

Compound	$d_{\text{XRD}}$ (nm)	$d_{\text{CALC}}$ (nm)
TaB <sub>2</sub>	3	10
ZrC	45	32
HfC	30	37
BN	3	436

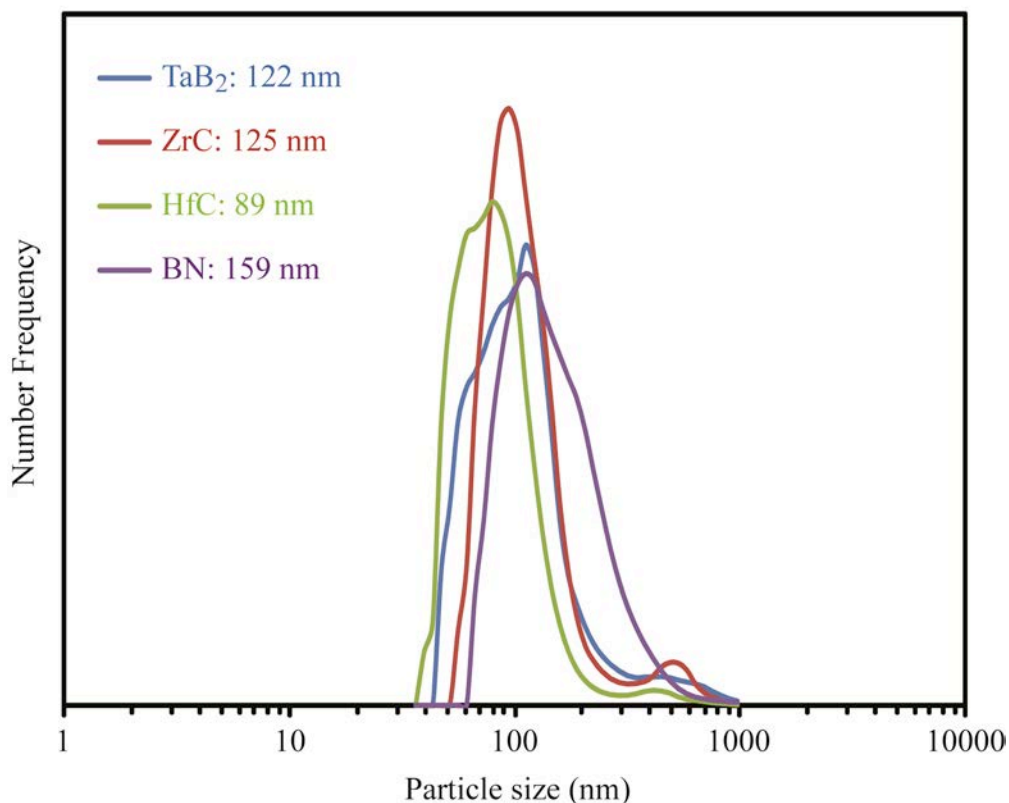


Figure 2 - 5. Particle size distributions of TaB<sub>2</sub>, ZrC, HfC, and BN measured by dynamic light scattering (average sizes are given in the legend). (With color)

Comparing the ratio of the average particle sizes to the average crystallite sizes gives a figure of merit of 41, 3, and 3 for the TaB<sub>2</sub>, HfC, and ZrC powders, respectively. This indicates a relatively large level of agglomeration for the TaB<sub>2</sub> powders, despite the relatively small particle sizes. Fine crystallites will have a high tendency for agglomeration. The HfC and ZrC powders, consisting of slightly larger crystallites, had a lower level of agglomeration. For all three of these powders, it is unclear whether the agglomeration is soft agglomeration or hard agglomeration (i.e. aggregation). It is impossible to distinguish without performing a dispersion study or obtaining direct evidence of particle necking from a technique such as transmission electron microscopy for example.

The particle size distribution for the BN powder is similar, but has a much broader primary size distribution from about 50 to 400 nm with an average particle size of 159 nm. This is smaller than the crystallite size that was calculated from density and

specific surface area measurements. Large differences between particle size analyses may be due to agglomeration of the powder, porosity in the particles, and/or a large deviation from spherical shape. Electron microscopy may help determine the cause.

TaB<sub>2</sub>, ZrC, HfC, and BN powders were evaluated by using back-scattered electron imaging with an accelerating potential of 20 kV. The micrographs, given in Figure 2-6, indicate that the powders have small primary particle sizes, agreeing well with the particle size analysis. There is little evidence of particles as large as the upper-tail size distributions given in Figure 2-5 (>200-400 nm), indicating that the tails are a result of agglomeration or aggregation. A lower accelerating potential, to reduce the interaction volume, would improve the analysis by providing better resolution. This is especially important for compounds with low average atomic number, such as BN.

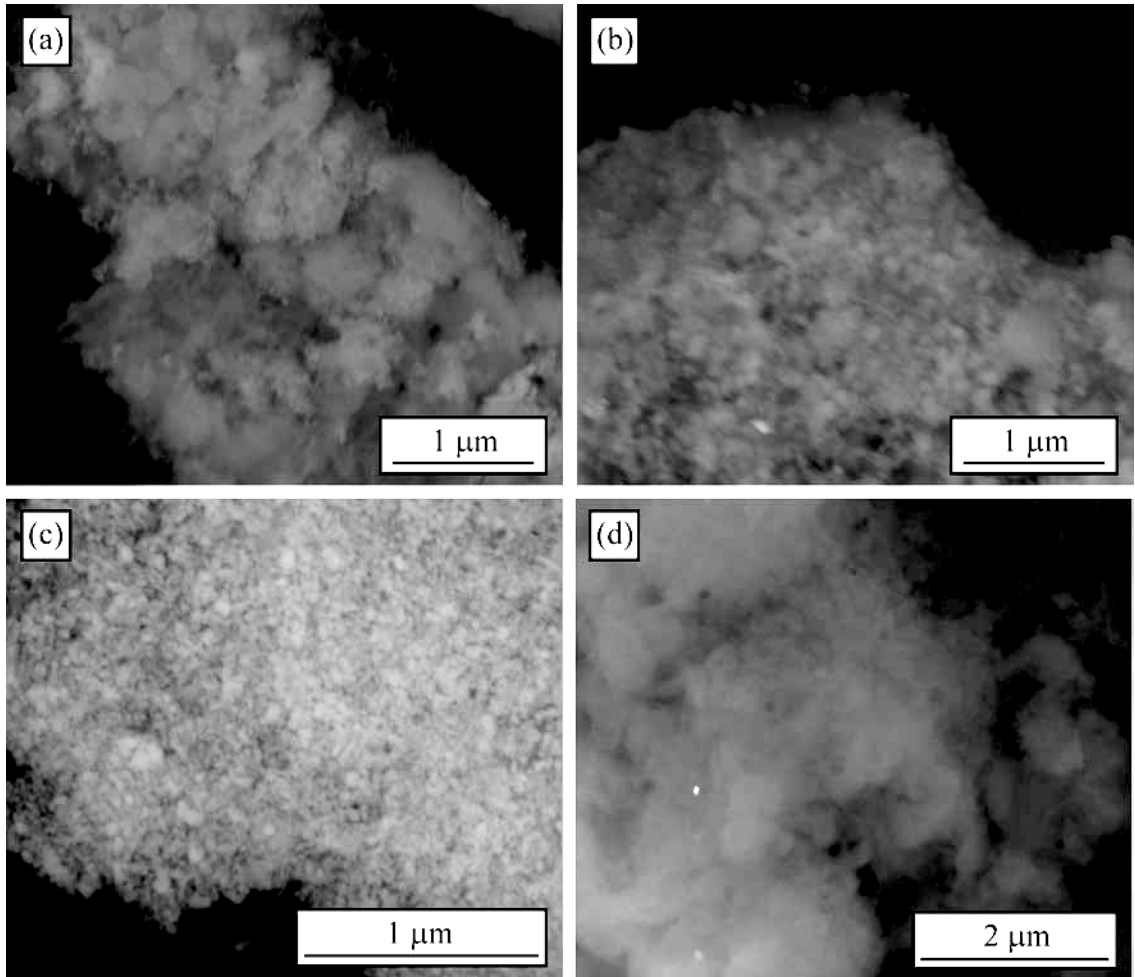


Figure 2 - 6. Back-scattered electron image of (a) TaB<sub>2</sub>, (b) ZrC, (c) HfC, and (d) BN powders.

The images given in Figure 2-6 suggest the powder grains are equiaxed rather than being fibrous or plate-like for example, but the poor resolution of the BN image (Figure 2-6d) is difficult to analyze. The secondary electron image of BN, which is produced from a smaller interaction volume, is given in Figure 2-7. Elongated structure is observed in the image that could result from a fibrous morphology or from the edge of a plate-like morphology. Fiber, whisker, tube, and platelet morphologies can be expected for BN, although equiaxed structure has also been observed for nanocrystalline t-BN.<sup>[72-75,99-103]</sup> These analyses support the particle size analysis by SSA and density measurements. It is impossible to distinguish whether the equiaxed particles have spherical or faceted morphology without high resolution images at high magnification, adding uncertainty to the particle size calculations based on SSA and density.

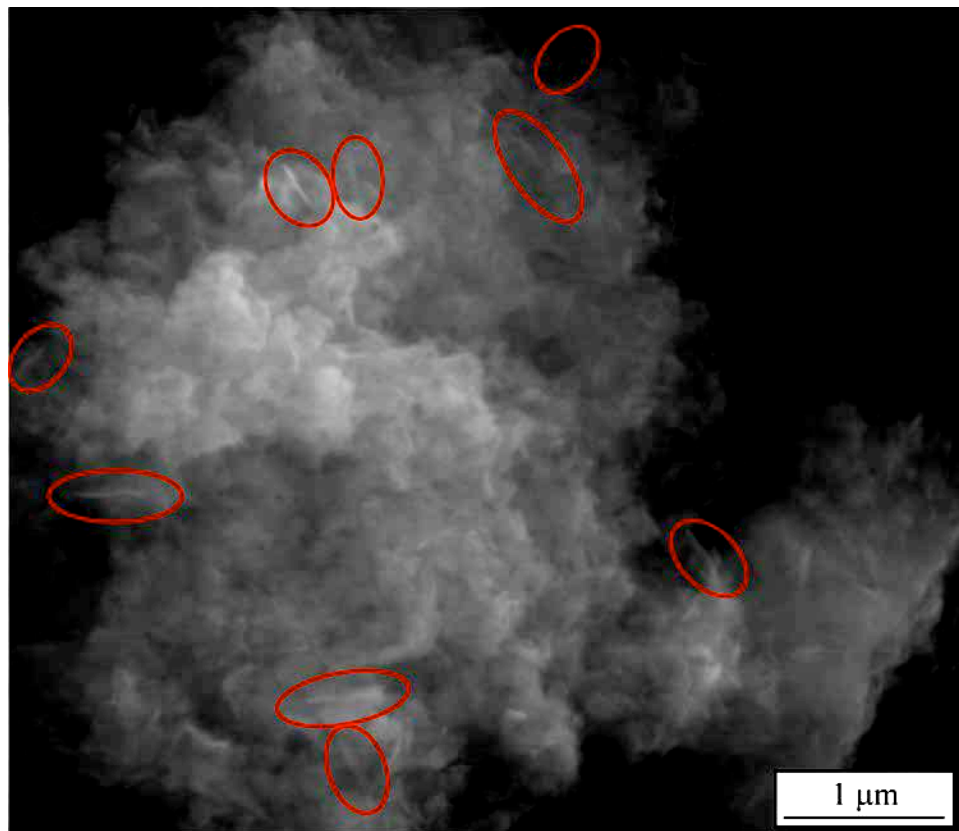


Figure 2 - 7. Secondary electron image of BN powders, highlighting a few examples of bright edges that could correspond to whisker or platelet morphologies. (With color)

The average particle size of TaB<sub>2</sub> obtained in this study is exceptionally small. TaB<sub>2</sub> prepared by reduction of Ta<sub>2</sub>O<sub>5</sub> using B<sub>4</sub>C resulted in average particle sizes of 400 nm.<sup>[86]</sup> This size was obtained via interpretation of images, a method that can result in artificially low particle sizes because it neglects aggregation. Necking between particles is observed in the images indicating that aggregation is present. Co-synthesis of TaB<sub>2</sub> with ZrB<sub>2</sub> by solution based processing and thermal treatments resulted in particle sizes between 200-600 nm, a range also determined from electron imaging.<sup>[41]</sup> There are few reports in the literature on the synthesis of TaB<sub>2</sub> in general.

The sizes of the ZrC and HfC are comparable to those found by other methods. Hafnium carbide has been produced by by mechanical activation of HfCl<sub>4</sub> + C + Mg followed by pyrolysis at 1373 K.<sup>[89]</sup> The technique was different than the solvothermal synthesis technique, but the fundamental reaction mechanisms are expected to be similar. However, impurities were not leached out resulting in the presence of MgO contaminant. The powders appear to be fine from electron imaging (primary particle sizes are less than 100 nm), but a true particle size analysis was not performed to make direct comparisons. Mechanical alloying, mechanically induced self-propagating reactions, and solution-based synthesis or laser pyrolysis to form nanocrystalline oxides followed by carbothermal reduction provided nanocrystalline ZrC or HfC according to X-ray diffraction, but particle sizes are again inadequately characterized.<sup>[90-95]</sup> Aggregation and grain sizes several micrometers in size are clearly evident in nanocrystalline ZrC powders produced by solution-based processing followed by carbothermal treatment.<sup>[96]</sup> Characterization of the particle size distribution is important for further processing of powders.

In comparison to the other techniques, the solvothermal synthesis technique is generally less energy intensive and requires similar if not less intensive post-synthesis processing than the other techniques producing fine nanopowders. Although similar primary particle sizes are achieved by other methods, it is not easy to make a direct comparison between the levels of aggregation in the powders produced by the different methods, though aggregation is clearly evident in some reports.

Thermogravimetric analysis (TGA) gives information about the presence of physisorbed molecules and oxidation. TGA results for the powders are given in Figure

2-8. All of the powders immediately begin to lose weight upon heating. The initial weight loss is likely caused by the release of physisorbed molecules, most likely water based on previous work on solvothermal synthesis.<sup>[97]</sup> The HfC powders lost approximately one weight percent mass, whereas the other powders lost about six weight percent. The BN powder has a secondary weight loss regime starting between 473 and 523 K. This may be caused by the release of physisorbed molecules with greater attraction to BN than those initially released, the release of chemisorbed molecules, the loss of intercalated atoms or molecules, or the burning of contaminant. The exact cause will require further study beyond the scope of this work.

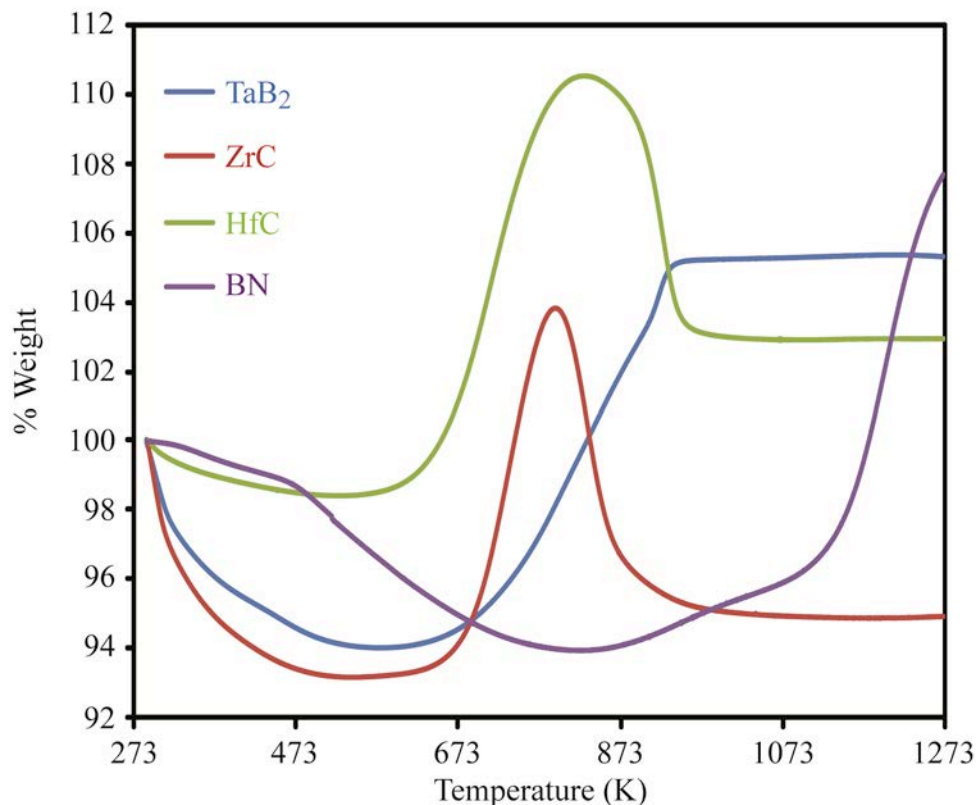


Figure 2 - 8. Thermogravimetric analysis of TaB<sub>2</sub>, HfC, ZrC, and BN powders. (With color)

After the primary weight losses, there is a weight gain assumed to be associated with oxidation of the powders. Figure 2-8 indicates that the onset of oxidation of TaB<sub>2</sub>, HfC, and ZrC powders all occur around 573 K. The initial oxidation is slow, but becomes quite significant above approximately 673 K. These values are lower than

typically reported for nanocrystalline borides and carbides and could be due to higher reactivity caused by smaller particle sizes.<sup>[98]</sup> Oxidation was complete for TaB<sub>2</sub>, HfC, and ZrC powders by heating to 973 K for all of these powders, occurring by slightly lower temperature for the ZrC and HfC powders. The BN powders are more oxidation resistant. The first weight gain for BN is observed at approximately 823 K. The oxidation of BN is relatively slow up to about 1098 K. Complete oxidation of BN was not achieved even at 1273 K.

For the ZrC and HfC powders, there is an additional weight loss after oxidation, assumed to be associated with the oxidation of free carbon. Residual carbon is expected from the reaction equation given in Table 2-II. The TaB<sub>2</sub> powders should also have residual boron in them, but boron is not lost as a result of oxidation and is a possible explanation for why there is no additional weight loss observed for this sample. This type of oxidation behavior is confirmed for HfB<sub>2</sub> as well.<sup>[34]</sup> Residual reactants should not be of concern for BN because excess nitrogen is lost as gas. This is demonstrated by the oxidation of TaN for example, which behaves similar to that demonstrated by the oxidation of TaB<sub>2</sub> in Figure 2-8.<sup>[47]</sup> The possible presence of residual reactants in the powders is a reminder that they should be removed from the powders prior to consolidation if they are undesirable for the end-use of these powders. This is an issue that should be addressed in a chemical purity study of the powders synthesized by the solvothermal method.

## **2. Potential of the Solvothermal Synthesis Technique**

The materials selected for this study were based on the basic concept developed for self-propagating high temperature synthesis (SHS).<sup>[14]</sup> In general, materials with adiabatic flame temperatures exceeding 2073 K by reaction from their metal and non-metal components are good candidates for SHS. However, self-propagating behavior is more complex for solvothermal synthesis. Many of these reactions proceed via metal nucleation and growth from decomposition of a precursor followed by diffusion of a non-metal into the metal.<sup>[23-24,26,32-33]</sup> This diffusion process is therefore important because the non-metal must be able to diffuse into the metal particle for the particle size, temperature, time, and concentration conditions. Self-propagating metathesis reactions in chlorides

also suggests that the adiabatic flame temperature for the reaction producing intermediates must exceed the melting temperature of the solvent in order to facilitate rapid mass transport to initiate and sustain the traditional SHS reaction from the intermediates.<sup>[30,33]</sup>

In the event that self-propagating behavior cannot be initiated by solvothermal synthesis, but otherwise would be for traditional SHS, reactions can be promoted by increasing the ignition temperature such that the adiabatic flame temperature is increased accordingly, by coupling with a self-propagating reaction, or by prolonged heating above the melting temperature of the solvent. Thus, compounds synthesized by traditional SHS remain great candidates for the solvothermal synthesis method by either self-propagating reactions or non-propagating reactions if the conditions are understood and the process modified accordingly. A partial list of over 500 materials synthesized by SHS are provided in Table 2-VI, after Moore and Feng.<sup>[27]</sup>

Table 2 – VI. Compounds Synthesized by Self-Propagating High-Temperature Synthesis. Adapted from Moore and Feng.<sup>[27]</sup>

<b>Borides</b>	CrB, HfB <sub>2</sub> , NbB, NbB <sub>2</sub> , TaB <sub>2</sub> , TiB, TiB <sub>2</sub> , LaB <sub>6</sub> , MoB, MoB <sub>2</sub> , MoB <sub>4</sub> , Mo <sub>2</sub> B, WB, W <sub>2</sub> B <sub>5</sub> , WB <sub>4</sub> , ZrB <sub>2</sub> , VB, V <sub>3</sub> B <sub>2</sub> , VB <sub>2</sub>
<b>Carbides</b>	TiC, ZrC, HfC, NbC, SiC, Cr <sub>3</sub> C <sub>2</sub> , B <sub>4</sub> C, WC, TaC, Ta <sub>2</sub> C, VC, Al <sub>4</sub> C, Mo <sub>2</sub> C
<b>Nitrides</b>	Mg <sub>3</sub> N <sub>2</sub> , BN, AlN, SiN, Si <sub>3</sub> N <sub>4</sub> , TiN, ZrN, HfN, VN, NbN, Ta <sub>2</sub> N, TaN (hexagonal and cubic)
<b>Silicides</b>	TiSi <sub>3</sub> , Ti <sub>5</sub> Si <sub>3</sub> , ZrSi, Zr <sub>5</sub> Si <sub>3</sub> , MoSi <sub>2</sub> , TaSi <sub>2</sub> , Nb <sub>5</sub> Si <sub>3</sub> , NbSi <sub>2</sub> , WSi <sub>2</sub> , V <sub>5</sub> Si <sub>3</sub>
<b>Aluminides</b>	NiAl, CoAl, NbAl <sub>3</sub>
<b>Hydrides</b>	TiH <sub>2</sub> , ZrH <sub>2</sub> , NbH <sub>2</sub> , CsH <sub>2</sub> , PrH <sub>2</sub> ,
<b>Intermetallics</b>	NiAl, FeAl, BnGe, NbGe <sub>2</sub> , TiNi, CoTi, CuAl
<b>Carbonitrides</b>	TiC-TiN, NbC-NbN, TaC-TaN, ZrC-ZrN
<b>Cemented carbides</b>	TiC-Ni, TiC-(Ni,Mo), WC-Co, Zr <sub>3</sub> C <sub>2</sub> -(Ni,Mo)
<b>Binary compounds</b>	TiB <sub>2</sub> -MoB <sub>2</sub> , TiB <sub>2</sub> -CrB <sub>2</sub> , ZrB <sub>2</sub> -CrB <sub>2</sub> , TiC-WC, TiN-ZrN, MoS <sub>2</sub> -NbS <sub>2</sub> , WS <sub>2</sub> -NbS <sub>2</sub>
<b>Chalcogenides</b>	MgS, NbSe <sub>2</sub> , TaSe <sub>2</sub> , MoS <sub>2</sub> , MoSe <sub>2</sub> , WS <sub>2</sub> , WSe <sub>3</sub>
<b>Composites</b>	TiB <sub>2</sub> -Al <sub>2</sub> O <sub>3</sub> , TiC-Al <sub>2</sub> O <sub>3</sub> , B <sub>4</sub> C-Al <sub>2</sub> O <sub>3</sub> , TiN-Al <sub>2</sub> O <sub>3</sub> , TiC-TiB <sub>2</sub> , MoSi <sub>2</sub> -Al <sub>2</sub> O <sub>3</sub> , MoB-Al <sub>2</sub> O <sub>3</sub> , Cr <sub>2</sub> C <sub>3</sub> -Al <sub>2</sub> O <sub>3</sub> , 6Vn-5Al <sub>2</sub> O <sub>3</sub> , ZrO <sub>2</sub> -Al <sub>2</sub> O <sub>3</sub> -2Nb

## E. Conclusions

Evaluation of nine different material systems, including borides, carbides, and nitrides indicates that self-propagating high-temperature solvothermal synthesis is a suitable technique to investigate for developing a variety of different non-oxide nanopowders for ultra-high-temperature applications. The technique produced the phases of interest for all nine material systems. Four of the nine systems resulted in high phase purity without process optimization.

Although the solvothermal synthesis method is ideal from many aspects (can produce nanocrystals having low levels of agglomeration, is a process that can be varied to allow for process control, is energy efficient, is fast, is scalable, and is diverse), there is still an issue of purity. Surface adsorption is readily apparent from this work, but has not been addressed extensively. Classifying the powders made by this synthesis method is also necessary to eliminate undesired large particles that may be detrimental to a final product.

Many of the fundamental aspects of the solvothermal synthesis process can be understood from the parent techniques: self-propagating high temperature synthesis and synthesis by metathesis reactions. The primary task for developing the fundamental understanding of the solvothermal synthesis technique is to establish the consequences of increased complexity of the reaction as a result of the various precursors that are used and the intermediates that may form during the reactions as a consequence of decomposition, metathesis reactions, nucleation and growth, diffusion, and reaction.

This work, the parent synthesis techniques, and the literature provide insight for selecting systems and processing parameters to perform solvothermal synthesis. The following general criteria are recommended for the successful utilization of the solvothermal synthesis technique:

- The compound of interest should have an adiabatic flame temperature greater than 2073 K for the stoichiometric reaction from the compound's elements and is the primary selection criterion.
- If the adiabatic flame temperature of the intermediate reactions exceeds the melting temperature of an intermediate component to promote mass

transport and is high enough to initiate the secondary reaction, then the reaction can proceed via self-propagating behavior.

- If the adiabatic flame temperature of the intermediate reaction does not exceed the melting temperature of an intermediate component, then mass transport will be hindered and self-propagation will not occur.
- In this case of non-propagating behavior, it may be possible to make the reaction self-propagating by providing additional energy (i.e. thermal energy, electric field enhancement, coupling with other self-propagating reactions, etc.).
- For self-propagating behavior that does not produce high product yield or in the absence of self-propagating behavior, sustained temperatures above the melting point of an intermediate component that facilitates mass transport and the reaction can be applied for extended periods of time to complete the reaction.
- The compound of interest should not react unfavorably with other components utilized in the solvothermal synthesis process.
- The compound of interest must be able to be separated from the reaction byproducts by chemical, thermal, physical, or other processes.

Many boride, carbide, nitride, silicide, aluminide, hydride, intermetallic, chalcogenide, and composite materials have been produced by self-propagating high-temperature synthesis, which is the primary selection criterion for the solvothermal synthesis technique. These materials have a diverse set of applications that include abrasives, cutting tools, polishing powders, resistive heating elements, shape-memory alloys, high-temperature materials, steel processing additives, corrosion protection, molten-metal containment, and those that take advantage of certain magnetic and electrical properties, demonstrating the wide diversity of materials and applications that may benefit from the solvothermal synthesis technique.

## F. References

- [1]. R.L. Riley, "Silicon Nitride and Related Materials," *J. Am. Ceram. Soc.*, **83** [2] 245-65 (2000).
- [2]. A. Rosenflanz, "Silicon Nitride and SiAlON Ceramics," *Curr. Opin. Solid State Mater. Sci.*, **4** [5] 453-9 (1999).
- [3]. G.P. Shveikin, N.V. Lukin, and L.B. Khoroshavin, "SiAlONs – Promising Refractory and Ceramic Materials," *Refract. Ind. Ceram.*, **44** [1] 52-8 (2003).
- [4]. V.N. Antisiferov, V.G. Gilev, and V.I. Karmanov, "Infrared Spectra and Structure of Si<sub>3</sub>N<sub>4</sub>, Si<sub>2</sub>ON<sub>2</sub>, and SiAlONs," *Refract. Ind. Ceram.*, **44** [2] 108-14 (2003).
- [5]. D.P. Thompson, "SiAlONs:  $\alpha$ -,  $\beta$ -,  $\gamma$ - and Beyond," *Silic. Ind.*, **69** [5/6] 1-8 (2004).
- [6]. L. Kaufman and E.V. Clougherty, "Investigation of Boride Compounds for High-Temperature Applications," *Plansee Proc.*, **1964**, 722-58 (1965).
- [7]. A.K. Kuriakose and J.L. Margrave, "The Oxidation Kinetics of Zirconium Diboride and Zirconium Carbide at High Temperatures," *J. Electrochem. Soc.*, **111** [7] 827-31 (1964).
- [8]. J.W. Hinze, W.C. Tripp, and H.C. Graham, "High-Temperature Oxidation Behavior of a Hafnium Boride + Silicon Carbide Composite," *J. Electrochem. Soc.*, **122** [9] 1249-54 (1975).
- [9]. J. Fuller, Y. Blum, J. Marschall, "Topical Issue on Ultra-High Temperature Ceramics," *J. Am. Ceram. Soc.*, **91** [5] 1397-502 (2008).
- [10]. J. Fuller and M. Sacks, *Special Section: Ultra-High Temperature Ceramics*, *J. Mater. Sci.*, **39** [19] 5885-6066 (2004).
- [11]. S.R. Levine, E.J. Opila, M.C. Halbig, J.D. Kiser, M. Singh, J.A. Salem, "Evaluation of Ultra-High Temperature Ceramics for Aeropropulsion Use," *J. Eur. Ceram. Soc.*, **22** [14-15] 2757-67 (2002).
- [12]. K. Upadhyaya, J.-M. Yang, and W.P. Hoffman, "Materials for Ultrahigh Temperature Structural Applications," *Am. Ceram.Soc. Bull.*, **76** [12] 51-6 (1997).
- [13]. J. Marschall and D.G. Fletcher, "High-Enthalpy Test Environments, Flow Modeling and *In Situ* Diagnostics for Characterizing Ultra-High Temperature Ceramics," *J. Eur. Ceram. Soc.*, **30** [11] 2323-6 (2010).

- [14]. A. Varma and J.P. Lebrat, "Combustion Synthesis of Advanced Materials," *Chem. Eng. Sci.*, **47** [9-11] 2179-94 (1992).
- [15]. Materials Science and Engineering Handbook, 3<sup>rd</sup> ed., Ch. 4, Edited by J.F. Shackelford and W. Alexander, CRC Press LLC, New York, 2001.
- [16]. K.G. Nickel, "Corrosion of Non-Oxide Ceramics," *Ceram. Int.*, **23** [2] 127-33 (1997).
- [17]. V. Medri, M Bracisiewicz, K. Krnel, F. Winterhalter, and A. Bellosi, "Degradation of Mechanical and Electrical Properties After Long-Term Oxidation and Corrosion of Non-Oxide Structural Ceramic Composites," *J. Eur. Ceram. Soc.*, **25** [10] 1723-31 (2005).
- [18]. M.M. Opeka, I.G. Talmy, and J.A. Zaykoski, "Oxidation-Based Materials Selection for 2000C + Hypersonic Aerosurfaces: Theoretical Considerations and Historical Experience," *J. Mater. Soc.*, **39** [19] 5887-904 (2004).
- [19]. X. Zhang, P. Hu, J. Han, and S. Meng, "Ablation behavior of ZrB<sub>2</sub>-SiC Ultra High Temperature Ceramics Under Simulated Atmospheric Re-entry Conditions," *Compos. Sci. Technol.*, **68** [7-8] 1718-26 (2008).
- [20]. X.-H. Zhang, P. Hu, J.-C. Han, L. Xu, and S.-H. Meng, "The Addition of Lanthanum Hexaboride to Zirconium Diboride for Improved Oxidation Resistance," *Scr. Mater.*, **57** [11] 1036-39 (2007).
- [21]. R.A. Andrievski, "Nanocrystalline High Melting Point Compound-Based Materials," *J. Mater. Sci.*, **29** [3] 614-31 (1994).
- [22]. S.C. Deevi, "Manufacturing of Covalent Ceramics by Exothermic Reactions," *Mat. Res. Soc. Symp. Proc.*, **327**, 171-6 (1994).
- [23]. J.P. Kelly, R. Kanakala, and O.A. Graeve, "A Solvothermal Approach for the Preparation of Nanostructured Carbide and Boride Ultra-High Temperature Ceramics," *J. Am. Ceram. Soc.*, in print (2010).
- [24]. J.P. Kelly and O.A. Graeve, "Statistical Experimental Design Approach for the Solvothermal Synthesis of Nanostructured Tantalum Carbide Powders," *J. Am. Ceram. Soc.*, submitted (2010).
- [25]. S.T. Aruna and A.S. Mukasyan, "Combustion Synthesis of Nanomaterials," *Curr. Opin. Solid State Mater. Sci.*, **12**, 44-50 (2008).
- [26]. A.M. Nartowski, I.P. Parkin, M. MacKenzie, A.J. Craven, and I. MacLeod, "Solid State Metathesis Routes to Transition Metal Carbides," *J. Mater. Chem.*, **9**, 1275-81 (1999).

- [27]. J.J. Moore and H.J. Feng, "Combustion Synthesis of Advanced Materials: Part I. Reaction Parameters," *Prog. Mater. Sci.*, **39**, 243-73 (1995).
- [28]. K.J. Nilsen and A.W. Weimer, "Chemical Purification," p. 479-503 in *Carbide, Nitride and Boride Materials Synthesis and Processing*. Edited by A.W. Weimer. Chapman & Hall, New York, NY, 1997.
- [29]. G.K. Williamson and W.H. Hall, "X-ray Line Broadening from Filled Aluminum and Tungsten," *Acta Metall.*, **1** [1] 22-31 (1953).
- [30]. S. Motojima and K. Suiyama, "Chemical Vapour Deposition of Tantalum Diboride," *J. Mater. Sci.*, **14**, 2859-64 (1979).
- [31]. M.N. Rahaman, *Ceramic Processing and Sintering*, Ch. 2 pp. 38-93. Marcel Dekker, New York, NY, 1995.
- [32]. L. Rao, E.G. Gillan, and R.B. Kaner, "Rapid Synthesis of Transition-Metal Borides by Solid-State Metathesis," *J. Mater. Res.*, **10** [2] 353-61 (1995).
- [33]. E.G. Gillan and R.B. Kaner, "Synthesis of Refractory Ceramics via Rapid Metathesis Reactions Between Solid-State Precursors," *Chem. Mater.*, **8**, 333-43 (1996).
- [34]. L. Chen, Y. Gu, L. Shi, Z. Yang, J. Ma, and Y. Qian, "Synthesis and Oxidation of Nanocrystalline HfB<sub>2</sub>," *J. Alloys Compd.*, **368**, 353-6 (2004).
- [35]. E. Barraud, S. Bégin-Colin, and G.L. Caër, "Nanorods of HfB<sub>2</sub> from Mechanically-Activated HfCl<sub>4</sub> and B-Based Powder Mixtures," *J. Alloys Compd.*, **398**, 208-18 (2005).
- [36]. A.K. Khanra, L.C. Pathak, S.K. Mishra, and M.M. Godkhindi, "Self-Propagating-High-Temperature Synthesis (SHS) of Ultrafine ZrB<sub>2</sub>," *J. Mater. Sci. Lett.*, **22**, 1189-91 (2003).
- [37]. A.K. Khanra, L.C. Pthak, and M.M. Godkhindi, "Carbothermal Synthesis of Zirconium Diboride (ZrB<sub>2</sub> Whiskers)," *Adv. Appl. Ceram.*, **106** [3] 155-60 (2007).
- [38]. A.L. Bowman, "The Variation of Lattice Parameter with Carbon Content of Tantalum Carbide," *J. Phys. Chem.*, **65** [9] 1596-8 (1961).
- [39]. A. Jain, "Synthesis and Processing of Nanocrystalline Zirconium Carbide Formed by Carbothermal Reduction," Master of Science Thesis. Georgia Institute of Technology, Atlanta, GA.

- [40]. R.W. Bartlett and F.A. Halden, "Study of Growth Parameters for Refractory Carbide single Crystals," SRI Project FMU-4892, Final Report, National Aeronautics and Space Administration, Washington, D.C., 1967.
- [41]. Y. Xie, T.H. Sanders Jr., R.F. Speyer, "Solution-Based Synthesis of Submicrometer ZrB<sub>2</sub> and ZrB<sub>2</sub>-TaB<sub>2</sub>," *J. Am. Ceram. Soc.*, **91** [5] 1469-74 (2008).
- [42]. N.I. Shurov, A.I. Anfinogenov, V.V. Chebykin, L.P. Klevtsov, and E.G. Kazanskii, "The Synthesis of Borides, Carbides, and Silicides of Refractory Metals in Ionic-Electronic Metls," pp. 81-6 in NATO ASI Series 3. High Technology, Vol. 53, *Refractory Metals in Molten Salts: Their Chemistry, Electrochemistry and Technology*, Edited by D.H. Kerridge and E.G. Polyakov, Springer, London, 1998.
- [43]. D. Choi and P.N. Kumta, "Synthesis, Structure, and Electrochemical Characterization of Nanocrystalline Tantalum and Tungsten Nitrides," *J. Am. Ceram. Soc.*, **90** [10] 3113-20 (2007).
- [44]. T. Mashimo, S. Tashiro, T. Toya, M. Nishida, H. Yamazaki, S. Yamaya, K. Oh-Ishi, Y. Syono, "Synthesis of the B1-Type Tantalum Nitride by Shock Compression," *J. Mater Sci.*, **28**, 3439-43 (1993).
- [45]. T. Mashimo, S. Tashiro, M. Nishida, K. Miyahara, and E. Eto, "B1-Type and WC-Type Phase Bulk Bodies of Tantalum Nitride Prepared by Shock and Static Compressions," *Physica B*, **239**, 13-5 (1997).
- [46]. B. Fu and L. Gao, "Synthesis of Nanocrystalline Cubic Tantalum (III) Nitride Powders by Nitridation-Thermal Decomposition," *J. Am. Ceram. Soc.*, **88** [12] 3519-21 (2005).
- [47]. L. Shi, Z. Yang, L. Chen, Y. Qian, "Synthesis and Characterization of Nanocrystalline TaN," *Solid State Comm.*, **133**, 117-20 (2005).
- [48]. B. Mazumbder and A.L. Hector, "Use of Low Temperature Solvothermal Reactions in the Synthesis of Nanocrystalline Tantalum Nitrides Including Nanorods," *J. Mater Chem.*, **18**, 1392-8 (2008).
- [49]. M.S. Chandrasekharaiah, J.L. Margrave, and P.A.G. O'Hare, "The Disilicides of Tungsten, Molybdenum, Tantalum, Titanium, Cobalt, and Nickel, and Platinum Monosilicide, A Survey of Their Thermodynamic Properties," *J. Phys. Chem. Ref. Data*, **22** [6] 1459-68 (1993).
- [50]. U. Gottlieb, J.C. Lasjaunias, O. Laborde, O. Thomas, and R. Madar, "Low Temperature Specific Heat Measurements of VSi<sub>2</sub>, NbSi<sub>2</sub> and TaSi<sub>2</sub>," *Appl. Surf. Sci.*, **73**, 232-6 (1993).

- [51]. J.H. Thomas, III and L.H. Hammer, "A Photoelectron Spectroscopy Study of  $\text{CF}_4/\text{H}_2$  Reactive Ion Etching Residue on Tantalum Disilicide," *J. Electrochem. Soc.*, **136** [7] 2004-10 (1989).
- [52]. F.A. Baiocchi, N. Lifshitz, T.T. Sheng, and S.P. Murarka, "Equilibration of Nonstoichiometric Ta-Si Deposits on Polycrystalline Silicon at High Temperatures," *J. Appl. Phys.*, **64**, 6490-5 (1988).
- [53]. T.R. Pampalone and F.A. Kuyan, "Contrast Enhancing Additives for Positive Photoresist," *J. Electrochem. Soc.*, **135** [2] 471-6 (1988).
- [54]. D.S. Williams, E. Coleman, and J.M. Brown, "Low Pressure Chemical Vapor Deposition of Tantalum Silicide," *J. Electrochem. Soc.*, **133** [2] 2637-2644 (1986).
- [55]. C. Wiczorek, "Chemical Vapour Deposition of Tantalum Disilicide," *Thin Solid Films*, **126**, 227-32 (1985).
- [56]. R.A. Levy and P.K. Gallagher, "Argon Entrapment and Evolution in Sputtered  $\text{TaSi}_2$  Films," *J. Electrochem. Soc.*, **132** [8] 1986-95 (1985).
- [57]. S.P. Murarka, "Effect of Oxygen Contamination on the Properties of Cosputtered Tantalum Silicide," *Appl. Phys. Lett.*, **45** [4] 392-4 (1984).
- [58]. R.R. Razouk, M.E. Thomas, and S.L. Pressacco, "Oxidation of Tantalum Disilicide/Polycrystalline Silicon Structures in Dry  $\text{O}_2$ ," *J. Appl. Phys.*, **53**, 5342-4 (1982).
- [59]. G.J. Campisi, A.J. Bevolo, H.R. Shanks, and F.A. Schmidt, "The Growth of Polycrystalline Silicon on Molybdenum, Tantalum, Tungsten, and Their Disilicides," *J. Appl. Phys.*, **53**, 1714-9 (1982).
- [60]. J. Angilello, J.E.E. Baglin, F. Cardone, J.J. Dempsey, F.M. d'Heurle, E.A. Irene, R. MacInnes, C.S. Petersson, R. Savoy, A. P. Segmuller, and E. Tierney, "Tantalum Silicide Films Deposited by DC Sputtering," *J. Electronic. Mater.*, **10** [1] 59-93 (1981).
- [61]. W. Wang, T. Nabatame, and Y. Shimogaki, "Preparation of Conductive HfN by Post Rapid Thermal Annealing-Assisted MOCVD and its Application to Metal Gate Electrode," *Microelec. Eng.*, **85**, 320-6 (2008).
- [62]. A. Arranz, "Synthesis of Hafnium Nitride Films by 0.5-5 keV Nitrogen Implantation of Metallic Hf: an X-ray Photoelectron Spectroscopy and Factor Analysis Study," *Surf. Sci.*, **563**, 1-12 (2004).

- [63]. J.P. Dauchot, R. Gouttebaron, D. Cornelissen, M. Wautelet, and M. Hecq, "Synthesis of Stoichiometric Zirconium Nitride by D.C. Reactive Magnetron Sputtering Pulsed at Low Frequency: Characterization by ESCA, SIMS and Electron Microprobe," *Surf. Interface Anal.*, **30**, 607-11 (2011).
- [64]. G.V. Golubkova, E.Yu. Belyaev, and O.I. Lomovsky, "Mechanochemical Synthesis of Nonstoichiometric Tantalum Disilicide," *J. Alloys Compd.*, **270**, 224-7 (1998).
- [65]. F. Maglia, C. Milanese, U. Anselmi-Tamburini, S. Doppiu, G. Cocco, and Z.A. Munir, "Combustion Synthesis of Mechanically Activated Powders in Ta-Si System," *J. Alloys Compd.*, **385** [1-2] 269-75 (2004).
- [66]. F. Maglia, U. Anselmi-Tamburini, N. Bertolino, C. Milanese, and Z.A. Munir, "Field-Activated Combustion Synthesis of Ta-Si Intermetallic Compounds," *J. Mater. Res.*, **16** [2] 534-44 (2001).
- [67]. A.M. Nartowski and I.P. Parkin, "Solid State Metathesis Synthesis of Metal Silicides; Reactions of Calcium and Magnesium Silicide with Metal Oxides," *Polyhedron*, **21** [2] 187-91 (2002).
- [68]. B. Fu and L. Gao, "Synthesis of Nanocrystalline Zirconium Nitride Powders by Reduction-Nitridation of Zirconium Oxide," *J. Am. Ceram. Soc.*, **87** [4] 696-8 (2004).
- [69]. Y. Gu, F. Guo, Y. Qian, H. Zheng, and Z. Yang, "A Benzene-Thermal Synthesis of Powdered Cubic Zirconium Nitride," *Mater. Lett.*, **57**, 1697-82 (2003).
- [70]. D.W. Davies, "Unique Preparation of Boron Nitrided for Ultra High Hardness Applications"; B.S. Thesis. Alfred University, Alfred, NY, 2012.
- [71]. B.M. Clark, J.P. Kelly, and O.A. Graeve, "Recent Advances on Bulk Tantalum Carbide Produced by Solvothermal Synthesis and Spark Plasma Sintering," *Mater. Res. Soc. Symp. Proc.*, submitted (2012).
- [72]. J. Lian, T. Kim, X. Liu, J. Ma, and W. Zheng, "Ionothermal Synthesis of Turbostratic Boron Nitride Nanoflakes at Low Temperature," *J. Phys. Chem. C*, **113**, 9135-40 (2009).
- [73]. L. Zhu, M. Tan, G. Lian, X. Zhang, D. Cui, and Q. Wang, "Investigation on the Synthesis of Turbostratic Boron Nitride by Solvothermal Hot-Press Method," *Solid State Sci.*, **12**, 1084-7 (2010).
- [74]. X. Shi, S. Wang, H. Yang, X. duan, and X. Dong, "Synthesis and Characterization of Bamboo-Like Turbostratic Boron Nitride Tubes," *Mater. Chem. Phys.*, **112**, 20-3 (2008).

- [75]. Q. Guo, Y. Xie, C. Yi, L. Zhu, and P. Gao, "Synthesis of Ultraviolet Luminescent Turbostratic Boron Nitride Powders via a Novel Low-Temperature, Low-Cost, and High-Yield Chemical Route," *J. Solid State Chem.*, **178**, 1925-28 (2005).
- [76]. B.P. Singh, S.K. Singhal, R. Chopra, K.D. Sharda, and E.S.R. Gopal, "Behaviour of Turbostratic Boron Nitride under High Pressure and Temperature in the Presence of a Non-Conventional Catalyst," *J. Mater. Sci. Lett.*, **16**, 1593-4 (1997).
- [77]. M. Hubáček and M. Ueki, "Chemical Reactions in Hexagonal Boron Nitride System," *J. Solid State Chem.*, **123**, 215-22 (1996).
- [78]. G.L. Doll, J.S. Speck, G. Dresselhaus, M.S. Dresselhaus, K. Nakamura, and S.-I. Tanuma, "Intercalation of Hexagonal Boron Nitride with Potassium," *J. Appl. Phys.*, **66** [6] 2554-8 (1989).
- [79]. T. Sato, H. Hiaoka, T. Endo, O. Fukunaga, and M. Iwata, "Effect of Oxygen on the Growth of Cubic Boron Nitride Using  $Mg_3N_2$  as a Catalyst," *J. Mater. Sci.*, **16**, 1829-34 (1981).
- [80]. M.M. Bindal, S.K. Singhal, B.P. Singh, R.K. Nayar, R. Chopra, and A. Dhar, "Synthesis of Cubic Boron Nitride Using Magnesium as the Catalyst," *J. Crystal Growth*, **112**, 386-401 (1991).
- [81]. G. Bocquillon, C. Loriers-Susse, and J. Loriers, "Synthesis of Cubic Boron Nitride Using Mg and Pure or M'-Doped  $Li_3N$ ,  $Ca_3N_2$ , and  $Mg_3N_2$  with M'=Al, B, Si, Ti," *J. Mater. Sci.*, **28**, 3547-56 (1993).
- [82]. R. Mota, P. Piquini, T.M. Schmidt, and A. Fazzio, "Electronic and Structural Properties of Defects in c-BN," *Intl. J. Quantum Chem.*, **65**, 941-6 (1997).
- [83]. V.Z. Turkevich, "The Parameters of Equilibrium Between Oxygen Solid Solutions in Cubic and Graphite-Like Hexagonal Boron Nitrides," *Diam. Relat. Mater.*, **8**, 2032-5 (1999).
- [84]. M. Bezhenar, "Non-Stoichiometry of Composition and Dissolution of Oxygen in the Cubic Boron Nitride Crystal Lattice," *Diam. Relat. Mater.*, **8**, 406-9 (1999).
- [85]. G. Qi and Y.-K. Le, "Influence of Oxygen on the Formation of Cubic Boron Nitride by R.F. Magnetron Sputtering," *Appl. Surf. Sci.*, **256**, 3249-52 (2010).
- [86]. J. Houska and S. Ulrich, "Stress Reduction in Cubic Boron Nitride by Oxygen Addition: Explanation of the Mechanism by Ab-Initio Simulations," *Surf. Coat. Technol.*, **206**, 2541-4 (2012).

- [87]. W.C. Yohe and R.L. Ruoff, "Ultrafine-Grain Tantalum Carbide by High Pressure Hot Pressing," *Ceram. Bull.*, **57** [12] 1123-30 (1978).
- [88]. X. Zhang, G.E. Hilmas, and W.G. Fahrenholtz, "Synthesis, Densification, and Mechanical Properties of TaB<sub>2</sub>," *Mater. Lett.*, **62**, 4251-3 (2008).
- [89]. E. Barraud, S. Bégin-Colin, G. Le Caër, O. Barres, and F. Villieras, "Mechanically Activated Solid-State Synthesis of Hafnium Carbide and Hafnium Nitride Nanoparticles," *J. Alloys Compd.*, **456**, 224-33 (2008).
- [90]. B.K. Yen, "X-Ray Diffraction Study of Mechanochemical Synthesis and Formation Mechanisms of Zirconium Carbide and Zirconium Silicides," *J. Alloys Compd.*, **268**, 266-69 (1998).
- [91]. M.D. Sacks, C.-A. Wang, Z. Yang, and A. Jain, "Carbothermal Reduction Synthesis of Nanocrystalline Zirconium Carbide and Hafnium Carbide Powders Using Solution-Derived Precursors," *J. Mater. Sci.*, **39**, 6057-66 (2004).
- [92]. Y. Yan, Z. Huang, X. Liu, and D. Jiang, "Carbothermal Synthesis of Ultra-Fine Zirconium Carbide Powders Using Inorganic Precursors via Sol-Gel Method," *J. Sol-Gel Sci. Technol.*, **44**, 81-5 (2007).
- [93]. L. Combemail, Y. Leconte, X. Portier, N. Herlin-Boime, and C. Reynaud, "Synthesis of Nanosized Zirconium Carbide by Laser Pyrolysis Route," *J. Alloys Compd.*, **483**, 468-72 (2009).
- [94]. X. Tao, W. Qiu, H. Li, and T. Zhao, "Synthesis of Nanosized Zirconium Carbide from Pre-ceramic Polymers by the Facile One-Pot Reaction," *Polym. Adv. Technol.*, **21**, 300-4 (2010).
- [95]. J.Y. Xiang, S.C. Liu, W.T. Hu, Y. Zhang, C.K. Chen, P. Wang, J.L. He, D.L. Yu, B. Xu, Y.F. Lu, Y.J. Tian, and Z.Y. Liu, "Mechanochemically Activated Synthesis of Zirconium Carbide Nanoparticles at Room Temperature: A Simple Route to Prepare Nanoparticles of Transition Metal Carbides," *J. Eur. Ceram. Soc.*, **31**, 1491-6 (2011).
- [96]. M. Dollé, D. Gosset, C. Bogicevic, F. Karolak, D. Simeone, and G. Baldinozzi, "Synthesis of Nanosized Zirconium Carbide by a Sol-Gel Route," *J. Eur. Ceram. Soc.*, **27**, 2061-7 (2007).
- [97]. B.M. Clark, J.P. Kelly, and O.A. Graeve, "Exploring the Synthesis Parameters and Spark Plasma Sintering of Tantalum Carbide Powders Prepared by Solvothermal Synthesis," *Mater. Res. Soc. Symp. Proc.*, **1373**, 7-17 (2010).
- [98]. V.V. Rudneva and G.V. Galevskii, "Thermoxidative Stability of Refractory Carbide and Boride Nanopowder," *Steel Transl.*, **37** [4] 329-32 (2007).

- [99]. L. Yu, T. Wang, C. Luan, Q. Wang, and D. Cui, "A New Stepwise-Pressing Reaction Method for Synthesizing Pure Turbostratic Boron Nitride," *Mater. Res. Bull.*, **45**, 1338-41 (2010).
- [100]. M. Li, L. Xu, C. Sun, Z. Ju, and Y. Qian, "Thermal-Induced Shape Evolution from Uniform Triangular to Hexagonal r-BN Nanoplates," *J. Mater. Chem.*, **19**, 8086-91 (2009).
- [101]. Y. Huang, Y. Bando, C. Tang, C. Zhi, T. Terao, B. Dierre, T. Sekiguchi, and D. Golberg, "Thin-Walled Boron Nitride Microtubes Exhibiting Intense Band-Edge UV Emission at Room Temperature," *Nanotechnol.*, **20**, 085705-1-7 (2009).
- [102]. L. Wang, L. Xu, C. Sun, and Y. Qian, "A General Route for the Convenient Synthesis of Crystalline Hexagonal Boron Nitride Micromesh at Mild Temperature," *J. Mater. Chem.*, **19**, 1989-94 (2009).
- [103]. L. Hou, F. Gao, G. Sun, H. Gou, and M. Tian, "Synthesis of High-Purity Boron Nitride Nanocrystal at Low Temperatures," *Cryst. Growth Design*, **7** [3] 535-40 (2007).

## CHAPTER 3: A SOLVOTHERMAL APPROACH FOR THE PREPARATION OF NANOSTRUCTURED CARBIDE AND BORIDE ULTRA-HIGH TEMPERATURE CERAMICS

### A. Introduction

Transition metal carbides, such as TaC, are some of the most refractory ceramics known, having melting temperatures up to ~4000 K. Besides being refractory, other beneficial properties include thermomechanical stability, thermochemical stability, corrosion and wear resistance, good creep and fatigue resistance, unique optical and electronic properties, high emissivity at elevated temperatures, and catalytic characteristics.<sup>[1-8]</sup> These materials are of particular interest in the aerospace industry, where re-entry conditions and internal rocket conditions result in harsh environments with demanding specifications. In addition to carbides, transition metal borides are also relevant materials for aerospace applications. In the case of ZrB<sub>2</sub>/SiC composites, the oxidation resistance can be significantly enhanced with additions of LaB<sub>6</sub> to provide outstanding behavior for temperatures up to 2673 K.<sup>[9]</sup>

Solvothermal synthesis for carbide materials has been independently demonstrated by Ma, Hu, Gu, and their co-workers.<sup>[6,10,11]</sup> The technique is historically defined as synthesis in a non-aqueous solvent by the application of temperature and pressure within the confines of an autoclave. This can result in heavily agglomerated powders due to the long processing times without a form of stabilization. Typical reactants include chloride compounds and alkali/alkaline earth metals where the metals reduce the chloride reactants and provide nascent metal seeds to form the desired materials, but other reactants, including metal powders, have been used to replace chloride compounds in some instances.

Due to the use of an autoclave for the process, the reaction is not directly observable. Lack of direct observation has made the fundamental mechanisms of this technique difficult to define. For purposes of this study, solvothermal synthesis will be redefined to include the synthesis in a heated solvent, but without pressure. Specifically, the focus of this work is to demonstrate a unique solvothermal synthesis approach where

synthesis is performed in transparent fused-silica test tubes, rather than in an autoclave, and to demonstrate the viability of using the technique to make carbide and boride nanopowders such as TaC and LaB<sub>6</sub>, while at the same time allowing direct observation of the reactions taking place during the process. This study confirms that the process is similar to a self-propagating high-temperature synthesis (SHS) process, eliminating the need for an autoclave and long processing times, and produces fine and unagglomerated powders.

## B. Experimental Procedures

Reactant weighing and mixing was performed in an argon-filled glove box. Three types of samples were prepared: (1) thermally-ignited TaC, (2) thermally-ignited LaB<sub>6</sub>, and chemically-ignited LaB<sub>6</sub>. For the case of the thermally-ignited TaC synthesis, 5.57 grams of TaCl<sub>5</sub> (99.8%, Alfa Aesar, Ward Hill, MA) and 0.56 grams of carbon (Lampblack 101, Degussa, Parsippany, NJ) were mixed using a mortar and pestle. The mixture was added to a fused-silica test tube with 1.62 grams of lithium (granular, 99%, Sigma-Aldrich, St. Louis, MO), mixed with a spatula, and sealed with a rubber stopper. A 50-g batch, using 92.8 grams of TaCl<sub>5</sub>, 9.3 grams of carbon, and 27.0 grams of lithium, was also performed in a 600 ml stainless steel beaker to demonstrate scale-up. The reactants were mixed using 3x carbon stoichiometry and 3x lithium stoichiometry according to the following equation:



A similar procedure was used for the synthesis of LaB<sub>6</sub>. Lanthanum (III) chloride hydrate (99.9%, Alfa Aesar, Ward Hill, MA), boron (Sigma-Aldrich, St. Louis, MO), and lithium granules were used. The amounts of lanthanum (III) chloride hydrate, boron, and lithium for the thermally-ignited sample were 3.82, 2.02, and 0.97 g, respectively, which correspond to 2x boron stoichiometry and 3x lithium stoichiometry. For the chemically-ignited sample, the reactant amounts were the same except for the amount of boron, which was reduced to 1.01 g, corresponding to 1x boron stoichiometry. The reaction stoichiometries were determined according to the following equation:



After mixing, the closed sample tubes were removed from the glove box for ignition underneath a chemical fume hood. Before ignition, the test tubes were hand rolled to achieve mixing of the lithium granules with the rest of the reactants. The thermally ignited samples were lowered into a tube furnace that was held at a temperature of 548 K, just above the self-ignition temperature of lithium, after loosening the rubber stoppers to allow for outgassing. Once ignition occurred, the sample was immediately removed from the furnace and allowed to air quench. For the chemically ignited sample, the rubber stopper was removed from the test-tube. Water was added into the test tube until ignition occurred and the sample was allowed to air-quench.

After air-quenching, the samples were solid reaction products, including lithium-based compounds. They were removed from the test tubes by adding water, forming lithium hydroxide and freeing the reaction products. The products were then poured into a 250 ml beaker. Enough water was added to create a 100 ml suspension, which was magnetically stirred for 15 min, followed by ultrasonication for 15 min, and magnetic stirring for another 15 min. The suspension was centrifuged at  $15,500 \times g$  for five minutes, decanted, and allowed to dry. The dried powders were lightly ground in a mortar and pestle to prepare them for washing procedures.

For washing, the TaC samples were magnetically stirred with 100 ml of concentrated nitric acid (15.8 N) for 30 min, followed by ultrasonication for 30 min, magnetic stirring for another 15 min, and centrifuging at  $15,500 \times g$  for five minutes. Two water rinses were performed by adding water to the centrifuge tubes and ultrasonicing for five minutes before centrifuging again. A final ethanol rinse was performed in a similar manner. After pouring of the supernatant, the sample was allowed to dry in air for 24 hours before mixing with a mortar and pestle and storing for characterization. A modified washing procedure was used for the 50-g batch of TaC. Three water washes, using a procedure similar to the nitric acid wash, were performed before drying and mixing. The washing procedure for the LaB<sub>6</sub> samples is described elsewhere.<sup>[12]</sup>

The samples were characterized by powder X-ray diffraction using a diffractometer (Siemens D5000, Siemens, New York, NY) by scanning from 15 to 85° 2θ using a step size of 0.04° 2θ and a dwell time of two seconds after dispersing the powders

onto a zero-background holder. Software (Jade 8, Materials Data Incorporated, Livermore, CA) was used to estimate the average crystallite sizes using the Williamson-Hall technique. For TaC, the analysis software was also used to perform profile fitting and unit-cell refinement to determine the lattice parameter. The lattice parameter was used to determine the compound stoichiometry according to the equation  $C/Ta = 6.398a - 17.516$ .<sup>[13]</sup> Dynamic light scattering (DLS) (Nanotracer™ ULTRA, Microtrac, Inc., Montgomeryville, PA) was used to determine the particle size distribution of 0.01 grams of powder dispersed in 25 ml of deionized water. The DLS samples were allowed to magnetically stir for 24 hours and were ultrasonicated for five minutes before the measurements were taken. Each DLS measurement consisted of an average of five 30-sec runs as is recommended by the manufacturer of the instrument and in conjunction with ASTM standard E2490-09. Scanning electron microscopy (SEM) was performed using a microscope (FEI™ Quanta 200F, FEI Company, Hillsboro, OR 97124) to observe particle morphology and supplement particle and crystallite size analyses. SEM samples were prepared by dispersing 0.01 grams of powder into 25 ml of acetone, magnetically stirring for 1 hour, ultrasonicated for 10 min, drop coating onto a silicon wafer, drying, and then carbon-coating. Specific surface area (SSA) measurements were performed using a surface area analyzer (Tristar 3000, Micromeritics, Norcross, GA 30093) after degassing in argon for 24 hours at 423 K. Density measurements were performed by helium pycnometry (AccuPyc II 1340, Micromeritics, Norcross, GA 30093) and was used with SSA measurements to calculate an average crystallite size for a comparison with the average crystallite sizes obtained by X-ray diffraction. The average crystallite size was calculated in nanometers according to  $6000/(SSA \cdot \rho)$ , where SSA is the specific surface area in  $m^2/g$ ,  $\rho$  is the density in  $g/cm^3$ , and the particles are assumed to be spherical.

## **G. Results and Discussion**

Direct observation of the solvothermal reaction suggests that it is a fast, self-sustaining reaction, requiring only ignition. Ignition can be achieved either thermally or chemically. To thermally ignite a sample, the self-ignition temperature of the lithium metal must be exceeded by the application of heat. Chemical ignition can be achieved by

reacting lithium with water to produce lithium hydroxide and hydrogen. Either process results in a strong exothermic reaction that propagates the combustion wave. Thermal ignition of other metals or the use of other exothermic reactions should be possible ignition methods. Once the system is ignited, molten lithium and/or lithium compounds form the solvent for chemical reactions to occur in. The temperatures achieved during ignition are well above the decomposition temperatures of the chlorides ( $\sim 513$  K for  $\text{TaCl}_5$  and  $\sim 1273$  K for  $\text{LaCl}_3$  versus reaction temperatures as high as  $\sim 1653$  K) and therefore the reaction to form TaC will proceed from the nascent metal particles and carbon or boron. The reactions to form TaC and  $\text{LaB}_6$  from their metal and non-metal result in exothermic combustion (having adiabatic flame temperatures of 2700 K and 2800 K, respectively).<sup>[14]</sup> The energy from the reaction has the capability of driving the temperature of the solvent up to, but not exceeding, the vaporization temperature until the reactants are depleted or not converted at a fast enough rate to prevent cooling. Figure 3-1 demonstrates the reaction sequence in real time snapshots, with images taken every two seconds after ignition for a total time of 30 sec.

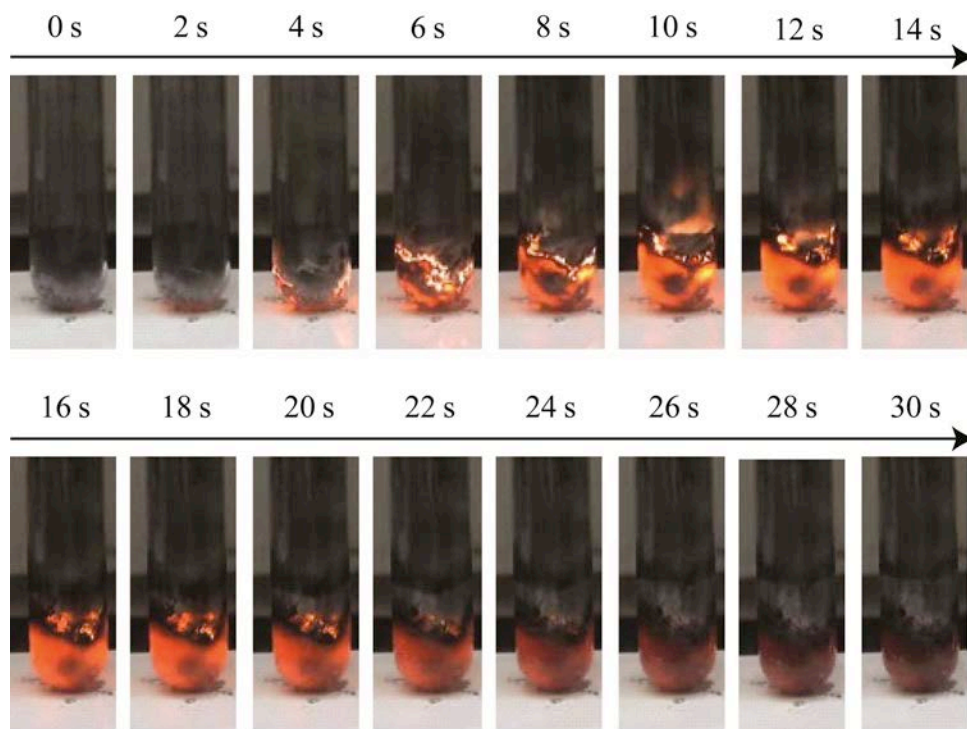


Figure 3 - 1. Images of the self-propagating solvothermal synthesis reaction, followed by cooling, for the synthesis of TaC. Images are taken every two seconds for 30 sec after ignition ( $t = 0$  s). (With color)

The higher the exothermicity of the reaction, the more likely this process will work for a given system. Based on similar reactions in chloride salts, it seems probable that self-propagating reactions will occur if the adiabatic temperature of the reaction is greater than the melting point of the solvent.<sup>[15]</sup> Faster heating and cooling rates can be achieved with this approach when compared to synthesis in a thick-walled autoclave vessel. This can inhibit grain growth during the process and prevent secondary reaction/crystallization events from occurring during a dwell or slow cool. Furthermore, the apparatus is simpler, costs much less, and can accommodate larger batch sizes more readily than an autoclave. To demonstrate the ease of scale-up, the 50-g batch was prepared in a larger container.

The X-ray diffraction patterns and calculated crystallite sizes for the three small-scale powders that have been washed are given in Figure 3-2. Results indicate that TaC and LaB<sub>6</sub> samples of high phase purity were obtained and the average crystallite sizes were 25, 84, and 81 nm for the TaC, thermally-ignited LaB<sub>6</sub>, and chemically-ignited LaB<sub>6</sub>, respectively. The source of ignition made no difference on the average crystallite size of the LaB<sub>6</sub> powders, suggesting that the mechanism for the synthesis of the powders is the same regardless of how the reaction is ignited and further supports the idea that the reaction proceeds by self-propagating synthesis from the reaction between the metal and non-metal as a secondary reaction. Since TaC properties are known to vary with compound stoichiometry (C/Ta), it is important to report this value. The compound stoichiometry, determined by lattice refinement, was 0.94. The 50-g batch was nearly phase-pure, containing a minor amount of tantalum metal (not shown). The decrease in phase purity is believed to be a result of mixing, where localized regions were carbon deficient and indicates that process optimization is required. The crystallite size for the large batch-size was 25 nm and the compound stoichiometry was 0.94 indicating no change from the smaller batch-size.

Figure 3-3 illustrates the dynamic light scattering (DLS) results for the three small-scale samples. TaC has an average particle size of 97 nm with a skewed upper-tail distribution that falls off rapidly (the majority of particles are below 200 nm). Similarly, the majority of particles were below 200 nm for the large-scale batch, but the average

particle size was 73 nm, indicating a small improvement in the particle size distribution. The average particle sizes of the two LaB<sub>6</sub> samples were larger than for the TaC samples. Furthermore, the two LaB<sub>6</sub> samples have a small bimodal peak in the upper-tail distribution. The second mode occurs around 500-600 nm and was more prevalent in the chemically-ignited sample.

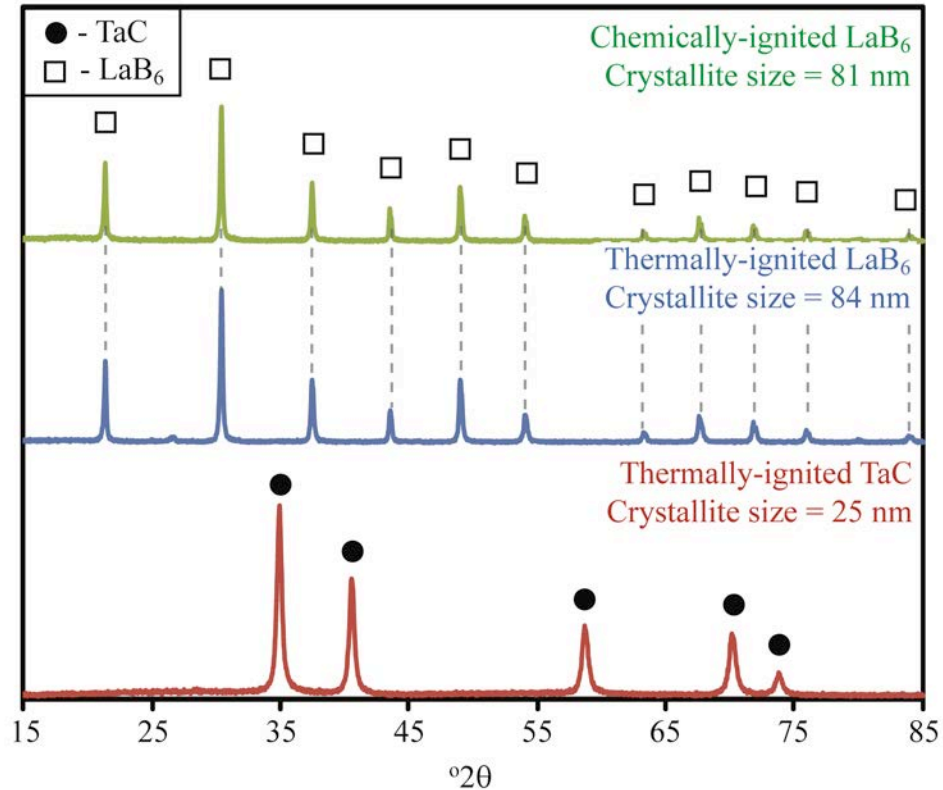


Figure 3 - 2. X-ray diffraction patterns for 3-g TaC and LaB<sub>6</sub> powders after washing. (With color)

A useful figure of merit to characterize the amount of particle aggregation is a ratio between the average particle size and average crystallite size. These figures of merit are 3.9, 1.6, and 2.0, for the TaC, thermally-ignited LaB<sub>6</sub>, and chemically-ignited LaB<sub>6</sub>, respectively, which suggest a low state of agglomeration for the powders. The figure of merit for the 50-g TaC batch is 3.0, indicating that scaling up assisted in achieving a lower extent of agglomeration. TaC synthesized via solvothermal synthesis and using an autoclave resulted in TaC with an average crystallite size of 40 nm, based on SEM imaging, but the powders are agglomerated due to their fine size making a particle size

analysis difficult.<sup>[6]</sup> However, particle necking is clearly evident from the images, indicating significant aggregation. Another study performing solvothermal synthesis of TaC in an autoclave report a crystallite size of 15-40 nm and slight agglomeration from TEM analysis.<sup>[11]</sup> Neither analysis presents the true particle size to obtain a figure of merit. Thus, it is proposed from the visual data that both sets of powders are heavily aggregated due to the long processing times and slow cooling from the use of an autoclave.

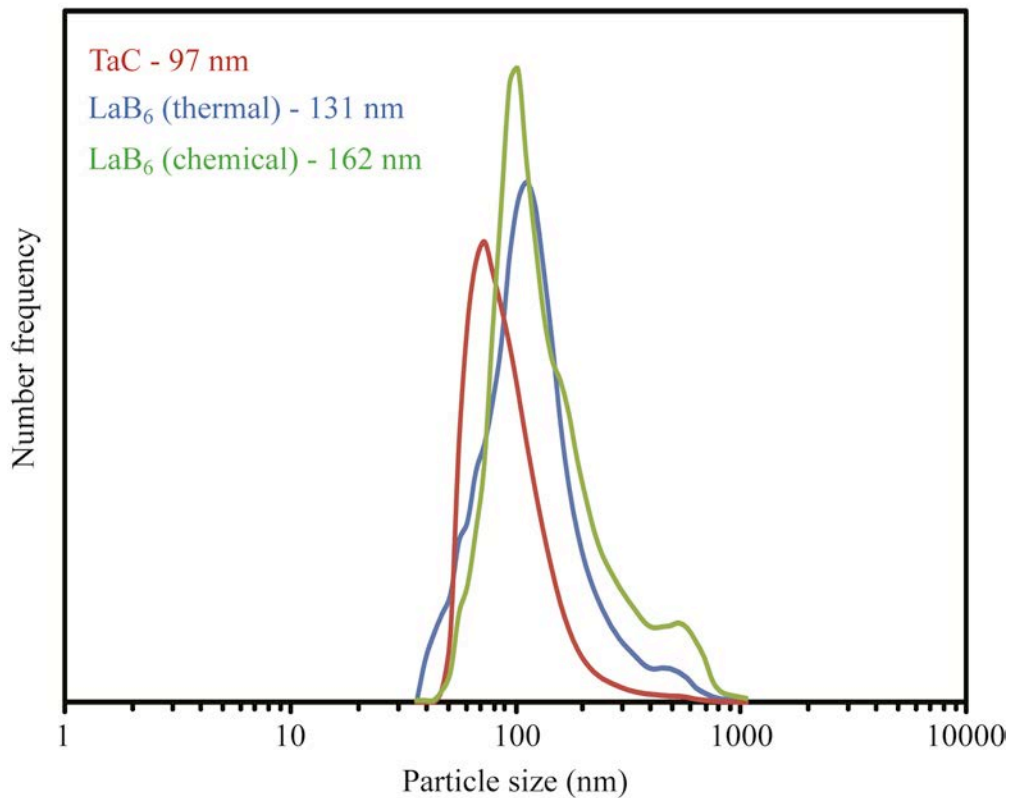


Figure 3 - 3. Particle size distributions for TaC and LaB<sub>6</sub> powders. Average particle sizes are given in the legend. (With color)

A scanning electron micrograph for the TaC samples is given in Figure 3-4. TaC grains appear to be equiaxed rather than elongated or plate-like and the images demonstrate that the individual grains are small, agreeing well with the crystallite size analysis. The specific surface area for the small-scale and large-scale synthesis of the TaC samples were 39.9 and 19.5 m<sup>2</sup>/g, respectively, while the measured densities were 7.6 and 9.7 g/cm<sup>3</sup>, respectively, much lower than the theoretical density of 14.5 g/cm<sup>3</sup>.

The disagreement could arise from free carbon or oxide contamination and requires further analysis. The estimated average crystallite sizes using the surface area and density data were 20 and 32 nm, respectively, and are in good agreement with the value of 24 nm determined by X-ray diffraction, supporting an equiaxed grain morphology although it is impossible to distinguish if the grains are rounded or faceted from this analysis.

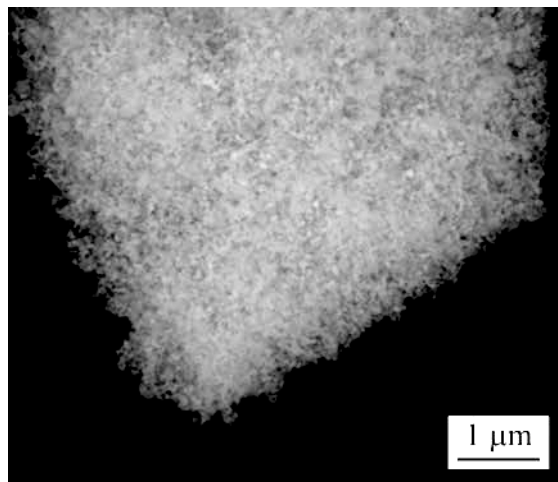


Figure 3 - 4. Back-scattered electron image of TaC powders.

Figure 3-5 demonstrates that the LaB<sub>6</sub> samples have a faceted morphology, most likely cubic. The cubic faces in LaB<sub>6</sub> correspond to the lower energy {100} planes of the cubic crystal structure in this material.<sup>[16]</sup> The cubic morphology forms during the washing procedure.<sup>[12]</sup> Larger grains up to one micrometer are evident for the LaB<sub>6</sub> samples, but the majority of grains appear to be submicron and below 300-400 nm, which agrees well with the upper limit of the smaller particle-size mode in the bimodal distribution of the DLS results presented in Figure 3-3. The larger grains are associated with the higher particle-size mode in the bimodal distribution, which is centered around 500-600 nm with the upper limit approaching one micrometer. Distinct particle necking is not clearly observed and the images complement the crystallite size and particle size distributions obtained from XRD and DLS.

The specific surface area of the thermally-ignited and chemically-ignited LaB<sub>6</sub> samples were 6.6 and 7.0 m<sup>2</sup>/g, respectively, while the density measurements were 2.9

and  $3.0 \text{ g/cm}^3$ , respectively, and also much lower than the theoretical density of  $4.7 \text{ g/cm}^3$ . The low densities can be attributed to impurity phases such as residual boron or oxides. The estimated average crystallite sizes from this data are 313 and 285 nm, respectively, and are larger than the average crystallite sizes determined by X-ray diffraction (84 and 81 nm respectively) as well as larger than the average particle sizes determined by DLS (131 and 162 nm respectively). The discrepancy is facilitated by the invalidity of the assumption that the particles are spherical for the calculation of particle size from surface area and density measurements. The low density of the powders indicates that they are contaminated, which may also contribute to the error. A low density phase that encapsulates the powders, preventing gas penetration, would result in overestimating the particle size because of underestimating both the density and the surface area of the powders. The purity of the powders needs to be further evaluated.

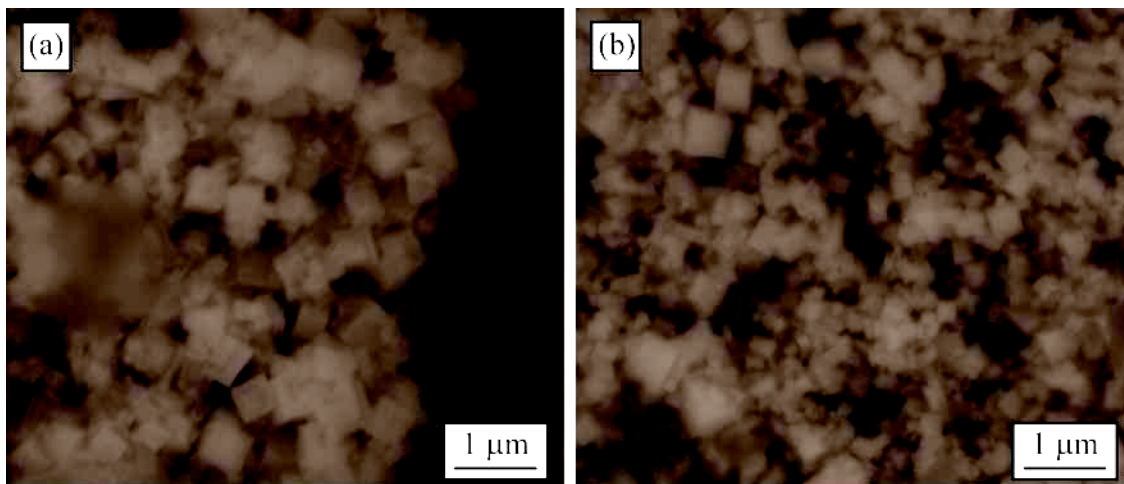


Figure 3 - 5. Back-scattered electron images of (a) thermally-ignited  $\text{LaB}_6$  and (b) chemically-ignited  $\text{LaB}_6$ .

## H. Conclusions

A new approach to solvothermal synthesis, without pressure and using both thermal and chemical ignition techniques, has been demonstrated. The visual observations of the reaction provide insight for the reaction mechanisms that would have been difficult to ascertain by performing the reaction in an autoclave. Little external

energy input is needed to carry out this process and the reactions proceed by a self-propagating high-temperature synthesis mechanism. The process has been demonstrated for obtaining two compounds, TaC and LaB<sub>6</sub>, that are highly exothermic by reaction from the metal and non-metal components. The characterization of the TaC and LaB<sub>6</sub> powders demonstrates that this technique is suitable for obtaining nanocrystalline non-oxide materials and is attributed to the fast reaction kinetics. Furthermore, the figures of merit that were obtained relating to particle dispersion indicate that the level of aggregation of the samples is low. This unique approach will aid in the development of nanocrystalline ultra-high temperature ceramics, and composites of them, and has the potential to satisfy other applications that require nanocrystalline and unagglomerated non-oxide powders. More understanding of the powder purity is necessary.

## I. References

- [1]. K. Balani, G. Gonzalez, and A. Agarwal, "Synthesis, Microstructural Characterization, and Mechanical Property Evaluation of Vacuum Plasma Sprayed Tantalum Carbide," *J. Am. Ceram. Soc.*, **89** [4] 1419-25 (2006).
- [2]. P.G. Li, M. Lei, B. Sun, L.Z. Cao, Y.F. Guo, X. Guo, W.H. Tang, "C<sub>3</sub>N<sub>4</sub> as a Precursor for the Synthesis of NbC, TaC, and WC Nanoparticles," *J. Alloys Compd.*, **430**, 237-40 (2007).
- [3]. C.L. Yeh and E.W. Liu, "Combustion Synthesis of Tantalum Carbides TaC and Ta<sub>2</sub>C," *J. Alloys Compd.*, **415**, 66-72 (2006).
- [4]. L. López-de-la-Torre, B. Winkler, J. Schreuer, K. Knorr, and M. Avalos-Borja, "Elastic Properties of Tantalum Carbide (TaC)," *Solid State Commun.*, **134**, 245-50 (2005).
- [5]. D.-H. Kwon, S.-H. Hong, and B.-K. Kim, "Fabrication of Ultrafine TaC Powders by Mechano-Chemical Process," *Mater. Lett.*, **58**, 3863-67 (2004).
- [6]. J. Ma, Y. Du, M. Wu, and M.C. Pan, "One Simple Synthesis Route to Nanocrystalline Tantalum Carbide via the Reaction of Tantalum Pentachloride and Sodium Carbonate with Metallic Magnesium," *Mater. Lett.*, **61**, 3658-61 (2007).
- [7]. H. Xiang, Y. Xu, L. Zhang, and L. Cheng., "Synthesis and Microstructure of Tantalum Carbide and Carbon Composite by Liquid Precursor Route," *Scr. Mater.*, **55**, 339-42 (2006).
- [8]. J.-G. Choi, "The Influence of Surface Properties on Catalytic Activities of Tantalum Carbides," *Appl. Catal., A*, **184**, 189-201 (1999).
- [9]. X.-H. Zhang, P. Hu, J.-C. Han, L. Xu, and S.-H. Meng, "The Addition of Lanthanum Hexaboride to Zirconium Diboride for Improved Oxidation Resistance," *Scr. Mater.*, **57**, 1036-39 (2007).
- [10]. J.Q. Hu, Z.Y. Lu, K.B. Tang, B. Deng, R.R. Jiang, Y.T. Qian, W.C. Yu, G.E. Zhou, X.M. Kiu, and J.X. Wu, "Synthesis and Characterization of SiC Nanowires through a Reduction-Carburization," *J. Phys. Chem. B*, **104**, 5251-54 (2000).
- [11]. Y. Gu, L. Chen, Y. Qian, W. Zhang, and J. Ma, "Synthesis of Nanocrystalline Boron Carbide via a Solvothermal Reduction of CCl<sub>4</sub> in the Presence of Amorphous Boron Powder," *J. Am. Ceram. Soc.*, **88** [1] 225-7 (2005).

- [12]. R. Kanakala, G. Rojas-George, and O.A. Graeve, "Unique Preparation of Hexaboride Nanocubes: A First Example of Boride Formation by Combustion Synthesis," *J. Am. Ceram. Soc.*, in print (2010).
- [13]. A.L. Bowman, "The Variation of Lattice Parameter with Carbon Content of Tantalum Carbide," *J. Phys. Chem.*, **65** [9] 1596-8 (1961).
- [14]. A. Varma and J.P. Lebrat, "Combustion Synthesis of Advanced Materials," *Chem. Eng. Sci.*, **47** [9-11] 2179-2194 (1992).
- [15]. E.G. Gillan and R.B. Kaner, "Synthesis of Refractory Ceramics via Rapid Metathesis Reactions between Solid-State Precursors," *Chem. Mater.*, **8** [2] 333-43 (1996).
- [16]. T. Nakano, S. Baba, A. Kobayashi, A. Kinbara, T. Kajiwara, and K. Watanabe, "Structure modification of radio frequency sputtered LaB<sub>6</sub> Thin Films by Internal Stress," *J. Vac. Sci. Technol., A*, **9** [3] 547-549 (1991).

## CHAPTER 4: STATISTICAL EXPERIMENTAL DESIGN APPROACH TO THE SOLVOTHERMAL SYNTHESIS OF NANOSTRUCTURED TANTALUM CARBIDE POWDERS

### A. Introduction

TaC is one of the most refractory ceramics known, having melting temperatures close to 4000 K and depending on compound stoichiometry. Besides being refractory, tantalum carbide is of particular interest as an ultra-high temperature ceramic (UHTC) and a material for composite UHTCs because of its thermomechanical and thermochemical stabilities. A significant number of researchers have reported results pertaining to the mechanical strength, fracture toughness, oxidation behavior, elastic properties, thermodynamic properties, hardness, ablative resistance, superconductivity, and electronic structure in the past few years, though research goes back much further.<sup>[1-8]</sup>

Kim and coworkers demonstrated that sintering of nanostructured TaC and the resulting mechanical properties were improved with finer initial powder size.<sup>[3]</sup> Current methods demonstrated for the synthesis of TaC include carbothermal reduction and subsequent carburization, impulse plasma synthesis in a liquid, gas-phase condensation, solvothermal synthesis, mechano-chemical synthesis, alkalide reduction, organometallic reactions, metathesis reactions, solid-state reactions, synthesis in ionic/electronic melts, and electrosynthesis.<sup>[9-21]</sup> Variations in these techniques include the use of metals and non-metals, compounds, or polymeric precursors as raw materials and the use of microwaves or electric fields to promote the reaction. These techniques have at least one of a few shortcomings, including the inability to produce nanostructured TaC, high energy input, long processing times, and/or issues with reaction scalability.

Solvothermal synthesis of TaC nanopowders has recently been reported.<sup>[22]</sup> The process is a slightly modified solvothermal synthesis technique such that the reaction does not occur within the confines of an autoclave, but in fused-silica test tubes. The observations indicate that the reaction is similar to a self-propagating high-temperature

synthesis (SHS) process and results in nanopowders with a low agglomeration state in contrast to traditional SHS reactions.<sup>[21]</sup>

The process is capable of producing nanostructured TaC with crystallite sizes of 25 nm, is easily scalable (50 grams batches have been produced and larger batch sizes or continuous processing could likely be accommodated), requires little external energy input and only minutes for the reaction to occur. Eliminating the use of an autoclave provided an opportunity to make many samples in a short period of time, since long heating and cooling times required in the autoclave and extensive preparation and cleaning of the autoclave were not necessary.

A large number of experiments provide insight into the process and an opportunity for an unprecedented systematic study. This work is focused on changing reactant types and concentrations to further study the reaction mechanism as well as to determine the process capabilities, including responses such as phase development, crystallite and particle size, and surface characteristics as it relates to these variables.

One difficulty in interpreting data for a process that is not already well defined and well studied is that process variation may be large enough to convolute the effects of changing process variables, making the interpretation of the data difficult without reproducing the experiments, possibly several times. Statistical process control can be used to understand the process variation and help eliminate some of the causes. One approach to this, as is often performed in manufacturing environments, is by repetition and monitoring of the process using various statistical tools.

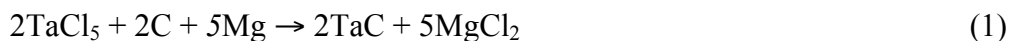
Research and development often does not provide the ability of reproducing many experiments many times, but there are statistical tools that can still be used to assist in the analysis of variation for better understanding of a process. Two mathematical approaches are used in this study to deconvolute the effects of variation in the solvothermal synthesis process in order to get a qualitative understanding of this process as it relates to the processing variables and variable interactions. Both experimental approaches use a factorial design. One approach is to perform experiments for a  $4 \times 4 \times 3$  full factorial design without replication, followed by an analysis that uses data smoothing algorithms to achieve response surfaces for a qualitatively understanding of the process. It is necessary to assume that the extent of smoothing is within processing variation. The

second approach is to perform experiments for a 2×2×2 factorial design with replication, followed by the mathematical analysis of variance (ANOVA) to separate the variation caused by processing variables, interactions between those variables, and random error to provide statistically significant verification of the qualitative interpretation of the data.

## B. Experimental Procedures

### 1. Experimental Methodologies

The stoichiometric reactions used in this study for TaC formation is given by Equations 1-3:



Factorial design principles are utilized for design of the experiments. The description of factorial designs is beyond the scope of this work and the reader is directed to consult a textbook on the topic for further information.<sup>[23]</sup> Synthesis was performed for a 4×4×3 factorial design matrix, without replication, where the three factors (variables) studied were carbon stoichiometry, reductant stoichiometry, and reductant type, respectively. These three factors correspond to differences in carbon concentration in the solvent, reactant dilution or solvent concentration, and reaction temperature for the solvothermal synthesis process.

Carbon stoichiometry and reductant stoichiometry factors were both varied over four levels (1×, 2×, 3×, and 4× reaction stoichiometry). The three reductants varied over 3 levels (magnesium, lithium, and calcium). The permutation of all of the three factor's levels, without replication, results in a total of 48 experiments. Samples containing 2× carbon and 2× reductant stoichiometries, 2× carbon and 4× reductant stoichiometries, 4× carbon and 2× reductant stoichiometries, and 4× carbon and 4× reductant stoichiometries were replicated for lithium and calcium reductants to generate a 2×2×2 factorial design with replication for statistical analyses (2× and 4× levels of the carbon stoichiometry factor, 2× and 4× levels of the reductant stoichiometry factor, and lithium and calcium levels for the reductant type factor). A permutation of this factorial design matrix, with 2

replications per experiment, results in a total of 16 experiments, 8 of which were already performed for the 4×4×3 design matrix.

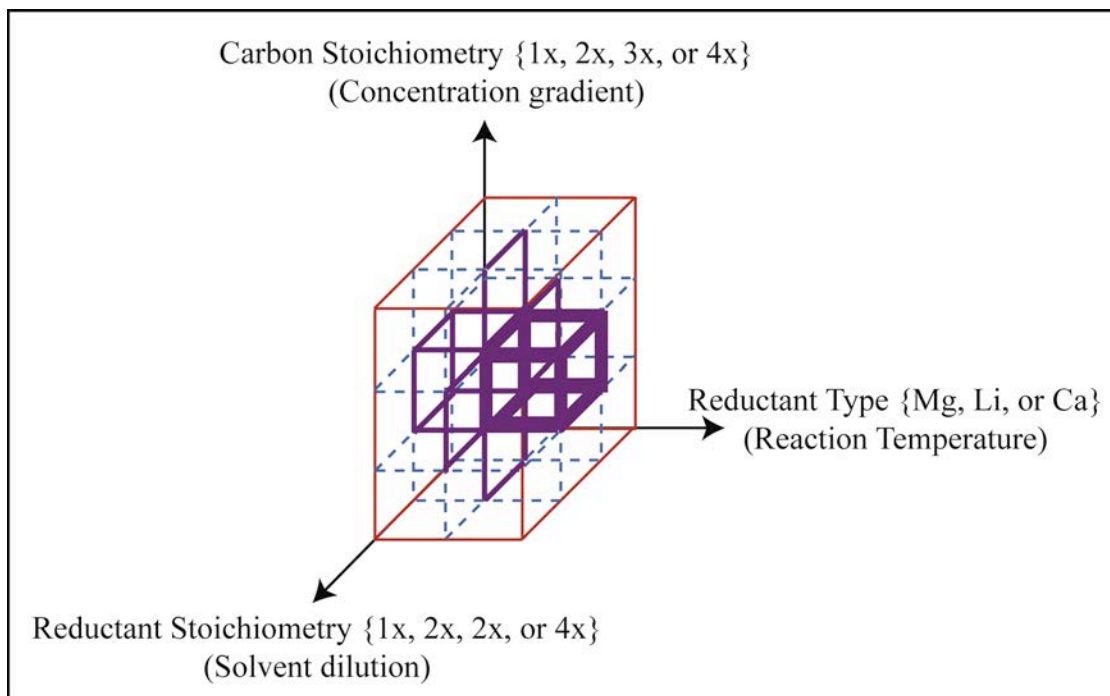


Figure 4 - 1. Experimental design space for the 48 experiments of the 4×4×3 full factorial design. The experiments are represented by intersecting lines. Red lines contain all experimental space, blue dotted lines are drawn for the interior of the outer surfaces of the design space, purple lines are drawn for space extending into the interior of the design space. (With color)

All batch calculations were done to produce a theoretical yield of three grams of TaC and mixing was performed in an argon atmosphere. In all cases 5.57 grams of TaCl<sub>5</sub> (99.8%, Alfa Aesar, Ward Hill, MA) and either 0.19, 0.37, 0.56, or 0.75 grams of carbon (Lampblack 101, Degussa, Parsippany, NJ), depending on stoichiometry, were hand mixed using a mortar and pestle to achieve homogeneity and then added to a 95 ml fused-silica test tube. Finally, the magnesium (reagent grade, Sigma-Aldrich, St. Louis) was added in amounts of 0.94, 1.89, 2.03, or 3.78 grams, the lithium (granular, 99%, Sigma-Aldrich, St. Louis, MO) was added in amounts of 0.54, 1.08, 1.62, or 2.16 grams, or the calcium (granular, 99%, Fisher Scientific, Pittsburgh, PA) was added in amounts of 1.56, 3.12, 4.67, or 6.23 g, depending on the permutation of reductant type, reductant stoichiometry, and carbon stoichiometry, to the test tube.

After mixing, the test tubes were removed from the argon atmosphere to be ignited underneath a chemical fume hood. The test tubes were rotated to mix in the reductant with the other reactants, which were not mixed previously because of the granular size that was used to limit reactivity. Prior to ignition, the test-tube stopper was loosened to allow for outgassing. The test tube was lowered into the center of a tube furnace that was held at 548 K when using lithium as the reductant and at 873 K when either magnesium or calcium were used as the reductant. Once the samples were ignited they were taken out of the furnace immediately and allowed to air quench.

After reaching room temperature, the reaction products were removed from the test tube by adding water, thus forming  $\text{Mg(OH)}_2$ ,  $\text{LiOH}$ , or  $\text{Ca(OH)}_2$  to free the reaction products, and emptied into a 250 ml beaker. Additional water was added to create a 100 ml suspension, which was magnetically stirred for 30 min, followed by ultrasonication for 30 min. All ultrasonication for this work was performed using an ultrasonic cleaner with the perforated tray accessory (Model FS30, Fisher Scientific, Pittsburgh, PA 15275). The ultrasonic cleaner was filled with water until the water level was even with level of suspension in the 250 ml beaker. An additional 15 min of magnetic stirring was performed after ultrasonication. The suspension was centrifuged at  $15,500 \times g$  for five minutes and decanted to prepare for the powder washing procedure.

$\text{Mg(OH)}_2$  and  $\text{Ca(OH)}_2$  have poor solubility in water so it is not removed from the powders when freeing the reaction products or with subsequent water washing. These samples were washed in a 100 ml suspension of concentrated  $\text{HNO}_3$  (15.8 N) for 30 min, followed by ultrasonication for 30 min, and an additional 15 min of magnetic stirring. The  $\text{HNO}_3$  reacts with the  $\text{Mg(OH)}_2$  or  $\text{Ca(OH)}_2$  to form  $\text{Mn(NO}_3)_2$  or  $\text{Ca(NO}_3)_2$ , which are more soluble. The samples were then centrifuged for five minutes at  $15,500 g$ , followed by decanting.

Two water rinses were performed by filling the centrifuge tubes with water, hand shaking for one minute, followed by five minutes of ultrasonication before centrifuging and decanting again. A final ethanol rinse was performed in a similar manner as the water rinses. After the final decant, the samples were allowed to dry in air for 24 hr before mixing with a mortar and pestle and stored for characterization. For consistency, the samples containing lithium as the reductant were washed in a similar manner.

The washing procedure eliminates the excess reductant, but does not remove excess carbon. Removing excess carbon was not considered in this study because excess carbon can assist in achieving full density during sintering by removing oxide impurities and assist in obtaining smaller grain sizes.<sup>[24-28]</sup> If it is determined that removal of some (if there is too much), or all, of the carbon would be beneficial, there are techniques available to do so.<sup>[29]</sup>

Powder X-ray diffraction (XRD) was performed on a diffractometer (Siemens D5000, Siemens, New York, NY 10022) by scanning from 20 to 80° 2θ using a step size of 0.04° 2θ and a dwell time of 15 sec after dispersing the powders on a zero-background holder. X-ray diffraction software (Jade 8, Materials Data Incorporated, Livermore, CA) was used to determine phase purity, the compound stoichiometry, and the crystallite size of the samples. The TaC lattice parameters were determined using *hkl* grating and least-squares refinement for purposes of calculating the compound stoichiometry, TaC<sub>x</sub>, where *x* varies with the lattice parameter “a” according to the relationship: C/Ta = 6.39795•a – 27.5157.<sup>[30]</sup> The crystallite sizes were determined using the Williamson-Hall technique.<sup>[31]</sup>

Since the X-ray diffraction measurements depend on accurate 2θ peak positions and full width at half maximum (FWHM) measurements of the peaks, sample displacement corrections were made using the software to reduce error in measuring peak positions and whole profile fitting was used to reduce error in the FWHM values. The software uses the error associated with these measurements to compute the error of the calculated crystallite size. The average computed error for the crystallite size calculations was approximately nine percent. However, measurement variation does not account for process variation and error associated with process variation could be the cause of greater error.

Specific surface area (SSA) measurements were performed using a surface area analyzer (Tristar 3000, Micromeritics, Norcross, GA) after degassing in argon for 24 hours at 423 K. Density measurements were performed by helium pycnometry (AccuPyc II 1340, Micromeritics, Norcross, GA) after drying in an oven at approximately 353 K for one hour. The crystallite size is computed from the SSA and density measurements to compare to the crystallite size calculated from the X-ray diffraction data.

Thermogravimetric analysis (TGA) was performed in air (Model Q50, TA Instruments, New Castle, DE). The samples were heated from room temperature to 1273 K using a heating rate of five Kelvin per minute to focus on surface adsorption.

Dynamic light scattering (DLS) was performed (Nanotracer™ ULTRA, Microtrac, Montgomeryville, PA) after dispersing 0.02 grams of powder in 30 ml of deionized water and allowing the suspension to magnetically stir for 24 hours, followed by five minutes of ultrasonication prior to measurement. The DLS measurements were repeated four times with an additional 30 sec ultrasonication between each measurement. Each run consisted of an average of five 30-sec runs as is recommended by the manufacturer of the instrument and ASTM standard E2490-09.<sup>[32]</sup>

## **2. Data Analysis**

The data generated from the 4×4×3 experimental design matrix was analyzed using software (Grapher 6, Golden Software, Golden, CO). The data was separated into two-factor response surfaces of varying carbon stoichiometry and reductant stoichiometry, with reductant type constant, to generate data contour maps. An advantage to this approach is that a large amount of data is processed, which establishes a way to visually observe trends in the data by evaluating the individual contour plots and making comparisons between the contour plots that were generated for the different reductants. Since replication was not used for the 4×4×3 experimental design matrix, process variation may convolute the trends if variation is significant and would make it difficult to analyze the trends without data smoothing.

A data smoothing algorithm, using a smoothing factor of one, was used to create the two-factor response surfaces assuming that the degree of smoothing is within the range of process variation. A contour map data smoothing algorithm uses the actual data to generate a surface, in a similar manner as fitting a curved line to a one-variable response, and then arbitrarily fits the surface with contours of constant response values for the surface despite the fact that each plot was made using 16 data points. In making this assumption, caution must be exercised in the interpretation of the results.

The purpose of the contour plots generated by data smoothing is to observe trends visually and to compare and contrast them rather than to give the absolute values for the

data within the plots. However, the plots will also contain actual data measurements superimposed on the contoured surface. The emphasis of this work is on obtaining a qualitative understanding of the process, rather than quantitative, to gain a more fundamental understanding of the process, which may not be readily apparent without removing process variation. The data smoothing approach can limit the number of experiments that are necessary. For example, assuming average of five replications are necessary for removing the effects of process variation, the number of experiments increases from 48 to 230 to generate these contour plots for a full factorial design.

To minimize resource requirements, it is easy to see the advantage, if not necessity, of the data smoothing for observing the qualitative trends. An experiment to study variation of one or some of the samples would be more beneficial for studying variation/reproducibility than repeating all of the experiments in this work. The approach used to strengthen the argument for the assumptions of data smoothing in this work is done by using analysis of variance (ANOVA).

In conjunction with observing trends using data smoothing algorithms, the  $2 \times 2 \times 2$  factorial design matrix was used to statistically verify a null hypothesis or an alternate hypothesis related to these trends by using ANOVA. A disadvantage of this technique is the difficulty in producing a large number of data points for generating a visual representation of the trends, because of the necessity of experiment replication to perform ANOVA. However, the advantage of this technique is that it takes process variation into account to determine the significance of a factor and so the two methods, data smoothing (outlined earlier) and ANOVA, complement each other well for establishing and visualizing trends in the process response variables.

ANOVA provides an F-statistic for each factor and the interactions amongst the factors. In critical F-statistics, a Type I error occurs if the null hypothesis is rejected when in fact it is true and a level of significance, or probability of making a Type I error, that correlates to a critical F-statistic is typically chosen prior to interpretation of the data by the amount of risk that can be tolerated for such an error.

In this work, the computed F-statistics are compared to the critical F-statistic for levels of significance of 1%, 5%, and 10%. A table of critical F-statistics can be found in textbooks on the subject.<sup>[23]</sup> If the F-statistic is less than the critical-statistic for a 10%

level of significance, then the null hypothesis is accepted due to insufficient statistical evidence, while the alternate hypothesis is rejected. In this case, a visually observed trend may not be real and could be due to normal process variation. The 10% level of significance, or probability of making a Type I error, is selected based on the low risk of assessing the data and the expected noise level of the crystallite size analysis. If the F-statistic is greater than the critical F-statistic for a 10% level of significance, but less than the critical F-statistic for a 1% level of significance, then the null hypothesis is rejected, indicating a significant factor or interaction, and a visually observed trend is considered significant. Furthermore, the probability of making a Type I error is estimated as a method to indicate the strength of a trend by extrapolating a level of significance from the F-statistic using a scatter plot with curved lines for the three critical F-statistics versus the three levels of significance. The null hypothesis is rejected and the visually observed trend that is observed is considered very strong if the F-statistic is greater than the critical F-statistic for a 1% level of significance.

The results of ANOVA will be provided in a table to compare to the results from data smoothing. Analyses by data smoothing and ANOVA have limitations, but observing the same results from the two separate analyses strengthen the confidence in making an assessment. If the two analyses disagree, then the assessment is more questionable would benefit from a more detailed study.

## **C. Results and Discussion**

### **1. Phase Development**

Figure 4-2 illustrates powder X-ray diffraction (XRD) patterns for several of the samples, demonstrating the effects of reductant type (Figure 4-2a), carbon stoichiometry (Figure 4-2b), and reductant stoichiometry (Figure 4-2c), through changes in peak intensities. For Figure 4-2a, demonstrating the effects of reductant type with reductant and carbon stoichiometries held constant, calcium is more effective than lithium, which is more effective than magnesium at converting the reactants to TaC as is observed by the increase in the intensity of the TaC peaks relative to the other phases' peaks for the three patterns.

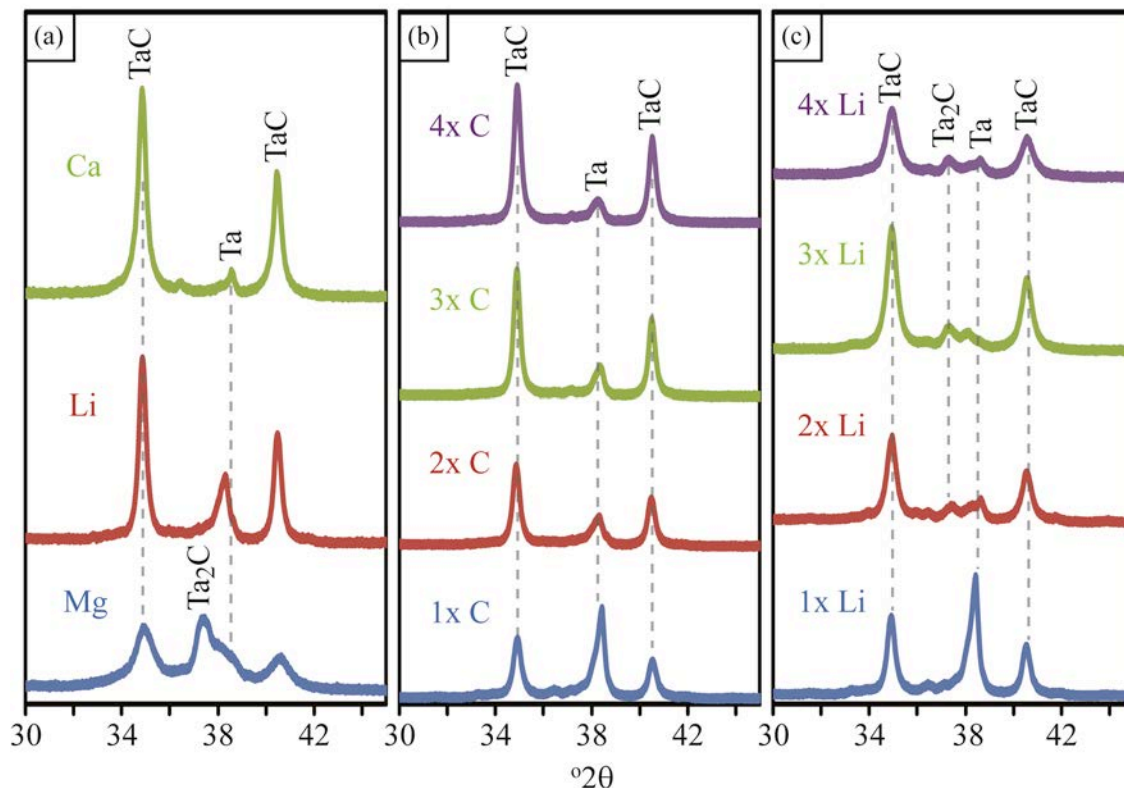


Figure 4 - 2. Powder X-ray diffraction patterns demonstrating the effects of (a) reductant type, (b) carbon stoichiometry, and (c) reductant stoichiometry on TaC phase development for solvothermal synthesis. (With color)

The TaC reaction proceeds from its elements within the molten metal reductant, with carbon diffusing into nascent tantalum particles.<sup>[22]</sup> The TaC reaction proceeding from tantalum and carbon is highly exothermic, having an adiabatic flame temperature of 2700 K.<sup>[33]</sup> Since the adiabatic flame temperature is greater than the vaporization temperature of the metal reductants (1363 K, 1615 K, and 1757 K for magnesium, lithium, and calcium, respectively), it will drive the temperature up to, but not exceeding the vaporization temperature of the molten metal. Any additional energy from the reaction would be consumed producing vapor. Therefore, the samples containing the metal with the highest vaporization temperature are expected to achieve the highest reaction temperature. The extent of phase conversion to TaC in Figure 4-2a correlates well with the vaporization temperature of the reductant and indicates a temperature driven diffusion mechanism. Specifically, the diffusion of carbon into the nascent

tantalum seeds is promoted by increasing the reaction temperature and provides greater phase purity.

In the case of magnesium, the diffusive process of carbon into the tantalum was slow enough such that insufficient carbon was incorporated into the tantalum resulting in the stabilization of the Ta<sub>2</sub>C phase in conjunction with TaC. The reaction temperature for lithium and calcium reductants was higher and enough carbon could diffuse into the metal to prevent the formation of the Ta<sub>2</sub>C phase. The reaction temperature for calcium is higher than for lithium and therefore conversion to TaC is more complete. For determining the effects of reductant and carbon stoichiometries in Figures 4-2b and 4-2c, lithium was selected as the reductant type because it was determined to be most suitable from a processing standpoint.

The increase in intensity of the TaC peaks relative to the other phases in Figure 4-2b indicate that TaC conversion was enhanced by increasing the carbon stoichiometry while holding the reductant type and stoichiometry constant. Since diffusion of carbon into the metal particles is an expected reaction mechanism, the improved phase conversion with increased carbon stoichiometry indicates a chemical gradient-driven diffusion mechanism in accordance with diffusion theory.

Figure 4-2c indicates that increasing the reductant stoichiometry enhanced TaC conversion as well, but also with similar limitations as was the case with carbon stoichiometry in Figure 3-1b. The initial increase as a result of increasing reductant stoichiometry is believed to be due to the ability of the molten metal reductant to fully encapsulate the reactants and/or provide more “fuel” for the reaction as the reductant is oxidized. The lack of a more substantial increase with further additions of reductant could be related to the dilution of carbon in the molten reductant resulting in a decrease in the chemical gradient. If this is true, then the combination of carbon and reductant stoichiometries have the potential to fully convert the reactants into TaC by providing a fully encapsulating melt with a sufficiently high carbon chemical gradient across the tantalum particle and sufficient fuel for the diffusive processes to occur in the short time period of the reaction.

Specific combinations of reductant type, reductant stoichiometry, and carbon stoichiometry are capable of yielding phase-pure TaC within the limits of detection for

XRD. Figure 4-3 classifies the phases of interest for each condition in the 4×4×3 experimental design matrix that was used.

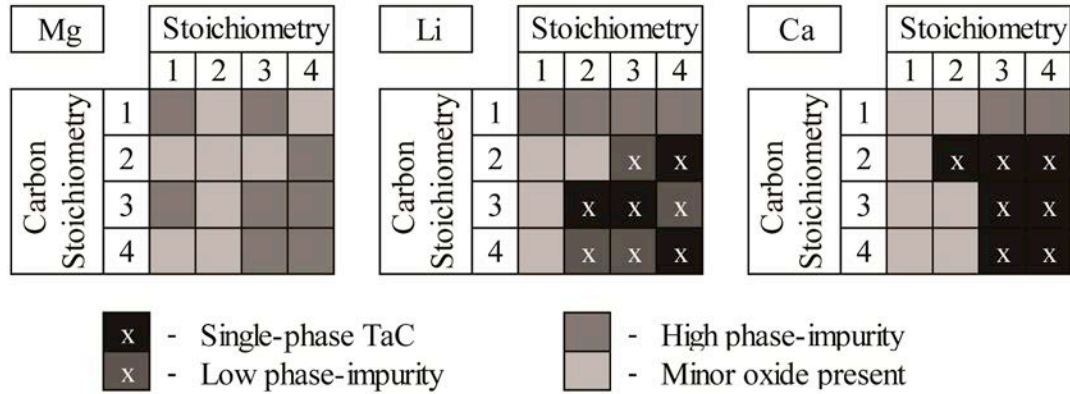


Figure 4 - 3. Qualitative phase analysis according to the reductant type, carbon stoichiometry, and reductant stoichiometry.

The classification scheme has four categories. Oxide phases are unfavorable for eventual sintering of the powders, so if a noticeable peak for oxide phases is observed, regardless of the other phases present, then the sample is placed in a category denoted “Minor oxide present” in the figure. The oxide phases were present as minor phases for all experimental conditions containing them. Oxide phases were found when synthesizing with low reductant stoichiometries, indicating that the reductant is a critical component, possibly acting as an oxygen-getter (reacting with oxygen so that it cannot react with the other components) or as an oxygen diffusion barrier.

The second category in Figure 4-3 is for samples that contained no detectable oxide phases, but significantly high amounts of impurity phases, either tantalum, Ta<sub>2</sub>C, or a combination of the two. This category is labeled “High phase-impurity” in the figure. This typically occurs at low carbon stoichiometry, when the chemical gradient is not sufficient enough for diffusion to complete phase development, but also occurs in high carbon and reductant stoichiometries for the case of magnesium reductant because the temperature is not sufficient enough for diffusion to complete phase development.

The third category includes samples with low amounts of impurity phases, such as tantalum metal and Ta<sub>2</sub>C that are barely detectable in the X-ray diffraction patterns, and

is labeled “Low phase-impurity”. This category was only significant when lithium was used as a reductant and only for four samples. TaC compound stoichiometry,  $x$  in  $\text{TaC}_x$ , can vary from an  $x$  value of 0.99 down to an  $x$  value of approximately 0.75.<sup>[23]</sup> Due to the ability of TaC to exhibit high carbon vacancies while maintaining stability, there is a chance that dense compacts produced from powders with small amounts of impurity phases may homogenize after heat treatments or during sintering, forming phase-pure TaC compacts, thus expanding the range of compound stoichiometries that can be obtained.

The fourth category is for samples that resulted in phase-pure TaC, of which there were eleven in the cases when lithium or calcium was used as the reductant. This occurs for high carbon and high reductant stoichiometries and agrees with the previous assessment that the combination of these two factors to create a fully encapsulating melt, sufficiently high carbon chemical gradient, and sufficient fuel for the diffusive processes to occur are sufficient for obtaining full conversion to TaC. Further analysis of the system using magnesium as the reductant was not undertaken because all the samples fell into categories with significant amounts of impurity phases.

Another notable observation from Figure 4-3 is that there are a few inconsistencies in that there are isolated blocks of one category that would not be expected according to the surrounding blocks, which belong to another category. What this suggests is that there is some level of process variation that is not properly controlled, but is beyond the scope of this work.

Since the TaC phase can incorporate a high concentration of carbon vacancies, it is important to characterize the compound stoichiometry,  $\text{TaC}_x$ . Figure 4-4 illustrates the TaC compound stoichiometry as determined from the lattice parameters. In general, it appears that the carbon stoichiometry is an important variable. As the reaction occurs, the carbon stoichiometry will influence the chemical gradient-induced diffusion.

A higher carbon stoichiometry will increase the chemical gradient and therefore increase the flux of carbon into the compound and a subsequent increase in carbon stoichiometry is observed. When calcium is used as the reductant, the compound stoichiometry is enhanced compared to the case when lithium is used as a reductant indicating that the reductant is also important. The reductant should control the reaction

temperature. An increase in reaction temperature when using calcium versus lithium will enhance temperature-induced diffusion resulting in an increase in the compound stoichiometry.

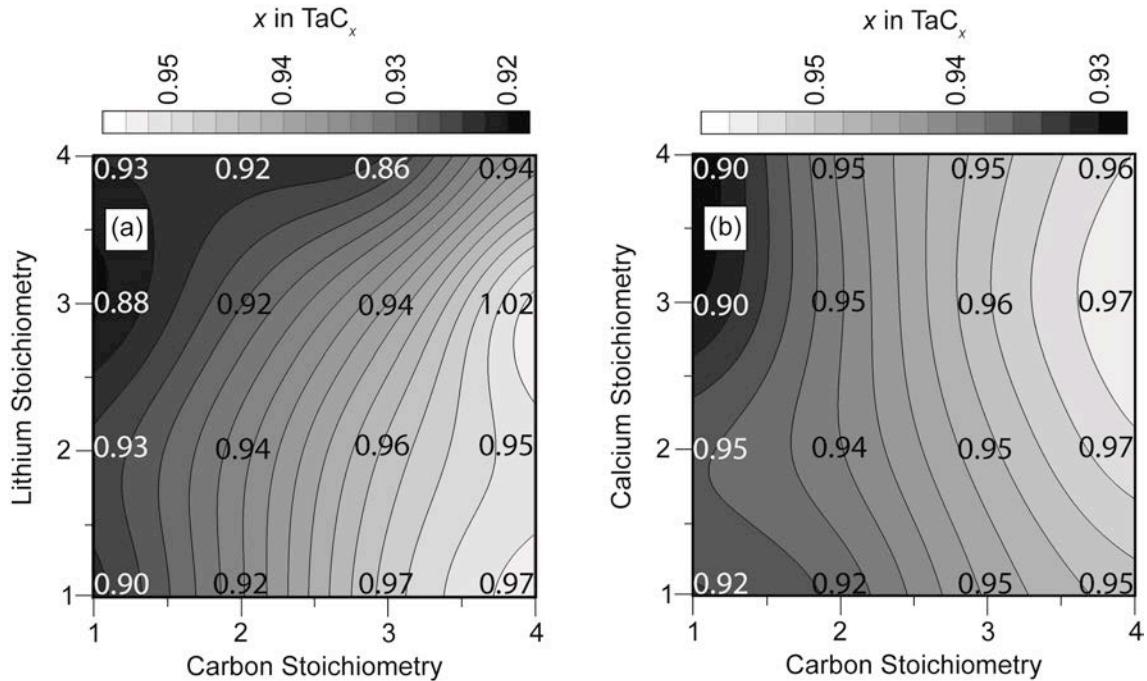


Figure 4 - 4. Compound stoichiometry of TaC, C/Ta, according to reductant type (a) lithium and (b) calcium, carbon stoichiometry, and reductant stoichiometry. Actual data is superimposed onto the plot.

Figure 4-4 suggests that a ternary interaction amongst reductant type and carbon and reductant stoichiometries may be defined as such: in the case of the system using lithium as the reductant, increasing carbon stoichiometry is more effective at increasing the compound stoichiometry for low reductant stoichiometries whereas for the system using calcium as the reductant, the effect of reductant stoichiometry is less apparent and perhaps non-existent. Increasing reductant acts as a diluent and decreases the chemical gradient of carbon, resulting in a decrease in the flux of carbon into tantalum. The decrease in chemical gradient as the reductant stoichiometry is increased is the same for both the lithium and calcium reductant systems. However, the temperature in the calcium system is higher resulting in an increase in temperature-induced diffusion and therefore the flux of carbon into tantalum, at least partially negating the effects due to the change in chemical gradient and making the effect less pronounced. The chemical gradient and

temperature are both important and are dictated by the combination of reductant type, reductant stoichiometry, and carbon stoichiometry.

## 2. Crystallite and Particle Size

Figure 4-5 gives the crystallite sizes as a function of carbon and reductant stoichiometries for the cases of lithium and calcium reductants. The crystallite sizes ranged from 17 to 38 nm for the samples containing lithium as the reductant and from 43 to 105 nm for the samples containing calcium as the reductant. Although the average calculated error in crystallite size using the software was computed to be ~9%, it is difficult to suggest what the processing error might be or the error after the data smoothing algorithm is used to reduce variation for the purposes of observing trends.

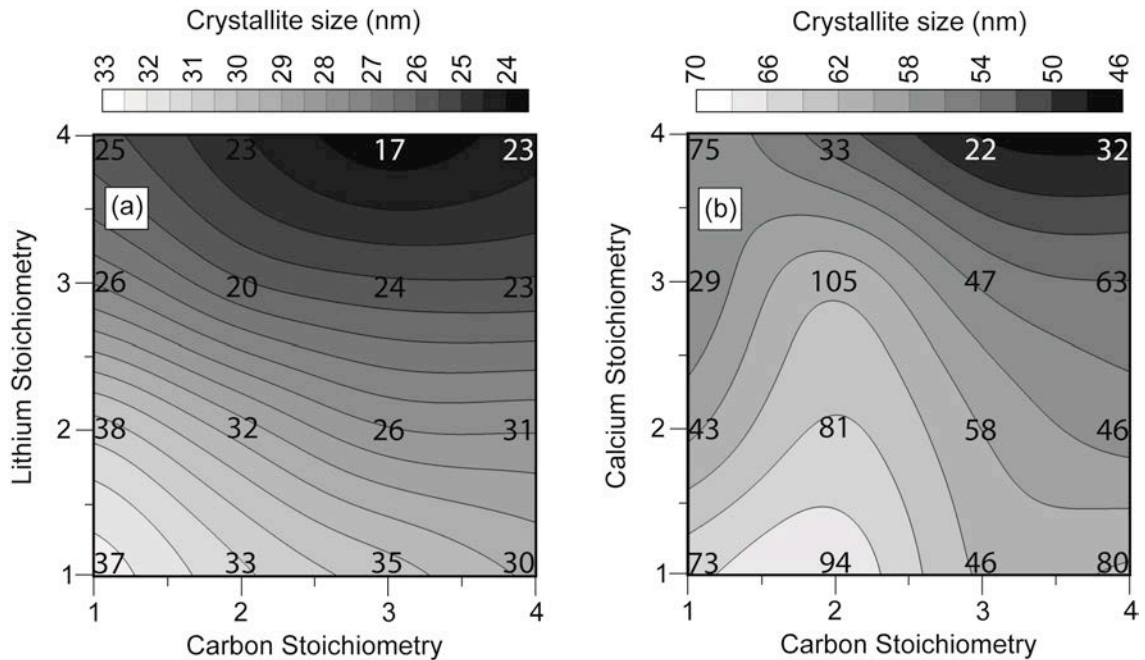


Figure 4 - 5. Crystallite sizes of TaC determined by XRD, according to reductant type (a) lithium and (b) calcium, carbon stoichiometry, and reductant stoichiometry. Actual data is superimposed onto the plot.

The change in the crystallite size due to changes in the carbon stoichiometry appears to be minimal. In general, high reductant stoichiometry favors smaller crystallite sizes for a given system. The molten metal reductant acts as a diluent for the system, which will control the concentration of reactants within the melt and therefore influence nucleation and growth of the nascent tantalum particles eventually forming TaC. The

reductant type also appears to be significant. Larger crystallite sizes are achieved when using calcium as the reductant compared to using lithium because the higher reaction temperature will also influence nucleation and crystallite growth of the nascent tantalum particles.

Figure 4-5 also indicates a ternary interaction: in the case of lithium reductant, there is roughly the same change in crystallite size with an increase in reductant stoichiometry for all of the carbon stoichiometries, whereas in the case of calcium reductant, reducing crystallite size is less effective at low carbon stoichiometries than at high carbon stoichiometries with respect to the calcium stoichiometry. This is difficult to explain and therefore discussion on the matter will be deferred until the ANOVA statistical analysis sub-section, which will help determine if this is a statistically significant factor or an erroneous result of data smoothing.

The general trends from data smoothing for specific surface area (SSA) are given in Figure 4-6. The SSA is related to the crystallite size and therefore should demonstrate similar dependencies. It is clear from Figure 4-6 that carbon stoichiometry has little influence, reductant stoichiometry and reductant type does, and that there might be a ternary interaction. This agrees well with the assessment of the dependence of SSA on crystallite size. SSA should increase with decreasing crystallite size and we see this opposite trend by comparing Figure 4-5 and Figure 4-6.

The trends are less apparent in the case of using calcium as the reductant. However, the range of SSA for the samples containing calcium is much smaller than the range for the samples containing lithium and the breakdown of the trend for the calcium samples might be related to normal process and measurement variation resulting from the small range of SSA values. This leads to the suggestion that there is an additional interaction between reductant stoichiometry and reductant type that was not present in the crystallite size analysis, where the reductant stoichiometry is more effective at increasing the SSA when lithium is used as a reductant compared to when calcium is used as a reductant. This interaction may also be related to the crystallite sizes. Although the range of crystallite sizes was narrower for samples prepared with lithium compared to the samples prepared with calcium, surface area is proportional to the square of the radius (assuming spherical morphology) and normalizing to weight results in larger changes in

the surface area as a result of a change in crystallite size when the crystallites are small relative to a similar change in crystallite size when the crystallites are larger. Scanning electron imaging, performed previously, indicate equiaxed grains and support the assumption, although some error may still be introduced due to faceting or deviation from sphere morphology.<sup>22</sup>

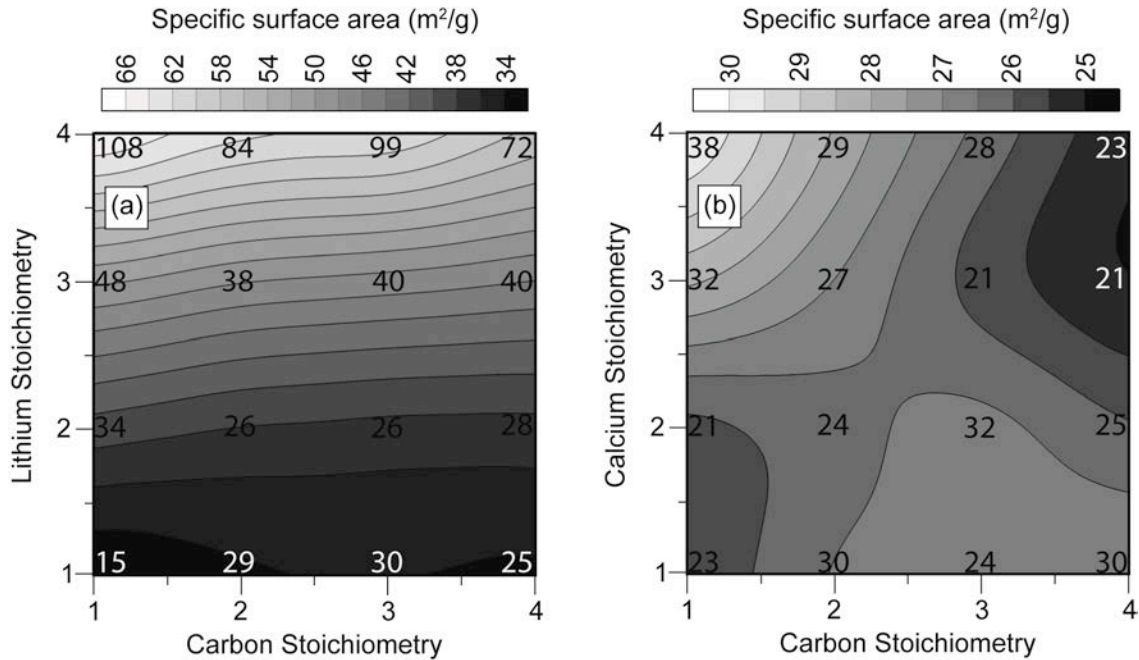


Figure 4 - 6. Specific surface area of TaC, according to reductant type (a) lithium and (b) calcium, carbon stoichiometry, and reductant stoichiometry. Actual data is superimposed onto the plot.

The crystallite sizes of the samples were calculated using the SSA in conjunction with density measurements, assuming spherical morphology, to compare to the crystallite sizes obtained by X-ray diffraction. The results of this comparison are given in Figure 4-7. Although the coefficient of correlation is low for this data ( $\sim 0.36$ ), the variation around the sample line having a perfect coefficient of correlation (included in the diagram) appears to be consistent and suggests that the measured and calculated crystallite sizes are in agreement over the size range shown.

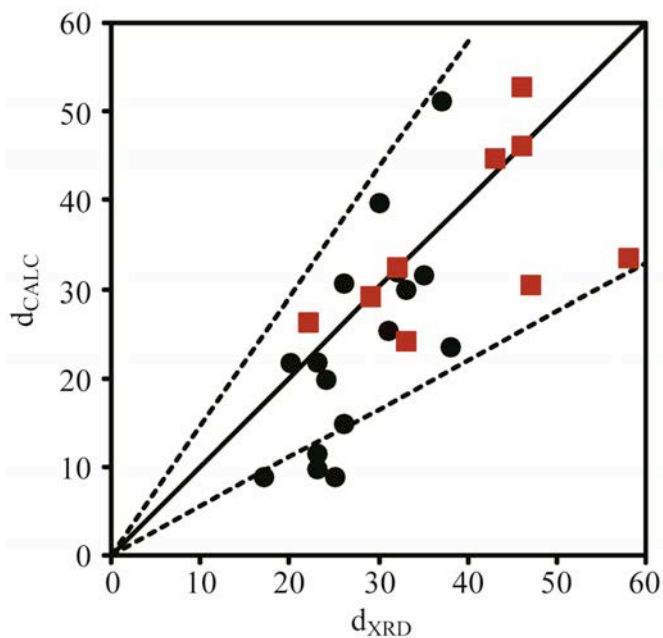


Figure 4 - 7. Comparison of the average crystallite sizes of TaC measured by powder X-ray diffraction ( $d_{XRD}$ ) versus calculation from specific surface area and density measurements ( $d_{CALC}$ ) assuming a spherical morphology. Black circles are lithium data, red squares are calcium data, perfect correlation is given as a solid line and 45% deviation from perfect correlation is given as dotted lines. (With color)

The effects of process and measurement variation could be reduced by repeating the synthesis and characterization of these samples multiple times and using process control principles, but this is beyond the scope of this work. The spread about the line of a perfect coefficient of correlation indicates the amount of error associated with the crystallite size analyses, representing compounded error from both measurement and process variation. In Figure 4-7, 84% of the data is within 45% from a perfect correlation and all of the data is within 65%. The compounded error is relatively high and indicates there are uncontrolled variables that need to be established. The data smoothing and analysis of variance performed in this work reduces noise from this variation to simplify interpretation.

The average particle sizes, measured by DLS, are reported in Figure 4-8. There appears to be an interaction between the reductant stoichiometry and the reductant type. In the case of lithium, the particle size increases with lithium stoichiometry, whereas for calcium, the particle size decreases with calcium stoichiometry. No other trends are

observable from the particle size information. This difference between the two reductant systems is related to powder agglomeration. In the case of lithium, the increase in particle size could be caused by the decrease in crystallite size, as was observed in Figure 4-5. Smaller crystallites will have a higher tendency to agglomerate due to the higher surface area. In the case of calcium, the crystallite sizes are greater than any of the samples prepared with lithium and therefore would have a lower tendency for agglomeration, but this does not explain the opposite trend that is observed for lithium and the relationship to crystallite size.

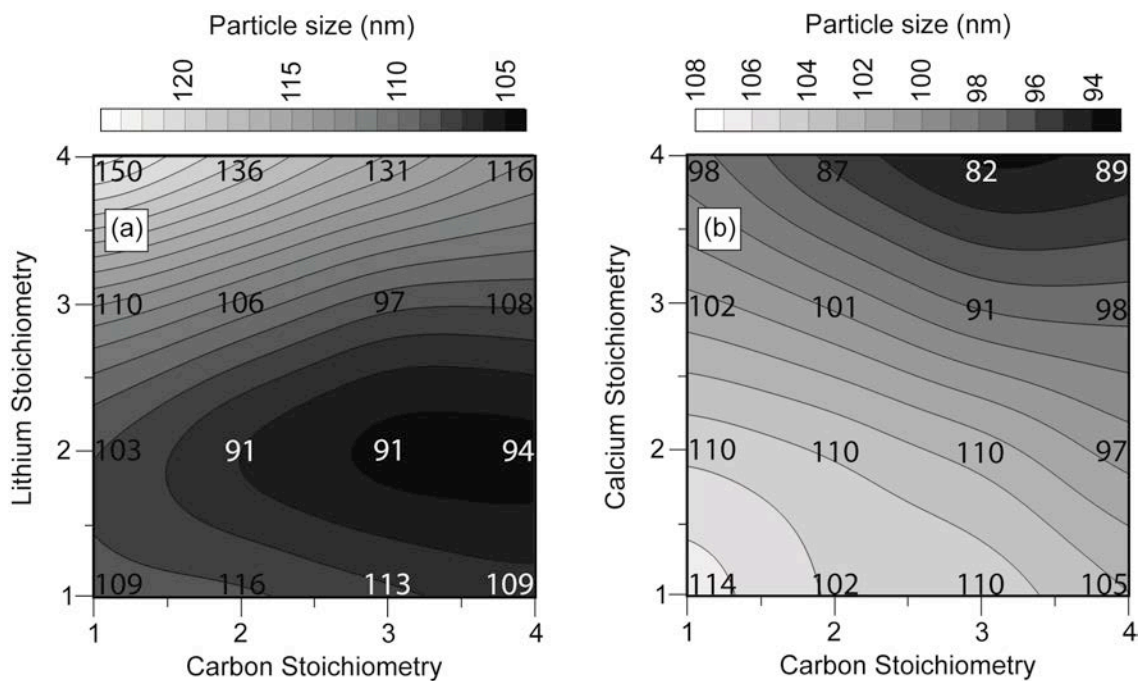


Figure 4 - 8. Average particle size of TaC according to reductant type (a) lithium and (b) calcium, carbon stoichiometry, and reductant stoichiometry. Actual data is superimposed onto the plot.

Although fewer crystallites are participating in agglomeration, it only takes a small amount of agglomeration to achieve the particle sizes that were observed for powders prepared by using calcium because the crystallite size is starting to approach the agglomerate size. This can be evaluated using a figure of merit relating the average particle size to the average crystallite size by a ratio where a value of unity represents complete dispersion and the further from unity, the more agglomerated the system is since more crystallites will make up each individual particle, on average. This figure of

merit for the synthesized powders is provided in Figure 4-9. Despite the contradictory trend observed for the average particle size information, the figure of merit follows a similar qualitative trend for both lithium and calcium reductants, indicating that the trend reversal in Figure 3-7 is likely caused by the crystallite size approaching the particle size, for which there is a lesser tendency for agglomeration.

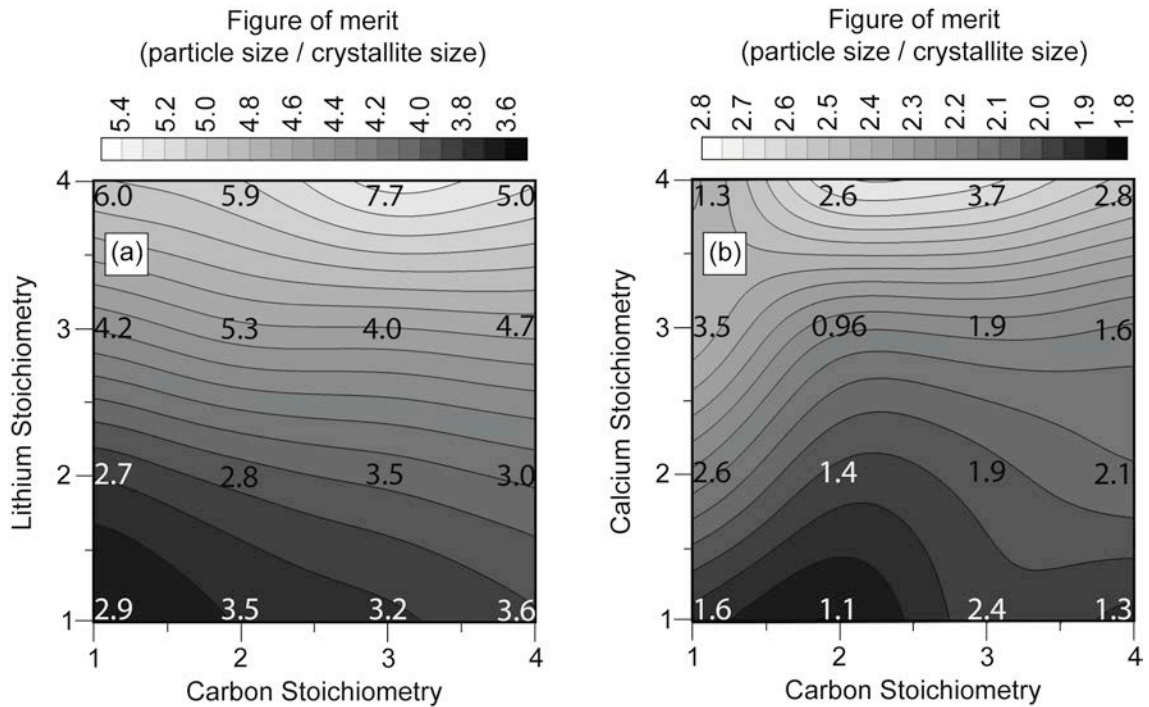


Figure 4 - 9. Figure of merit of TaC powders according to reductant type (a) lithium and (b) calcium, carbon stoichiometry, and reductant stoichiometry. Actual data is superimposed onto the plot.

The level of agglomeration, which is indicated by the figure of merit, should be related to the SSA in Figure 4-6 and we should expect to see similar variable dependencies. From this assessment, the reductant stoichiometry, reductant type, an interaction between these two variables, and an interaction between all three variables should be significant. Comparing Figure 3-5 and Figure 3-8 agrees well with this assessment. Since the SSA is indirectly related to the crystallite size, we should also expect to see opposite trends between Figure 3-4 and Figure 3-8, which is also in agreement. By considering both of these comparisons, it is evident that the agglomeration is more directly related to SSA than the crystallite size since the figure of

merit and SSA plots followed similar trends and both indicate an additional binary interaction that is not apparent in the crystallite size data. A figure of merit is a more efficient way to evaluate agglomeration than by considering particle size alone, which was not directly comparable to the crystallite size and SSA analyses.

### **3. Surface Characteristics**

During a typical TGA measurement, the samples would lose weight from room temperature to approximately 673 K, where a large weight gain occurs due to oxidation of the TaC. The initial weight loss is of interest because it indicates the amount of physisorbed molecules onto the surfaces of the particles. These weight losses that were observed from TGA, after data smoothing, are given in Figure 4-10. By comparing the reductant types, the weight loss range for the calcium samples is less than for the lithium samples demonstrating that the reductant type is important. All other influences/interactions are difficult to distinguish from the data.

The lithium samples have smaller crystallite sizes than the calcium samples, resulting in an increase in the available surfaces for physisorption, which is supported by the SSA results. The extent of physisorption is expected to correspond well with SSA measurements. The trends between physisorption and SSA are similar for powder prepared with calcium reductant, but not for the use of lithium. If lithium is the reductant, the SSA is strongly correlated to the lithium stoichiometry and carbon stoichiometry has little influence, but the opposite is true for the amount of physisorbed material. Overall, there is little difference in the weight losses for a given reductant and may explain the difficulties analyzing this data.

There is a significant amount of impurities adsorbed on the surfaces of the particles, ranging from about 1.2-6.4% on a weight basis. Assuming a worst case scenario (highest weight loss, theoretical density of TaC, and the lowest density washing solvent is absorbed on the surfaces), the volume percentage of surface adsorbed species is estimated to be 45%. Assuming a best case scenario (lowest weight loss, theoretical density of TaC, and highest density washing solvent on the surfaces), the volume percentage of surface adsorbed species is estimated to be 12%. There is a significant amount of surface impurities, but discussing what it is and how to remove it is beyond the scope of this work.

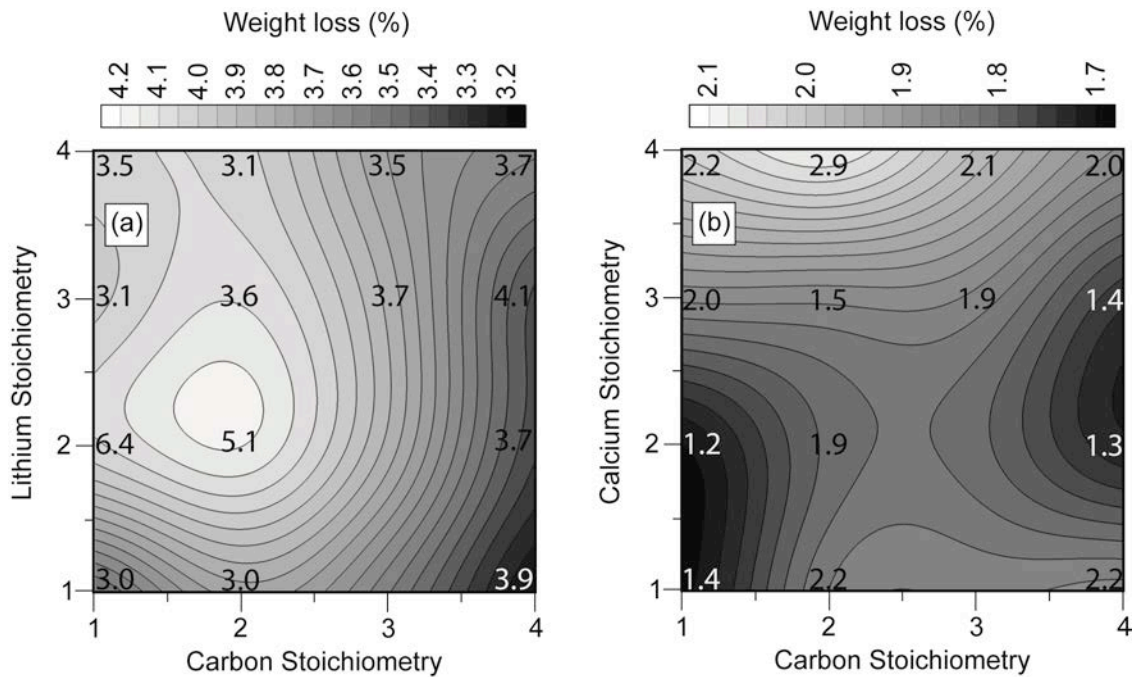


Figure 4 - 10. Percent weight loss of tantalum carbide powders up to 400°C in air according to (a) lithium and (b) calcium, carbon stoichiometry, and reductant stoichiometry. Actual data is superimposed onto the plot.

#### 4. Evaluating Trends using Analysis of Variance

So far, all data has been interpreted according to the output of data smoothing algorithms, but requires the assumption that the degree of smoothing is within process and measurement variation. Using analysis of variance (ANOVA), the variation is analyzed using repetition of experiments to distinguish between within-group and amongst-group variation. This provides a mathematical distinction of whether or not there is sufficient variation due to a change in the processing variable relative to error to justify it as a significant factor.

ANOVA requires a lower number of experiments than the previous approach, especially if the previous approach was subjected to repetition to more accurately address variation, and at the same time is a complementary technique that can provide support for the previous discussions. An additional advantage is that it considers interactions between variables, which can be difficult to properly define using the previous approach. Table 3-I contains the results of the ANOVA analyses for the several response variables

that have been discussed in previous sections and makes direct comparisons between the ANOVA results and the trends that were observed using the data smoothing algorithm.

The F-statistic values are provided in Table 4-I, which was compared to critical F-statistics. Based on this comparison, the null hypothesis was either rejected or accepted, meaning there was statistical variation in the processing variable or interactions amongst variables relative to the process and measurement variation or that there was not, respectively. All instances of previous discussion in previous sections are highlighted in the table. A comparison of the previous assessments using the contour maps and the results from ANOVA are all in good agreement, strengthening the assessments with regards to compound stoichiometry, crystallite size, SSA, and the figure of merit.

The probability that the results obtained by ANOVA are incorrect also indicate that the assessments are reasonably strong as is realized by the low probability of making a Type I error for instances when the null hypothesis was rejected. In general, trends that were not mentioned in the previous sections are considered insignificant factors and interactions. The ANOVA analysis also reinforces this assessment since the probability of making a Type I error was greater than 10% in all of the instances in the table where the comparison was not defined. Table 3-I is then in agreement with previous discussion.

To summarize, compound stoichiometry is dependent on chemical gradient-induced and temperature-induced diffusion. The crystallite size is dependent on dilution, reaction temperature, and an interaction between the three variables studied. SSA depends on crystallite size and the figure of merit associated with evaluating the level of agglomeration is related to the SSA.

An earlier discussion on the ternary interaction between carbon stoichiometry, reductant stoichiometry, and reductant type on the crystallite size analysis was deferred until post-ANOVA analysis. The general trend was that the change in crystallite size as a function of lithium stoichiometry was similar for all carbon stoichiometries, but was not the case when calcium was used as the reductant. In this case, the change in crystallite size was smaller for low carbon stoichiometries than at high carbon stoichiometries. Since the reaction temperature should not vary significantly for all experiments using calcium as the reductant, then the effect, considering only the calcium plot, simplifies the interaction to one of three possible effects.

Table 4 – I. Analysis of Variance (ANOVA) Summary Containing F-statistics, Rejection or Acceptance of the Null Hypothesis Stating No Significant Contribution for a 10% Confidence Interval, Highlighting for Comparisons to Prior Discussion, and the Estimated Probability (P) of a Type I Error

Factor/Interaction	F-statistic	Null hypothesis	Comparison	P (type I error, %)
Compound stoichiometry (TaC <sub>x</sub> )				
A	8.46	Reject	Agrees	2
B	0.27	Accept	Not defined	> 10
C	12.97	Reject	Agrees	< 1
AB	0.61	Accept	Not defined	> 10
AC	0.00	Accept	Not defined	> 10
BC	0.83	Accept	Not defined	> 10
ABC	7.84	Reject	Agrees	3
Primary particle size (nm)				
A	0.19	Accept	Agrees	> 10
B	20.08	Reject	Agrees	< 1
C	24.04	Reject	Agrees	< 1
AB	0.36	Accept	Not defined	> 10
AC	0.06	Accept	Not defined	> 10
BC	1.83	Accept	Not defined	> 10
ABC	15.02	Reject	Agrees	< 1
Specific surface area (m <sup>2</sup> /g)				
A	0.22	Accept	Agrees	> 10
B	10.17	Reject	Agrees	2
C	11.07	Reject	Agrees	1
AB	0.49	Accept	Not defined	> 10
AC	0.04	Accept	Not defined	> 10
BC	12.37	Reject	Agrees	< 1
ABC	7.22	Reject	Agrees	4
Figure of merit (particle size/primary particle size)				
A	0.08	Accept	Not defined	> 10
B	12.06	Reject	Agrees	< 1
C	17.74	Reject	Agrees	< 1
AB	0.07	Accept	Not defined	> 10
AC	0.01	Accept	Not defined	> 10
BC	4.59	Reject	Agrees	6
ABC	9.98	Reject	Agrees	2

A: carbon stoichiometry, B: reductant stoichiometry, C: reductant type.

The trend observed must be due to reactant concentrations at the higher reaction temperature when compared to the use of lithium reductant. The three possible explanations are that it is related to calcium stoichiometry, it is related to the carbon stoichiometry, or that it is related to a combination of these two variables. The first two can be ruled out because no binary interactions were observed. A binary interaction between reductant stoichiometry and carbon stoichiometry seems probable due to the difference in the effect of the reductant stoichiometry with carbon stoichiometry, although it is considered a ternary interaction overall because it is not observed to such an extent for samples with lithium that have a lower reaction temperature. The interaction is a result of both chemical and thermal diffusion mechanisms and may be influenced by the nucleation and growth of the intermediate nascent tantalum particles. Performing experiments without carbon to study the tantalum nucleation and growth could provide further insight.

#### **D. Conclusions**

This study provides a better understanding of the solvothermal synthesis process and its capabilities for the synthesis of TaC powders through the observation of general trends and statistical analyses of several response variables. Reductant type, carbon stoichiometry, and reductant stoichiometry were all critical variables. Lithium and calcium were found to be suitable reductants for the process. Phase-pure TaC could be achieved using a combination of these three variables to control the reaction temperature and reactant concentrations, which control diffusion, crystallization, and growth processes. Specifically, reactions with at least twice the stoichiometric amount of carbon and at least three times the stoichiometric amount of reductant produced TaC of high phase purity if the reductant metal had a vaporization temperature of at least 1615 K. Below these minimum conditions, Ta<sub>2</sub>C, tantalum, and/or Ta<sub>2</sub>O<sub>5</sub> phases were observed.

Qualitative trends were visually observed and analysis of variance was used to support the findings. While interesting from the perspective of developing a qualitative understanding of the responses as they relate to the expected reaction mechanisms and developing support for those mechanisms, there is relatively little flexibility to control the TaC responses for conditions producing high phase purity. The reductant type has the

largest influence, indicating the importance of the reaction temperature. The composition of the molten phase during reaction can be modified to control reaction temperature.

TaC produced by the solvothermal synthesis and subjected to the current processing methods is susceptible to surface impurities. Higher reaction temperature reduced the amount of surface contamination, probably by increasing the crystallite size and reducing the surface area. The extent of agglomeration, measured as a figure of merit, is also reduced with increased reaction temperature. Optimizing the reaction temperature is recommended for obtaining larger crystallite sizes, to reduce surface area and therefore adsorption sites, without significantly increasing the particle size. The quantity of excess carbon, impurities on the surface, and lattice impurities still need to be investigated.

## E. References

- [1]. D. Sciti, L. Silvestroni, S. Guicciardi, D. Dalle Fabbiche, and A. Bellosi, "Processing, Mechanical Properties and Oxidation Behavior of TaC and HfC Composites Containing 15 vol% TaSi<sub>2</sub> or MoSi<sub>2</sub>," *J. Mater. Res.*, **24** [6] 2056-65 (2009).
- [2]. F. Peng, L Han, H. Fu, and X. Cheng, "First-Principles Calculations on Elasticity and the Thermodynamic Properties of TaC Under Pressure," *Phys. Status Solidi B*, **246** [7] 1590-6 (2009).
- [3]. B.-R. Kim, K.-D. Woo, J.-M. Doh, J.-K. Yon, and I.-J. Shon, "Mechanical Properties and Rapid Consolidation of Binderless Nanostructured Tantalum Carbide," *Ceram. Int.*, **35** [8] 3395-400 (2009).
- [4]. Y. Zhang, C. Zhang, H. Hu, and Y. Zhou, "Preparation and Properties of 2D C/SiC-TaC Composites," *Key Eng. Mater.*, **362-372** [2] 1771-3 (2008).
- [5]. X. Zhang, G.E. Hilmas, and W.G. Fahrenholtz, "Densification, Mechanical Properties and Oxidation Resistance of TaC-TaB<sub>2</sub> Ceramics," *J Am. Ceram. Soc.*, **91** [12] 4129-32 (2008).
- [6]. J. Noffsinger, F. Giustino, S.G. Louie, and M.L. Cohen, "First-Principles Study of Superconductivity and Fermi-Surface Nesting in Ultrahard Transition Metal Carbides," *Phys. Rev. B.*, **77** [18] 180507/1-4 (2008).
- [7]. A.A. Lavrentyev, B.V. Gabrelian, V.B. Vorzhev, I.Y. Nikiforov, O.Y. Khyzhun, and J.J Rehr, "Electronic Structure of Cubic Hf<sub>x</sub>Ta<sub>1-x</sub>C<sub>y</sub> Carbides from X-ray Spectroscopy Studies and Cluster Self-Consistent Calculations," *J. Alloys Compd.*, **462** [1-2] 4-10 (2008).
- [8]. X. Guo, L. Li, Z. Liu, D. Yu, J. He, R. Liu, B. Xu, Y. Tian, and H.-T. Wang, "Hardness of Covalent Compounds: Roles of Metallic Component and D Valence Electrons," *J. Appl. Phys.*, **104** [2] 023503 (2008).
- [9]. B.M. Eick and J.P. Youngblood, "Carbothermal Reduction of Metal-Oxide Powders by Synthetic Pitch to Carbide and Nitride Ceramics," *J. Mater. Sci.*, **44** [5] 1159-71 (2009).
- [10]. S. Sulaimankulova, E. Saadat, J. Jasnakunov, A. Abdykerimova, H. Gafforova, and A. Mametova, "New Preparation Method of Nanocrystalline Materials by Impulse Plasma in Liquid," *J. Cluster Sci.*, **20** [1] 37-49 (2009).

- [11]. A. Vorobev, O. Zikanov, and P. Mohanty, "Modelling of the In-Flight Synthesis of TaC Nanoparticles from Liquid Precursor in Thermal Plasma Jet," *J. Phys. D: Appl. Phys.*, **41** [8] 085302 (2008).
- [12]. M. Lei, H. Z. Zhao, H. Yang, B. Song, and W.H. Tang, "Synthesis of Transition Metal Carbide Nanoparticles Through Melamine and Metal Oxides," *J. Eur. Ceram. Soc.*, **28** [8] 1671-7 (2008).
- [13]. J. Ma, D. Yihong, M. Wu, and M.-C. Pan, "One Simple Synthesis Route to Nanocrystalline Tantalum Carbide via the Reaction of Tantalum Pentachloride and Sodium Carbonate with Metallic Magnesium," *Mater. Lett.*, **61** [17] 3658-61 (2007).
- [14]. D.-H. Kwon, S.-H. Hong, and B.-K. Kim, "Fabrication of Ultrafine TaC Powders by Mechano-Chemical Process," *Mater. Lett.*, **58** [30] 3863-7 (2004).
- [15]. J.A. Nelson and M.J. Wagner, "High Surface Area Nanoparticulate Transition Metal Carbides Prepared by Alkalide Reduction," *Chem. Mater.*, **14** [10] 4460-3 (2002).
- [16]. Y.-H. Chang, C.-W. Chiu, Y.-C. Chen, C.-C. Wu, C.-P. Tsai, J.-L. Wang, and H.-T. Chiu, "Synthesis of Nano-Sized Cubic Phase Early Transition Metal Carbides from Metal Chlorides and n-Butyllithium," *J. Mater. Chem.*, **12** [8] 2189-91 (2002).
- [17]. A.M. Nartowski, I.P. Parkin, M. Mackenzie, and A.J. Craven, "Solid State Metathesis: Synthesis of Metal Carbides from Metal Oxides," *J. Mater. Chem.*, **11** [12] 3116-9 (2001).
- [18]. C.P. Souza, C. Favotto, P. Satre, A.L. Honore, and M. Roubin, "Preparation of Tantalum Carbide from an Organometallic Precursor," *Braz. J. Chem. Eng.*, **16** [1] 1-6 (1999).
- [19]. N.I. Shurov, A.I. Anfinogenov, V.V. Chebykin, L.P. Klevtsov, and E.G. Kazanskii, "Synthesis of Borides, Carbides, and Silicides of Refractory Metals in Ionic-Electronic Melts," pp.81-6 in *Refractory Metals in Molten Salts: Their Chemistry, Electrochemistry, and Technology*, Vol. 53, Sub-Series 3, NATO ASI SERIES. Edited by D.H. Kerridge and E.G. Polyakov. Kluwer Academic Publishers, Netherlands, 1998.
- [20]. A.J. Hockman, and R.S. Feigelson, "Low Temperature Electrosynthesis of Tantalum and Niobium Monocarbides," *J. Electrochem. Soc.*, **130** [1] 221-4 (1983).
- [21]. O.A. Graeve and Z.A. Munir, "Electric Field Enhanced Synthesis of Nanostructured Tantalum Carbide," *J. Mater. Res.*, **17** [3] 609-13 (2002).

- [22]. J.P. Kelly, R. Kanakala, and O.A. Graeve, "A Solvothermal Approach for the Preparation of Nanostructured Carbide and Boride Ultra-High Temperature Ceramics," *J. Am. Ceram. Soc.*, in print (2010).
- [23]. D.M. Levine, P.P. Ramsey, and R.K. Smidt, *Applied Statistics for Engineers and Scientists Using Microsoft Excel® and MINITAB®*, p. 469-566. Prentice Hall, Upper Saddle River, NJ, 2001.
- [24]. A. Kaza, M. Matthewson, M. John, D. Niesz, R.L. Haber, and M.A. Rossi, "A Model of Gas-Phase Transport During the Initial Stages of Sintering of Silicon Carbide," *J. Am. Ceram. Soc.*, **92** [11] 2517-27 (2009).
- [25]. A. Gubernat and L. Stobierski, "Fractography of Dense Metal-Like Carbides Sintered with Carbon," *Key Eng. Mater.*, **409**, 287-90 (2009).
- [26]. W.G. Fahrenholtz, G.E. Hilmas, S.C. Zhang, and S. Zhu, "Pressureless Sintering of Zirconium Diboride: Particle Size and Additive Effects," *J. Am. Ceram. Soc.*, **91** [5] 1398-1404 (2008).
- [27]. X. Zhang, G.E. Hilmas, W.G. Fahrenholtz, G. William, and D.M. Deason, "Hot Pressing of Tantalum Carbide with and without Sintering Additives," *J. Am. Ceram. Soc.*, **90** [2] 393-401 (2007).
- [28]. L. Stobierski and A. Gubernat, "Sintering of Silicon Carbide I. Effect of Carbon," *Ceram. Int.*, **29** [3] 287-92 (2003).
- [29]. K.J. Nilsen, and A.W. Weimer, "Chemical Purification," p. 479-503 in *Carbide, Nitride and Boride Materials Synthesis and Processing*. Edited by A.W. Weimer. Chapman & Hall, New York, NY, 1997.
- [30]. A.L. Bowman, "The Variation of Lattice Parameter with Carbon Content of Tantalum Carbide," *J. Phys. Chem.*, **65** [9] 1596-8 (1961).
- [31]. G.K. Williamson and W.H. Hall, "X-ray Line Broadening from Filled Aluminum and Tungsten," *Acta Metall.*, **1** [1] 22-31 (1953).
- [32]. "Standard Guide for Measurement of Particle Size Distribution of Nanomaterials in Suspension by Photon Correlation Spectroscopy," ASTM Designation E2490-09. ASTM International, West Conshohocken, PA.
- [33]. A. Varma and J.P. Lebrat, "Combustion Synthesis of Advanced Materials," *Chem. Eng. Sci.*, **47** [9-11] 2179-94 (1992).

## CHAPTER 5: RESISTANCE SINTERING OF TANTALUM CARBIDE NANOPOWDERS PRODUCED BY SOLVOTHERMAL SYNTHESIS

### A. Introduction

TaC is one of the most refractory ceramics known with a melting temperature of around 4000 K. Therefore, this material is potentially useful for applications that include space reentry vehicles and high mach aircraft, where extreme temperatures are reached. Other properties, including hardness, fracture toughness, elastic moduli, oxidation behavior, electronic structure, and optical properties, have also been investigated for this material.<sup>[1-4]</sup>

The preparation of bulk nanoceramics can result in improved material properties. Maintaining a nanostructure can modify electrical properties and mechanical properties, for instance.<sup>[5-7]</sup> Properties that did not exist in a material with grain sizes in the micrometer range can potentially exist when the grain size is reduced to the nanometer scale.<sup>[8]</sup> Obtaining nanostructured TaC is difficult, with sintering being accompanied by rapid grain growth due to the similar activation energies for grain growth and sintering being cited as an explanation.<sup>[9-16]</sup>

Resistance sintering is a useful technique to consolidate powders because of the simultaneous pressure and current applied to create fast heating rates and sintering cycles, which can substantially limit the amount of grain growth of a sintered specimen.<sup>[17-18]</sup> This technique is investigated for sintering TaC nanopowders synthesized by a solvothermal synthesis method. Resistance sintering can produce fully dense TaC from submicron powders utilizing a uniaxially applied pressure of at least 263 MPa.<sup>[19-20]</sup> However, the issue of grain growth was not resolved. It has been determined experimentally that an applied pressure near three gigapascal is necessary to completely inhibit grain growth.<sup>[10]</sup>

Thus, the goal of this work is to understand the general densification behavior of TaC nanopowders produced by the solvothermal synthesis method. While significant progress towards obtaining fully dense TaC can be expected, the problem of grain growth

will not be addressed at this time. The effects of temperature and carbon on the microstructure are explored.

## **B. Experimental Procedures**

Previous sintering work revealed that the scaled-up synthesis of TaC powders produced by solvothermal synthesis, which were subsequently sintered, still contained LiOH left over from the synthesis and post-synthesis processes.<sup>[21]</sup> TaC powders were synthesized using the solvothermal technique previously established to produce a 50 g theoretical yield of powder.<sup>[22-23]</sup> The synthesis method is rapid and could be scaled to produce large quantities of powder in a continuous type of process. The parent techniques have been used to produce kilogram quantities of powders.<sup>[24-26]</sup> After synthesis, one gram of the powders were oxidized by heat treating in air at 1173 K for one hour and then characterized by X-ray diffraction (XRD), which revealed a LiTaO<sub>3</sub> phase due to residual LiOH remaining from the synthesis and post-synthesis processes.

LiOH is formed by the reaction of lithium and lithium oxide with water when freeing the reaction products after the reaction cools.<sup>[23]</sup> The synthesized powders were divided into two sets of powders for washing experiments to explore the removal of the excess LiOH. LiOH is water soluble. Additions of HNO<sub>3</sub> can form LiNO<sub>3</sub> from the LiOH, which has a higher solubility limit in water than LiOH and is a method that has been used to eliminate LiOH, Mg(OH)<sub>2</sub>, and Ca(OH)<sub>2</sub> from powders made by the same process.<sup>[23]</sup>

One set of powders was washed with water and the other set was washed with a dilute HNO<sub>3</sub> solution. The HNO<sub>3</sub> solution was made by mixing a volumetric ratio of 1:19 acid to water volume, using a 15.8 N HNO<sub>3</sub> acid stock solution. Both sets of powders were washed in 500 ml of solution. One complete washing cycle consisted of 30 min of magnetic stirring, 30 min of ultrasonication, 15 min of magnetic stirring, and centrifuging, until the powders were separated and the supernatant could be poured off. A small portion of powder was oxidized after each wash, in the same manner as outlined previously, and XRD was performed to confirm whether or not the LiTaO<sub>3</sub> phase, indicating residual LiOH in the powders, was present or not.

LiOH could no longer be detected after HNO<sub>3</sub> washing and was used to process powders for resistance sintering experiments. One sample was sintered to a measured temperature of 2323 K for 30 s, using at a heating rate of 100°C/min and a 50 MPa uniaxial pressure to observe the general densification behavior. In general, the measured temperature, which is measured a few mm away from the sample, is expected to be lower than the sample temperature. The resulting displacement curve demonstrates five distinct displacement rate peaks at different temperatures. Subsequent powders were milled for 2 hours by cascade milling in a 250 ml nalgene bottle before sintering. Sintering of samples to maximum temperatures of 1073, 1373, 1773, and 2223 K for 30 sec was carried out to investigate the causes for these densification regimes. XRD and scanning electron microscopy (SEM) was used to study the sintering behavior for each of these temperatures.

Additions of carbon can enhance the sintering behavior and inhibit grain growth in TaC, presumably by eliminating oxide contaminants.<sup>[20,27-28]</sup> Carbon was mixed with the TaC powders and sintered at 2423 K for 10 min to compare the resulting microstructures. Using the best results from the experiments with carbon additions, the heating rate was investigated using heating rates of 200, 300, and 400 K/min. Some common features were observed, including apparent vaporization. Reduction in sintering temperature with a 10 min hold time to reduce vaporization was also investigated. All sintering is done in a vacuum environment.

### **C. Results and Discussion**

Relevant XRD patterns associated with the washing procedure are given in Figure 5-1. The as-synthesized powders contain a large proportion of LiOH because high purity LiTaO<sub>3</sub> phase is observed in the XRD pattern after the powders have been oxidized. TaC powders washed with two dilute HNO<sub>3</sub> washes was able to reduce the LiOH below detectable levels after two washing cycles. Ta<sub>2</sub>O<sub>5</sub> phase, without a trace of the previously observed LiTaO<sub>3</sub> phase, was observed in the XRD pattern when the HNO<sub>3</sub> washed powders were oxidized.

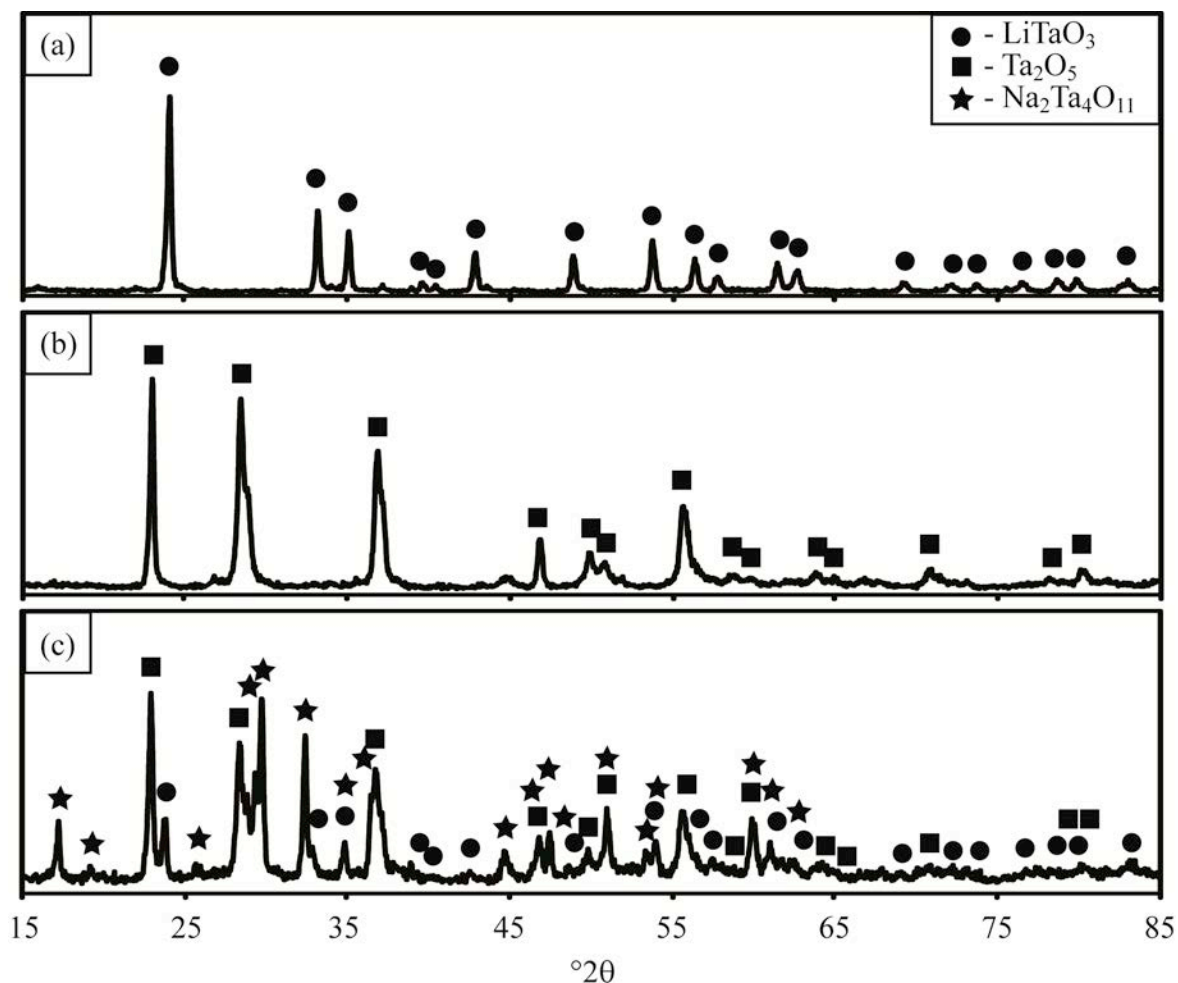


Figure 5 - 1. Phase analysis for powder XRD patterns for oxidized (a) as-synthesized powders, (b) powders after two nitric acid washing cycles, and (c) powders after nine water washes.

In comparison, powders washed only with water reduced  $\text{LiOH}$ , but did not eliminate it after nine washing cycles. The  $\text{LiTaO}_3$  phase was still observed in the XRD pattern after the powders were oxidized, although the peaks are of lower intensity and the  $\text{Ta}_2\text{O}_5$  phase is also observed. A third phase was found and is indicated by additional peaks in the XRD pattern compared to the as-synthesized and  $\text{HNO}_3$  washed powders. The third phase is most likely related to  $\text{LiTaO}_3$ , deficient in lithium. The phase was strongly matched to natrotantite ( $\text{Na}_2\text{Ta}_4\text{O}_{11}$ ), but since there is no sodium source the phase is likely a lithium-containing phase of similar structure although no such phase was found in the database. If the chemical formula for natrotantite is assumed as a guide, then the compound would have stoichiometry of  $\text{Li}_2\text{Ta}_4\text{O}_{11}$ , which has the same chemistry as

four  $\text{LiTaO}_3$  units deficient in one  $\text{Li}_2\text{O}$  unit, agreeing with the assessment that the phase is related to lithium deficient  $\text{LiTaO}_3$ .

$\text{LiOH}$  is less soluble in water than  $\text{LiNO}_3$  and can explain the improved washing efficiency when using nitric acid. The observations agree with our hypothesis outlined in the experimental procedure and our previous work concerning the effect of nitric acid.<sup>[23]</sup> Water washing was abandoned after the ninth washing cycle due to the decreased efficiency of removing the  $\text{LiOH}$  by water washing.

The displacement rate curve for the sample sintered at 2323 K is displayed in Figure 5-2a. There are five distinct displacement rate peaks of the curve that indicate densification: near 1023, 1198, 1573, 1923 and 2023 K. The two distinct peaks at 1923 K and 2023 K are thought to be an artifact because a single peak is observed for other samples. Figure 5-2 also displays the XRD patterns for four samples sintered to temperatures just above temperatures corresponding to these displacement rate peaks. The emergence of an oxide phase is found for the sample sintered at 1023 K. At 1373 K, the relative peak intensities of the oxide and carbide phases, without significant differences in peak broadening, indicate that the level of the oxide phase is increased. The presence of the oxide phase after sintering to 1773 K appears to decrease based on peak intensities, but is difficult to conclude because peak broadening of  $\text{TaC}$  is diminished and indicates that grain growth may be causing the observation. The oxide phase is eliminated by sintering at 2223 K as is indicated by the elimination of the oxide peaks in the XRD patterns.

It is assumed that the first densification peak is related to the formation of the oxide phase in some way. XRD of a sample subjected to a sintering temperature just below this densification event could provide further insight. Previous work indicated that the powders produced by solvothermal synthesis had a significant quantity of water adsorbed onto the surfaces of the  $\text{TaC}$ .<sup>[21]</sup> The water could not be removed completely by thermal treatments below 873 K in an argon atmosphere and simultaneous oxidation can occur at temperatures in excess of 473 K. A solvent exchange process could be implemented to remove the water from the surfaces. Chemisorbed oxygen contamination or lattice oxygen would be more difficult to remove. Despite the presence of an oxide

phase at lower temperatures, it is eliminated at higher temperatures and so is not a concern for this study.

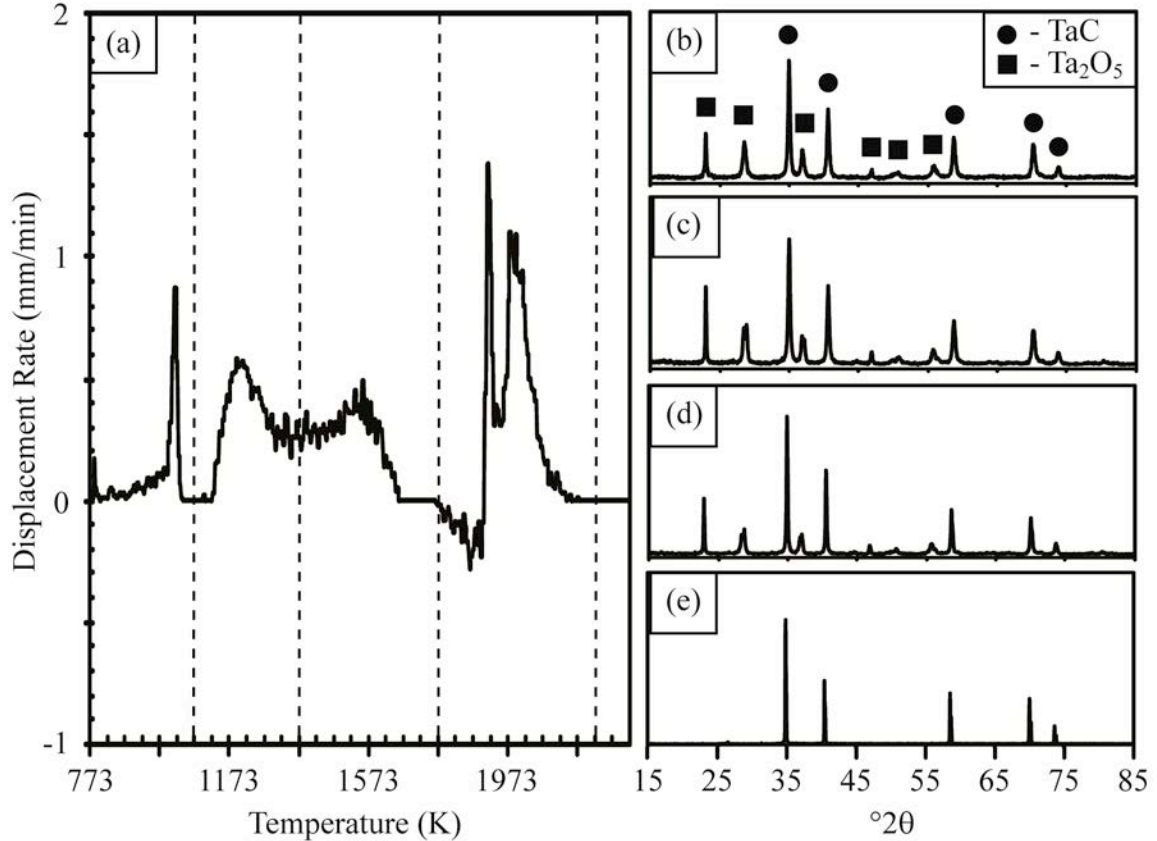


Figure 5 - 2. (a) Displacement rate curve for a resistance sintered TaC at 2323 K. Dotted lines in this curve are cut-off temperatures, held for 30 s, for the sintering of secondary specimens used to generate the XRD patterns given in (b)-(e). The XRD patterns correspond to specimens sintered to temperatures of (b) 1073 K, (c) 1373 K, (d) 1773 K, and (e) 2223 K.

There are a few potential explanations for the second displacement rate peak, which occurs for measured temperatures ranging from 1123-1373 K. This is also the temperature range for which the onset of densification has been reported for TaC nanopowders, based on reports in the literature, which are expected to sinter by a different mechanisms than coarser powders.<sup>[4,9,11]</sup> Oxygen or metallic impurities might be responsible for low-temperature sintering as suggested by Sautereau and Mocellin.<sup>[11]</sup> The analysis thus far indicates a significant amount of oxygen in the TaC powders. Further development of the oxide phase could be at least partially responsible for some of

the densification, observed by comparing Figure 5-2b to Figure 5-2c. This also is a temperature range at which glide of screw dislocations is expected to be thermally activated over the Peierls barrier, possibly activating a plastic deformation sintering mechanism, accomplished by motion of  $a/2\langle 011 \rangle$  edge dislocations gliding along  $\{111\}$ .<sup>[29]</sup> The likely cause can not be discerned from the data presented thus far.

The third densification event in Figure 5-2a occurs over the measured temperature range of 1373-1673 K. Comparing Figure 5-2b to Figure 5-2c indicates that the oxide content could be reduced over this temperature range. This is consistent with the reaction between  $Ta_2O_5$  and free carbon.<sup>[27]</sup> Consequently, this is a typical temperature range used to perform carbothermal reduction and carburization to synthesize TaC. Liu *et al* has observed similar densification behavior during resistance sintering and they reported outgassing for the latter densification peak, consistent with carbothermal reduction of the oxide phase.<sup>[30]</sup> A second mechanism for dislocation motion might also be activated in this temperature range.<sup>[29]</sup> Sub-grain formation for samples subjected to creep testing near these temperatures indicate the activation of dislocation climb that may contribute to densification. The cause for densification is not distinguishable from the data presented, but will be evaluated further using microscopy.

SEM images of fracture surfaces for the specimen sintered at 1073 K are given in Figure 5-3. The sample has agglomerate structures with size of a few micrometers and consists of small nanostructured grains. An impurity phase has been identified in the images that were not identified for any other sample. The secondary electron images indicate the impurity phase forms spherical droplets of a few hundred nanometers in size. The darker contrast in the back-scattered electron image indicates that the phase has a lower average atomic number than the rest of the sample.

The low-density phase could be free carbon or residual LiOH. Excess carbon is introduced in the initial reaction and observed indirectly by thermogravimetric analysis.<sup>[21]</sup> However, the droplet morphology of this phase suggests that it may have been a non-wetting liquid at the sintering temperature and would suggest LiOH rather than carbon. This phase may be a consequence of residual LiOH in the powders that was not removed during the washing procedures and below the detection limits of XRD such that it was not observed. If this is the case, then it can be removed further optimization of

the post-synthesis processing. This phase may be directly responsible for the densification event occurring immediately prior to reaching the sintering temperature as well as the formation of the oxide phase. Thus, it seems likely that the first displacement peak observed can be explained by the formation of an oxide phase and the formation of a liquid phase presumed to be a result of residual LiOH impurity from the synthesis process. The two effects cannot be decoupled from this study.

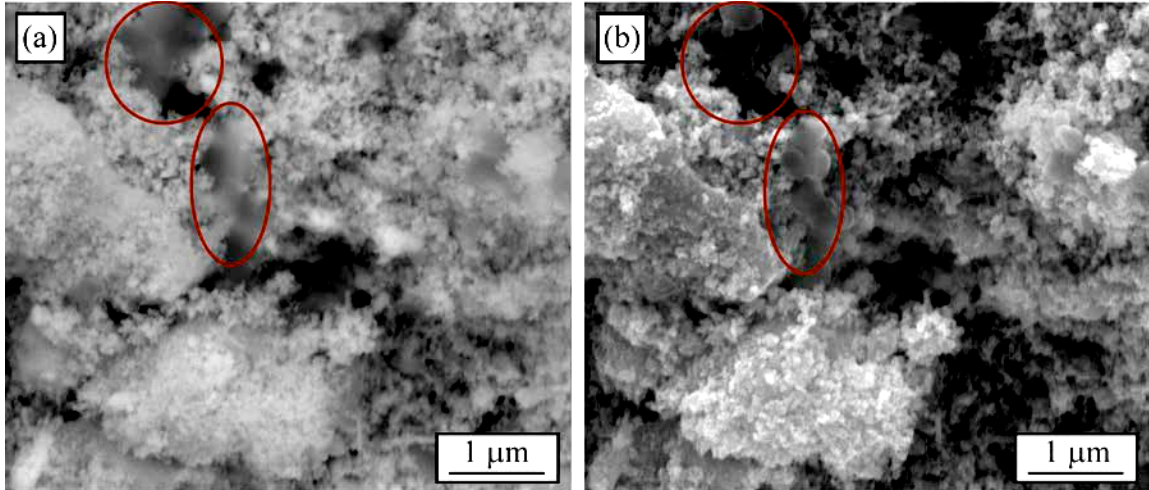


Figure 5 - 3. (a) Back-scattered electron image and (b) secondary electron image of the fracture surface for a specimen that was sintered at 1073 K using resistance sintering. An impurity phase is circled. (With color)

Figure 5-4 gives images of the fracture surface for the sample sintered at 1773K. Regions of lower average atomic number appear as a phase with darker contrast in the back-scattered electron image. Figure 5-2d indicates the presence of  $\text{Ta}_2\text{O}_5$  and TaC at this sintering temperature. The darker phase in Figure 5-4a is identified as  $\text{Ta}_2\text{O}_5$  (average atomic number of 27) while the brighter phase corresponds to the TaC phase (average atomic number of 40). The  $\text{Ta}_2\text{O}_5$  and TaC phases have heterogeneous distributions in the microstructure.

Evaluation of the microstructures given in Figure 5-3 and Figure 5-4 indicates that TaC grains have grown from being nanograins into the submicron regime when increasing the sintering temperature from 1073 K to 1773 K. An early report on sintering ultrafine TaC powders concluded that oxygen impurities were removed by thermal treatments, but that the grain growth also grew the grains into the submicron size

regime.<sup>[11]</sup> Therefore, it is of interest to remove the oxygen impurities by another method that does not result in grain growth or to remove the oxide *in situ* (as is done in this study) to minimize exposure time to conditions resulting in grain growth.

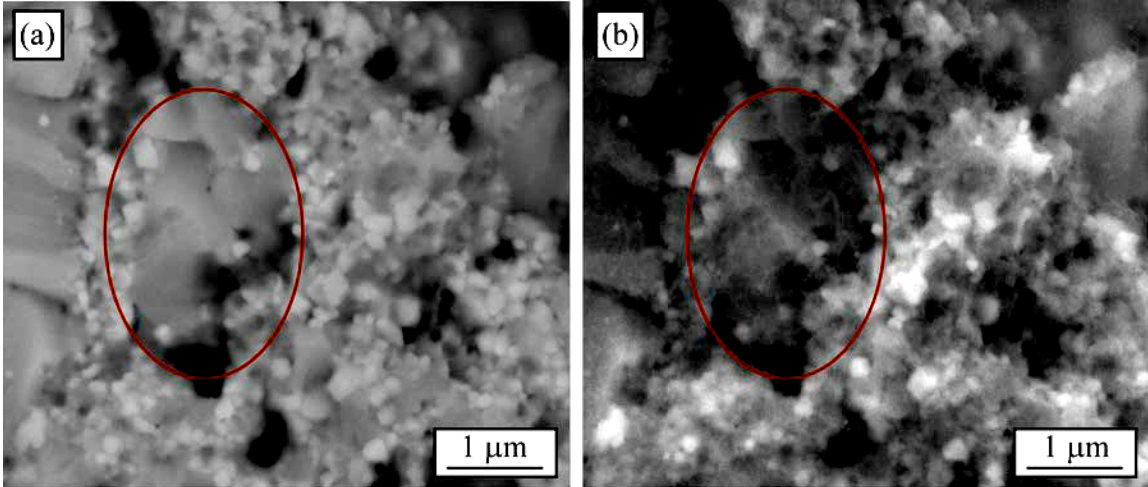


Figure 5 - 4. (a) Back-scattered electron image and (b) secondary electron image of the fracture surface for a specimen that was sintered at 1773 K using resistance sintering. Heterogeneous distribution of Ta<sub>2</sub>O<sub>5</sub> impurity phase is demonstrated by red circle. (With color)

Further increase in sintering temperature results in carbothermal reduction of the Ta<sub>2</sub>O<sub>5</sub> phase and densification of TaC according to Figure 5-2a and Figure 5-2e. The negative displacement of the pressing rams is most likely a result of the release of CO gas during carbothermal reduction. The release of a vapor accompanying final stages of sintering were also noted for the sintering of TaC with B<sub>4</sub>C additions.<sup>[13]</sup> If significant carbothermal reduction of Ta<sub>2</sub>O<sub>5</sub> occurs above 1773K, then it rules it out as a densification mechanism at temperatures lower than this. This observation and the lack of more significant grain growth concurrent with densification that other authors report when sintering TaC suggests that the densification occurring at temperatures ranging from 1123-1673 K is a result of the oxide phase and not from dislocation climb and glide that has been reported to occur in this temperature range.<sup>[9-16,29]</sup>

Figure 5-5 displays back-scattered electron images of the specimens sintered at 2223 K and 2323 K. The heterogeneous microstructure observed in Figure 5-4 is no longer observed in the microstructure because the removal of Ta<sub>2</sub>O<sub>5</sub>. When sintering to 2223 or 2323 K, significant grain growth of TaC is observed and the submicron

microstructure is lost, agreeing well with concurrent grain growth and sintering of TaC that is reported in the literature.<sup>[9-16,19,20,27]</sup> The grain size is approximately one micrometer after sintering at 2223 K and approximately two micrometers after sintering at 2323 K according to the interpretation of the micrographs, indicating that higher sintering temperature results in increased grain growth. The increase in sintering temperature did not eliminate porosity in the microstructure.

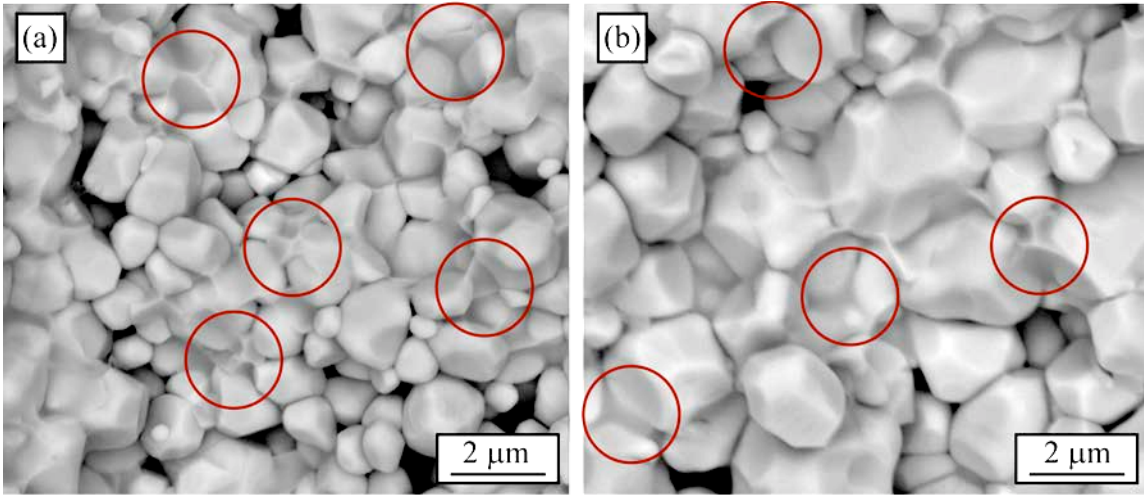


Figure 5 - 5. Back-scattered electron images of fracture surfaces for specimens sintered at (a) 2223 K and (b) 2323 K for 30 sec by resistance sintering. Phase of lower average atomic number at grain boundaries are highlighted. (With color)

Although large grains of Ta<sub>2</sub>O<sub>5</sub> are not observed in Figure 5-5 or detected in the XRD pattern of Figure 5-2e, phase contrast is observed in the back-scattered electron images of Figure 5-4, indicating that the oxide phase exists at the grain boundaries. The phase is highlighted in Figure 5-5. Ta<sub>2</sub>O<sub>5</sub> is a liquid at sintering temperatures of 2223 K and higher and could form a liquid grain boundary phase that encapsulates the TaC grains. The reduction of the oxide appears incomplete. Either there were not enough reactants to complete the reaction or not enough time to allow the reaction to complete before densification hindered the reaction. In the former case, additions of free carbon or B<sub>4</sub>C can be used to eliminate the oxide phase.<sup>[27]</sup> Evaluation of Figure 5-2a indicates that rapid densification began before the reaction was complete, suggesting that time of removal can't be ruled out as a contribution to residual Ta<sub>2</sub>O<sub>5</sub>. A temperature dwell

before significant densification occurs, at 1823-1873 K for example, or a slower heating rate would allow more time for the removal of the oxide phase. However, grain growth is still expected at these temperatures and the process should be optimized to complete the oxide reduction, but minimize exposure time to grain growth. Carbon additions and faster heating rates will be explored in greater detail. A faster heating rate was explored to try to reduce grain size, but would presumably increase the oxide at the TaC grain boundaries.

Based on the oxygen and free carbon contents given in a previous study, an addition of approximately three weight percent carbon is needed to remove all of the oxygen from the TaC nanopowders.<sup>[21]</sup> Samples were sintered with zero, three, five, and six weight percent carbon at 2423 K for 10 min and the results are given in Figure 5-6.

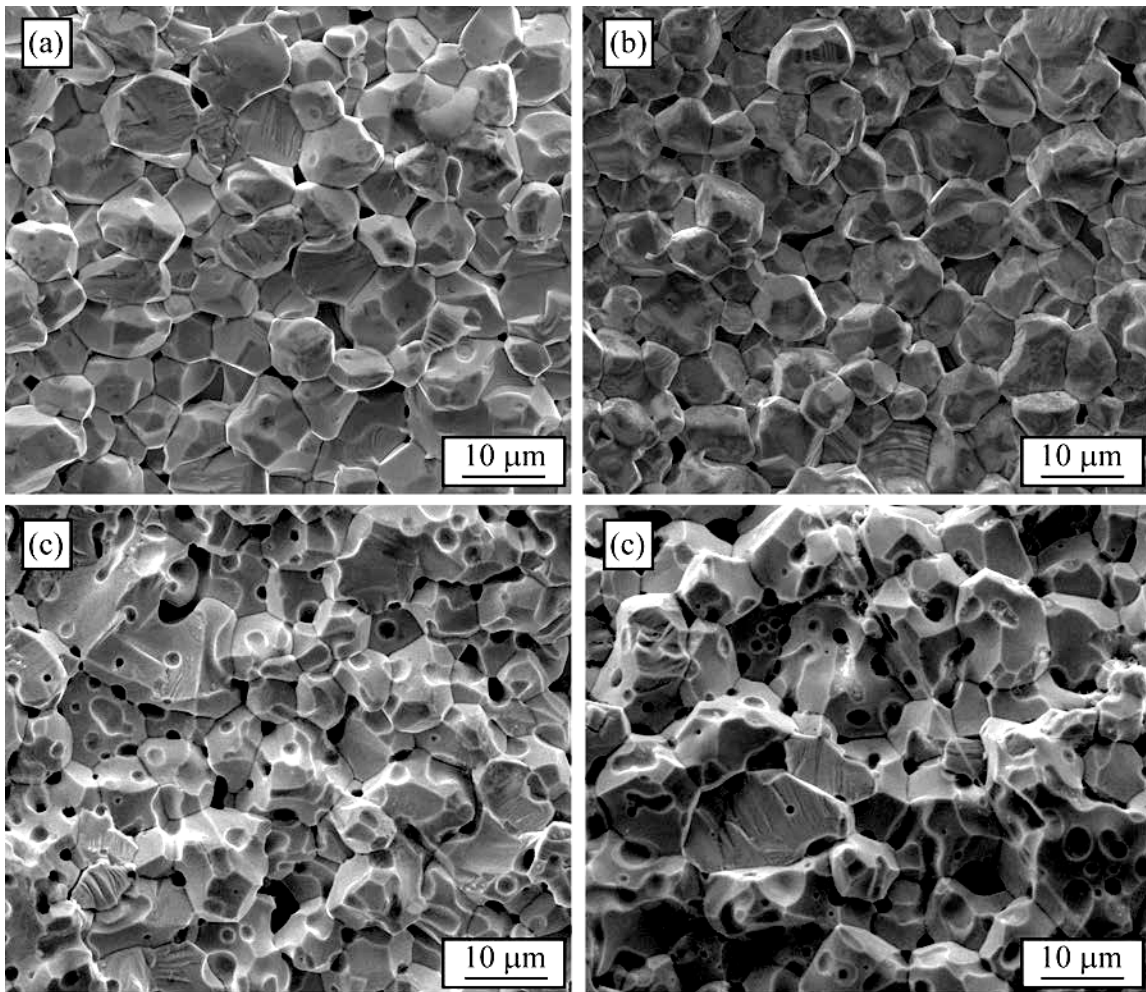


Figure 5 - 6. Secondary electron images of specimens from powders containing (a) zero, (b) three, (c) five, and (d) six weight percent addition of carbon and sintered at 2473 K for 10 min by resistance sintering.

Additions of three percent carbon had little effect on morphology of the grains, but five or six percent carbon resulted in irregular morphology with many pores at the surfaces of the grains. The pores have smooth curvature that suggests they are a result of a vapor. The vapor is unlikely formed by reduction of the oxide or this type of microstructure would be observed for a three percent carbon addition as well. Instead, free carbon not used to reduce oxygen or react with TaC, but at the TaC grain boundaries, is suspected to be important for the mechanism resulting in the microstructure observed for greater carbon additions.

Images taken at higher magnification for the sample with six percent carbon added is given in Figure 5-7. The secondary electron image indicates that there is a film of material located in the pores that is not readily apparent in the back-scattered electron image. The film is likely carbon, which would not be easily detected using back-scattered electrons because of the low atomic number, but produce a suitable signal from secondary electrons. The porosity shown in Figure 5-6c and Figure 5-6d is likely the result of excess carbon in the microstructure, which forms a vapor at high temperatures in the vacuum environment. Thus, excess free carbon in the microstructure is detrimental for densification at high temperatures in a vacuum because of the formation of a vapor.

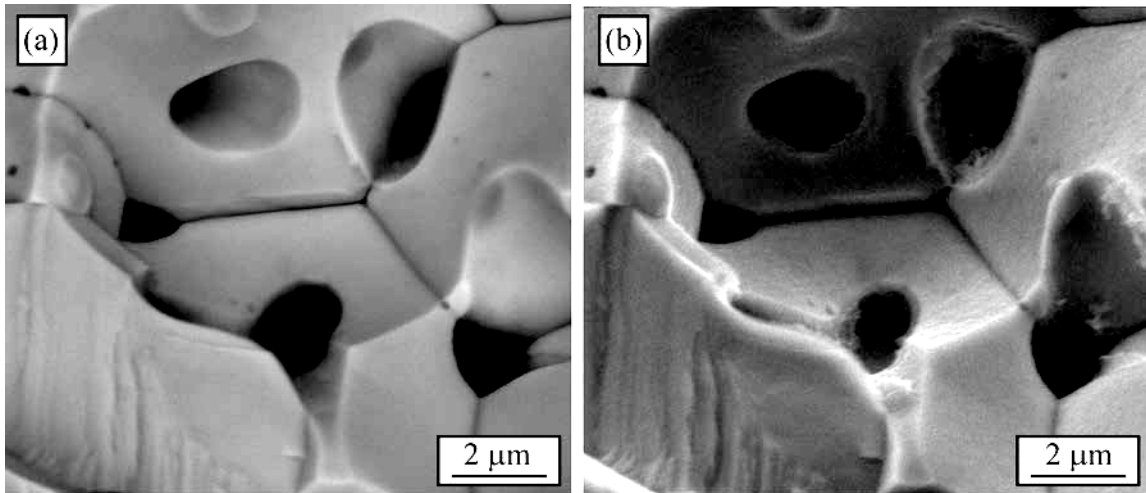


Figure 5 - 7. (a) Back-scattered electron image and (b) secondary electron image of TaC with six percent carbon added and sintered at 2473 K for 10 min by resistance sintering.

Talmy *et al.* determined that the type of carbon and amount of carbon resulted in significant differences in microstructural development.<sup>[28]</sup> Carbon with high surface area resulted in larger grains and possible vaporization that resulted in entrapped porosity. In another study, an interaction occurred between a TaC grain and a carbon nanotube that was described as partial melting of the TaC grains.<sup>[20]</sup> It was suggested that local heating of well dispersed carbon produced hot spots that could melt TaC. This could occur due to difference in current density passing through the two materials. Melting and evaporation as a consequence of excess carbon in the microstructure that causes local hot spots could be responsible for the microstructures that were observed in Figure 5-5b and Figure 5-5c, but would require further investigation. If this is true, it should be a unique consequence of the current applied during resistance sintering and should not occur for sintering techniques relying solely on thermal transport to heat the sample, which would heat the sample more uniformly.

The results of using faster heating rates are demonstrated in Figure 5-8. The heating rate does not have a strong influence on the grain size that was achieved. The faster heating rates were expected to trap more oxide in the microstructure because of the limited time for carbothermal reduction to occur. Figure 5-8 indicates that there is a significant amount of grain boundary phase and the dark contrast compared to the grains suggest that it is an oxide phase, supporting the expectations. Since a faster heating rate promotes entrapment of the oxide phase, it seems reasonable that decreasing the heating rate during the reduction of the oxide may also promote its removal by allowing enough time for the carbothermal reduction to complete. A combination of optimum carbon addition and slower heating rates are expected to assist more complete removal of the oxide phase.

Inclusions in the faces of TaC grains are observed in Figure 5-8c and spherical cavities on the faces of TaC grains are observed in Figure 5-6d. It is possible that the spherical cavities are left behind after the inclusions are pulled out during fracture. An alternate explanation is that these inclusions are from vapor formation, ultimately leaving behind a spherical cavity as it is removed. The appearance is similar to the observations detailed in Figure 5-6 and Figure 5-7 and suggests that localized areas of the microstructure have excess carbon that facilitates the formation of a vapor. A vapor mass

transport mechanism is detrimental, causing grain coarsening without densification and can generate the cavities observed in Figure 5-8d. Volatilization can also be influenced by temperature. Sintering with a lower temperature was performed, maintaining a sintering time of 10 min, in an attempt to avoid vaporization. A sintering temperature of 2123 was selected based on Figure 5-2a, where the last displacement rate peak is diminished. The result of this experiment is given in Figure 5-9. Cavities like those in Figure 5-8 are not observed in Figure 5-9 at the TaC interfaces at this lower sintering temperature.

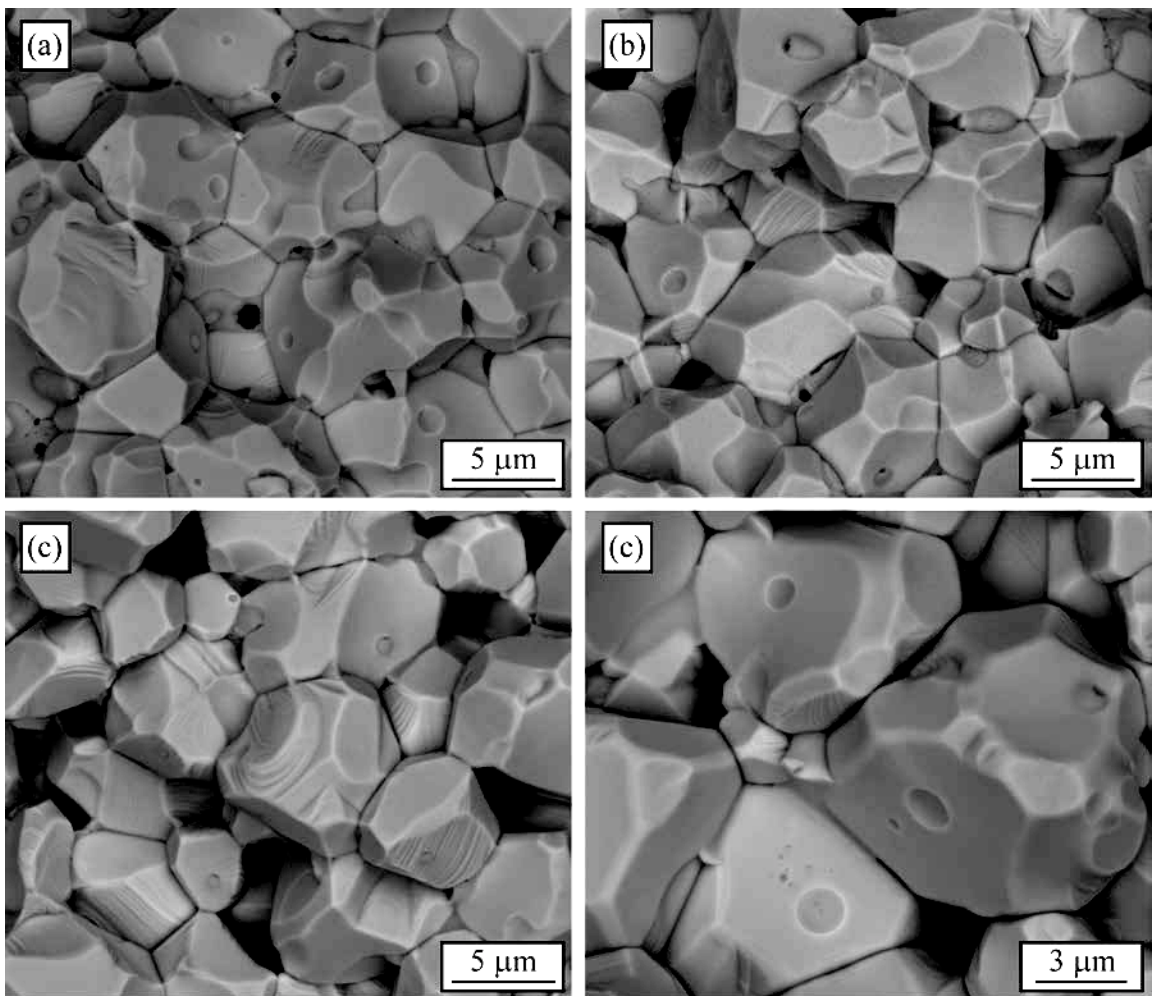


Figure 5 - 8. Back-scattered electron images of TaC specimens with three percent carbon added and sintered at 2473 K for 10 min by resistance sintering and using heating rates of (a) 200 K/min, (b) 300 K/min, and (c)/(d) 400 K/min.

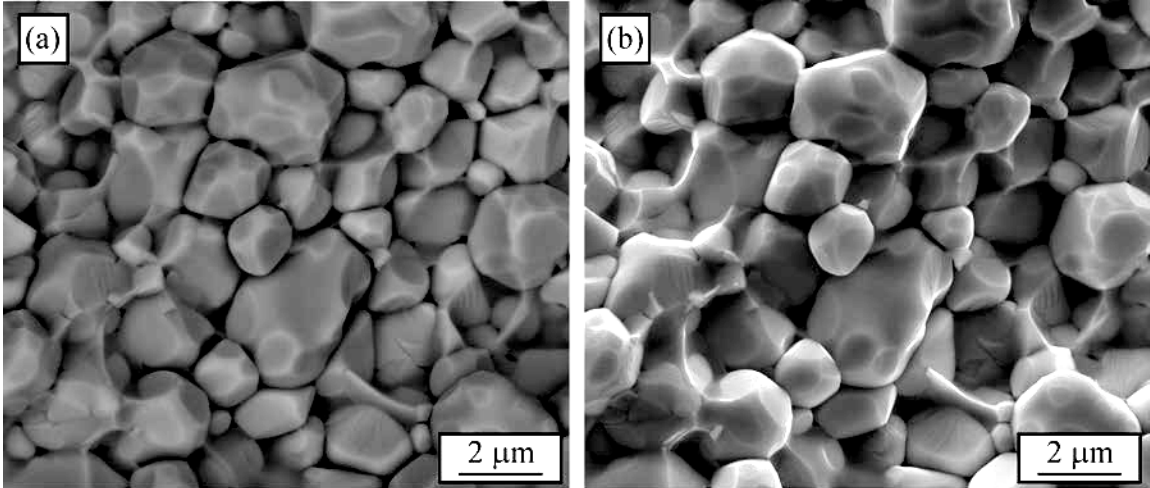


Figure 5 - 9. (a) Back-scattered electron image and (b) secondary electron images for TaC specimens with three percent carbon added sintered using a heating rate of 400 K/min, a dwell temperature of 2123 K, and a dwell time of 10 min.

#### D. Conclusions

The washing procedure for removing LiOH impurity from TaC nanopowders produced by solvothermal synthesis was developed in this study. Nine water washing cycles were not able to reduce LiOH below detectable limits. However, two dilute HNO<sub>3</sub> washes did reduce the LiOH below detectable limits. Thus, dilute HNO<sub>3</sub> washing is an efficient method for removing LiOH impurities from TaC nanopowders produced by the solvothermal synthesis method when using lithium as the reductant metal/solvent. The HNO<sub>3</sub> washing produced powders suitable for sintering experiments.

The general densification behavior of the TaC nanopowders during resistance sintering in vacuum and using a heating rate of 100 K/min was evaluated. Three distinct densification regimes prior to reaching 1673 K are most likely associated with an oxide that develops during the sintering cycle and not caused by the sintering of TaC. A carbothermal reduction of the Ta<sub>2</sub>O<sub>5</sub> phase was initiated at about 1773 K, which was followed by sintering of the TaC phase and simultaneous grain growth. The displacement rate of the pressing rams approached zero at 2173 K, indicating completion of densification.

Evaluation of the microstructural development indicated remnants of Ta<sub>2</sub>O<sub>5</sub> at the grain boundaries of TaC after the carbothermal reduction and sintering process. Optimization of the free carbon content and a temperature dwell during the carbothermal reduction of Ta<sub>2</sub>O<sub>5</sub>, prior to sintering, or a slower heating rate is recommended, which may allow the carbothermal reduction process to complete and produce TaC of higher purity.

Excess carbon in the microstructure and high temperatures facilitated the formation of cavities at the interfaces of TaC grains, likely caused by the formation of a vapor, which can be detrimental to TaC densification. An optimum amount of carbon would completely remove the Ta<sub>2</sub>O<sub>5</sub> impurity phase without having excess carbon in the microstructure. The optimum addition is expected to be close to three percent. Five percent was too much carbon. Further work is necessary to determine the optimum carbon addition. A reduced sintering temperature at 2123 K eliminated the formation of cavities that were observed when sintering at 2473 K. Therefore, optimization of the sintering temperature to prevent cavity formation and promote sintering needs further study. The combination of optimized carbon addition and optimized temperature is expected to promote obtaining high density TaC.

## E. References

- [1] A. Dashora and B.L. Ahuja, Electronic Structure, Compton Profiles and Optical Properties of TaC and TaN, *Radiat. Phys. Chem.*, **79**, 1103-10 (2010).
- [2]. M. Desmaison-Brut, N. Alexandre, and J. Desmaison, Comparison of the Oxidation Behaviour of Two Dense Hot Isostatically Pressed Tantalum Carbide (TaC and Ta<sub>2</sub>C) Materials, *J. Eur. Ceram Soc.*, **17**, 1325-34 (1997).
- [3]. I.-J. Shon, D.-M. Lee, J.-M. Doh, J.-K. Yoon, and I.-Y. Ko, Consolidation and Mechanical Properties of Nanostructured MoSi<sub>2</sub>-SiC-Si<sub>3</sub>N<sub>4</sub> from Mechanically Activated Powder by High Frequency Induction Heated Sintering, *Mater. Sci. Eng., A*, **528**, 1212-5 (2011).
- [4]. L. Silvestroni, A. Bellosi, C. Melandri, D. Sciti, J.X. Liu, and G.J. Zhang, Microstructure and Properties of HfC and TaC-Based Ceramics Obtained by Ultrafine Powder, *J. Eur. Ceram. Soc.*, **32**, 619-27 (2011).
- [5]. H. Hahn and R.S. Averback, High Temperature Mechanical Properties of Nanostructured Ceramics, *Nanostruct. Mater.*, **1**, 95-100 (1992).
- [6]. T. Hungría, H. Amorín, M. Algueró, and A. Castro, Nanostructured Ceramics of BiSCO<sub>3</sub>-PbTiO<sub>3</sub> with Tailored Grain Size by Spark Plasma Sintering, *Scr. Mater.*, **64**, 97-100 (2011).
- [7]. D.G. Lamas, M.F. Bianchetti, M.D. Cabezas, and N.E.W. de Reça, Nanostructured Ceramic Materials: Applications in Gas Sensors and Solid-Oxide Fuel Cells, *J. Alloys Compd.*, **495**, 548-51 (2010).
- [8]. P. Bowen and C. Carry, From Powders to Sintered Pieces: Forming, Transformations and Sintering of Nanostructured Ceramic Oxides, *Powder Technol.*, **128**, 248-55 (2002).
- [9]. P.S. Kislyi, S.A. Shvab, and F.F. Egorov, "Sintering Kinetics of Tantalum Carbide," *Powder Metall. And Met. Ceram.*, **21** [10] 765-7 (1982).
- [10]. W.C. Yohe and A.L. Ruoff, "Ultrafine-Grain Tantalum Carbide by High Pressure Hot Pressing," *Ceram. Bull.*, **57** [12] 1123-30 (1978).
- [11]. J. Sautereau and A. Mocellin, "Sintering Behavior of Ultrafine NbC and TaC Powders," *J. Mater. Sci.*, **9**, 761-71 (1974).
- [12]. S.A. Shvab and F.F. Egorov, "Structure and Some Properties of Sintered Tantalum Carbide," *Sov. Powder. Metall. Met. Ceram.*, **21** [11] 894-7 (1982).

- [13]. L. Liu, F. Ye, X. He, and Y. Zhou, "Densification Process of TaC/TaB<sub>2</sub> Composite in Spark Plasma Sintering," *Mater. Chem. Phys.*, **126**, 459-62 (2011).
- [14]. Y.E. Geguzin and Y.I. Klinchuk, "Mechanism and Kinetics of the Initial Stage of Solid-Phase Sintering of Compacts from Powders of Crystalline Solids," *Poroshk. Metall.*, [7] 17-25 (1976).
- [15]. M.F. Ashby and H.A. Verral, "Diffusion-Accommodated Flow and Superplasticity," *Acta Metall.*, **21**, 149-63 (1974).
- [16]. Y.E. Geguzin, "Diffusional Deformation of Porous Crystalline Structures," *Fiz. Tverd. Tela*, **17** [7] 1950-4 (1957).
- [17]. Z.A. Munir, D.V. Quach, M. Ohyanagi, "Electric Current Activation of Sintering: A Review of the Pulsed Electric Current Sintering Process," *J. Am. Ceram. Soc.*, **94** [1] 1-19 (2011).
- [18]. R. Orrù, R. Licheri, A.M. Locci, A. Cincotti, and G. Cao, "Consolidation/Synthesis of Materials by Electric Current Activated/Assisted Sintering," *Mater. Sci. Eng. R*, **63**, 127-287 (2009).
- [19]. S.R. Bakshi, V. Musaramthota, D. Lahiri, V. Singh, S. Seal, and A. Agarwal, "Spark Plasma Sintered Tantalum Carbide: Effect of Pressure and Nano-Boron Carbide Addition on Microstructure and Mechanical Properties," *Mater. Sci. Eng. A*, **528**, 1287-95 (2011).
- [20]. S.R. Bakshi, V. Musaramthota, D.A. Virzi, A.K. Keshri, D. Lahiri, V. Singh, S. Seal, and A. Agarwal, "Spark Plasma Sintered Tantalum Carbide-Carbon Nanotube Composite: Effect of Pressure, Carbon Nanotube Length and Dispersion Technique on Microstructure and Mechanical Properties," *Mater. Sci. Eng. A*, **528**, 2538-47 (2011).
- [21]. B.M. Clark, J.P. Kelly, and O.A. Graeve, Exploring the Synthesis Parameters and Spark Plasma Sintering of Tantalum Carbide Powders Prepared by Solvothermal Synthesis, *Mater. Res. Soc. Symp. Proc.*, **1373**, 7-17 (2012).
- [22]. J.P. Kelly, R. Kanakala, and O.A. Graeve, A Solvothermal Approach for the Preparation of Nanostructured Carbide and Boride Ultra-high Temperature Ceramics, *J. Am. Ceram. Soc.*, **93**, 3035-8 (2010).
- [23]. J.P. Kelly and O.A. Graeve, Statistical Experimental Design Approach for the Solvothermal Synthesis of Nanostructured Tantalum Carbide Powders, *J. Am. Ceram. Soc.*, **94**, 1706-15 (2011).
- [24]. S.T. Aruna and A.S. Mukasyan, "Combustion Synthesis of Nanomaterials," *Curr. Opin. Solid State Mater. Sci.*, **12**, 44-50 (2008).

- [25]. A.M. Nartowski, I.P. Parkin, M. MacKenzie, A.J. Craven, and I. MacLeod, "Solid State Metathesis Routes to Transition Metal Carbides," *J. Mater. Chem.*, **9**, 1275-81 (1999).
- [26]. J.J. Moore and H.J. Feng, "Combustion Synthesis of Advanced Materials: Part I. Reaction Parameters," *Prog. Mater. Sci.*, **39**, 243-73 (1995).
- [27]. X. Zhang, G.E. Hilmas, and W.G. Fahrenholtz, "Hot Pressing of Tantalum Carbide With and Without Sintering Additives," *J. Am. Ceram. Soc.*, **90** [2] 393-401 (2007).
- [28]. I.G. Talmy, J.A. Zaykoski, and M.M. Opeka, "Synthesis, Processing and Properties of TaC-TaB<sub>2</sub>-C Ceramics," *J. Eur. Ceram. Soc.*, **30**, 2253-63 (2010).
- [29]. C. Kim, G. Gottstein, and D.S. Grummon, "Plastic Flow and Dislocation Structures in Tantalum Carbide: Deformation at Low and Intermediate Homologous Temperatures," *Acta Metall. Mater.*, **42** [7] 2291-2301 (1994).
- [30]. L. Liu, F. Ye, and Y. Zhou, "New Route to Densify Tantalum Carbide at 1400°C by Spark Plasma Sintering," *Mater. Sci. Eng. A*, **528**, 4710-14 (2011).
- [31]. M. Hoffman and W.S. Williams, "A Simple Model for the Deformation Behavior of Tantalum Carbide," *J. Am. Ceram. Soc.*, **69** [8] 612-14 (1986).

## **CHAPTER 6: THE EFFECT OF SINTERING TEMPERATURE ON CARBON VOLATILITY DURING RESISTANCE SINTERING OF TANTALUM CARBIDE NANOPOWDERS PRODUCED BY SOLVOTHERMAL SYNTHESIS**

### **A. Introduction**

TaC has a high melting temperature as a consequence of the strong covalent bonding resulting from the d-orbital/p-orbital interactions between tantalum and carbon.<sup>[1-3]</sup> High melting temperature and covalent bonding create processing challenges and TaC is a difficult material to sinter to full density. Sintering of TaC into high-density specimens has proven to be a challenge. Fully dense TaC has recently been reported in the literature using resistance sintering at 2123 K in argon atmosphere.<sup>[4-5]</sup> Sub-micron powders were used and applied pressures of 263 MPa or 363 MPa resulted in full density. If 100 MPa of pressure was applied, then a density only 89% of theoretical was obtained and was similar whether sintering at 2073 or 2423 K.

In another example, 97.5% of theoretical density was obtained by conventional sintering in the temperature range of 2423-2623 K, without the application of pressure and in a flowing argon atmosphere.<sup>[6]</sup> At 2423 K, the density was near 95%, with slight improvement at the higher temperatures. The relatively good densities were attributed to a small particle size with a narrow particle size distribution (average particle size of 250 nm). A density between 70-80% was obtained for coarser powders having an average particle size of 600 nm, but having a wide distribution containing particle sizes greater than one micrometer.

Other reports highlight enhanced densification when using small particle sizes.<sup>[7-9]</sup> Decreasing the particle size reduces sintering temperature and apparently changes the mechanism for mass transport, and therefore the sintering mechanism. Densification is simultaneously accompanied by rapid grain growth unless pressure greater than 1.5 GPa is applied and has been commonly cited for poor densification behavior, via entrapment of porosity.<sup>[7,10-16]</sup> The rapid grain growth has been described as a consequence of grain boundary sliding, and alternatively by the similar activation energies for sintering and grain growth (activation energy for mass transport processes being higher than that for

grain growth). However, higher densities have been obtained in the presence of additives that resulted in even greater grain growth, indicating that grain growth is not the primary cause for poor densification behavior.<sup>[17]</sup>

An initial sintering study of TaC nanopowder produced by solvothermal synthesis indicated that spherical pores formed on flat interfaces between grains at higher temperatures that were not observed at lower temperatures.<sup>[18]</sup> The difference in shape and size of the triple-point porosity and the pores at the grain interfaces suggest two separate pore populations exist. The triple-point porosity is irregular in shape and the interface porosity is spherical and smaller. The spherical morphology of the pore distribution at the interfaces was observed when sintering at 2473 K and not at a sintering temperature of 2123 K. Furthermore, excessive amounts of carbon, with five percent or more, produced microstructures with an abundance of spherical pores at TaC interfaces. The two observations indicate that a vapor facilitated by excess carbon in the microstructure likely produces the spherical cavities. A vapor transport mechanism could explain the coarsening without densification that is commonly observed for TaC and should be avoided for obtaining high density TaC.

Another mechanism that can lead to mass transport by vaporization is by reaction of residual oxide with TaC to produce carbon monoxide vapor.<sup>[19]</sup> Three percent carbon additions to TaC reduced the presence of spherical pores at TaC interfaces after sintering, most likely because of more complete elimination of the oxide.<sup>[18]</sup> Other authors have explained poor densification behavior as a result of surface oxides and removal of these oxides were found to promote densification.<sup>[11,17]</sup> A combination of optimized carbon addition to TaC powders and optimized sintering temperature are expected to promote densification by reducing vapor transport.

This work studies the concepts of densification and vapor transport more systematically as a function of temperature to establish optimum sintering temperatures. Microstructural development, grain growth, porosity/density, and stoichiometry of the resulting TaC during resistance sintering is investigated. Carbon loss from TaC is observed above a critical temperature for the current process that should not be exceeded. Two basic mechanisms for the initiation of vapor transport in TaC are suggested in addition to vapor formation facilitated by excess carbon in the microstructure.

## B. Experimental Procedures

TaC powders were prepared by methods previously developed.<sup>[18,20-22]</sup> The average primary particle size, particle size, and C/Ta ratio were 25 nm, 73 nm, and 0.94, respectively. For each sample, 14.55 grams of TaC and 0.45 grams of carbon (Lampblack 101, Degussa, Parsippany, NJ) were added to a 125 ml nalgene bottle along with 80 grams of spherical zirconia media (~5 mm diameter) and tumbled for 30 min to form more uniform agglomerates. The powder was separated from the media and then added to a graphite-foil lined graphite die with an 18.75 mm diameter. Pressing of the powders in the die was performed using a uniaxial pressure of 30 MPa before sintering.

The powders were sintered using a resistance sintering furnace (Model HP D 25, FCT Systeme, GmbH, Frankenblick, Germany). A uniaxial pressure of 50 MPa was applied prior to heating. A heating rate of 50 K/min was applied to various dwell temperatures. Dwell time was a constant 10 min after which the electrical power supply was shut off. Temperature was measured at the outside surface of the graphite die. The measured temperature at the outside of the die is lower than the sample temperature. The measured temperature was calibrated to correspond to the axial temperature measurement resulting from the standard 20 mm die configuration that is supplied by FCT Systeme, GmbH for making future comparisons. Dwell temperatures from 1973-2373 K were evaluated.

Scanning electron microscopy (SEM) was performed (FEI™ Quanta 200F, FEI Company, Hillsboro, OR) to observe the microstructural evolution. An accelerating potential of 20 kV at a working distance from 10-12 mm was used for the imaging. Samples were fractured for grain size measurements. Four random fragments were imaged. Two random imaging locations on each fragment were selected. Two lines were drawn across the eight images in random locations and the grain diameters of grains that the lines intersected were measured. A minimum of one hundred grain diameters were measured. Any additional measurements, up to two hundred grain diameters, were found to produce an average grain diameter varying by 2% or less using this method. X-ray diffraction (XRD) measurements were performed on a diffractometer (D2 Phaser, Bruker AXS, Inc., Madison, WI) by scanning from 15-115 °2θ using a step size of 0.04 °2θ and a dwell time of two seconds. Lattice parameters were measured by cell refinement using

software (Jade 8, Materials Data, Inc., Livermore, CA). Porosity was analyzed by measuring density by the immersion technique (ASTM C830-00 standard technique)<sup>[23]</sup> and then considering the bulk density, apparent specific gravity, and theoretical density of 14.5 g/cm<sup>3</sup>.

### C. Results and Discussion

*In situ* ram displacement and displacement rate during resistance sintering is demonstrated in Figure 6-1. A slight negative displacement is observed prior to sintering because of a carbothermal reduction (CR) reaction between free carbon and Ta<sub>2</sub>O<sub>5</sub> impurities.<sup>[18]</sup> The CR process is assumed to be complete before sintering of the TaC phase because the displacement stops completely before rapidly increasing due to sintering. Densification of TaC begins just below 1873 K. Most of the densification is complete by 1973 K, but continues slowly with increasing temperature or dwell time.

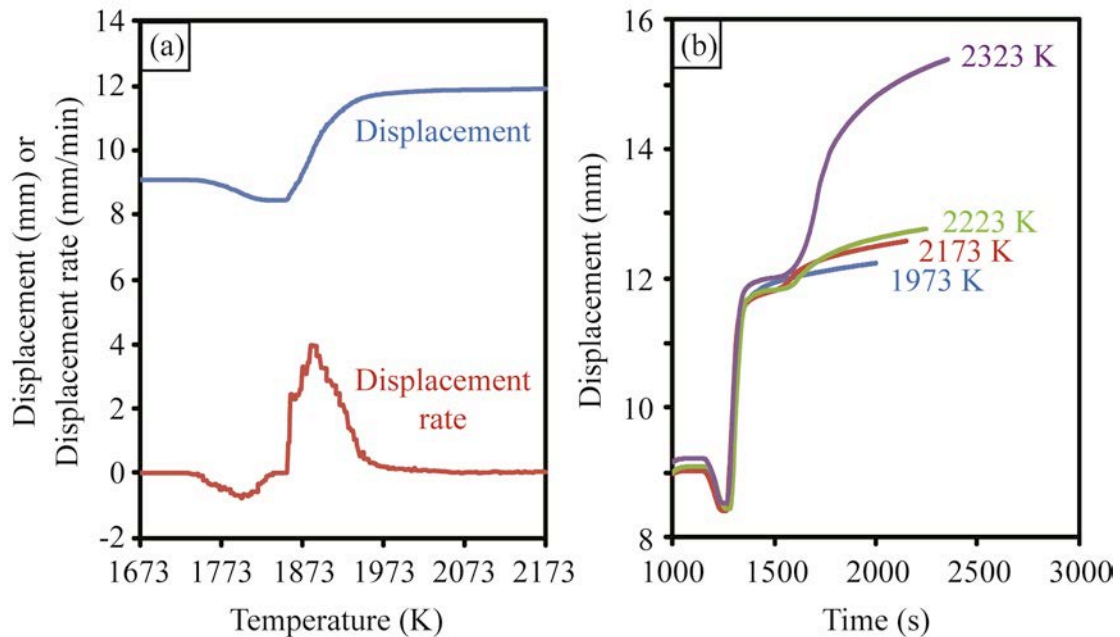


Figure 6 - 1. (a) Displacement and displacement rate during resistance sintering of tantalum carbide as a function of temperature and (b) displacement as a function of time at different sintering temperatures. (With color)

Figure 6-1b demonstrates that the sintering, up to the beginning of the dwell period, was essentially identical for all samples. This is because the majority of

densification occurs prior to the lowest dwell temperature that was used, 1973 K. The displacement continued during the dwell period when sintering at 1973 K at a slightly decreasing rate. When the dwell temperature was 2173 K or more, an increase in displacement rate was observed at the beginning of the dwell that was followed by a slow decay in the rate with time. The extent of the displacement during temperature dwelling was amplified with increasing temperature.

It became evident that TaC was being extruded out of the die between the punches and the die wall after removing the samples from the dies and could account for additional displacement during the dwell time. Plastic deformation has been observed in TaC previously at temperatures as low as 1553 K.<sup>[24,25]</sup> Plastic flow is considered a dominant sintering mechanism leading to densification in TaC, at least in early stages, and could explain why extrusion is observed.<sup>[7,26]</sup> At a dwell temperature of 2373 K, there is an additional contribution caused by permanent deformation of the punches.

Displacement caused by extrusion and deformation of the die did not occur until reaching the dwell temperature. This is possibly explained by the thermal distribution in the die. If there is a more direct path for current to pass through the punches and sample rather than the die, then more resistance heating of the punches will occur relative to the die resulting in higher punch temperatures. The higher temperature of the punches compared to the die would cause them to expand more than the die, closing the gap between them. As the dwell temperature is reached and the temperature becomes distributed more evenly, a small gap between the die and punches can develop allowing material to be extruded into the gap.

Since there is displacement caused by extrusion of material from the die and deformation of punches during the dwell period, it is impossible to make any general conclusions concerning the *in situ* displacement and displacement rate caused by densification of TaC during the dwell time. Since the displacement rate does not completely reach zero for any of the samples before the dwell temperature, it cannot be concluded whether or not densification had stopped, making it difficult to make any general conclusions concerning the final stages of sintering from the *in situ* data. Tighter fitting die/punch combinations could be used, but comes with a risk of breaking the dies during outgassing.

The microstructural development as result of varying dwell temperature is demonstrated in Figure 6-2. When the sintering temperature is 2173 K or lower, the porosity is primarily limited to the triple points and grain growth is observed as the temperature is increased. When the temperature is increased from 2173 K to 2233 K, there is a transition in the microstructural development. Some intragranular fracture becomes evident and grains take on an irregular morphology because of spherical pores that develop at the interfaces between grains. The spherical pores at the interfaces indicate the initiation of vapor formation. A further increase in temperature, up to 2373 K for example, results in reduction of the triple point porosity, but an increase in spherical pores that remain at the TaC grain interfaces.

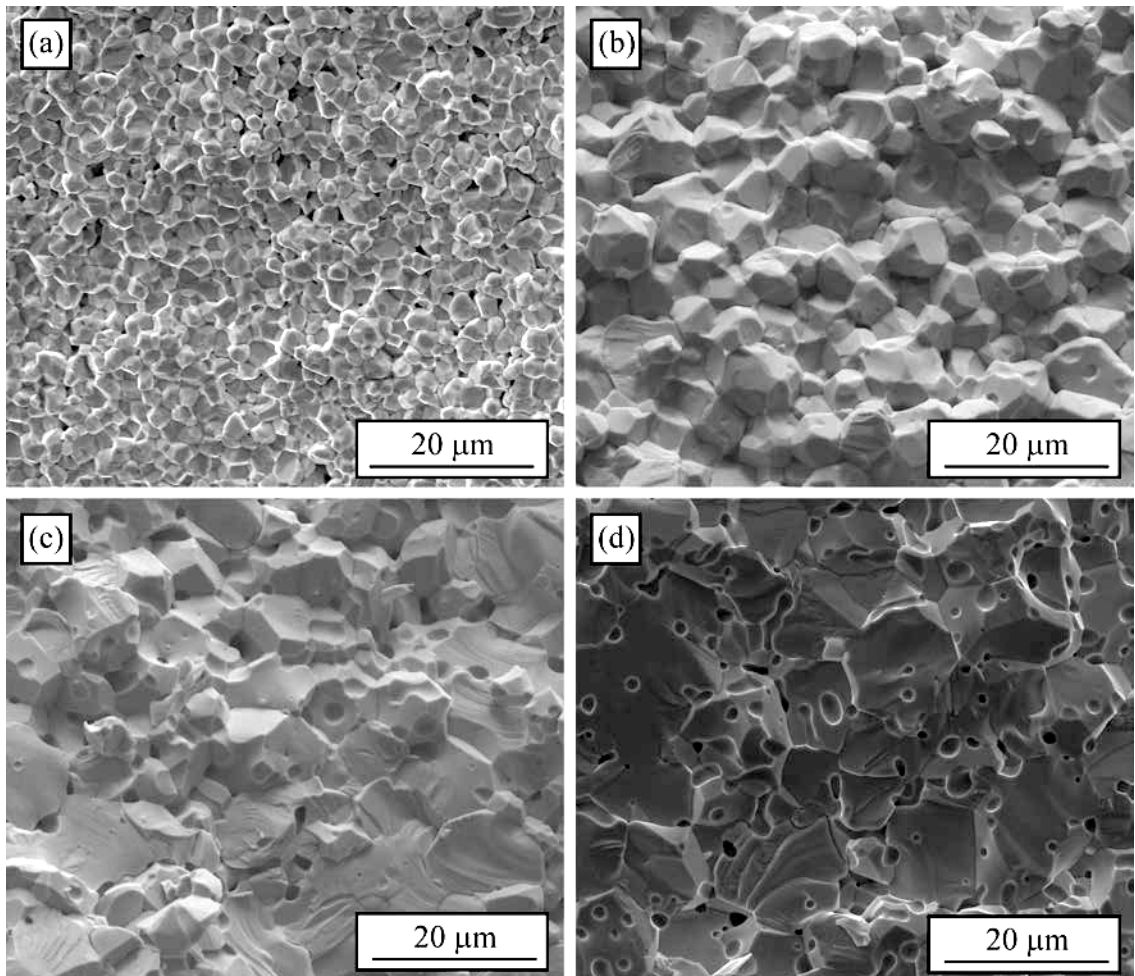


Figure 6 - 2. Secondary electron micrographs of TaC and produced by resistance sintering at (a) 1973 K, (b) 2173 K, (c) 2233 K, and (d) 2373 K.

The transition between 2173 K and 2233 K is explored in more detail to attempt to establish the basic mechanism(s) leading to the poor densification behavior in TaC that result in the microstructures like that observed in Figure 6-2d. This type of microstructure is found frequently in recent literature.<sup>[6,9,27]</sup>

The average grain sizes of the samples are provided in Figure 6-3. When sintering at 1973 K, the size was approximately 2.5  $\mu\text{m}$ . This represents grain growth over two orders of magnitude during resistance sintering of TaC nanopowders and without entrapping porosity. Further increases in temperature, up to 2233 K, resulted in grain growth up to 8.1  $\mu\text{m}$ . Based on these results and previous work that used shorter dwell times, most of the grain growth occurs during the temperature ramp.<sup>[18]</sup> The rapid grain growth over orders of magnitude during early stages of sintering, followed by slow growth thereafter, has been reported by other researchers.<sup>[7,12-16]</sup> Therefore it is highly unlikely that the transition in the microstructure and poor densification behavior are a consequence of entrapping porosity as a result of grain growth because it is minimal over the temperature range studied in comparison to the grain growth that occurs during early stages of sintering. A predictive equation for the grain size as a function of temperature was developed for the sintering conditions of this study and is provided in Figure 6-3.

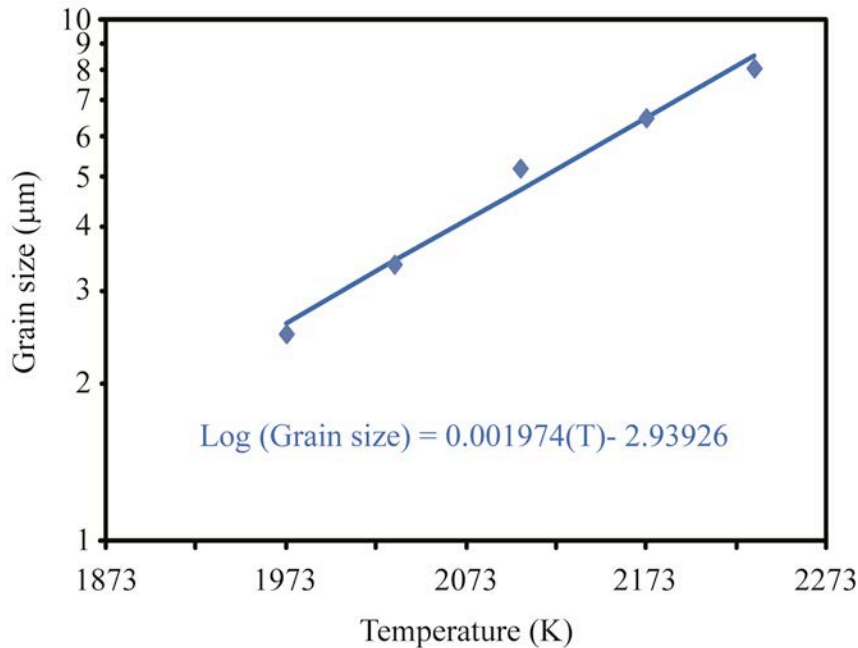


Figure 6 - 3. Average grain sizes (with fitted line) of TaC sintered by resistance sintering of nanopowders produced by solvothermal synthesis. (With color)

The measured porosities are given in Figure 6-4. All of the measured densities are within the range of 93-94% of theoretical density, indicated by the total porosity. With an increase in sintering temperature, from 1973 K to 2173 K, a slight improvement in density was observed and can be attributed to a decrease in closed porosity. Further increases in temperature did not improve the density. Closed porosity continues to be eliminated by increasing sintering temperature up to 2233 K, but open porosity increases and indicates the formation of a new pore population. Discussion for the new pore population will be discussed further with microstructural characterization. At temperatures above 2233 K, the same sintering temperature for which a fundamental change in the microstructure was observed, the closed porosity begins to increase and closed porosity increases. Apparently, the newly formed open pore distribution is becoming pinched off and forming closed porosity.

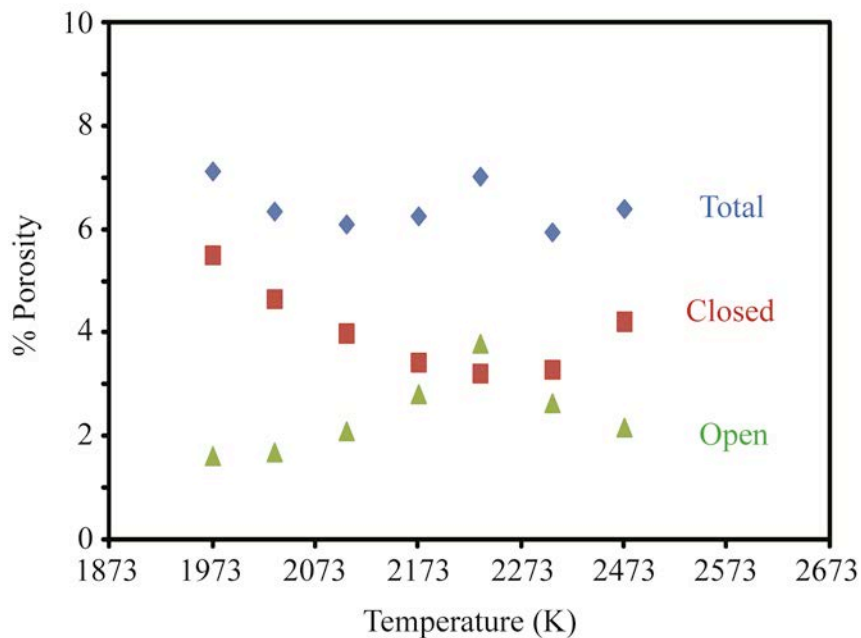


Figure 6 - 4. Total, closed, and open porosity of TaC sintered at various temperatures and calculated by the immersion technique. (With color)

A closer look at the microstructure of the sample sintered at 2233 K, where the new pore population is observed in the microstructure and a transition in the porosity occurred, provides insight into the cause for the microstructural transition with increasing temperature and overall poor densification behavior. Two likely causes have been

identified. The first cause is a residual oxide phase, which has previously been suggested as a root cause for the poor densification behavior of TaC.<sup>[11,17]</sup> This will be referred to as Type I pore generation. The second cause is associated with direct loss of carbon from TaC and will be referred to as Type II pore generation. A previous study (chapter five) indicated a third cause: vapor formation as a result of excess carbon in the microstructure and will be referred to as Type III pore generation. Type II pore generation is an intermediate step providing excess carbon, ultimately leading to Type III pore generation, but given as a unique type because of the different sources for carbon. Type I and Type II pore generation can be supported by microstructural observations.

A porous inclusion on the flat face of a TaC grain is observed in Figure 6-5. The phase contrast in the back-scattered electron image given in Figure 6-5a indicates the inclusion has a lower average atomic number than the TaC grain. These are typically found in close to a grain boundary phase with similar phase contrast, also identified in Figure 6-5, presumed to be Ta<sub>2</sub>O<sub>5</sub>. An oxide phase is known to exist at intermediate temperatures for the resistance sintering of TaC powders produced by solvothermal synthesis.<sup>[18]</sup> The carbothermal reduction reaction appears to have gone to completion prior to sintering, according to Figure 6-1. Therefore, residual Ta<sub>2</sub>O<sub>5</sub> indicates that there was not enough free carbon to completely remove Ta<sub>2</sub>O<sub>5</sub> from the TaC by carbothermal reduction. This suggests that Type III pore generation is not likely.

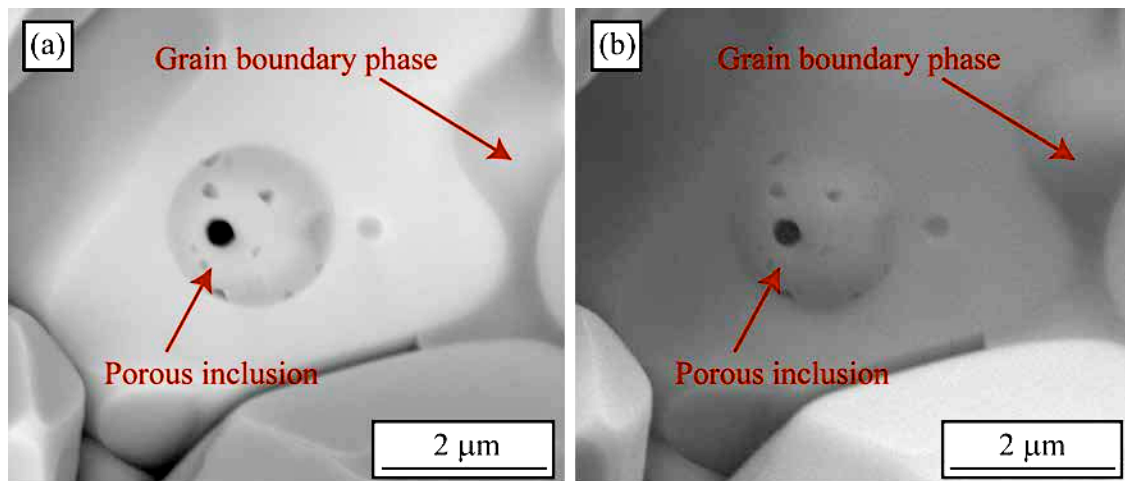


Figure 6 - 5. (a) Back-scattered electron image and (b) secondary electron image of an inclusion leading to Type I pore generation at high temperature. (With color)

The reaction between  $Ta_2O_5$  and TaC will form sub-stoichiometric TaC and CO vapor. The removal of the  $Ta_2O_5$  inclusions at the interfaces between TaC grains by a reaction between them would create a pore via Type I pore formation. Removal of  $Ta_2O_5$  from the grain boundary at higher temperatures, as it pools up at grain interfaces or vaporizes directly, may cause the formation of an open porosity network where the grain boundary impurity phase was and would explain the increase in open porosity with initial increase in sintering temperature, as observed in Figure 6-4.

Observation of inclusions that could lead to Type II pore formation is demonstrated in Figure 6-6. In this case, there is either no phase contrast in the back-scattered electron image or the inclusions are actually brighter than the TaC grain and indicate a higher average atomic number. An inclusion with brighter phase contrast could be observed if an area of the TaC grain is becoming carbon deficient/tantalum rich, resulting in a higher average atomic number. For example, stoichiometric TaC has an average atomic number of 39.5 and  $TaC_{0.8}$  has an average atomic number 43.2, which would manifest as a darker and brighter phase in back-scattered electron imaging mode, respectively.

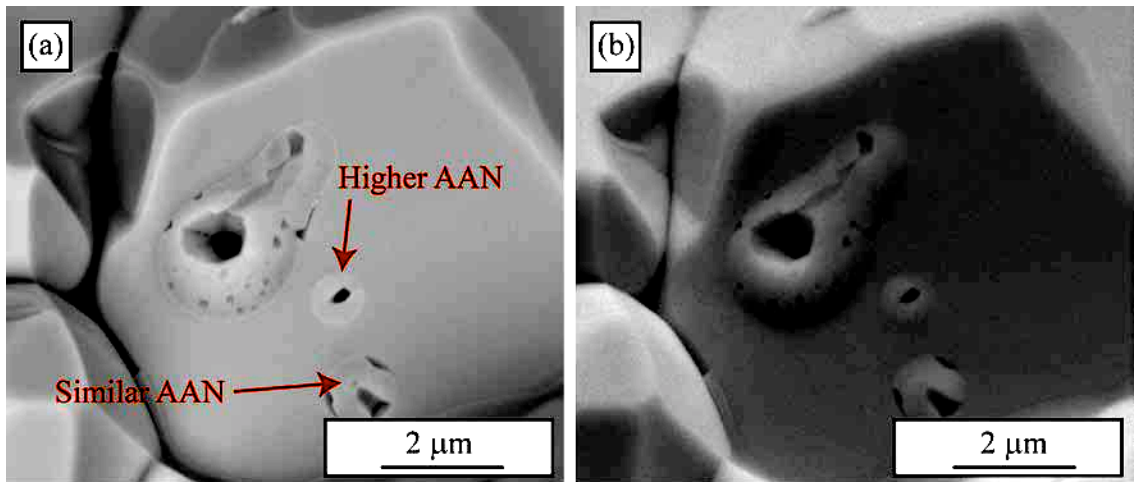


Figure 6 - 6. (a) Back-scattered electron image and (b) secondary electron image demonstrating inclusions of higher average atomic number (AAN) or similar AAN that could lead to Type II pore generation.

The generation of sub-stoichiometry in an inclusion above a critical temperature could be caused by the direct vaporization of TaC. The vaporization behavior of TaC has been studied by several researchers.<sup>[28-31]</sup> The vaporization rate depends on composition and temperature. TaC vaporizes congruently at a single composition that depends on temperature. For carbon stoichiometries higher than this composition, carbon will be preferentially lost from TaC. Conversely, tantalum will be preferentially lost if the stoichiometry is lower than this composition.

The congruently vaporizing composition at 2173 K corresponds to  $C/Ta = 0.92$ . Such a composition would have an average atomic number of 40.9 and produce brighter phase contrast relative to stoichiometric TaC. The actual sample temperature for a measured sintering temperature of 2173 K in this study would be higher than measured. As temperature is increased, the congruently vaporizing composition shifts towards greater carbon deficiency. Between 2573-2673 K, the congruently vaporizing composition is no longer corresponds to sub-stoichiometric TaC, but to the Ta<sub>2</sub>C phase. Direct carbon vaporization from TaC, without requiring a reaction with Ta<sub>2</sub>O<sub>5</sub>, is a possible source for the observations in Figure 6-2c/d via Type II pore formation.

Both Type I and Type II pore formation requires the loss of carbon from TaC and increases sub-stoichiometry. To verify the loss of carbon from TaC, the lattice parameter was determined for the samples sintered at various temperatures. The lattice parameter is directly related to TaC compound stoichiometry.<sup>[32]</sup> The measured lattice parameters and corresponding carbon stoichiometries are given in Figure 6-7. There is little change in the lattice parameter for a sintering temperature up to 2273 K. The lattice parameter corresponds to carbon stoichiometry of  $0.945 \pm 0.002$  for these temperatures. This corresponds well with the stoichiometry of the powders indicating that free carbon in the powders did not react with TaC to increase the compound carbon stoichiometry. Since no free carbon was observed in the microstructure it is expected to have reacted with the oxide phase and since Ta<sub>2</sub>O<sub>5</sub> remains in the microstructure, it is assumed that the carbon is depleted. Above a sintering temperature of 2173 K, where the transition in the microstructural development was found to occur, the lattice parameter begins to decrease. This corresponds to loss of carbon from TaC, presumably as a vapor since residual carbon was not observed in the microstructure. Similarly, Liu *et al.* noted that a vapor

was released at 2173 K during resistance sintering of a TaC/TaB<sub>2</sub> composite.<sup>[13]</sup> The decrease in the carbon stoichiometry is approximately linear up to a sintering temperature of 2373 K, which corresponded to a carbon stoichiometry of 0.912. Loss of carbon from TaC has been observed in previous research with increasing temperature.<sup>[9]</sup>

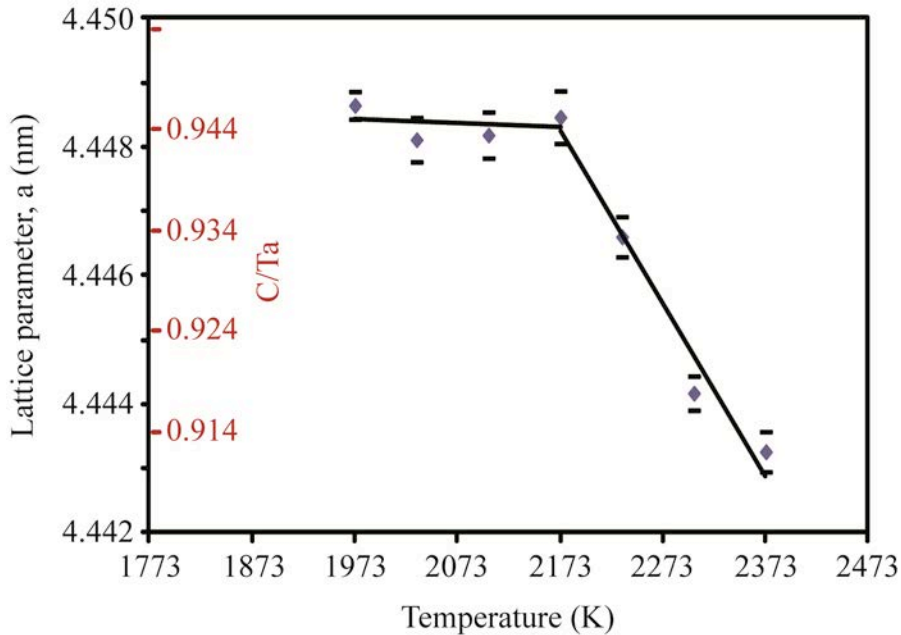


Figure 6 - 7 Lattice parameter of tantalum carbide after resistance sintering at different temperatures. The scale to the right corresponds to the carbon stoichiometry from Bowman.<sup>[32]</sup> (With color)

A recent report has proposed an evaporation/condensation sintering mechanism, presumed to be a result of oxide impurity phases, to be the cause of poor densification behavior of TaC.<sup>[13,19]</sup> Although a detrimental effect of oxide phase is often reported, its effect on grain growth and pore entrapment is commonly cited without establishing a mechanism. It is likely that the presence of an oxide phase may contribute to the formation of a vapor by reacting with TaC to assist the initiation of a non-densifying evaporation/condensation sintering mechanism. The unique aspect of this work is that direct carbon volatility from TaC is also observed. Both vapor forming mechanisms occurred for a sintering temperature greater than 2173 K. The initiation sites for vaporization appear to be on flat interfaces between TaC grains.

To obtain fully dense TaC, it will be necessary to avoid an evaporation/condensation sintering mechanism. Removing the oxide phase via improved

powder processing or by optimization of free carbon additions to remove the oxide phase *in situ* are reasonable approaches. However, it will also be necessary to stay below temperatures at which TaC begins to lose carbon. This work and recent literature suggests resistance sintering should be performed at temperatures below 2173 K to achieve this.<sup>[13]</sup>

Zhang *et al.* have suggested that the best sintering aids for TaC would be those that promoted densification below the temperatures where rapid grain growth occurs.<sup>[17]</sup> However, this hypothesis is flawed since grain growth was determined not to be the cause for poor densification. The best sintering aids will be those that promote densification while inhibiting carbon loss because the carbon facilitates vapor formation. One possible approach is to inhibit carbon diffusion in TaC. Assuming that the carbon loss occurs at the TaC interfaces and is a carbon sink, and that carbon in the bulk of the grain is a source, then the inhibition of carbon diffusion in the bulk will inhibit the transport of carbon to the surface. Reduced carbon supply to the interface could inhibit availability for forming a vapor.

#### **D. Conclusions**

Densification of TaC nanopowders occurred primarily during the heating cycle when using resistance sintering to sinter in the range of 1973-2373 K. The grain growth over this temperature range was not significant compared to grain growth during the early stages of sintering (i.e. during heating). A significant amount of trapped porosity in the microstructure was observed at sintering temperatures that were 2233 K or higher, but not at the lower sintering temperatures. Therefore, entrapment of porosity as a result of grain growth is discredited as the cause for poor densification behavior of TaC.

Entrapped porosity in the microstructure was observed above 2173 accompanied by loss of carbon from TaC. Loss of carbon from TaC via vapor formation appears to be initiated at the interfaces between TaC grains. Two types of pore formation mechanisms were identified. Type I pore formation is likely a result of reaction between TaC and residual Ta<sub>2</sub>O<sub>5</sub>. Residual Ta<sub>2</sub>O<sub>5</sub> can remain from incomplete carbothermal reduction if there is insufficient carbon during carbothermal reduction. Type II pore formation could occur by direct loss of carbon from TaC in vacuum. Complete removal of Ta<sub>2</sub>O<sub>5</sub> will

prevent Type I pore generation from occurring. Resistance sintering of TaC nanopowders at 2173 K or less can be used to inhibit Type II pore generation.

## E. References

- [1]. D.L. Price, J.M. Wills, and B.R. Cooper, "Linear-Muffin-Tin-Orbital Calculation of TaC(001) Surface Relaxation," *Phys. Rev. B*, **48** [20] 15301-10 (1993).
- [2]. G.V. Samsonov, "How the Defect Content of the Carbon Sublattice Influences the Properties of Refractory Transition-Metal Carbides," *Inorg. Mater.*, **9** [12] 1893-8 (1973).
- [3]. M. Sahnoun, C. Daul, J.C. Parlebas, C. Demangeat, and M. Driz, "Electronic Structure and Optical Properties of TaC from the First Principles Calculation," *Eur. Phys. J. B*, **44** [3] 281-6 (2005).
- [4]. S.R. Bakshi, V. Musaramthota, D.A. Virzi, A.K. Keshri, D. Lahiri, V. Singh, S. Seal, and A. Agarwal, "Spark Plasma Sintered Tantalum Carbide-Carbon Nanotube Composite: Effect of Pressure, Carbon Nanotube Length and Dispersion Technique on Microstructure and Mechanical Properties," *Mater. Sci. Eng. A*, **528**, 2538-47 (2011).
- [5]. S.R. Bakshi, V. Musaramthota, D. Lahiri, V. Singh, S. Seal, and A. Agarwal, "Spark Plasma Sintered Tantalum Carbide: Effect of Pressure and Nano-Boron Carbide Addition on Microstructure and Mechanical Properties," *Mater. Sci. Eng. A*, **528**, 1287-95 (2011).
- [6]. J.-X. Liu, Y.-M. Kan, and G.-J. Zhang, "Pressureless Sintering of Tantalum Carbide Ceramics without Additives," *J. Am. Ceram. Soc.*, **93** [2] 370-73 (2010).
- [7]. P.S. Kislyi, S.A. Shvab, and F.F. Egorov, "Sintering Kinetics of Tantalum Carbide," *Powder Metall. And Met. Ceram.*, **21** [10] 765-7 (1982).
- [8]. B.-R. Kim, K.-D. Woo, J.-M. Doh, J.-K. Yoon, and I.-J. Shon, "Mechanical Properties and Rapid Consolidation of Binderless Nanostructured Tantalum Carbide," *Ceram. Intl.*, **35**, 3395-400 (2009).
- [9]. I.G. Talmy, J.A. Zaykoski, and M.M. Opeka, "Synthesis, Processing and Properties of TaC-TaB<sub>2</sub>-C Ceramics," *J. Eur. Ceram. Soc.*, **30**, 2253-63 (2010).
- [10]. W.C. Yohe and A.L. Ruoff, "Ultrafine-Grain Tantalum Carbide by High Pressure Hot Pressing," *Ceram. Bull.*, **57** [12] 1123-30 (1978).
- [11]. J. Sautereau and A. Mocellin, "Sintering Behavior of Ultrafine NbC and TaC Powders," *J. Mater. Sci.*, **9**, 761-71 (1974).
- [12]. S.A. Shvab and F.F. Egorov, "Structure and Some Properties of Sintered Tantalum Carbide," *Sov. Powder. Metall. Met. Ceram.*, **21** [11] 894-7 (1982).

- [13]. L. Liu, F. Ye, X. He, and Y. Zhou, "Densification Process of TaC/TaB<sub>2</sub> Composite in Spark Plasma Sintering," *Mater. Chem. Phys.*, **126**, 459-62 (2011).
- [14]. Y.E. Geguzin and Y.I. Klinchuk, "Mechanism and Kinetics of the Initial Stage of Solid-Phase Sintering of Compacts from Powders of Crystalline Solids," *Poroshk. Metall.*, [7] 17-25 (1976).
- [15]. M.F. Ashby and H.A. Verral, "Diffusion-Accommodated Flow and Superplasticity," *Acta Metall.*, **21**, 149-63 (1974).
- [16]. Y.E. Geguzin, "Diffusional Deformation of Porous Crystalline Structures," *Fiz. Tverd. Tela*, **17** [7] 1950-4 (1957).
- [17]. X. Zhang, G.E. Hilmas, and W.G. Fahrenholtz, "Hot Pressing of Tantalum Carbide With and Without Sintering Additives," *J. Am. Ceram. Soc.*, **90** [2] 393-401 (2007).
- [18]. B.M. Clark, J.P. Kelly, and O.A. Graeve, "Recent Advances on Bulk Tantalum Carbide Produced by Solvothermal Synthesis and Spark Plasma Sintering," *Mater. Res. Soc. Symp. Proc.*, submitted (2012).
- [19]. L. Liu, F. Ye, and Y. Zhou, "New Route to Densify Tantalum Carbide at 1400°C by Spark Plasma Sintering," *Mater. Sci. Eng. A*, **528**, 4710-14 (2011).
- [20]. J.P. Kelly, R. Kanakala, and O.A. Graeve, "A Solvothermal Approach for the Preparation of Nanostructured Carbide and Boride Ultra-High-Temperature Ceramics," *J. Am. Ceram. Soc.*, **93** [10] 3035-38 (2010).
- [21]. J.P. Kelly and O.A. Graeve, "Statistical Experimental Design Approach for the Solvothermal Synthesis of Nanostructured Tantalum Carbide Powders," *J. Am. Ceram. Soc.*, **94** [6] 1706-15 (2011).
- [22]. B.M. Clark, J.P. Kelly, and O.A. Graeve, "Exploring the Synthesis Parameters and Spark Plasma Sintering of Tantalum Carbide Powders Prepared by Solvothermal Synthesis," *Mater. Res. Soc. Symp. Proc.*, **1373**, 7-17 (2010).
- [23]. "Standard Test Methods for Apparent Porosity, Liquid Absorption, Apparent Specific Gravity, and Bulk Density of Refractory Shapes by Vacuum Pressure," ASTM Designation C830-00, ASTM International, West Conshohocken, PA.
- [24]. C. Kim, G. Gottstein, and D.S. Grummon, "Plastic Flow and Dislocation Structures in Tantalum Carbide: Deformation at Low and Intermediate Homologous Temperatures," *Acta Metall. Mater.*, **42** [7] 2291-2301 (1994).

- [25]. P.F. Becher, "Mechanical Behaviour of Polycrystalline TaC," *J. Mater. Sci.*, **6**, 79-80 (1971).
- [26]. F.V. Samanov and R.Y. Petrikina, "Sintering of Metals, Carbides, and Oxides by Hot Pressing," *Phys. Sintering*, **2** [3] 1-20 (1970).
- [27]. E. Khaleghi, Y.-S. Lin, M.A. Meyers, and E.A. Olevsky, "Spark Plasma Sintering of Tantalum Carbide," *Scripta Materialia*, **63**, 577-80 (2010).
- [28]. A.I. Gusev, "The Evaporation of Vanadium, Niobium, and Tantalum Cubic Carbides," *High Temp.*, **31** [2] 182-7 (1993).
- [29]. T.A. Nikol'skaya and R.G. Avarbé, "Temperature Dependence and Velocity of the Congruent Evaporation of the Tantalum Carbide Phase," *High Temp.*, **7** [6] 1021-5 (1969).
- [30]. R.W. Bartlett and F.A. Halden, "Study of Growth Parameters for Refractory Carbide single Crystals," SRI Project FMU-4892, Final Report, National Aeronautics and Space Administration, Washington, D.C., 1967.
- [31]. D.L. Deadmore, "Vaporization of Tantalum-Carbide-Hafnium-Carbide Solid Solutions at 2500° to 3000° K," NASA TN D-2512, National Aeronautics and Space Administration, Washington, D.C., 1964.
- [32]. A.L. Bowman, "The Variation of Lattice Parameter with Carbon Content of Tantalum Carbide," *J. Phys. Chem.*, **65** [9] 1596-8 (1961).

## CHAPTER 7: OBTAINING HIGH DENSITY TANTALUM CARBIDE COMPACTS VIA RESISTANCE SINTERING OF NANOPOWDERS PRODUCED BY THE SOLVOTHERMAL SYNTHESIS METHOD

### A. Introduction

TaC has been a material of interest for several applications that include high temperature crucibles, abrasion/wear resistant coatings, diffusion barriers, catalysts, filaments, aluminum metal processing, solid rocket motor nozzles, and thermionic energy conversion and emitters.<sup>[1-15]</sup> TaC is unique in that it has a mixture of ceramic-like and metallic-like properties and is a direct consequence of bonding. For example, TaC has a high melting temperature (~4000 K) because of the covalent d-orbital/p-orbital interactions between the tantalum and carbon atoms, but has metallic-like electrical and thermal conductivity because of overlapping of these same bands, providing empty states just above the Fermi energy, and an extra tantalum d-orbital electron.<sup>[16-18]</sup>

Despite the interesting properties of TaC, the prospect of using TaC as a high temperature structural material has been dismal because of limitations in mechanical properties and poor oxidation resistance in comparison with other structural materials.<sup>[19-29]</sup> The goal of this work is to begin to address the mechanical properties issue via obtaining high density TaC. The mechanical strengths reported in the literature range from approximately 100-700 MPa with a clear trend towards higher strengths with higher densities. This is because of the reduction of strength-limiting flaws. Besides higher densities, reduction of grain sizes can also improve the mechanical strength. However, densification of TaC is also accompanied by rapid grain growth during the initial stages of sintering fine powders.<sup>[11,30-35]</sup> The focus of this work is to produce high density TaC as a first step.

The sintering of TaC to full density has been a challenge. Only recently has fully dense TaC of high quality been reported in the literature, by the use of resistance sintering.<sup>[19,36]</sup> Submicron powders were used and applied pressures exceeding the capability of the commonly used graphite hardware was necessary. It would be beneficial to sinter TaC to full density at more modest pressures.

Liu *et al.* used pressureless sintering and were able to produce TaC that was as much as 97.5% dense.<sup>[22]</sup> They found that the use of submicron powders with a narrow particle size distribution and with oxygen content less than 0.5% resulted in the highest densities. This stresses the importance of powder processing. It is also worth noting that carbon stoichiometry is not reported in their study, which could affect the sintering behavior. It seems that the combination of powder processing, to produce suitable TaC with a small and narrow particle size distribution, and the use of moderate pressure could produce fully dense TaC.

A solvothermal synthesis method has been developed for the synthesis of TaC nanopowders.<sup>[37-39]</sup> Some flexibility of the process has been demonstrated for modifying the characteristics of the resulting TaC powders. A resistance sintering process, using TaC nanopowders has also been developed.<sup>[40]</sup> Recent results (chapter six) have suggested that optimization of free carbon additions to TaC, for complete removal of Ta<sub>2</sub>O<sub>5</sub> impurity, and sintering at temperatures of 2173 K or less, to prevent carbon loss from TaC, is promising for obtaining high-density TaC by resistance sintering. This work explores this concept in more detail.

The densification behavior, microstructure, grain size, density, and the lattice parameter of TaC are monitored to establish the optimum amount of added carbon necessary to produce high density TaC from nanopowders produced by the solvothermal synthesis method. Further process optimization that could assist obtaining fully dense TaC is discussed.

## **B. Experimental Procedures**

TaC powders with an average primary particle size of 25 nm, particle size of 73 nm, and C/Ta ratio of 0.94 were prepared by methods previously developed.<sup>[37-40]</sup> For each sample, 15 grams of TaC and carbon (Lampblack 101, Degussa, Parsippany, NJ) were added to a 125 ml nalgene bottle along with 80 grams of cylindrical ZrO<sub>2</sub> media (~8 mm diameter and height) and tumbled for 30 min to form more uniform agglomerates. Samples containing 2.50, 2.75, 3.00, 3.25, and 3.50 weight percent carbon were prepared and will be referred to as T250, T275, T300, T325, and T350, respectively. The powder was separated from the media and then added to a graphite-foil lined graphite die with a

18.75 mm diameter. Pressing of the powders in the die was performed using a uniaxial pressure of 30 MPa before sintering.

The powders were sintered using a resistance sintering furnace (Model HP D 25, FCT Systeme, GmbH, Frankenblick, Germany). A uniaxial pressure of 50 MPa was applied prior to heating. A heating rate of 50 K/min was applied from 723 K to 2173 K. The temperature was dwelled for 10 min. Cooling was performed at a rate of 50 K/min from 2173 K to 723 K while the pressure was linearly released from 50 MPa to 10 MPa to prevent cracking, which was previously found to be problematic. Temperature was measured with two pyrometers directed at the side of the die and the top of the punches. The die temperature was used to normalize the punch temperature reported in this work.

Imaging was performed with a scanning electron microscopy (SEM) (FEI™ Quanta 200F, FEI Company, Hillsboro, OR) to observe the microstructural evolution. An accelerating potential of 20 kV at a working distance from 10-12 mm was used for the imaging. Samples were fractured for grain size measurements. Four random fragments were imaged. Two random imaging locations on each fragment were selected. Two lines were drawn across the eight images in random locations and the grain diameters of the grains that the lines intersected were measured. A minimum of one hundred grain diameters were measured. Any additional measurements, up to two hundred grain diameters, were found to produce grain diameters varying by 2% or less. X-ray diffraction measurements were performed on a diffractometer (D2 Phaser, Bruker AXS, Inc., Madison, WI) by scanning from 15-115 °2θ using a step size of 0.04 °2θ and a dwell time of two seconds. Lattice parameters were measured by cell refinement using software (Jade 8, Materials Data, Inc., Livermore, CA). The immersion technique was used to measure density.

### C. Results and Discussion

The *in situ* ram displacement during resistance sintering is demonstrated in Figure 7-1. The curves correspond to events observed in a previous study that includes degassing, particle rearrangement, Ta<sub>2</sub>O<sub>5</sub>, carbothermal reduction of Ta<sub>2</sub>O<sub>5</sub>, and the sintering of TaC.<sup>[40]</sup> The displacement corresponding to degassing, particle rearrangement, and Ta<sub>2</sub>O<sub>5</sub> formation, occurring below 1773 K, will be known as

presintering. The *in situ* results for TaC sintering without presintering is given in Figure 7-1b.

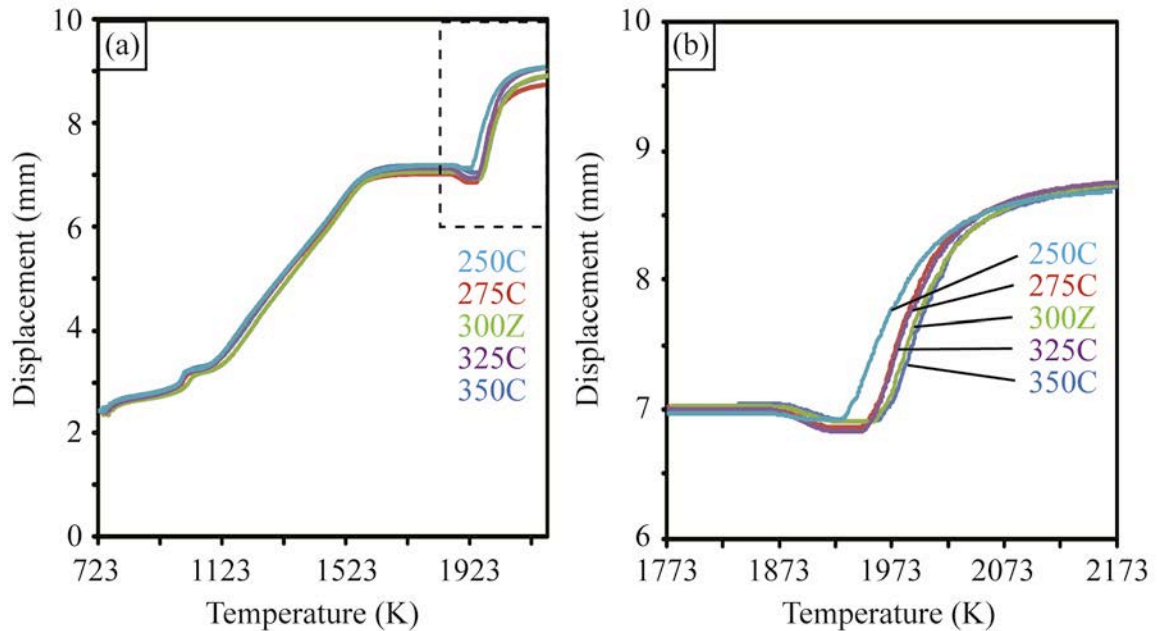


Figure 7 - 1. (a) Ram displacement during the resistance sintering of TaC/C mixtures as a function of temperature and (b) the data presented again using truncated scales and with normalized displacement. (With color)

The densification for T250 began about 20 K lower than it did for the other samples, at approximately 1933 K. Recent results (chapter five and chapter six) demonstrated the formation of a Ta<sub>2</sub>O<sub>5</sub> phase at the grain boundary, presumably liquid at higher temperatures. More Ta<sub>2</sub>O<sub>5</sub> as a result of the lower free carbon addition may have promoted earlier sintering of sample T250 and the reduction in oxide with higher carbon contents could delay densification of the other samples. However, these experiments were only performed once and verification of the results will be required before further analysis.

The microstructures of the TaC samples are demonstrated in Figure 7-2. Besides more porosity in the T250 microstructure, there does not appear to be much difference between the samples. Figure 7-2 is an image of the whole tantalum carbide samples, demonstrating that fracturing (previously an issue) was prevented by slowly cooling and releasing the pressure.

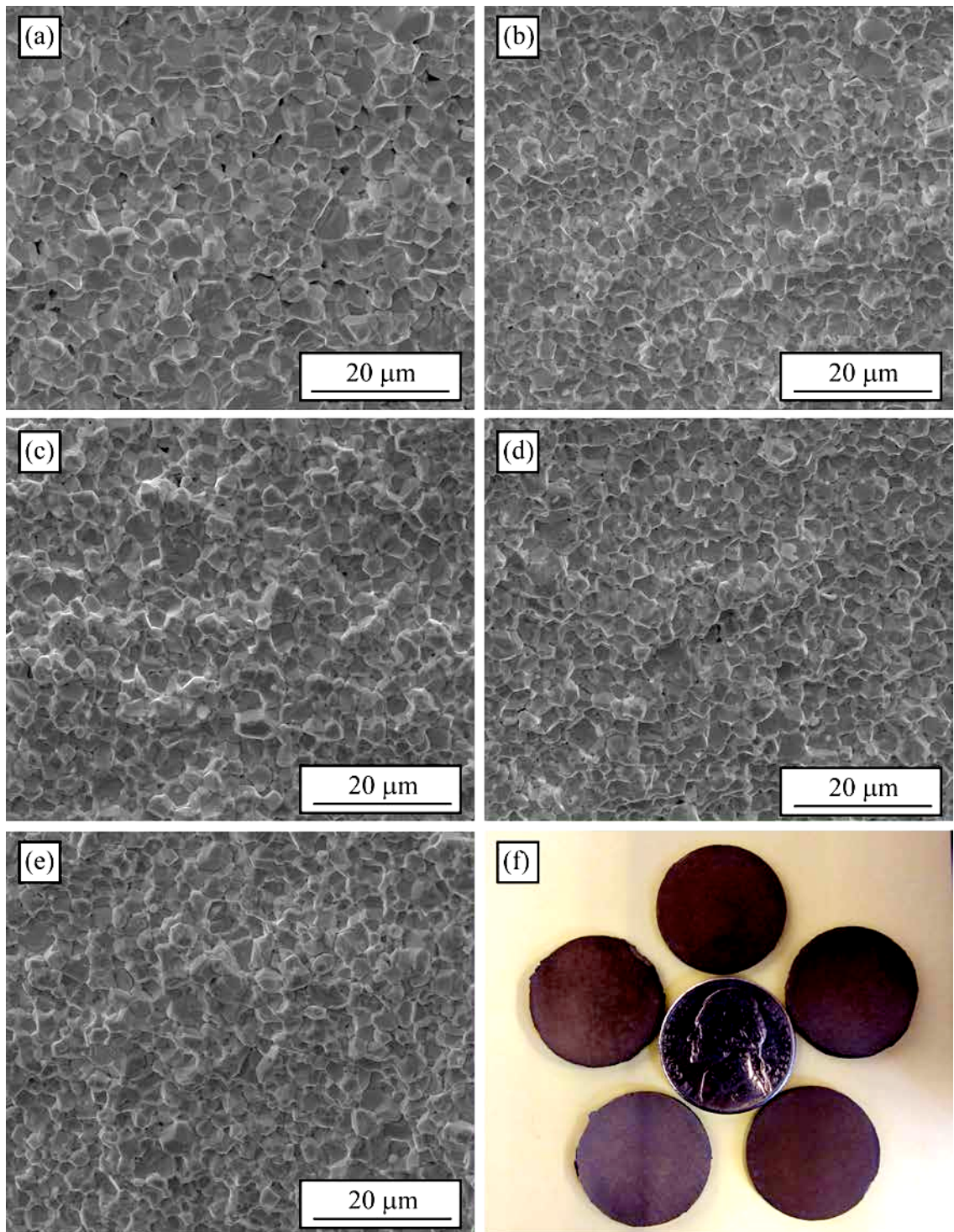


Figure 7 - 2. Secondary electron images of samples (a) T250, (b) T275, (c) T300, (d) T325, and (e) T350. (f) Optical images of the TaC samples with different free carbon contents.

The grain size measurements are given in Figure 7-3. The grain size did not change significantly with different carbon content. Assuming that free carbon content reduces the Ta<sub>2</sub>O<sub>5</sub> contaminant phase, the grain size results indicate that the amount of oxygen impurity does not affect grain growth within the range of this study. It is difficult to make any further conclusions about the effect of oxygen impurity without knowing the amount of oxygen impurity in each sample.

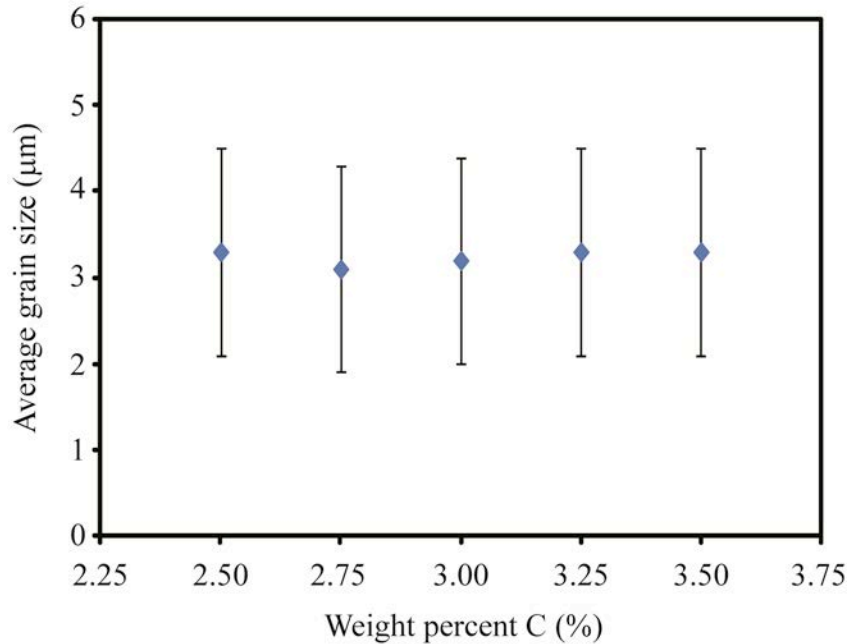


Figure 7 - 3. The average grain sizes and plus or minus one standard deviation measured for TaC as a function of carbon additions after resistance sintering at 2173 K for 10 min with an applied pressure of 50 MPa. (With color)

Sautereau and Mocellin suggest that oxygen impurities can promote grain growth at intermediate temperatures, due to the formation of a liquid phase (although they could not rule out the contribution of metallic impurities), which has been a longstanding viewpoint.<sup>[33,41]</sup> Furthermore, they observed abnormal grain growth with sintering at extended times where there was a higher content of a liquid phase and suggest that a minimum of 1% volume fraction of liquid phase is necessary to promote grain growth. Other researchers have observed abnormal grain growth in TaC/C mixtures, where the samples were deficient in carbon, which may have prevented elimination of oxygen impurities locally.<sup>[36]</sup> Yohe and Ruoff have suggested that the presence of an oxide phase

might contribute to grain growth inhibition, opposite of previous conclusions.<sup>[42]</sup> However, they do not provide support for this observation. The effect of oxygen on grain growth of TaC is unclear.

The density of the samples as a function of carbon additions to the TaC powders is given in Figure 7-4. Sample T250 had a density that was about 95% of theoretical, whereas sample T275 had a density near 97.5% of theoretical, comparable to the result obtained by Liu and coworkers by pressureless sintering.<sup>[22]</sup> Sample T300 had a density of about 98% of theoretical and further increase in carbon content did not improve the density any further, and may actually decrease the density slightly.

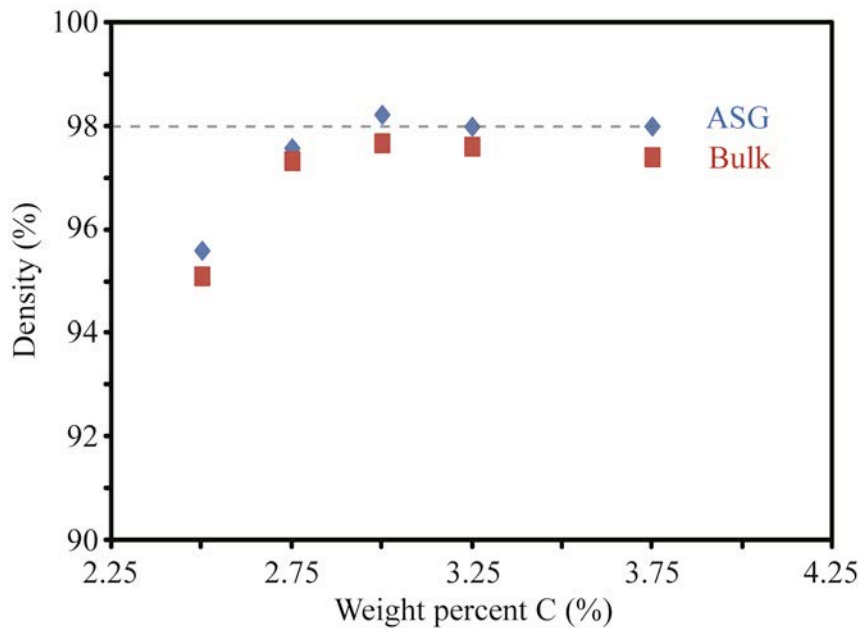


Figure 7 - 4. Apparent specific gravity (ASG) and bulk density of TaC/C mixtures sintered via resistance sintering at 2173 K for 10 min and with an applied pressure of 50 MPa. (With color)

It is interesting that T300 sample is approximately 98% dense. The same powder composition resulted in densities that were only 94% dense when processed differently. The difference in processing provides insight for improving the density. The first difference is that the TaC and carbon were mixed using different shaped mixing media. The spherical media used in the previous study only provides energy to break and reform agglomerates through point-contact collisions. Cylindrical media used in this study also provides shearing action along surfaces to assist breaking and reforming of the

agglomerates. Optimization of the agglomerate structure may enhance the elimination of porosity by more uniform densification.<sup>[40]</sup> The effect of forming adequate agglomerate structures for pressing operations to facilitate uniform densification is already well established in ceramic processing.

The second difference in processing was that the temperature was controlled with a pyrometer aimed at a surface that was closer to the sample than in previous chapters. Although the final temperatures of the two different temperature control methods were calibrated, a 50 K/min heating rate is slower when measuring the temperature closer to the sample. It may be possible that improved densification is a result of using a lower heating rate, as a result of the different temperature control methods. Reduced heating rate is thought to allow for more complete removal of the oxide phase as well, which would assist obtaining higher densities (see chapter five).

A third difference in processing is how the samples were cooled during sintering. In the previous study, pressure was maintained through quenching, by shutting off the power supply. This study gradually reduces pressure and temperature during a cooling segment that is about three times longer than quenching. During quenching, the cooling is more rapid initially. Further densification might be facilitated by the initial period of time during slow cooling. Based on the concept of densification occurring at temperatures lower than the current dwell temperature, it is worth exploring a two-step sintering process, which is known to activate sintering while suppressing grain growth during the final stages of sintering.<sup>[43-46]</sup> The feasibility of doing this is demonstrated by resistance sintering of TaC using a non-conventional heating schedule.<sup>[20]</sup>

The lattice parameter of TaC as a function of percent carbon added was studied to establish the optimum carbon amount for future studies. The lattice parameter is directly related to the carbon stoichiometry of TaC.<sup>[47]</sup> The lattice parameters and the corresponding carbon stoichiometries are provided in Figure 7-5. Three specific regimes were identified, corresponding to free carbon additions below 3.00%, between 3.00-3.25%, and above 3.25% carbon.

Initial carbon additions of up to 3.00 percent to TaC resulted in a relatively small linear increase in the TaC lattice parameter. It is assumed that the small increase is a result of the dual functionality of the carbon: the carbon is simultaneously contributing

to oxygen removal and to the TaC compound stoichiometry. The increase in lattice parameter by adding between 3.00% and 3.25% carbon is greater than the increase observed for the lower carbon contents. It is assumed that carbon is no longer contributing to oxygen removal and all of the additional carbon is contributing to increasing the lattice parameter. Further carbon additions above 3.25% did not greatly affect the lattice parameter and stoichiometric TaC is not obtained.

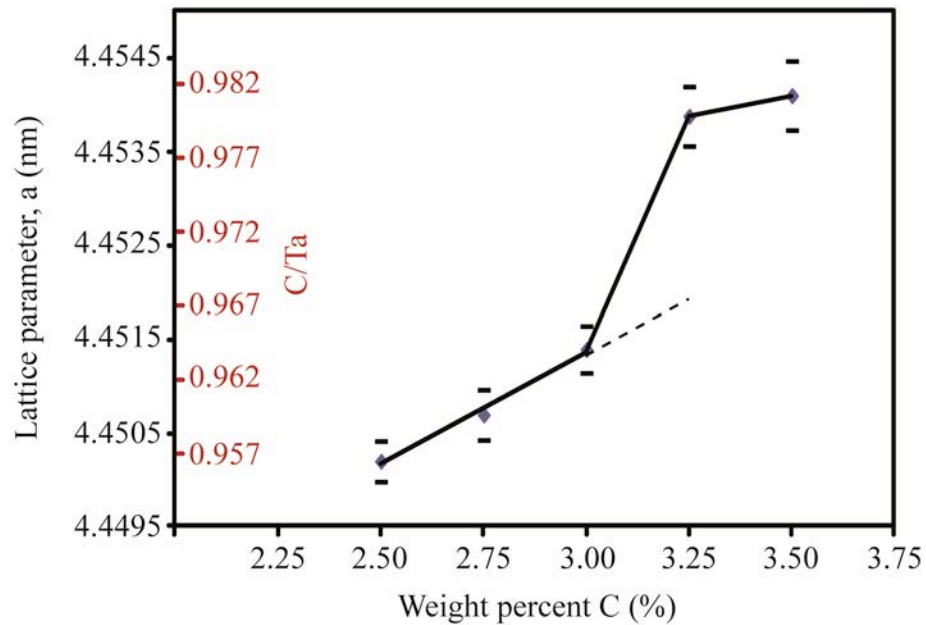


Figure 7 - 5. Lattice parameters and corresponding carbon stoichiometry of TaC with different carbon additions. (With color)

The maximum carbon stoichiometry that was obtained corresponds to  $0.981 \pm 0.003$ . Apparently, the formation of free carbon in equilibrium with TaC near stoichiometric values is more favorable than further increasing the carbon stoichiometry. The density results in Figure 7-4 and the assumptions concerning Figure 7-5 indicate that oxygen impurity in TaC inhibits densification and that a carbon addition between 3.00% and 3.25% is needed to remove it to the extent that is possible by the current processing methods. Additions of greater than 3.25% will introduce free carbon into the microstructure.

The radius ratio in TaC facilitates an open rocksalt structure where the metal lattice contact is not preserved because the carbon is not small enough to fit into the

interstitial position.<sup>[48]</sup> It has been proposed that the rocksalt structure becomes progressively unstable as the radius ratio increases above 0.414. The ratio for TaC is 0.57, close to the theoretical limit of 0.59 that would correspond to a structural change and may make it difficult to achieve a stoichiometric composition. However, nearly stoichiometric compositions with carbon stoichiometry of  $0.994 \pm 0.005$  have been prepared by Bowman for example.<sup>[47]</sup> It is likely that there is another cause for no further increase in the lattice parameter above 0.98 with increased carbon addition for this study. The possible effect of oxygen solubility in the lattice of TaC cannot be neglected, which may also explain the inability to obtain lattice parameters corresponding to stoichiometric compositions.

A reduced lattice parameter with oxygen contamination has been demonstrated for ZrC, for example.<sup>[49]</sup> For a carbon stoichiometry of 0.98 and assuming that the remainder of carbon sites are filled oxygen atoms and do not contribute significantly to the lattice parameter, giving a composition of  $\text{Ta}(\text{C}_{0.98}\text{O}_{0.02})$  and an oxygen solubility of 0.17 weight percent. This value is reasonable considering the oxygen content of sintered samples reported in the literature, which are slightly higher.<sup>[41]</sup> It is also consistent with oxygen contents reported for powders, especially when the powders are fine.<sup>[19-20,22,30,33,36,42,50-51]</sup> A more detailed analysis of the oxygen content is necessary for further analysis, but beyond the scope of this work.

Oxygen solubilized in TaC could explain peculiar features that have been observed in this work and in the literature and is demonstrated in Figure 7-6. A back-scattered electron image of sample T350 is given in Figure 7-6a. Presumably, the oxide phase has been removed to the extent possible by carbothermal reduction as has been discussed previously. However, grains can be found in the microstructure of T350 appearing as if they were melting during sintering, like the grain pointed out in Figure 7-6a, despite using a sintering temperature near half of the melting temperature for TaC. The localized melting behavior could be an effect of local oxygen concentration.

At least one other author has reported partial melting of TaC and is demonstrated by Figure 7-6b, which is an image of a carbon nanotube penetrating through a TaC grain.<sup>[36]</sup> The encapsulation of the carbon nanotube was described as impossible without local melting of TaC. The proposed mechanism was a greater joule heating of the carbon

nanotubes during resistance sintering due to the difference in the properties between carbon and TaC. Therefore, free carbon in the microstructure could also be a cause for localized melting.

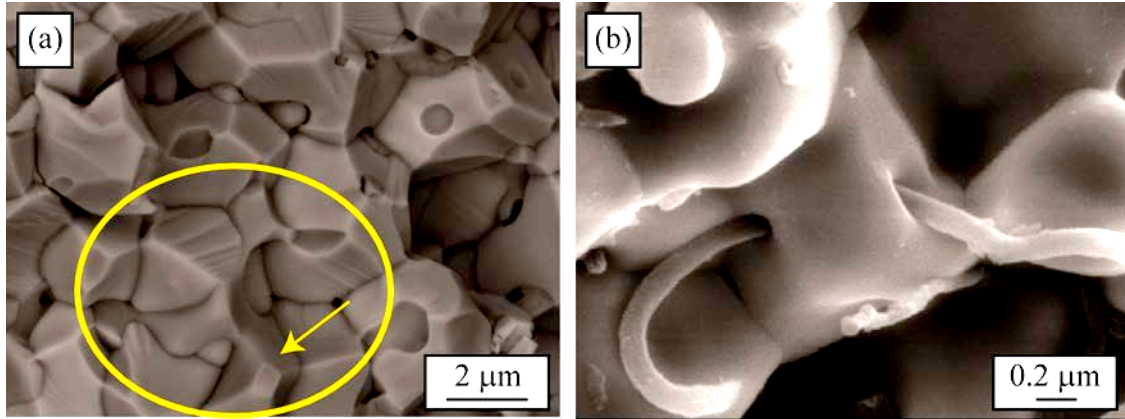


Figure 7 - 6. (a) Backscattered electron image of T350 demonstrating a “melted” TaC grain. (b) Secondary electron image of TaC grain “melted” around a carbon nanotube.<sup>[36]</sup> (With color)

While there could be other causes of localized heating, it seems plausible that oxygen solubility in the TaC lattice could be the cause for melting. Perhaps local oxygen concentrations can cause local heating during resistance sintering given the metallic-like conductivity of TaC and the insulating characteristic of oxides. It would be interesting to see if the melting effect is observed by other sintering techniques or if it is unique to field-assisted sintering because of the differences in electrical properties between the two phases. Such a mechanism has not been reported previously and is in need of further investigation.

Exploring the literature provides support for oxygen solubility in the TaC lattice. In the work by Leipold and Becher, Ta<sub>2</sub>O<sub>5</sub> was found to segregate at grain boundaries after reheating the sintered sample to 2623 K in vacuum.<sup>[51]</sup> This is demonstrated in Figure 7-7a. The oxide segregation was not noted after sintering, prior to reheating, suggesting that the oxygen may have been dissolved in the TaC lattice initially, only segregating after the reheat process.

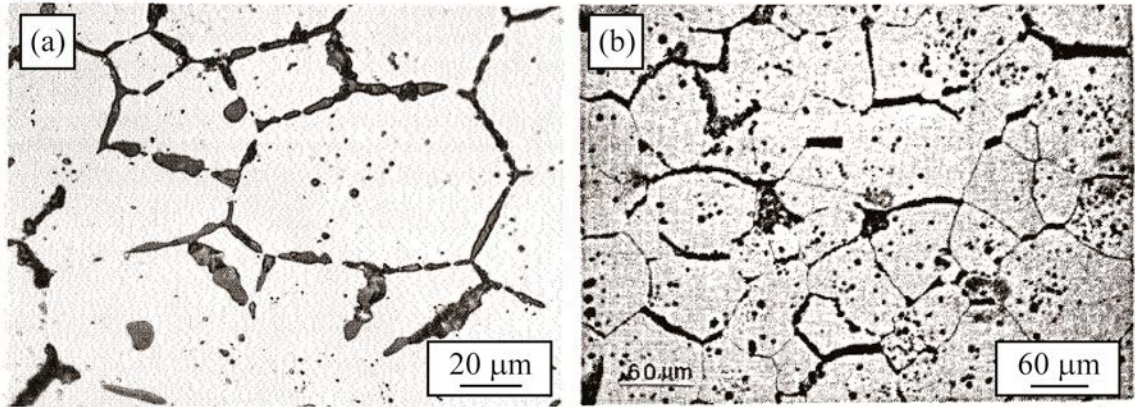


Figure 7 - 7. (a) Oxide segregation at grain boundary following 2673 K reheat treatment.<sup>[52]</sup> (b) Decohesive grain boundaries observed after creep testing at 1500°C/60 MPa for 60-70 hours, followed by 50%HF-50%HNO<sub>3</sub> etching.<sup>[53]</sup>

Decoherent grain boundaries were observed by Kim *et al.* after creep testing TaC at 1773 K and a 60 MPa pressure for a period of 60-70 hours.<sup>[53]</sup> They described this to be a consequence of grain boundary sliding, controlled by dislocation climb, resulting in cavitation and coalescence of cavities at the grain boundaries. It may be possible that cavitation mechanism did not occur, or at least is not the only contribution to formation of the observed microstructure. The 50%HF-50%HNO<sub>3</sub> etching treatment cannot be ignored, which may have removed Ta<sub>2</sub>O<sub>5</sub> from the grain boundaries to produce the microstructure. This can be imagined by comparing Figure 7-7a to Figure 7-7b. The two microstructures look similar, but the Ta<sub>2</sub>O<sub>5</sub> phase observed in Figure 7-7a is replaced by cavities and decoherent grain boundaries in Figure 7-7b.

#### D. Conclusions

The resistance sintering of TaC nanopowders prepared by solvothermal synthesis was used to obtain high-density TaC by optimizing carbon addition to the powders. A carbon addition between 3.00% and 3.25% by weight was determined to be an optimum range. A carbon addition of 3.00% and using a sintering temperature of 2173 K, a temperature previously determined to be below the temperature for which carbon is lost from TaC, resulted in densities as high as 98% of theoretical. Carbon addition below 3.00% resulted in lower density presumably because of remnant oxide phase. Carbon additions greater than 3.25% did not have a significant affect on the density or TaC

carbon stoichiometry. Grain size of TaC was unaffected by carbon additions when using the same sintering conditions.

Three processing approaches that may further enhance the density to values above 98% of theoretical were identified: improving agglomerate structure and sizes, using slower heating rates, and/or two-step sintering processes. The latter technique is also promising for reducing grain size. Applied pressure and temperature dwell time are also in need of further study. Microstructural observations similar to those observed in chapter six indicate that further reduction in the sintering temperature could be beneficial. Obtaining fully dense TaC with small grain sizes is important for obtaining suitable mechanical properties.

While structural instability may explain the difficulty achieving stoichiometric TaC, oxygen solubility on carbon lattice sites cannot be ruled out as a cause. It could also explain local melting of TaC that was observed during resistance sintering and segregation of Ta<sub>2</sub>O<sub>5</sub> at the grain boundary during prolonged heating of TaC. However, a study establishing the fundamental mechanisms of such phenomenon is lacking.

## E. References

- [1]. C. Hartmann, J. Wollweber, M. Albrecht, and I. Rasin, "Preparation and Characterization of Tantalum Carbide as an Optional Crucible Material for Bulk Aluminium Nitride Crystal Growth via Physical Vapour Transport," *Phs. Stat. Sol.*, **3** [6] 1608-12 (2006).
- [2]. E. Martínez, U. Wiklund, J. Esteve, F. Montalà, and L.L. Carreras, "Tribological Performance of TiN Supported Molybdenum and Tantalum Carbide Coatings in Abrasion and Sliding Contact," *Wear*, **253**, 1182-7 (2002).
- [3]. T. Laurila, K. Zeng, J.K. Kivilahti, J. Molarius, T. Rierkkinen, and I. Suni, "Tantalum Carbide and Nitride Diffusion Barriers for Cu Metallisation," *Microelectron. Eng.*, **60**, 71-80 (2002).
- [4]. S.J. Wang, H.Y. Tsai, and S.C. Sun, "A Comparative Study of Sputtered TaC<sub>x</sub> and WC<sub>x</sub> Films as Diffusion Barriers Between Cu and Si," *Thin Sol. Films*, **394**, 180-8 (2001).
- [5]. H.Y. Tsai, S.C. Sun, and S.J. Wang, "Characterization of Sputtered Tantalum Carbide Barrier Layer for Copper Metallization," *J. Electrochem. Soc.*, **147** [7] 2766-72 (2000).
- [6]. D.M. Li, R. Hernberg, and T. Mäntylä, "Catalytic Dissociation of Hydrogen on a Tantalum Carbide Filament in the HFCVD of Diamond," *Diam. Relat. Mater.*, **7**, 1709-13 (1998).
- [7]. J. Imahori, T. Oku, and M. Murakami, "Diffusion Barrier Properties of TaC between Si and Cu," *Thin Sol. Films*, **301**, 142-8 (1997).
- [8]. J.G. Chen, Carbide and Nitride Overlayers on Early Transition Metal Surfaces: Preparation, Characterization and Reactivities," *Chem. Rev.*, **96**, 1477-98 (1996).
- [9]. C.W. Colling and L.T. Thompson, "The Structure and Function of Supported Molybdenum Nitride Hydrodenitrogenation Catalysts," *J. Catal.*, **146** [1] 193-203 (1994).
- [10]. S.T. Oyama, Preparation and Catalytic Properties of Transition Metal Carbides and Nitrides," *Catal. Today*, **15**, 179-200 (1992).
- [11]. S.A. Shvab and F.F. Egorov, "Structure and Some Properties of Sintered Tantalum Carbide," *Sov. Powder. Metall. Met. Ceram.*, **21** [11] 894-7 (1982).
- [12]. L. Honeycutt III, W.H. Jennings, and C.R. Manning Jr., "High Temperature Erosion of Tantalum Carbide Composites," *Wear*, **37**, 209-216 (1976).

- [13]. J.C. Blais and G. Bolbach, "Study of Negative Surface Ionization on Complex Emitters," *Intl. J. Mass Spectrom. Ion Phys.*, **24**, 413-27 (1977).
- [14]. D. Steward, P.D. Wilson, R.V. Latham, and N.K. Allen, "Energy Spectra of Electrons Field Emitted from a Broad Area Composite Cathode of Tantalum Carbide," *J. Mater. Sci.*, **16**, 111-17 (1981).
- [15]. W.J. Baxter, "Work Function of Tantalum Carbide and Effects of Adsorption and Sputtering of Cesium," *J. Appl. Phys.*, **42** [7] 2682-8 (1971).
- [16]. D.L. Price, J.M. Wills, and B.R. Cooper, "Linear-Muffin-Tin-Orbital Calculation of TaC(001) Surface Relaxation," *Phys. Rev. B*, **48** [20] 15301-10 (1993).
- [17]. G.V. Samsonov, "How the Defect Content of the Carbon Sublattice Influences the Properties of Refractory Transition-Metal Carbides," *Inorg. Mater.*, **9** [12] 1893-8 (1973).
- [18]. M. Sahnoun, C. Daul, J.C. Parlebas, C. Demangeat, and M. Driz, "Electronic Structure and Optical Properties of TaC from the First Principles Calculation," *Eur. Phys. J. B*, **44** [3] 281-6 (2005).
- [19]. S.R. Bakshi, V. Musaramthota, D. Lahiri, V. Singh, S. Seal, and A. Agarwal, "Spark Plasma Sintered Tantalum Carbide: Effect of Pressure and Nano-Boron Carbide Addition on Microstructure and Mechanical Properties," *Mater. Sci. Eng. A*, **528**, 1287-95 (2011).
- [20]. L. Liu, F. Ye, and Y. Zhou, "New Route to Densify Tantalum Carbide at 1400°C by Spark Plasma Sintering," *Mater. Sci. Eng. A*, **528**, 4710-14 (2011).
- [21]. E. Khaleghi, Y.-S. Lin, M.A. Meyers, and E.A. Olevsky, "Spark Plasma Sintering of Tantalum Carbide," *Scripta Materialia*, **63**, 577-80 (2010).
- [22]. J.-X. Liu, Y.-M. Kan, and G.-J. Zhang, "Pressureless Sintering of Tantalum Carbide Ceramics without Additives," *J. Am. Ceram. Soc.*, **93** [2] 370-73 (2010).
- [23]. K. Hackett, S. Verhoef, R.A. Cutler, and D.K. Shetty, "Phase Constitution and Mechanical Properties of Carbides in the Ta-C System," *J. Am. Ceram. Soc.*, **92** [10] 2404-7 (2009).
- [24]. P.F. Becher, "Mechanical Behaviour of Polycrystalline TaC," *J. Mater. Sci.*, **6**, 79-80 (1971).
- [25]. J. Ma, Y. Du, M. Wu, and M. Pan, "One Simple Synthesis Route to Nanocrystalline Tantalum Carbide via the Reaction of Tantalum Pentachloride

- and Sodium Carbonate with Metallic Magnesium,” *Mater. Lett.*, **61**, 3658-61 (2007).
- [26]. L. Shi, Y. Gu, L. Chen, Z. Yang, J. Ma, and Y. Qian, “Formation of TaC Nanorods with a Low-Temperature Chemical Route,” *Chemistry Lett.*, **33** [12] 1546-7 (2004).
- [27]. M. Johnsson and S. Shimada, “Oxidation of  $Ta_xTi_{1-x}C$  Whiskers Under Formation of Carbon,” *J. Mater. Sci. Lett.*, **21**, 955-8 (2002).
- [28]. M. Desmaison-Brut, N. Alexandre, and J. Desmaison, “Comparison of the Oxidation Behavior of Two Dense Hot Isostatically Pressed Tantalum Carbide (TaC and  $Ta_2C$ ) Materials,” *J. Eur. Ceram. Soc.*, **17**, 1325-34 (1997).
- [29]. É.I. Golovko, L.F. Ochkas, M.S. Koval’chenko, and A.F. Nikityuk, “Oxidation of Tantalum Carbide Alloys,” *Poroshkovaya Metallurgiya*, **166** [10] 51-4 (1976).
- [30]. L. Liu, F. Ye, X. He, and Y. Zhou, “Densification Process of TaC/TaB<sub>2</sub> Composite in Spark Plasma Sintering,” *Mater. Chem. Phys.*, **126**, 459-62 (2011).
- [31]. P.S. Kislyi, S.A. Shvab, and F.F. Egorov, “Sintering Kinetics of Tantalum Carbide,” *Powder Metall. And Met. Ceram.*, **21** [10] 765-7 (1982).
- [32]. Y.E. Geguzin and Y.I. Klinchuk, “Mechanism and Kinetics of the Initial Stage of Solid-Phase Sintering of Compacts from Powders of Crystalline Solids,” *Poroshk. Metall.*, [7] 17-25 (1976).
- [33]. J. Sautereau and A. Mocellin, “Sintering Behavior of Ultrafine NbC and TaC Powders,” *J. Mater. Sci.*, **9**, 761-71 (1974).
- [34]. M.F. Ashby and H.A. Verral, “Diffusion-Accommodated Flow and Superplasticity,” *Acta Metall.*, **21**, 149-63 (1974).
- [35]. Y.E. Geguzin, “Diffusional Deformation of Porous Crystalline Structures,” *Fiz. Tverd. Tela*, **17** [7] 1950-4 (1957).
- [36]. S.R. Bakshi, V. Musaramthota, D.A. Virzi, A.K. Keshri, D. Lahiri, V. Singh, S. Seal, and A. Agarwal, “Spark Plasma Sintered Tantalum Carbide-Carbon Nanotube Composite: Effect of Pressure, Carbon Nanotube Length and Dispersion Technique on Microstructure and Mechanical Properties,” *Mater. Sci. Eng. A*, **528**, 2538-47 (2011).
- [37]. J.P. Kelly, R. Kanakala, and O.A. Graeve, “A Solvothermal Approach for the Preparation of Nanostructured Carbide and Boride Ultra-High-Temperature Ceramics,” *J. Am. Ceram. Soc.*, **93** [10] 3035-38 (2010).

- [38]. J.P. Kelly and O.A. Graeve, "Statistical Experimental Design Approach for the Solvothermal Synthesis of Nanostructured Tantalum Carbide Powders," *J. Am. Ceram. Soc.*, **94** [6] 1706-15 (2011).
- [39]. B.M. Clark, J.P. Kelly, and O.A. Graeve, "Exploring the Synthesis Parameters and Spark Plasma Sintering of Tantalum Carbide Powders Prepared by Solvothermal Synthesis," *Mater. Res. Soc. Symp. Proc.*, **1373**, 7-17 (2010).
- [40]. B.M. Clark, J.P. Kelly, and O.A. Graeve, "Recent Advances on Bulk Tantalum Carbide Produced by Solvothermal Synthesis and Spark Plasma Sintering," *Mater. Res. Soc. Symp. Proc.*, submitted (2012).
- [41]. X. Zhang, G.E. Hilmas, and W.G. Fahrenholtz, "Hot Pressing of Tantalum Carbide With and Without Sintering Additives," *J. Am. Ceram. Soc.*, **90** [2] 393-401 (2007).
- [42]. W.C. Yohe and A.L. Ruoff, "Ultrafine-Grain Tantalum Carbide by High Pressure Hot Pressing," *Ceram. Bull.*, **57** [12] 1123-30 (1978).
- [43]. X.H. Wang, X.Y. Deng, H. Zhou, L.T. Li, and I.W. Chen, "Bulk Dense Nanocrystalline BaTiO<sub>3</sub> Ceramics Prepared by Novel Pressureless Two-Step Sintering," *J. Electroceram.*, **21**, 230-3 (2008).
- [44]. X.H. Wang, P.L. Chen, and I.W. Chen, "Two-Step Sintering of Ceramics with Constant Grain-Size, II: BaTiO<sub>3</sub> and Ni-Cu-Zn," *J. Am. Ceram. Soc.*, **89**, 438-43 (2006).
- [45]. X.H. Wang, P.L. Chen, and I.W. Chen, "Two-Step Sintering of Ceramics with Constant Grain-Size, I: Y<sub>2</sub>O<sub>3</sub>," *J. Am. Ceram. Soc.*, **89**, 431-7 (2006).
- [46]. I.-W. Chen and X.-H. Wang, "Sintering Dense Nanocrystalline Ceramics without Final-Stage Grain Growth," *Nature Lett.*, **404**, 168-71 (2000).
- [47]. A.L. Bowman, "The Variation of Lattice Parameter with Carbon Content of Tantalum Carbide," *J. Phys. Chem.*, **65** [9] 1596-8 (1961).
- [48]. D.J. Rowcliffe and G.E. Hollox, "Hardness Anisotropy, Deformation Mechanisms and Brittle-to-Ductile Transition in Carbides," *J. Mater. Sci.*, **6** [10] 1270-6 (1971).
- [49]. A. Jain, "Synthesis and Processing of Nanocrystalline Zirconium Carbide Formed by Carbothermal Reduction," Master of Science Thesis. Georgia Institute of Technology, Atlanta, GA, 2004.

- [50]. L. Silvestroni, A. Bellosi, C. Melandri, D. Sciti, J.X. Liu, G.J. Zhang, "Microstructure and Properties of HfC and TaC-Based Ceramics Obtained by Ultrafine Powder," *J. Eur. Ceram. Soc.*, **31** [4] 619-27 (2011).
- [51]. I.G. Talmy, J.A. Zaykoski, and M.M. Opeka, "Synthesis, Processing and Properties of TaC-TaB<sub>2</sub>-C Ceramics," *J. Eur. Ceram. Soc.*, **30**, 2253-63 (2010).
- [52]. M.H. Leipold and P.F. Becher, "Fabrication of Hot-Pressed Tantalum Carbide," Technical Report 32-1204, National Aeronautics and Space Administration, 1967.
- [53]. C. Kim, G. Gottstein, and D.S. Grummon, "Plastic Flow and Dislocation Structures in Tantalum Carbide: Deformation at Low and Intermediate Homologous Temperatures," *Acta Metall. Mater.*, **42** [7] 2291-2301 (1994).

## CHAPTER 8: THE EFFECT OF TUNGSTEN CARBIDE AND ZIRCONIUM CARBIDE ADDITIONS ON THE DENSIFICATION AND GRAIN GROWTH OF TANTALUM CARBIDE

### A. Introduction

TaC has a melting temperature near 4000 K, making it of interest for ultra-high temperature applications. Despite the appealing properties of TaC, the prospect of using TaC as a high temperature structural material has been dismal because of limitations in mechanical properties and poor oxidation resistance in comparison with other structural materials.<sup>[1-11]</sup> There is a clear trend towards higher strengths for increasing density, although achieving full density is difficult. Small grain sizes will also facilitate higher strengths.

Achieving nanostructured TaC is expected to improve the mechanical strength, but densification of TaC is also accompanied by rapid grain growth during the initial stages of sintering that would make nanostructuring difficult.<sup>[12-18]</sup> Yohe and Ruoff found that an applied pressure of 3.0 GPa was necessary to achieve densification without grain growth.<sup>[19]</sup> They were able to obtain an average grain size near 20 nm. They also had high oxygen contamination that produced about 12% by weight Ta<sub>2</sub>O<sub>5</sub>, making it difficult to make the same conclusions for purer TaC. However, Bakshi *et al.* sintered sub-micron TaC powders of higher purity at a pressure of 363 MPa and obtained large final grain sizes near five micrometers, supporting the idea that high pressures are needed to inhibit grain growth in TaC.<sup>[1]</sup>

There are few reports of having a final average grain size that is in the sub-micron regime without the use of high pressure. The majority of these reports pertain to samples with density lower than 90% of theoretical.<sup>[1,3,20-21]</sup> Higher densities are reported by these researchers as well, but the average grain sizes extend into the micrometer range.

Kim *et al.* report the sintering of powders prepared by planetary milling and using high frequency induction heating.<sup>[22]</sup> The sintering process is rapid (approximately three minutes) and resulted in a density as high as 96% of theoretical. Densification was complete within two minutes and at 1373 K for powders milled for 10 hours. Average

grain sizes as low as 33 nm were reported, based on X-ray line broadening. However, the small sizes obtained by X-ray line broadening could be from sub-grain structure as a result of the planetary milling and not representative of the grain size. Regardless, extreme heating conditions were utilized.

Densification of fine TaC powders proceeds by plastic flow and grain boundary sliding.<sup>[12-15,17-18,23-24]</sup> It is difficult to obtain fully dense TaC with small grain sizes because of the similar activation energies for grain growth and sintering. The activation energy for grain growth during isothermal holding at temperatures from 2673-2973 K was determined to be 380 kJ/mol, while the activation energy for plastic flow during hot pressing at 16 MPa and 3323 K was determined to be 406 kJ/mol.

Zhang *et al.* suggested that the best sintering aids would be those that promote densification below temperatures where rapid grain growth occurs, but that it is unclear which additives would be most beneficial.<sup>[23]</sup> Furthermore, it seems reasonable to assume that if nanostructured TaC is to be obtained without the use of extreme heating or pressure conditions, then it will be necessary to find suitable additives to control the microstructural development. These concepts will be explored via solid solutions and secondary phases using additions of WC and ZrC and observing the effects on densification and grain growth.

TaC is typically considered to be brittle, but ductility has been demonstrated at room temperature under sharp diamond indentation.<sup>[25-26]</sup> Slip occurs within the  $\langle 100 \rangle, \{111\}$  system, accomplished mainly by the motion of  $\frac{a}{2}\langle 011 \rangle$  edge dislocation glide. This is similar to the behavior of face-centered cubic (FCC) metals and is attributed to the FCC tantalum lattice. However, unlike pure FCC metals, bulk plastic deformation is prevented by the interstitial carbon resulting in Suzuki hardening.<sup>[27]</sup>

If sintering occurs by plastic flow, then the diffusion of carbon must occur to overcome Suzuki hardening, which becomes appreciable only at higher temperatures. Bulk plastic deformation has been observed at temperatures above 1553 K.<sup>[6,25]</sup> The transition temperature from brittle-to-ductile behavior is smaller for lower strain rates and sub-stoichiometric TaC, which facilitate carbon diffusion and plastic flow in the absence of brittle failure. Grain-boundary sliding, controlled by dislocation climb, is another deformation mechanism that is activated at slightly higher temperatures.

WC or ZrC in a solid solution with TaC are expected to change the activation energy for carbon diffusion, and therefore densification and grain growth. The smaller size of tungsten on a tantalum lattice site is expected to decrease the activation energy for carbon diffusion and the larger size of zirconium on a lattice site is expected to increase the activation energy for carbon diffusion. Thus, these additives are expected to influence the densification behavior of TaC. It is unclear how grain growth will be affected by these chemical modifications, but is also of interest. Secondary phases in the microstructure may prevent grain growth. Consequently, understanding the mechanisms leading to both enhanced densification and inhibited grain growth will provide opportunity to improve the properties of TaC-based materials through refinement of the microstructure and chemistry.

## **B. Experimental Procedures**

TaC powders with an average primary particle size of 25 nm, a particle size of 73 nm, and C/Ta ratio of 0.94 were prepared by methods previously developed.<sup>[28-31]</sup> Other raw materials include carbon black (Lampblack 101, Degussa, Parsippany, NJ), WC (99.9%, 0.3% O, <0.08% free carbon, 55 nm, hexagonal, US Research Nanomaterials, Inc., Houston, TX), and ZrC (99+%, <1% O, 20 nm, cubic, US Research Nanomaterials, Inc., Houston, TX).

Powders were batched to produce compositions having approximately 0.1, 1, 10, 20, and 30 mole percent of the additives and will be referenced to according to the following scheme: M#### where M is W or Z and represents either WC or ZrC as the additive phase, respectively, and #### are digits corresponding to the tens, ones, and tenths places of the target mole percent. For example, W200 represents a target composition of 80% TaC and 20% WC.

The actual compositions are listed in Table 9-I and vary from target compositions because of the computations used to additive amounts. Carbon additions were made to TaC based on experiments in chapter seven, which indicated that 3.1% by weight is an optimal substitution for TaC. Carbon substitutions for WC and ZrC additions were made under the assumption that they contained 0.3% and 1.0% by weight oxygen contamination, respectively, and 0.05% and 0% by weight free carbon contents,

respectively. These values are either directly given or assumed from the manufacturer's specifications.

Table 9 – I. Compositions of TaC-Based Composites with WC, ZrC, and carbon Added.

<b>Sample</b>	<b>TaC (g)</b>	<b>TaC (mol)</b>	<b>WC or ZrC (g)</b>	<b>WC or ZrC (mol)</b>	<b>C (g)</b>	<b>Mole % Additive</b>
<b>W001</b>	14.513	0.0752	0.015	0.0001	0.472	0.1
<b>W010</b>	14.382	0.0745	0.150	0.0008	0.468	1.0
<b>W100</b>	13.075	0.0678	1.497	0.0076	0.428	10.1
<b>W200</b>	11.622	0.0602	2.995	0.0153	0.383	20.2
<b>W300</b>	10.169	0.0527	4.492	0.0229	0.339	30.3
<b>Z001</b>	14.513	0.0752	0.006	0.0001	0.472	0.1
<b>Z010</b>	14.382	0.0745	0.063	0.0006	0.468	0.8
<b>Z100</b>	13.075	0.0678	0.631	0.0061	0.430	8.3
<b>Z200</b>	11.622	0.0602	1.263	0.0122	0.388	16.9
<b>Z300</b>	10.169	0.0527	1.894	0.0183	0.345	25.8

Each composition was added to a 125 ml nalgene bottle with 80 grams of cylindrical zirconia media (~8 mm diameter and height). The mixture was tumbled for 30 min at a rotation speed that maximizes cascading to form a more uniform agglomerate distribution. The powders were separated from the media using a sieve and collection pan and then added to a graphite-foil lined graphite die with a 19.5 mm diameter. Uniaxial pressing of the powders in the die was performed using an applied pressure of 30 MPa before sintering.

The powders were sintered using a resistance furnace (Model HP D 25, FCT Systeme, GmbH, Frankenblick, Germany) using an FCT Systeme standard die configuration. A uniaxial pressure of 50 MPa was applied prior to heating. A heating rate of 50 K/min was applied from 723 K to 2173 K. The temperature was dwelled for 10 min at 2173 K. Cooling was performed at a rate of 50 K/min to 723 K while the pressure was linearly released from 50 MPa to 10 MPa to prevent cracking from thermal shock or residual stresses. Temperature was measured with an axially position pyrometer and is the temperature reported in this work. The top and bottom layers of the samples were removed prior to characterization.

X-ray diffraction measurements were performed on a diffractometer (D2 Phaser, Bruker AXS, Inc., Madison, WI) by scanning from 15-115 °2θ using a step size of 0.04 °2θ and a dwell time of two seconds. Lattice parameters were measured by cell refinement using software (Jade 8, Materials Data, Inc., Livermore, CA). Scanning electron microscopy (SEM) was performed on a field emission microscope (FEI™ Quanta 200F, FEI Company, Hillsboro, OR) to observe the microstructural evolution. Four random fracture surfaces were imaged. Two random imaging locations on each fragment were selected.

### C. Results and Discussion

The *in situ* ram displacement and displacement rate of TaC/WC composites are demonstrated in Figure 8-1. The displacement is representative of densification. Several densification regimes, as a function of temperature, are consistent with previous findings.<sup>[28]</sup> All densification regimes occur at slightly higher temperatures with increasing WC. This is demonstrated by the gray arrows in Figure 9-1. The sintering rate in the first and second densification regimes, starting just above 923 K and 1023 K, decreased with WC content. The densification rate in the third densification regime, occurring above 1323 K, did not change with WC additions. The negative displacement occurring just above 1823 K is attributed to carbothermal reduction of the oxide phase and the displacement rate generally increases with increasing WC content and suggests improved oxygen removal. WC was found to be more efficient than several other metal carbides for removing oxygen impurities from ZrB<sub>2</sub> as well.<sup>[32]</sup>

The onset temperature for sintering of sample W001 and W010 was approximately 1923 K, which is about 30 K lower than the sintering of pure TaC, based on results in chapter seven. This is demonstrated in Figure 8-1b. This agrees with the hypothesis that tungsten would decrease the activation energy for carbon diffusion and therefore promote densification. However, this is an oversimplification because the onset temperature for densification does not continue to decrease with increasing WC content. The onset temperature for densification increased to higher temperatures with further additions of WC and is an unexpected result. The onset temperature for samples W100 and W200 is near that of TaC, while that of W300 exceeds that of TaC. The effect of

various sintering additives will need to be better defined. The sintering rate increased and occurred over a narrower temperature range with increasing WC addition and is demonstrated by the increased and narrower displacement rate peak in Figure 8-1a.

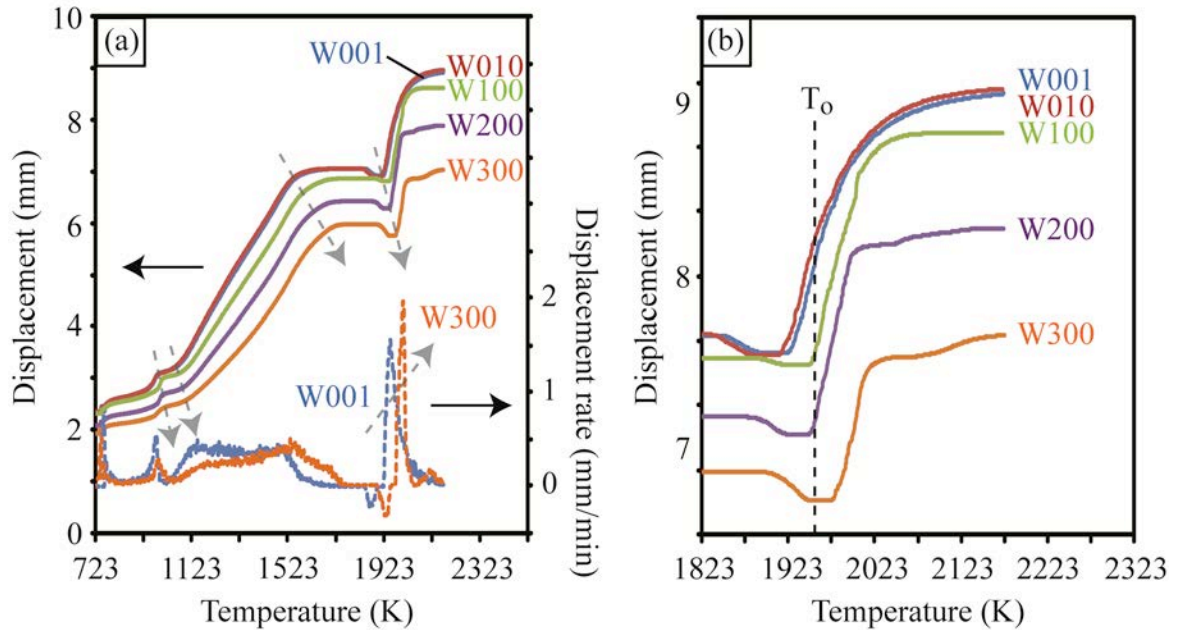


Figure 8 - 1. (a) Ram displacement and displacement rate for TaC-WC composites during resistance sintering. (b) The ram displacement is provided again with a truncated scale and with the onset temperature,  $T_o$ , for densification of TaC without WC. (With color)

*In situ* ram displacement and displacement rate of TaC/ZrC composites are demonstrated in Figure 8-2. An extra and rapid densification event is observed at low temperatures (near 873 K). The low temperature densification event is thought to be related to the formation of oxide phases.<sup>[28]</sup> Thus, it is assumed that the densification event just above 873 K is related to the formation of  $ZrO_2$ , while the typical densification event just above 923 K is from the formation of  $Ta_2O_5$ . The rapid displacement as a result of  $ZrO_2$  formation in comparison to  $Ta_2O_5$  formation (which is nearly eliminated for sample Z300) suggests preferential formation of  $ZrO_2$ .  $ZrO_2$  is found to be quite stable in the presence of TaC, even at temperature as high as 2273 K.<sup>[32]</sup>

Similar to WC additions, ZrC additions extend the densification regimes starting just above 1023 K and 1323 K to higher temperatures. Conversely, the densification rate of the event at lower temperature remains the same while that of the event at higher

temperature decreases. A more detailed study similar to our previous work, but with WC and ZrC additions, would provide more insight for the cause of the densification events and changes in densification rate during presintering and how they are being affected by the additives.<sup>[28]</sup>

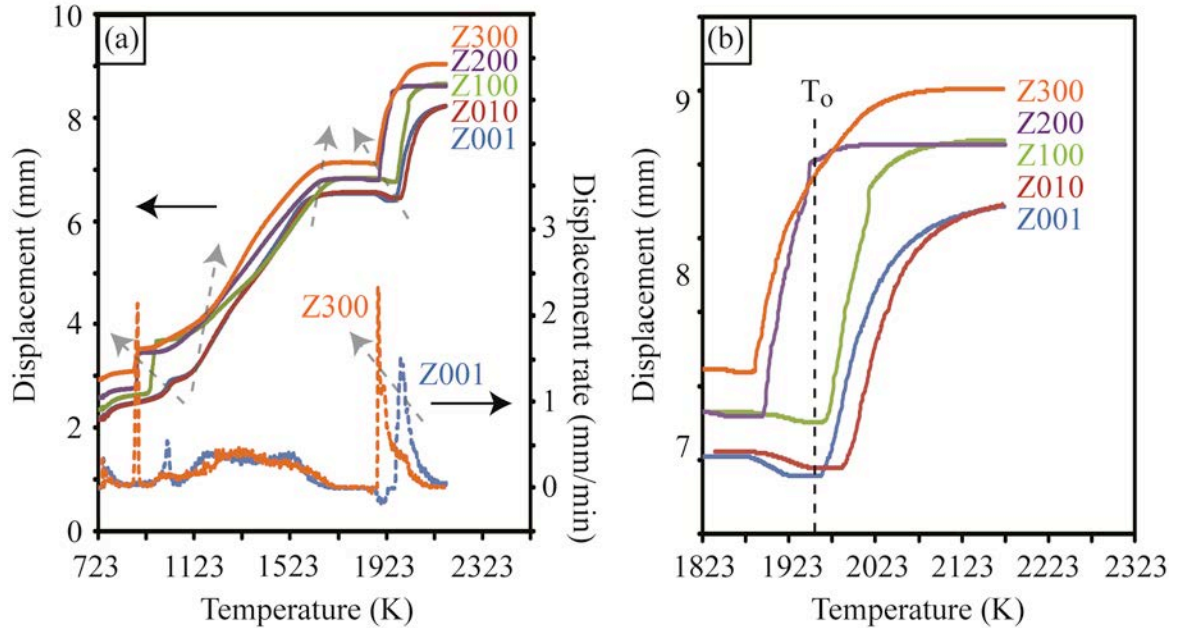


Figure 8 - 2. (a) Ram displacement and displacement rate for TaC-ZrC composites during resistance sintering. (b) The ram displacement is provided again with a truncated scale and with the onset temperature,  $T_o$ , for densification of TaC without WC. (With color)

The sintering behavior of the TaC-ZrC composite powders, without including the pre-sintering behavior, are given in Figure 8-2b. The onset temperature for densification of sample Z001 was similar to that of TaC and was shifted about 30 K higher compared to TaC for sample Z010. This also supports the hypothesis that substitution of zirconium for tantalum in the TaC lattice would increase the activation energy for carbon diffusion and inhibit sintering. However, like in the case of tungsten carbide additions, the trend is reversed for higher ZrC additions and the onset temperature for densification is reduced.

Samples Z200 and Z300 began to sinter about 80 K lower than TaC, near 1873 K. This is in the typical temperature range for which carbothermal reduction is expected. Rapid sintering at this low of a temperature can inhibit the carbothermal reduction

process, making it difficult to remove oxygen impurities and will need to be investigated in more detail.

X-ray diffraction (XRD) patterns of the composite materials are given in Figure 8-3. Samples W001, W010, W100, and W200 are single phase, indicating that all of the WC is in solid solution. However, the solid solution limit has been exceeded for sample W300 and a WC phase is observed in the XRD pattern. Samples Z001, Z010, Z100 also appear to form a complete solid solution. However,  $ZrO_2$  is observed in the XRD patterns for samples Z200 and Z300.

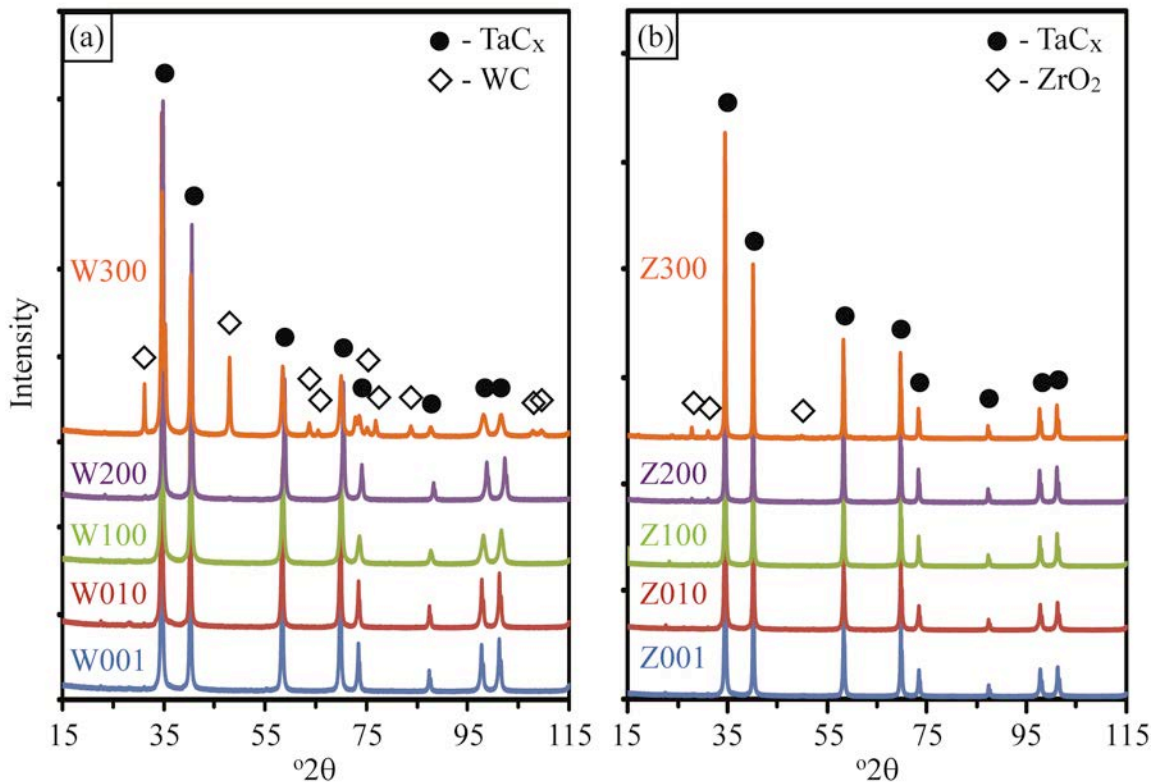


Figure 8 - 3. X-ray diffraction patterns for tantalum carbide-based composites having tungsten carbide or zirconium carbide additions. (With color)

The microstructures for the TaC-WC composites are demonstrated in Figure 8-4. Comparison of the microstructures in Figure 8-4a-d indicates that grain growth is activated by increasing WC content in solid solution with TaC, suggesting that decreasing the activation energy for carbon diffusion increases grain growth and that increasing the activation energy for carbon diffusion would suppress grain growth.

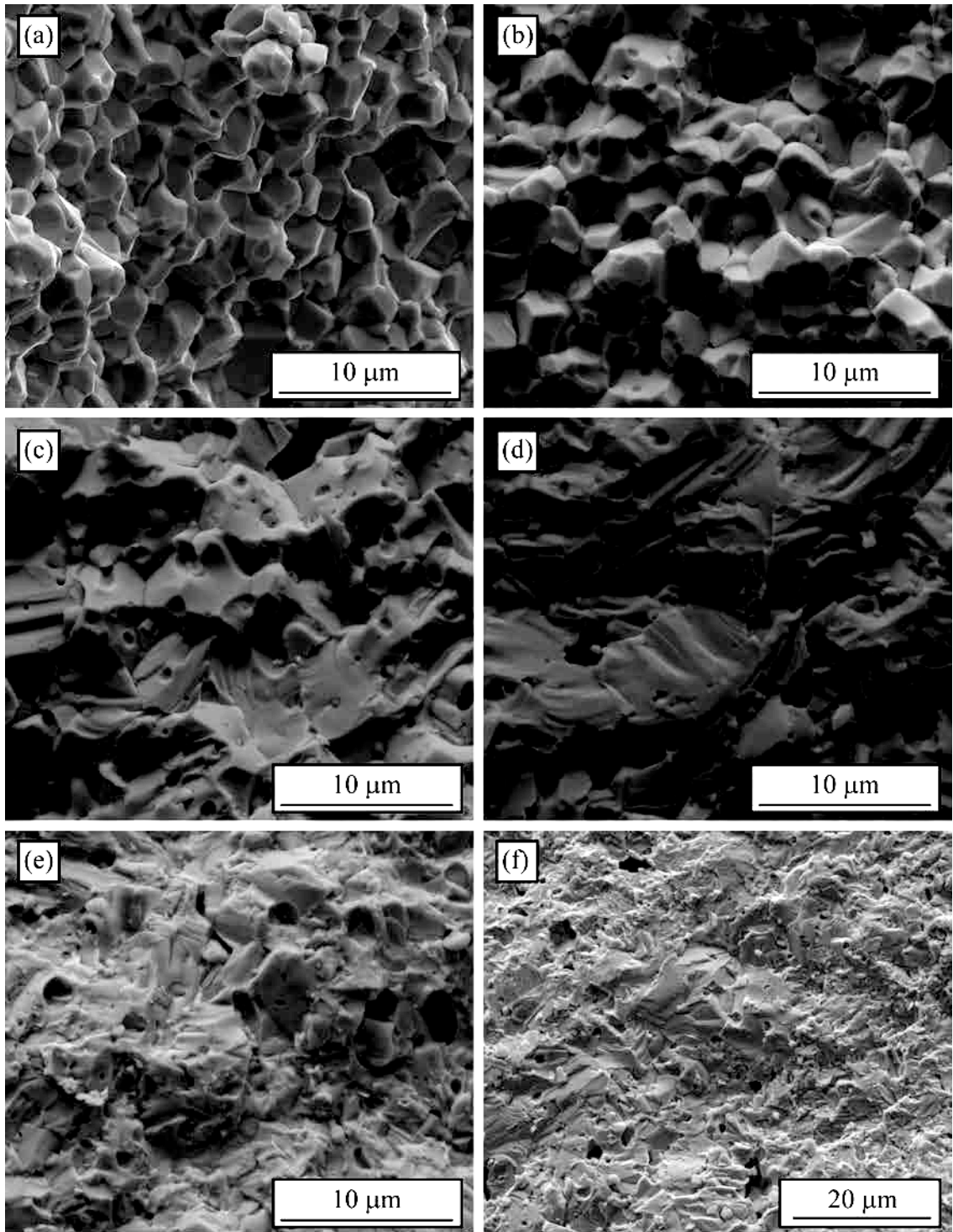


Figure 8 - 4. Secondary electron images of samples (a) W001, (b) W010, (c) W100, (d) W200, (e) W300, and (f) W300 (lower magnification).

Another notable feature is observed in the microstructures with increased WC content: development of porosity at grain interfaces that indicate the activation of a vapor mass transport mechanism. This phenomenon is most obvious for sample W100 in Figure 8-4d, for example. A previous study indicated such features are promoted by the presence of free carbon (see chapter six). Carbon loss from TaC was noted above 2173 K that could activate an evaporation/condensation sintering mechanism and form pores at the interfaces between grains that could be observed on the fracture surfaces.

Increasing WC additions apparently initiated an evaporation/condensation sintering mechanism at a lower temperature because sintering was performed at the previously established temperature limit that would prevent vapor formation. Optimizing the sintering behavior of these compositions will require sintering at lower temperatures to avoid vapor formation. Sintering at lower temperatures is necessary to establish the potential of using WC as a sintering aid, although grain growth will not be avoided.

For sample W300, refinement of the microstructure is observed. This is demonstrated in Figure 8-4e and Figure 8-4f. Based on the XRD data provided in Figure 8-3, it appears that the WC phase present above the solubility limit in TaC provides grain boundary pinning to inhibit grain growth. Optimization of the sintering temperature and composition may produce nanostructured composites.

The microstructures for the TaC-ZrC composites are demonstrated in Figure 8-5. For samples Z001, Z010, and Z100, there is little, if any, change in the grain growth behavior. ZrC did not promote vapor formation, presumably because the addition of ZrC to TaC increases the activation energy for carbon diffusion. Similar observations have been made for hafnium carbide additions, which would also increase the activation energy for carbon diffusion.<sup>[43]</sup> Grain growth is inhibited for samples Z200 and Z300, samples that also contained ZrO<sub>2</sub> according to Figure 8-3. ZrO<sub>2</sub> is observed in Figure 8-5d as a dark phase in back-scattered electron image because of the lower average atomic number of ZrO<sub>2</sub> compared to TaC. There is a need to establish if grain growth inhibition of TaC-ZrC composites is a result of ZrC or ZrO<sub>2</sub> and will be addressed later.

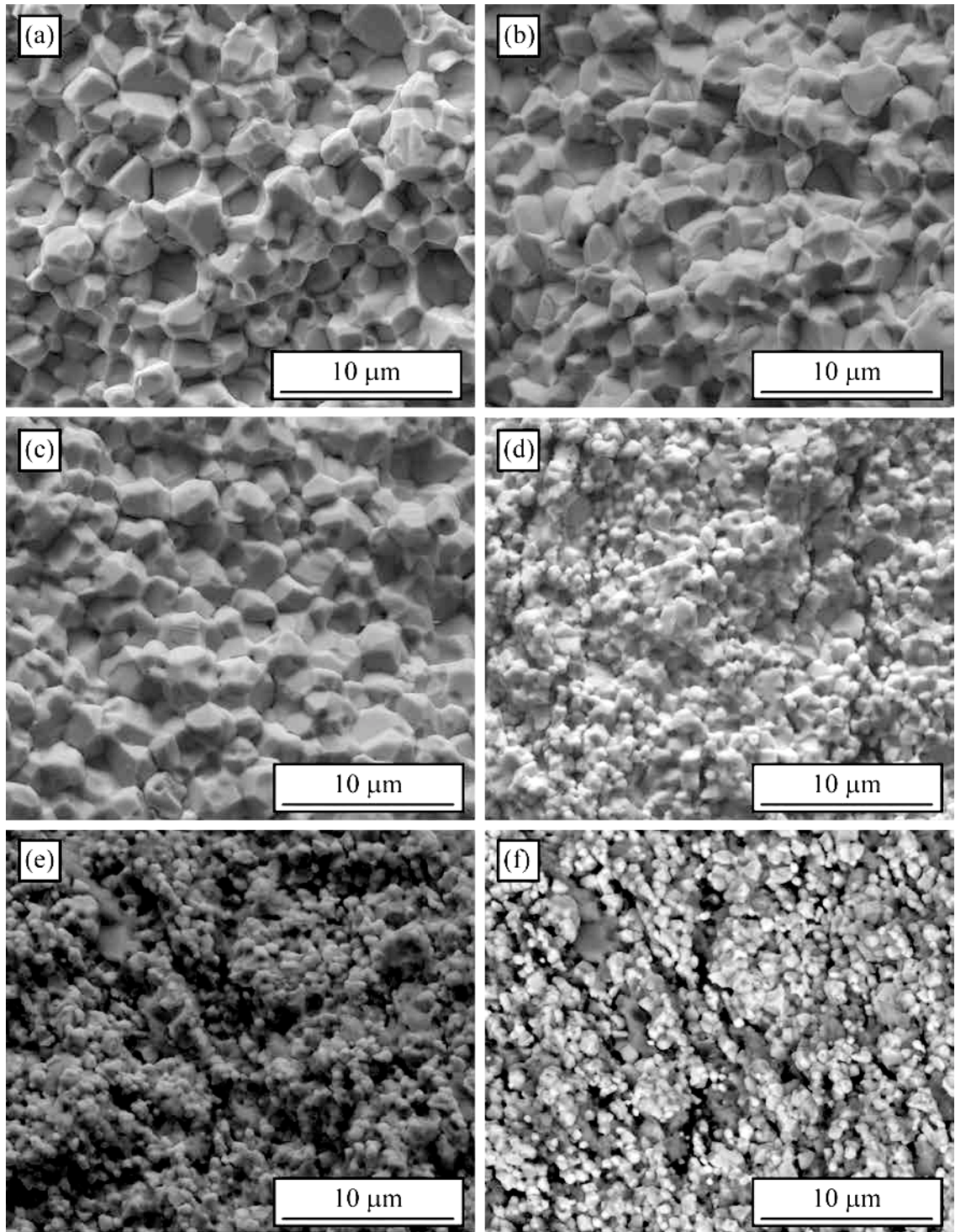


Figure 8 - 5. Secondary electron images of samples (a) Z001, (b) Z010, (c) Z100, (d) Z200, (e) Z300, and (f) a back-scattered electron image of Z300.

The lattice parameters of various carbide phases are given in Figure 8-6. Figure 8-6a demonstrates that the lattice parameter of TaC is intermediate between WC and ZrC.

HfC is also included to demonstrate the similarity to ZrC. Thus, WC will decrease the lattice parameter of TaC in solid solution while ZrC will increase the lattice parameter according to Vegard's law. Furthermore, the lattice parameters of the binary cubic monocarbides decrease with decreasing carbon stoichiometry and is demonstrated in Figure 8-6a. The predicted and experimental lattice parameters for TaC-WC composites, based on Vegard's law for  $MC_{0.98}$  compounds and assuming complete solubility is given in Figure 8-6b.

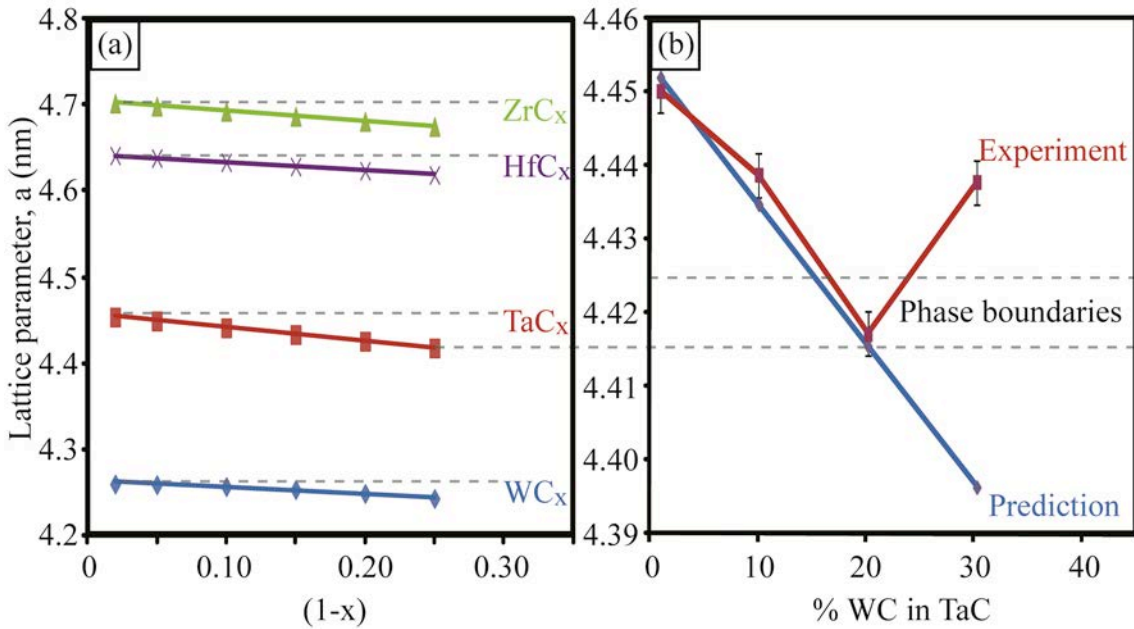


Figure 8 - 6. Lattice parameters of (a) binary cubic monocarbides, derived from literature, and of (b)  $(W,Ta)C_{0.98}$  composites based on mole percentages and using Vegard's law.<sup>[44-47]</sup> (With color)

The experimentally determined lattice parameters for TaC-WC composites followed predictions based on Vegard's law for nearly stoichiometric compounds up to a critical WC addition. The critical WC addition corresponds to a lattice parameter at the phase boundary for the substoichiometric  $\zeta$ - $Ta_4C_3$  phase, indicated by the lower phase boundary in Figure 8-6b, suggesting that this lattice parameter can be used to define the solubility limit of WC into TaC without destabilizing the TaC phase.

The formation of the  $\zeta$ - $Ta_4C_3$  phase begins to form at a composition close to  $TaC_{0.8}$ , in equilibrium with the monocarbide phase (possibly with vacancy ordering to form the  $Ta_6C_{5-x}$  at lower temperatures.<sup>[48]</sup> The lattice parameter corresponding to the

upper limit is marked as the upper phase boundary in Figure 8-6b. This could be the cause of faceted grain structuring that was most obviously observed in sample W200 in Figure 8-4d. However, if a  $\zeta$ -Ta<sub>4</sub>C<sub>3</sub>-type structure is formed, then it is a small amount because it is lost in the background of the XRD pattern.

The experimental lattice parameters match well with the lattice parameters calculated using Vegard's law for nearly stoichiometric compounds. This would suggest that the microstructures similar to that in Figure 8-3c are not caused by vapor promoted by free carbon in the microstructure. However, stacking faults are thought to be structurally and chemically similar to M<sub>2</sub>C.<sup>[25-27,40-42,49]</sup> In sub-stoichiometric TaC, the stacking faults are generated by dissociation of dislocations into Shockley partials, which are a pair of dislocations that bound a stacking a fault. For a solid solution, the stacking fault could be formed as a result of the chemical modification. The transition to M<sub>2</sub>C chemistry at the stacking faults can provide excess carbon that could be the source for volatility to describe the observations of Figure 8-3. If this is the case, then carbon volatility should be related to the stacking fault formation, and therefore dislocations. Such a mechanism can be supported by the literature.

Figure 8-7 demonstrates grain and subgrain structure of TaC that was obtained by Bartlett and Halden.<sup>[47]</sup> A closer look at the sub-grain boundaries indicate that they consist of a network of dislocations. The replica image given in Figure 8-7c demonstrates a sub-grain boundary consisting of dislocation etch pits in a sub-grain boundary that intersects a (100) face. The linear dislocation density was determined to be 30 dislocations/micrometer, corresponding to a 0°12' twist boundary. Stacking faults are generated from dissociated dislocations and could provide a pathway for carbon transport to the grain boundary.<sup>[27]</sup>

An analysis of the lattice parameter was performed for TaC-ZrC composites and is given in Figure 8-8. The lattice parameter of TaC with ZrC additions did not follow the predicted values. This is most likely because of the difficulties eliminating the oxide phase that is indicated by the XRD and microstructural analyses presented in Figure 8-3 and Figure 8-5. The small change in the lattice parameter indicates why little difference is observed in the grain growth between samples Z001, Z010, and Z100 in Figure 8-5. The small change in the lattice parameter would result in a small change in the activation

energy for carbon diffusion. If grain growth is affected by the activation energy for carbon diffusion, then little difference in grain growth is to be expected.

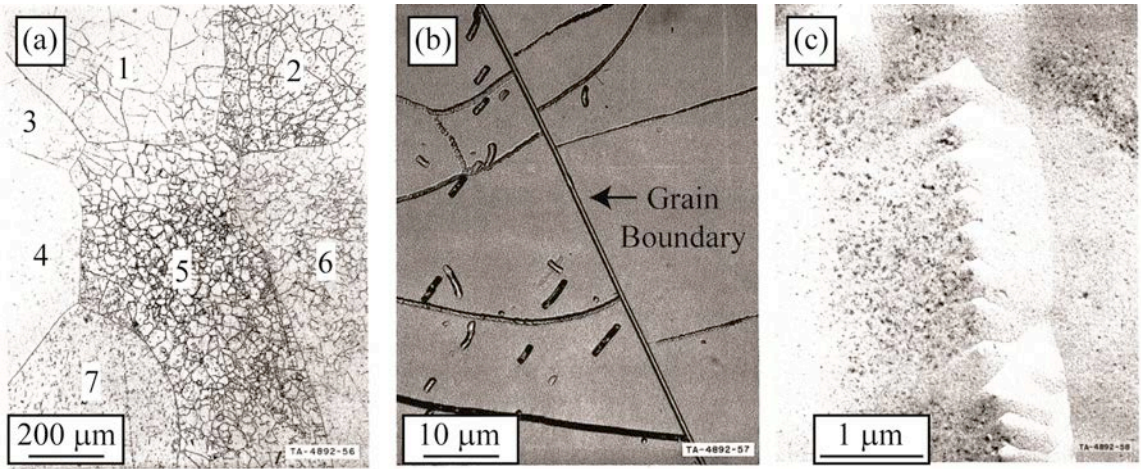


Figure 8 - 7. Images of TaC grain boundary and sub-grain boundary structures: (a) Seven TaC grains containing sub-grain boundaries, (b) a single grain boundary with sub-grain boundaries intersecting, and (c) a replica of dislocation etch pits making up a sub-grain boundary.<sup>[47]</sup>

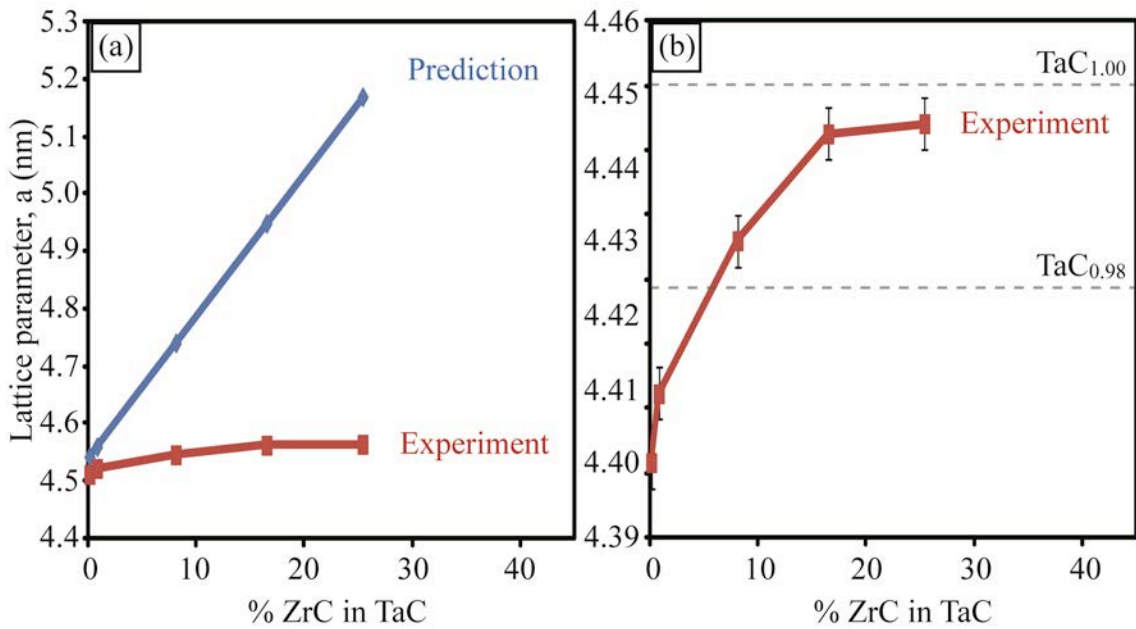


Figure 8 - 8. (a) Experimental and predicted lattice parameters for  $(Zr,Ta)C_{0.98}$  composites based on mole percentages and Vegard's law and (b) provided again with a truncated scale. (With color)

The experimental lattice parameters for samples Z200 and Z300, where grain growth was suppressed, highlights a possible mechanism for suppression of grain growth besides grain boundary pinning via  $ZrO_2$  found in the microstructure. Grain growth was suppressed when the lattice parameter was close to that of the stoichiometric TaC phase. Stacking faults would be eliminated as the lattice parameter approaches that for stoichiometric TaC and would eliminate the pathway for carbon transport to the grain boundaries. Microstructural observations provide support for this mechanism.

A back-scattered electron image of sample Z300 at higher magnification is given in Figure 8-9, along with energy dispersive spectroscopy of selected regions of the microstructure. There are three distinct regions labeled in Figure 8-9a. Region B is rich in tantalum and carbon, region C contains a significant concentration of zirconium and oxygen, and region D is primarily carbon and is demonstrated by the energy dispersive spectra given in Figure 8-9b, Figure 8-9c, and Figure 8-9d, respectively. Therefore, regions B, C, and D correspond to TaC,  $ZrO_2$ , and carbon phases.

Three (Zr,Ta)C clusters are circled in Figure 8-9a. Grain boundaries in these clusters appear to be free of the secondary phases that might lead to grain boundary pinning. In the absence of grain boundary pinning, the grains are still smaller than the average grain size obtained for lower ZrC content (i.e. samples Z001, Z010, and Z100). The average grain size in these clusters is less than one micrometer, more than three times smaller than the average grain size with no ZrC added (about three micrometers). Thus, approaching the lattice parameter for stoichiometric TaC appears to be a viable method of suppressing grain growth in TaC.

Increasing the lattice parameter with ZrC additions, to suppress grain growth, will require improvements in processing to eliminate the  $ZrO_2$  phase. *In situ* removal of the oxide does not seem like a viable option because sintering begins before significant carbothermal reduction takes place. The addition of WC can completely reduce  $ZrO_2$  below 1923 K if there is three moles of WC per mole of  $ZrO_2$ .<sup>[32]</sup> However, this will not be an adequate approach if the amount of WC necessary to remove the oxide decreases the lattice parameter more than the ZrC increases the lattice parameter.

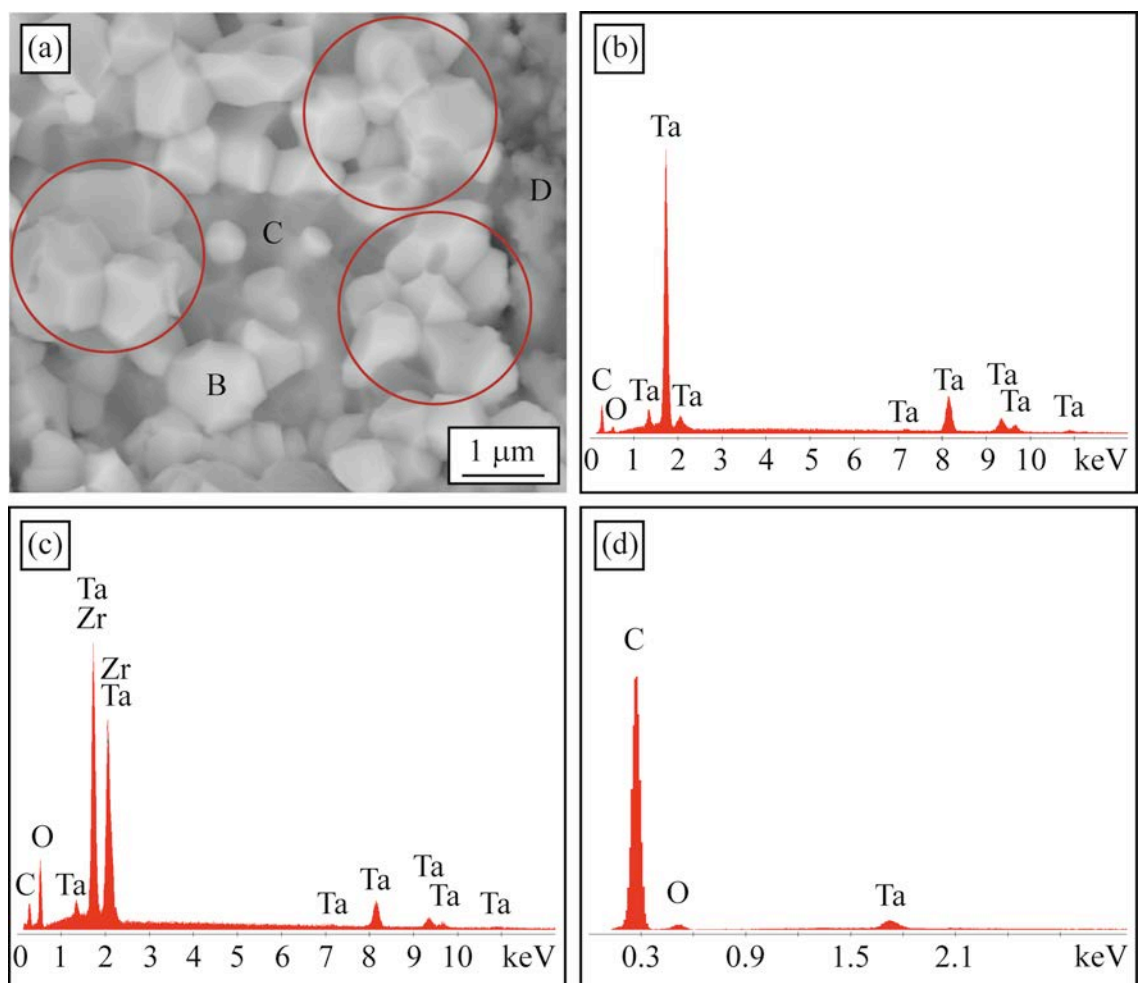


Figure 8 - 9. (a) Back-scattered electron image of the fracture surface of sample Z300 and energy dispersive spectra of (b) region B, (c) region C, and region D. Circled regions are clusters of (Zr,Ta)C grains. (With color)

An alternate option is to use powders with lower oxygen content. Smaller is not always better because intra-aggregate sintering is likely to occur before inter-aggregate sintering so that the obtainable grain size approaches that of the aggregate size.<sup>[50]</sup> Previous studies guide optimization of the solvothermal synthesis method to obtain a particle size to primary particle size near unity, corresponding to an optimization between maximizing surface area and minimizing aggregate size.<sup>[30]</sup>

For the currently developed solvothermal synthesis method, water on the surfaces of particles is the main source for oxygen contamination.<sup>[29]</sup> The water is strongly adsorbed on the powder surfaces, requiring temperatures as high as 873 K to be removed. However, oxidation of the powders was observed at temperatures as low as 473 K.

Therefore, more creative methods of removing water are necessary, such as water displacing solvent washing for example.

If the oxygen content of the nanopowders can be reduced to suitable levels, then achieving lattice parameters greater than that of stoichiometric TaC are obtainable. This is demonstrated in Figure 8-10, which provides the predicted lattice parameter of TaC-HfC composites, along with some experimental data points from the literature. The  $(\text{Hf}_{0.2}\text{Ta}_{0.8})\text{C}_{1-x}$  composition has been studied previously.<sup>[43,47]</sup> This composition is of interest because it has the highest melting temperature in the Hf-Ta-C system and the lowest vaporization rate at a given temperature. This composition also has superior hardness compared to other Hf-Ta-C compositions.

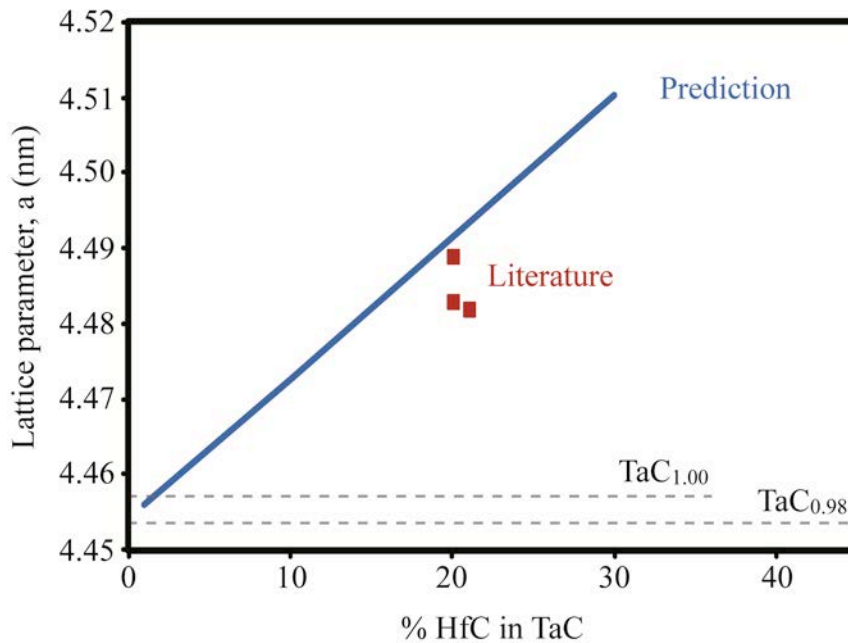


Figure 8 - 10. Predicted lattice parameter of TaC-HfC composites, including experimental data points from the literature.<sup>[43,47]</sup> (With color)

#### D. Conclusions

Changing the activation energy for carbon diffusion appears to influence the sintering behavior of TaC according to the original hypothesis only at low additive concentrations. With higher concentrations the trends are reversed and eventually oppose the hypothesis, indicating that the influence of carbon diffusion on sintering is more complex. The results are also complicated by the formation of secondary phases. In

general, the sintering behavior is quite complex and would benefit from further investigation. Overall the onset temperature for densification could be varied approximately 100°C.

Grain growth was apparently affected by carbon diffusion, possibly via formation of stacking faults. Solid solutions of WC in TaC could induce the formation of stacking faults, which would promote carbon diffusion and promote grain growth. Solid solution of ZrC in TaC could inhibit grain growth as the lattice parameter approached that of stoichiometric TaC, which could eliminate stacking faults and inhibit carbon diffusion. Grain growth could also be suppressed by adding WC in concentrations above the solubility limit, which was above 20 mole percent. WC additions to TaC are likely to have activated an evaporation/condensation sintering mechanism at lower temperature than for TaC without WC additions. Optimization of the sintering procedures are recommended for avoiding vapor phase formation. Removal of oxygen from the TaC-ZrC system also needs further development.

## References

- [1]. S.R. Bakshi, V. Musaramthota, D. Lahiri, V. Singh, S. Seal, and A. Agarwal, "Spark Plasma Sintered Tantalum Carbide: Effect of Pressure and Nano-Boron Carbide Addition on Microstructure and Mechanical Properties," *Mater. Sci. Eng. A*, **528**, 1287-95 (2011).
- [2]. L. Liu, F. Ye, and Y. Zhou, "New Route to Densify Tantalum Carbide at 1400°C by Spark Plasma Sintering," *Mater. Sci. Eng. A*, **528**, 4710-14 (2011).
- [3]. E. Khaleghi, Y.-S. Lin, M.A. Meyers, and E.A. Olevsky, "Spark Plasma Sintering of Tantalum Carbide," *Scripta Materialia*, **63**, 577-80 (2010).
- [4]. J.-X. Liu, Y.-M. Kan, and G.-J. Zhang, "Pressureless Sintering of Tantalum Carbide Ceramics without Additives," *J. Am. Ceram. Soc.*, **93** [2] 370-73 (2010).
- [5]. K. Hackett, S. Verhoef, R.A. Cutler, and D.K. Shetty, "Phase Constitution and Mechanical Properties of Carbides in the Ta-C System," *J. Am. Ceram. Soc.*, **92** [10] 2404-7 (2009).
- [6]. P.F. Becher, "Mechanical Behaviour of Polycrystalline TaC," *J. Mater. Sci.*, **6**, 79-80 (1971).
- [7]. J. Ma, Y. Du, M. Wu, and M. Pan, "One Simple Synthesis Route to Nanocrystalline Tantalum Carbide via the Reaction of Tantalum Pentachloride and Sodium Carbonate with Metallic Magnesium," *Mater. Lett.*, **61**, 3658-61 (2007).
- [8]. L. Shi, Y. Gu, L. Chen, Z. Yang, J. Ma, and Y. Qian, "Formation of TaC Nanorods with a Low-Temperature Chemical Route," *Chemistry Lett.*, **33** [12] 1546-7 (2004).
- [9]. M. Johnsson and S. Shimada, "Oxidation of Ta<sub>x</sub>Ti<sub>1-x</sub>C Whiskers Under Formation of Carbon," *J. Mater. Sci. Lett.*, **21**, 955-8 (2002).
- [10]. M. Desmaison-Brut, N. Alexandre, and J. Desmaison, "Comparison of the Oxidation Behavior of Two Dense Hot Isostatically Pressed Tantalum Carbide (TaC and Ta<sub>2</sub>C) Materials," *J. Eur. Ceram. Soc.*, **17**, 1325-34 (1997).
- [11]. É.I. Golovko, L.F. Ochkas, M.S. Koval'chenko, and A.F. Nikityuk, "Oxidation of Tantalum Carbide Alloys," *Poroshkovaya Metallurgiya*, **166** [10] 51-4 (1976).
- [12]. S.A. Shvab and F.F. Egorov, "Structure and Some Properties of Sintered Tantalum Carbide," *Sov. Powder. Metall. Met. Ceram.*, **21** [11] 894-7 (1982).

- [13]. L. Liu, F. Ye, X. He, and Y. Zhou, "Densification Process of TaC/TaB<sub>2</sub> Composite in Spark Plasma Sintering," *Mater. Chem. Phys.*, **126**, 459-62 (2011).
- [14]. P.S. Kislyi, S.A. Shvab, and F.F. Egorov, "Sintering Kinetics of Tantalum Carbide," *Powder Metall. And Met. Ceram.*, **21** [10] 765-7 (1982).
- [15]. Y.E. Geguzin and Y.I. Klinchuk, "Mechanism and Kinetics of the Initial Stage of Solid-Phase Sintering of Compacts from Powders of Crystalline Solids," *Poroshk. Metall.*, [7] 17-25 (1976).
- [16]. J. Sautereau and A. Mocellin, "Sintering Behavior of Ultrafine NbC and TaC Powders," *J. Mater. Sci.*, **9**, 761-71 (1974).
- [17]. M.F. Ashby and H.A. Verral, "Diffusion-Accommodated Flow and Superplasticity," *Acta Metall.*, **21**, 149-63 (1974).
- [18]. Y.E. Geguzin, "Diffusional Deformation of Porous Crystalline Structures," *Fiz. Tverd. Tela*, **17** [7] 1950-4 (1957).
- [19]. W.C. Yohe and A.L. Ruoff, "Ultrafine-Grain Tantalum Carbide by High Pressure Hot Pressing," *Ceram. Bull.*, **57** [12] 1123-30 (1978).
- [20]. L. Silvestroni, A. Bellosi, C. Melandri, D. Sciti, J.X. Liu, G.J. Zhang, "Microstructure and Properties of HfC and TaC-Based Ceramics Obtained by Ultrafine Powder," *J. Eur. Ceram. Soc.*, **31** [4] 619-27 (2011).
- [21]. S.R. Bakshi, V. Musaramthota, D.A. Virzi, A.K. Keshri, D. Lahiri, V. Singh, S. Seal, and A. Agarwal, "Spark Plasma Sintered Tantalum Carbide-Carbon Nanotube Composite: Effect of Pressure, Carbon Nanotube Length and Dispersion Technique on Microstructure and Mechanical Properties," *Mater. Sci. Eng. A*, **528**, 2538-47 (2011).
- [22]. B.-R. Kim, K.-D. Woo, J.-M. Doh, J.-K. Yoon, and I.-J. Shon, "Mechanical Properties and Rapid Consolidation of Binderless Nanostructured Tantalum Carbide," *Ceram. Intl.*, **35**, 3395-400 (2009).
- [23]. X. Zhang, G.E. Hilmas, and W.G. Fahrenholtz, "Hot Pressing of Tantalum Carbide With and Without Sintering Additives," *J. Am. Ceram. Soc.*, **90** [2] 393-401 (2007).
- [24]. G.V. Samonov and R.Y. Petrikina, "Sintering of Metals, Carbides, and Oxides by Hot Pressing," *Phys. Sintering*, **2** [3] 1-20 (1970).
- [25]. C. Kim, G. Gottstein, and D.S. Grummon, "Plastic Flow and Dislocation Structures in Tantalum Carbide: Deformation at Low and Intermediate Homologous Temperatures," *Acta Metall. Mater.*, **42** [7] 2291-2301 (1994).

- [26]. D.J. Rowcliffe and G.E. Hollox, "Hardness Anisotropy, Deformation Mechanisms and Brittle-to-Ductile Transition in Carbides," *J. Mater. Sci.*, **6** [10] 1270-6 (1971).
- [27]. M. Hoffman and W.S. Williams, "A Simple Model for the Deformation Behavior of Tantalum Carbide," *J. Am. Ceram. Soc.*, **69** [8] 612-14 (1986).
- [28]. B.M. Clark, J.P. Kelly, and O.A. Graeve, "Recent Advances on Bulk Tantalum Carbide Produced by Solvothermal Synthesis and Spark Plasma Sintering," *Mater. Res. Soc. Symp. Proc.*, submitted (2012).
- [29]. B.M. Clark, J.P. Kelly, and O.A. Graeve, "Exploring the Synthesis Parameters and Spark Plasma Sintering of Tantalum Carbide Powders Prepared by Solvothermal Synthesis," *Mater. Res. Soc. Symp. Proc.*, **1373**, 7-17 (2010).
- [30]. J.P. Kelly and O.A. Graeve, "Statistical Experimental Design Approach for the Solvothermal Synthesis of Nanostructured Tantalum Carbide Powders," *J. Am. Ceram. Soc.*, **94** [6] 1706-15 (2011).
- [31]. J.P. Kelly, R. Kanakala, and O.A. Graeve, "A Solvothermal Approach for the Preparation of Nanostructured Carbide and Boride Ultra-High-Temperature Ceramics," *J. Am. Ceram. Soc.*, **93** [10] 3035-38 (2010).
- [32]. J. Zou, G.-J. Zhang, S.-K. Sun, H.-T. Liu, Y.-M. Kan, J.-X. Liu, and C.-M. Xu, "ZrO<sub>2</sub> Removing Reactions of Groups IV-VI Transition Metal Carbides in ZrB<sub>2</sub> Based Composites," *J. Eur. Ceram. Soc.*, **31**, 421-7 (2011).
- [33]. V.N. Lipatnikov and A.A. Rempel, "Formation of the Incommensurate Ordered Phase in TaC<sub>y</sub> Carbide," *JETP Lett.*, **81** [7] 326-30 (2005).
- [34]. A.I. Gusev, A.A. Rempel, and V.N. Lipatnikov, "Heat Capacity of Niobium and Tantalum Carbides NbC<sub>y</sub> and TaC<sub>y</sub> in Disordered and Ordered States below 300 K," *Phys. Stat. Sol. B*, **194**, 467-82 (1996).
- [35]. A.I. Gusev, A.A. Rempel, and V.N. Lipatnikov, "Incommensurate Ordered Phase in Non-Stoichiometric Tantalum Carbide," *J. Phys.: Condens. Matter*, **8** [43] 8277-93 (1996).
- [36]. A.I. Gusev, A.A. Rempel, and V.N. Lipatnikov, "Incommensurate Superlattice and Superconductivity in Tantalum Carbide," *Sov. Phys. Solid State*, **33** [8] 1295-1299 (1991).
- [37]. A.A. Rempel, V.N. Lipatnikov, and A.I. Gusev, "The Superstructure in Nonstoichiometric Tantalum Carbide," *Sov. Phys. Dokl.*, **35** [2] 103-6 (1990).

- [38]. A.I. Gusev, "Atomic Ordering and the Order Parameter Functional Method," *Philos. Mag.*, **60** [3] 307-324 (1989).
- [39]. V.N. Lipatnikov, A.I. Gusev, A.A. Rempel, and G.P. Shveikin, "Effect of a Structural Transition on the Magnetic Susceptibility of Tantalum Carbide," *Sov. Phys. Dokl.*, **32** [12] 988-90 (1987).
- [40]. M.A. Khusainov, G.M. Demyshav, and M.M. Myshlyayev, "Mechanical Properties and Structure of Carbide Coatings of Niobium and Tantalum on Graphite," *Russ. Metall.*, [5] 139-42 (1990).
- [41]. C. Allison, M. Hoffman, and W.S. Williams, "Electron Energy Loss Spectroscopy of Carbon in Dissociated Dislocations in Tantalum Carbide," *J. Appl. Phys.*, **53** [10] 6757-61 (1982).
- [42]. D.J. Rowcliffe and G.E. Hollox, "Plastic Flow and Fracture of Tantalum Carbide and Hafnium Carbide at Low Temperatures," *J. Mater. Sci.*, **6** [10] 1261-9 (1971).
- [43]. D.L. Deadmore, "Vaporization of Tantalum-Carbide-Hafnium-Carbide Solid Solutions at 2500° to 3000° K," NASA TN D-2512, National Aeronautics and Space Administration, Washington, D.C., 1964.
- [44]. A.L. Bowman, "The Variation of Lattice Parameter with Carbon Content of Tantalum Carbide," *J. Phys. Chem.*, **65** [9] 1596-8 (1961).
- [45]. A.S. Kurlov and A.I. Gusev, "Phase Equilibria in the W-C System and Tungsten Carbides," *Russ. Chem. Rev.*, **75** [7] 617-36 (2006).
- [46]. A. Jain, "Synthesis and Processing of Nanocrystalline Zirconium Carbide Formed by Carbothermal Reduction," Master of Science Thesis. Georgia Institute of Technology, Atlanta, GA.
- [47]. R.W. Bartlett and F.A. Halden, "Study of Growth Parameters for Refractory Carbide single Crystals," SRI Project FMU-4892, Final Report, National Aeronautics and Space Administration, Washington, D.C., 1967.
- [48]. A.I. Gusev, A.S. Kurlov, and V.N. Lipatnikov, "Atomic and Vacancy Ordering in Carbide  $\zeta$ -Ta<sub>4</sub>C<sub>3-x</sub> (0.28 ≤ x ≤ 0.4) and Phase Equilibria in the Ta-C System," *J. Solid State Chem.*, **180** [11] 3234-46 (2007).
- [49]. D.J. Rowcliffe and W.J. Warren, "Structure and Properties of Tantalum Carbide Crystals," *J. Mater. Sci.*, **5** [4] 345-50 (1970).
- [50]. J.P. Kelly and O.A. Graeve, "Effect of Powder Characteristics on Nanosintering," in: *Novel Sintering Processes, Nanosintering & Grain Growth*, edited by R.H.R. Castro (Springer Science, New York, USA, 2012), in press.

## CHAPTER 9: CONTROL OF MICROSTRUCTURAL DEVELOPMENT IN ULTRA-HIGH TEMPERATURE CERAMICS

### A. Introduction

Ultra-high temperature ceramics (UHTCs) represent a class of materials with the capability to withstand extreme heating conditions. UHTCs are typically composite materials based on group IV-VI transition metal non-oxides, which form interstitial compounds. The key property they have is a high melting temperature, but their metallic-like properties also allow them to conduct heat away from a hot zone and make them suitable for advanced thermal protection systems that can withstand extreme heat and remove it quickly. The two greatest limitations of UHTCs correspond to the oxidation resistance and the mechanical properties (primarily fracture toughness).

The most well-studied ultra-high-temperature ceramic (UHTC) system is the  $\text{MB}_2/\text{SiC}$  composite system because of its excellent oxidation/ablation resistance in comparison to other UHTC systems, attributed to the complex oxide scale that develops on the surface (Figure 9-1a), but fracture toughness is not adequate.<sup>[1]</sup> The oxide scale consists of a liquid penetrating a porous oxide scaffold. The liquid prevents rapid oxygen diffusion inwards while the rigid oxide scaffold keeps shear forces from removing the liquid. On the other hand, TaC-based composites are of interest, but are less studied.  $\text{Ta}_4\text{C}_3$  is a nanolamellar phase consisting of alternating face-centered cubic and body-centered cubic layering. This results in a highly faceted microstructure (Figure 9-1b) that results in remarkable fracture toughness without the need for fiber/whisker reinforcement, but oxidation resistance is not adequate.<sup>[2-4]</sup> Fiber/whisker reinforcement may improve the fracture toughness of  $\text{MB}_2$ -based composites, but also provides direct pathways for rapid degradation at high temperatures if they become exposed, unless more suitable fibers are developed. An alternate approach is to begin with tougher TaC-based composites and develop improved oxidation resistance based on the empirical lessons learned from the oxidation of  $\text{MB}_2$ -type composites.

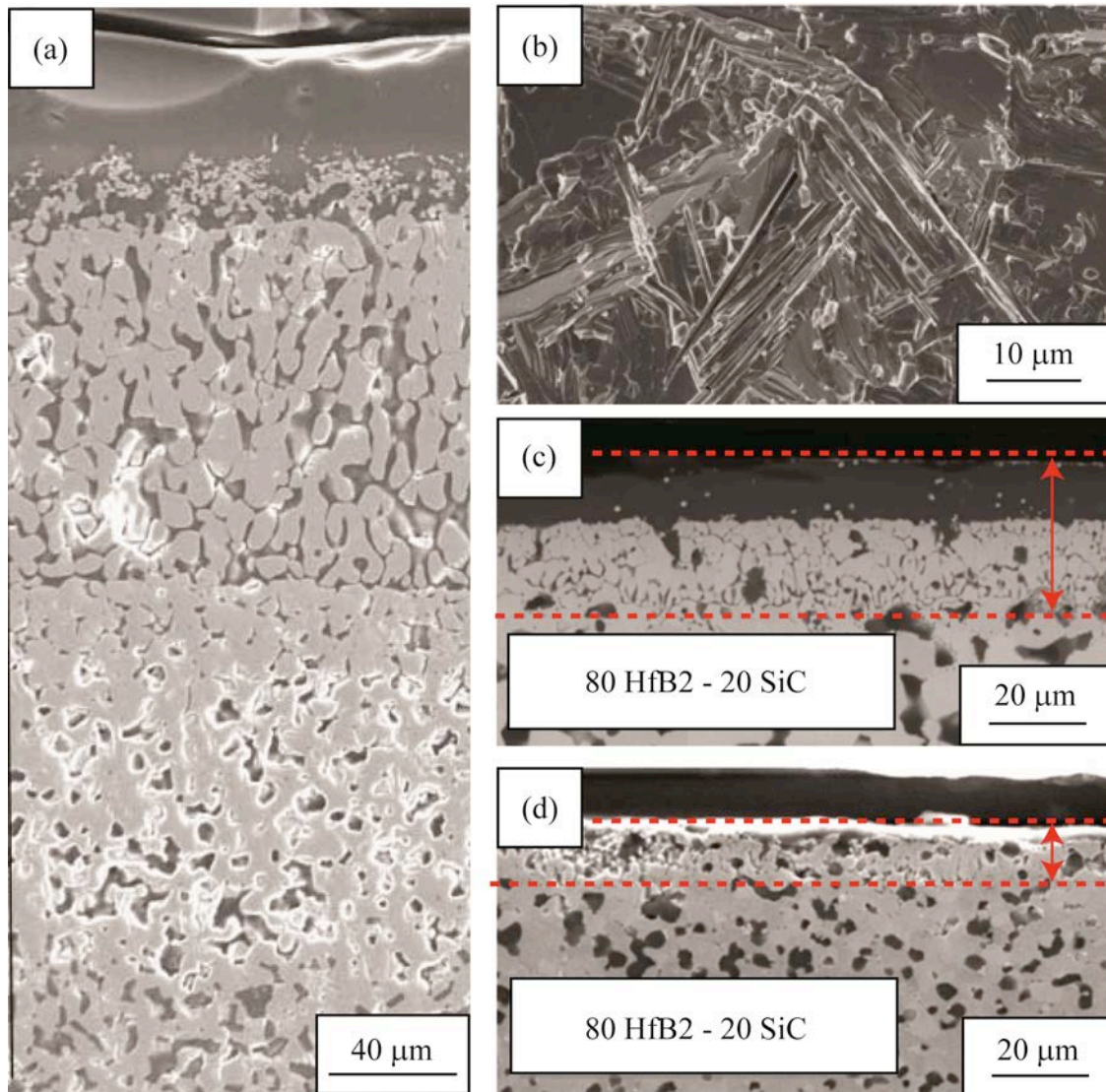


Figure 9 - 1. (a) Oxide scale features of MB<sub>2</sub>/SiC composite, (b) microstructure of the nanolamellar Ta<sub>4</sub>C<sub>3</sub> phase, and (c)/(d) reduced oxide scale thickness with decreased grain size.<sup>[1,2,7]</sup> (With color)

It is also apparent from studying the MB<sub>2</sub>/SiC system that decreasing grain size has major benefits. Research supports enhanced strength from ~400 MPa to greater than 1000 MPa by decreasing the grain size from ~10 μm to ~3 μm.<sup>[5]</sup> Brittle-to-ductile transition temperature and thickness of the oxidation scale are both decreased for similar decreases in grain size.<sup>[6,7]</sup> The reduction in oxide scale thickness is demonstrated in Figure 9-1c and Figure 9-1d. Reducing grain sizes into the nanostructured regime through enhancements in processing remains a challenging interest for potential improvements to UHTC properties.

A hybrid synthesis method that takes advantage of self-propagating high temperature synthesis and metathesis synthesis has recently been developed.<sup>[8,9]</sup> Both parent processes can produce kilogram quantities, possibly producing ton quantities per year.<sup>[10-12]</sup> The advantage of this technique is that small quantities can be made quickly, in a continuous fashion, to produce large yields safely and has greater process control than the parent techniques. This technique has been used to demonstrate the synthesis of nanopowders for nearly a dozen UHTC materials (see chapter two).

It is difficult to obtain nanostructuring of pure UHTC materials without using high pressures because of simultaneous densification and grain growth.<sup>[13,14]</sup> It is estimated that ~3.0 GPa is required to obtain densification without grain growth in TaC for example. If nanostructured UHTCs are to be obtained without extreme pressures, then it will be necessary to find suitable additives to control the microstructural development. Specific hypotheses concerning UHTC phase interactions have been developed based on work in earlier chapters and work available in the literature. These hypotheses are expected to guide nanostructuring developments. TaC was used as a model system and will be discussed in detail, then the implications for other systems will be discussed.

## **B. TaC-Based Composites**

The effects of WC or ZrC additions on the densification and grain growth of tantalum carbide nanopowders have recently been explored (see chapter eight). Based on this study, it is proposed that grain growth is strongly influence by solid solutions. Dislocations can dissociate into Shockley partials to form a stacking fault, a mechanism expected for sub-stoichiometric TaC.<sup>[15]</sup> Our work suggests that additives to TaC resulting in a reduced lattice parameter also generate stacking faults, possibly generating dislocations to accommodate the fault. Additions such as WC to TaC would have this effect. Additives that increase the lattice paramteter of TaC reduced grain growth when the lattice parameters approached that of stoichiometric TaC, believed to be caused by eliminating the stacking faults.

Results of adding WC and ZrC to TaC are given in Figure 9-2, which demonstrates nanostructuring techniques for TaC-based composites based on the hypotheses outlined

above. The samples were consolidated using the same exact sintering parameters to make direct comparisons (50 MPa applied pressure, 50 K/min heating rate, a measured dwell temperature of 2173 K, 10 minute temperature dwell, and a 50 K/min cooling rate with pressure gradually reduced. The first nanostructuring scheme takes advantage of the formation of stacking faults, which can generate nanolamellar sub-grain structure, and a second phase to pin grain growth. The second scheme is to use additives that eliminate stacking faults. The initial results are positive and justify further optimization of these techniques.

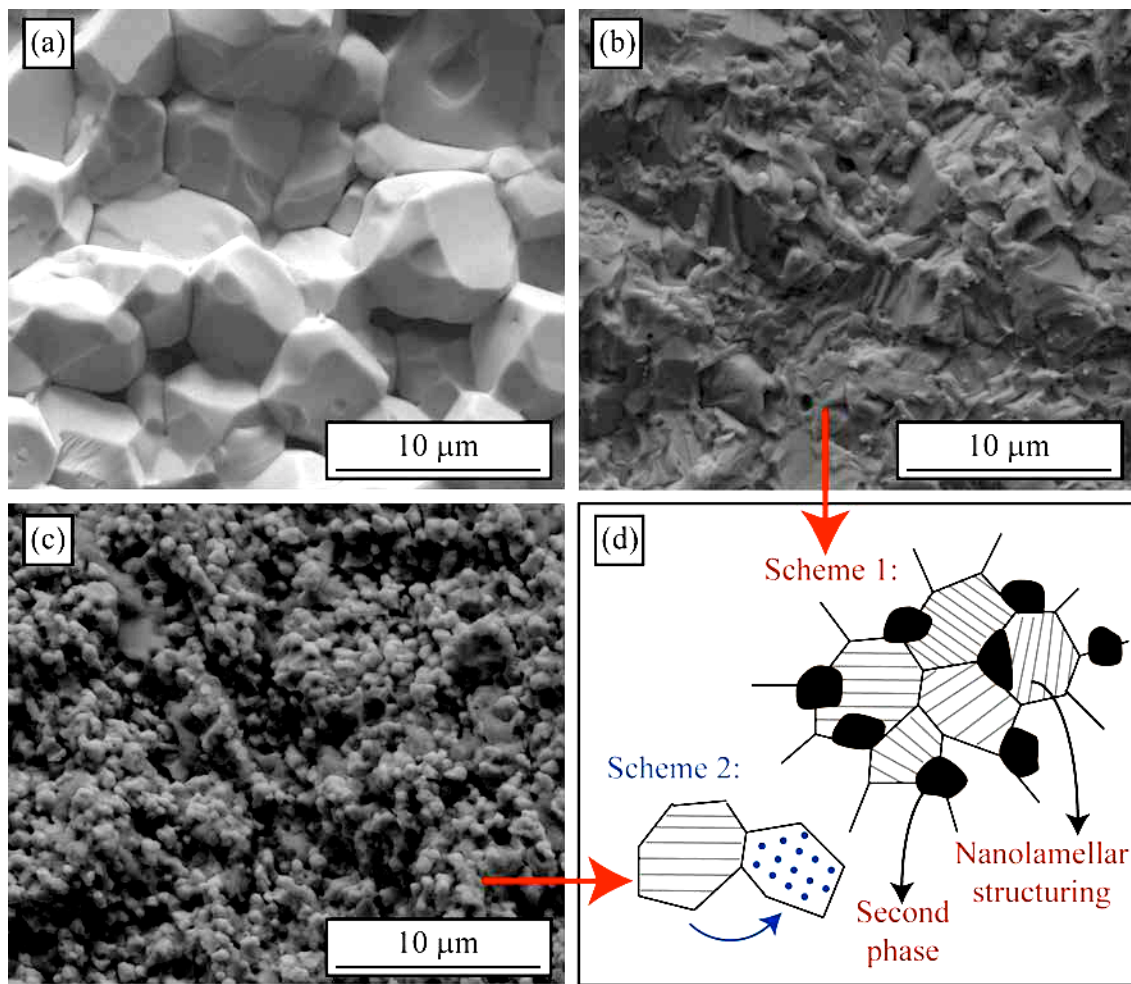


Figure 9 - 2. (a) TaC, (b) TaC-WC composite, (c) and TaC-ZrC composite sintered by resistance sintering with the same parameters. (d) Proposed nanostructuring schemes include nanolammelar structuring with stacking faults with a second phase to pin grain growth and solid solutions that remove stacking faults. (With color)

Other chemical modifications are expected to be useful for these nanostructuring schemes. Carbides of Ti, V, Cr, Nb, Mo, and W would reduce the lattice parameter to produce stacking faults, forming nanolamellar structuring within grains. Slightly exceeding the solubility limit of those carbides having a different crystal structure than TaC will produce a second phase for grain boundary pinning. The use of pure metals instead of the carbides could produce a similar result, but the contribution of carbon vacancies should be taken into consideration and if the metal will react with the carbide in excess of the solubility limit. It seems reasonable that N from TaN, being slightly smaller than C, could also produce stacking faults for nanostructuring. This is supported by the work of Urbonaite *et al.*, who demonstrated that the lattice parameter of TaC is gradually reduced by substituting in N for C.<sup>[16]</sup> Dual contributions can be obtained by using nitrides of Ti, V, Cr, Nb, Mo, and W.

Stacking faults can be removed by carbides of Zr and Hf, according to the second scheme in Figure 9-2. Using metals would not work for this scheme because the lattice parameter would be decreased when taking carbon vacancies into account. Ta, Hf, and Zr compounds of B, Si, P, and S are also expected to remove stacking faults from TaC. Additives such as SiC or B<sub>4</sub>C, which only target carbon site substitution, are expected to produce a similar result. Si<sub>3</sub>N<sub>4</sub>, which contains both lattice decreasing and increase elements, would remove stacking faults because of the greater contribution of Si compared to N, assuming both substitute. Grain boundary pinning above solubility limits may also facilitate nanostructuring. Greater complexity to chemical modifications is possible, by using two types of the additives for example.

Grain growth inhibition of TaC by addition of B<sub>4</sub>C and using similar sintering conditions has been demonstrated in the literature.<sup>[17]</sup> The inhibition of grain growth was attributed to grain boundary pinning of TaC by TaB<sub>2</sub> and C. B<sub>4</sub>C is not chemically compatible with TaC, forming TaB<sub>2</sub> and free carbon.<sup>[18]</sup> Both TaB<sub>2</sub> and C will increase the lattice parameter of TaC and is demonstrated in the literature.<sup>[19,20]</sup> According to the hypotheses developed here, this would reduce stacking faults and could be responsible for the reduced grain growth.

The effects of  $B_4C$  are demonstrated in Figure 9-3. Grain growth is reduced by adding  $B_4C$  (compare Figure 9-3a to Figure 9-3b). If the TaC-TaB<sub>2</sub> system is similar to the TiC-TiB<sub>2</sub> system, then the TaB<sub>2</sub> forms pseudo stacking faults of TaB<sub>2</sub> in TaC grains.<sup>[32]</sup> These are different than the M<sub>2</sub>C stacking faults produced by lattice decreasing type modifications because they do not produce carbon sub-lattice deficiency. Sintering and grain growth is believed to be controlled by carbon diffusivity.<sup>[18]</sup> Therefore, these pseudo stacking faults are not expected to promote grain growth the same way as M<sub>2</sub>C faults.  $B_4C$  helps eliminate detrimental Ta<sub>2</sub>C-type stacking faults, which can be used as a nanostructuring mechanism according to scheme 2 outlined in Figure 9-2, and could provide an additional nanostructuring feature via the formation of TaB<sub>2</sub> faults.

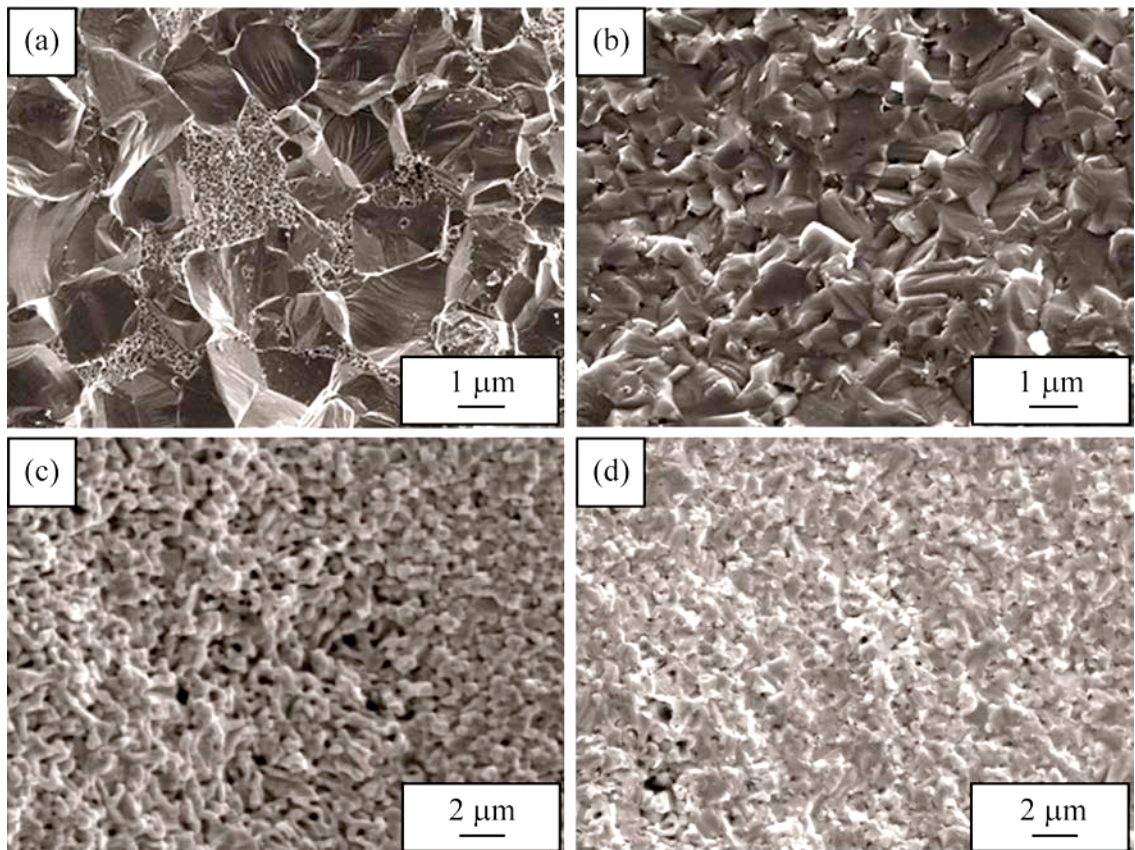


Figure 9 - 3. Microstructural comparison of fully dense (a) TaC and (b) TaC-1%B<sub>4</sub>C and partially dense (c) TaC and (d) TaC-1%B<sub>4</sub>C. Fully dense samples are prepared using similar conditions and partially dense samples are produced using similar conditions (images reproduced from Bakshi *et al.*).<sup>[17]</sup>

Other reports in the literature are contradictory, indicating that  $B_4C$  promotes grain growth rather than inhibiting grain growth when using similar sintering parameters.<sup>[20]</sup> Comparison of Figure 9-3c and Figure 9-3d help explain the discrepancy. These micrographs are given by the same author reporting grain growth inhibition by adding  $B_4C$ .<sup>[17]</sup> However, the grain size of the sample with  $B_4C$  is larger than without it in this case. It is not because  $B_4C$  promotes grain growth, but because it promoted sintering, which is accompanied by grain growth. The TaC samples without  $B_4C$ , having smaller grain sizes, are less dense and the samples are not directly comparable because of the difference in density.

The diverse chemical modifications for producing TaC-based nanocomposites offer a unique opportunity to improve the properties compared to single-phase TaC. Improvements in fracture toughness can be made by additions of chemicals that produce stacking faults to produce nanolamellar structuring. Similar fracture toughness values to that obtained by decreasing TaC carbon stoichiometry can be expected, more than double that of unfaulted TaC.<sup>[2]</sup> Some of these modifications may also lead to improved oxidation resistance, but will need to be developed empirically.

For the Group III-VI/Row 4-6 block in the periodic table, group variation across a row represents different levels of d-orbital filling while row variation down a group changes the principal quantum number of the d-orbital. Similarly, group variation from the Group XIII-XVI/Row 2-3 block changes the p-orbital hybridization. Group IV-VI lanthanides may change the properties due to the unique contribution of the f-orbital. The relative contributions of covalent, metallic, and ionic bonding, as a consequence of the various electron configurations, are expected to alter the properties of TaC-based nanocomposites by these types of chemical modifications.

### **C. $MB_2$ -Based Composites**

$ZrB_2$  and  $HfB_2$  are similar compounds and known to have dislocations and stacking faults.<sup>[22-23]</sup> Similar to TaC, this may help explain the difficulty in producing dense monoliths of these materials and the rapid grain growth that occurs during sintering. The hypotheses for nanostructuring outlined previously are expected to be applicable to composites of these materials as well, due to similar mechanisms.

The most studied MB<sub>2</sub>-based composite is that with SiC because of the beneficial oxidation resistance of the composite, but SiC also inhibits grain growth.<sup>[24,25]</sup> This is mostly attributed to the grain boundary pinning as a result of the presence of SiC in the microstructure. However, the elimination of stacking faults cannot be ruled out as a contributing factor for the suppression of grain growth as a consequence of Si and C substitution on B sites. This can be realized by how other additives affect grain growth. ZrC was reported to decrease the lattice parameters and enhance grain growth in ZrB<sub>2</sub>, despite the possibility for ZrC to contribute to grain boundary pinning for example.<sup>[26]</sup>

Figure 9-4 demonstrates possible grain size refinement of HfB<sub>2</sub>-SiC composites by the substitution of TaSi<sub>2</sub> for SiC. Grain boundary pinning is not likely to be the cause of the reduced grain size because volume of secondary phase for the two samples was constant. A greater defect reduction by addition of TaSi<sub>2</sub> in comparison to SiC is expected and could explain the grain size reduction. However, it is not possible to verify this exclusively because of the unknown interdiffusion between the phases and the fact that the experimental procedure provided does not guarantee the samples were sintered using the same exact conditions.<sup>[7]</sup> The grain size of the sample with TaSi<sub>2</sub> had larger grain sizes if prepared by hot pressing instead of resistance sintering, but the sintering parameters were not exclusively reported to know if they were the same for both samples. Instead, a range of sintering temperatures and times are given. Furthermore, differences in densities complicate the interpretation. Other reports suggest grain growth inhibition by addition of TaSi<sub>2</sub>, but the volume percentage of secondary phase is not constant.<sup>[27]</sup>

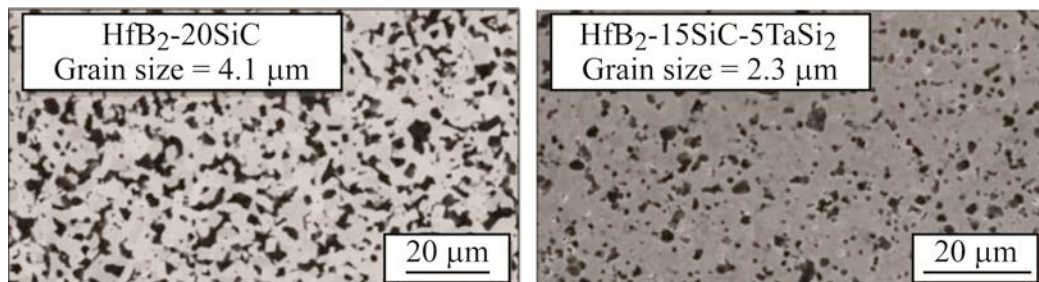


Figure 9 - 4. Microstructural comparison of HfB<sub>2</sub>-based composites prepared by resistance sintering and demonstrating refinement in microstructure by substitution of TaSi<sub>2</sub> for SiC (images reproduced from Gasch and Johnson).<sup>[7]</sup>

While some evidence exists to support the applicability of the developed hypotheses for nanostructuring to the MB<sub>2</sub>-based composite systems, the lack of more systematic studies make the claim difficult to accurately assess. In almost all cases, a secondary phase is present in the microstructure and it is difficult to separate out the effect of grain boundary pinning by secondary phases and the effect of solid solution caused by interdiffusion. In other cases, interdiffusion of phases is clearly evident, but the sintering parameters are such that direct comparison cannot be made or core-shell structures indicate that interdiffusion is incomplete suggesting that the true effect of the solutions may not be fully observed.<sup>[28,29]</sup> The use of nanopowders and more carefully designed experiments can help ensure completion of interdiffusion during sintering and assist in establishing solubility limits and the effects of solution phases.

#### **D. Other UHTC Systems**

It is expected that the knowledge gained from studying densification and grain growth in TaC-based nanocomposites will be broadly applicable to other UHTC systems, assuming some degree of metallicity. This has now been highlighted for MB<sub>2</sub>/SiC composites. A literature search was performed to check if the nanostructuring hypotheses apply to other systems and have found examples agreeing with the hypotheses.

Shvab and Egorov studied the addition of TaC to TiB<sub>2</sub> on microstructural development.<sup>[30]</sup> The average particle size of the starting powder mixtures were near three micrometers. The solubility of TaC in TiB<sub>2</sub> and vice versa is small. However, some solubility of TaC into TiB<sub>2</sub> is noted by the increase in TiB<sub>2</sub> lattice parameter. Ta substitution for Ti appears to be dominant in comparison with C substitution for B. Based on the nanostructuring hypotheses, this is an interaction that would remove stacking faults, assuming previous sub-stoichiometry, and result in refining the microstructure. A higher addition of TaC refined the microstructure and is demonstrated in Figure 9-5. The observations are consistent with scheme two as a possible nanostructuring technique, provided in Figure 9-2, with the additional benefit of a second phase of low solubility, but the two effects cannot be separated at this point.

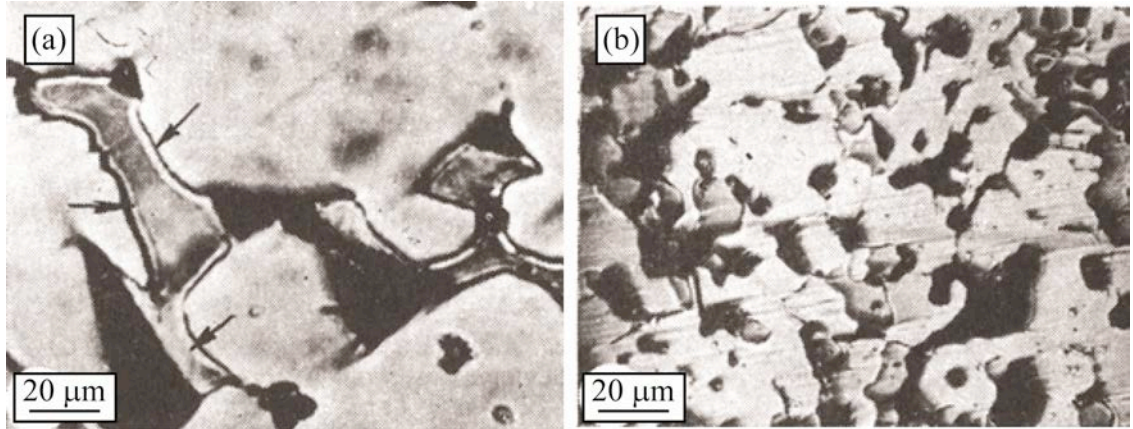


Figure 9 - 5. Microstructural comparison of (a) 90TiB<sub>2</sub>-10TaC and (b) 80TiB<sub>2</sub>-20TaC (images reproduced from Shvab and Egorov).<sup>[30]</sup>

Unlike TaC, dislocations in TiC do not dissociate into Shockley partials, presumably because of the low stability of the Ti<sub>2</sub>C, which would be the chemistry and structure expected in the stacking fault.<sup>[31]</sup> Despite the lack of stacking faults, lattice parameter increasing solid solutions such as TaC additions to TiC are found to inhibit grain growth.<sup>[32]</sup> The results were explained as a consequence of reducing the imperfections in the carbon sublattice and consequently, in the diffusion mobility of carbon atoms. Even without the presence of stacking faults, the concept of lattice increasing and decreasing additives seem to produce a similar effect described by our hypotheses. Vacancies facilitate mass transport as well and solid solutions that remove vacancies instead of stacking faults will have a similar effect.

It has also been demonstrated that stacking faults are generated by adding B, Al, or Si into TiC.<sup>[32,33]</sup> The stacking faults have TiB<sub>2</sub>, (Ti,Al)<sub>2+x</sub>C, or (Ti,Si)<sub>2</sub>C<sub>1-x</sub> type chemistry in the cubic TiC matrix. The formation of hexagonal TiB<sub>2</sub> stacking faults indicate that lattice parameter increasing phases can also form stacking faults, extending our hypotheses. This highlights the idea that microstructural design can be obtained via the nanostructuring hypotheses for materials that would not otherwise be expected to, based on intrinsic and extrinsic stacking fault formation.

The nanolamellar M<sub>1+n</sub>AX<sub>n</sub> compositions, known collectively as MAX phases, are structurally similar the sub-stoichiometric ζ-Ta<sub>4</sub>C<sub>3</sub> nanolamellar phase, but by using chemistry to generate stacking faults instead of sub-stoichiometry. A review of MAX phases is given by Barsoum and co-workers.<sup>[34,35]</sup> Their structural similarity is based on a

high density of ordered stacking faults, transitioning between structures every few planes of atoms. It is not surprising that TaC-based MAX phases have been found, such as  $Ta_2AlC$ ,  $Ta_3AlC_2$  and  $Ta_4AlC_3$ . Recently, more complex chemistries besides  $M_{1+n}AX_n$  are being found, having  $M_{2+n}A_{1+n}C_n$  chemistry.<sup>[36]</sup>

Outgassing and more extensive grain growth is observed in TiC by substituting N for C and is outlined in Figure 9-6 by comparing the two microstructures.<sup>[16]</sup> This is consistent with the observations that have been found exploring scheme one for nanostructuring that is outlined in Figure 9-2. Outgassing can be influenced by stacking faults that have  $M_2X$  chemistry and structure or vacancies, producing excess X, where X can be N or C depending on the specific defect chemistry in this case. Figure 9-7b demonstrates the microstructure for  $TiN_{0.8}C_{0.2}$ , and agrees with the hypothesis that C substitution for N in the TaN lattice will remove defects and suppress grain growth, consistent with scheme two for nanostructuring that is outlined in Figure 9-2.

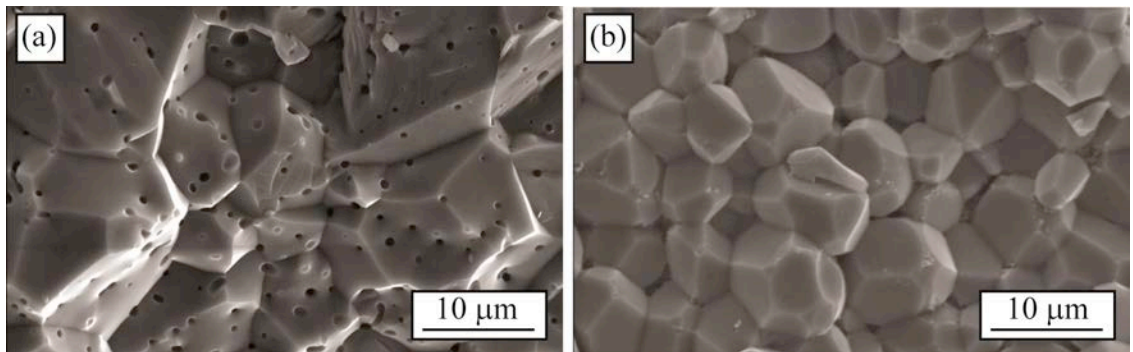


Figure 9 - 6. Microstructural comparison of (a)  $TiC_{0.8}N_{0.2}$  and (b)  $TiN_{0.8}C_{0.2}$  compositions (images reproduced from Urbonaite *et al.*).<sup>[16]</sup>

## E. Summary

Two schemes for nanostructuring TaC-based UHTCs are proposed. The hypotheses are supported by literature and extend to other UHTC systems. Investigating the literature has further enhanced the hypotheses by highlighting additional nanostructuring schemes. These schemes are based on two basic concepts: control of the defect structure and grain boundary pinning. Phases of low solubility in TaC can reduce

grain growth by grain boundary pinning. Phases of moderate and full solubility can produce nanostructuring via defect control and grain boundary pinning.

Defect structure promoting non-metal diffusion is expected to promote grain growth and enhance evaporation/condensation kinetics. Soluble additives that decrease the TaC lattice parameter are expected to do this. The formation of 2D defects, such as dislocations and stacking faults, are particularly important because diffusion is typically enhanced through these defects in comparison to 1D vacancy controlled diffusion, for example. The formation of these defects provides an opportunity for nanostructuring via lamellar structuring of the grains. Phases of moderate solubility are recommended for this technique, to have the option of grain boundary pinning via a second phase for counteracting grain growth.

Defect structure that promotes carbon diffusion can be removed from TaC by additives that increase the lattice parameter. Grain growth is inhibited when the lattice parameter is similar to that of stoichiometric TaC. Further increases to the lattice parameter could further inhibit grain growth. It also might be possible to form lamellar defect structure that does not promote carbon diffusion with further additions, therefore providing another form of nanostructuring.

Investigation of the literature demonstrates that these techniques might be generally applicable to UHTCs capable of having an extensive range of chemistries and varying levels of secondary phase solubility. However, the prospect of nanostructuring other UHTC systems is difficult to fully assess because while grain growth is suppressed in many examples, grain sizes are typically in the micrometer range and produced from powders of similar dimension. Interdiffusion is sometimes observed without completion. Further experiments, using nanopowders, with systematic chemistry variation, and allowing interphase diffusion processes to complete would be of great benefit to establish the viability of using these nanostructuring schemes more broadly, for other UHTC systems.

## F. References

- [1]. S.R. Levine, E.J. Opila, M.C. Halbig, J.D. Kiser, M. Singh, and J.A. Salem, "Evaluation of Ultra-High Temperature Ceramics for Aeropropulsion Use," *J. Eur. Ceram. Soc.*, **22** [14-15] 2757-67 (2002).
- [2]. K. Hackett, S. Verhoef, R.A. Cutler, and D.K. Shetty, "Phase Constitution and Mechanical Properties of Carbides in the Ta-C System," *J. Am. Ceram. Soc.*, **92** [10] 2404-7 (2009).
- [3]. M. Desmaison-Brut, N. Alexandre, and J. Desmaison, "Comparison of the Oxidation Behavior of Two Dense Hot Isostatically Pressed Tantalum Carbide (TaC and Ta<sub>2</sub>C) Materials," *J. Eur. Ceram. Soc.*, **17**, 1325-34 (1997).
- [4]. É.I. Golovko, L.F. Ochkas, M.S. Koval'chenko, and A.F. Nikityuk, "Oxidation of Tantalum Carbide Alloys," *Poroshkovaya Metallurgiya*, **166** [10] 51-4 (1976).
- [5]. S.M. Johnson, "Ultra High Temperature Ceramics: Application, Issues and Prospects," *2<sup>nd</sup> Ceramic Leadership Summit*, Baltimore, MD, August 3, 2011.
- [6]. P. Hu and Z. Wang, "Flexural Strength and Fracture Behavior of ZrB<sub>2</sub>-SiC Ultra-High Temperature Ceramic Composites at 1800°C," *J. Eur. Ceram. Soc.*, **30**, 1021-6 (2010).
- [7]. M. Gasch and S. Johnson, "Physical Characterization and Arcjet Oxidation of Hafnium-Based Ultra High Temperature Ceramics Fabricated by Hot Pressing and Field-Assisted Sintering," *J. Eur. Ceram. Soc.*, **30**, 2337-44 (2010).
- [8]. J.P. Kelly, R. Kanakala, and O.A. Graeve, "A Solvothermal Approach for the Preparation of Nanostructured Carbide and Boride Ultra-High Temperature Ceramics," *J. Am. Ceram. Soc.*, in print (2010).
- [9]. J.P. Kelly and O.A. Graeve, "Statistical Experimental Design Approach for the Solvothermal Synthesis of Nanostructured Tantalum Carbide Powders," *J. Am. Ceram. Soc.*, **94** [6] 1706-15 (2011).
- [10]. S.T. Aruna and A.S. Mukasyan, "Combustion Synthesis of Nanomaterials," *Curr. Opin. Solid State Mater. Sci.*, **12**, 44-50 (2008).
- [11]. A.M. Nartowski, I.P. Parkin, M. MacKenzie, A.J. Craven, and I. MacLeod, "Solid State Metathesis Routes to Transition Metal Carbides," *J. Mater. Chem.*, **9**, 1275-81 (1999).
- [12]. J.J. Moore and H.J. Feng, "Combustion Synthesis of Advanced Materials: Part I. Reaction Parameters," *Prog. Mater. Sci.*, **39**, 243-73 (1995).

- [13]. S.R. Bakshi, V. Musaramthota, D.A. Virzi, A.K. Keshri, D. Lahiri, V. Singh, S. Seal, and A. Agarwal, "Spark Plasma Sintered Tantalum Carbide-Carbon Nanotube Composite: Effect of Pressure, Carbon Nanotube Length and Dispersion Technique on Microstructure and Mechanical Properties," *Mater. Sci. Eng. A*, **528**, 2538-47 (2011).
- [14]. W.C. Yohe and A.L. Ruoff, "Ultrafine-Grain Tantalum Carbide by High Pressure Hot Pressing," *Ceram. Bull.*, **57** [12] 1123-30 (1978).
- [15]. M. Hoffman and W.S. Williams, "A Simple Model for the Deformation Behavior of Tantalum Carbide," *J. Am. Ceram. Soc.*, **69** [8] 612-14 (1986).
- [16]. S. Urbonaitė, M. Johnsson, and G. Svensson, "Synthesis of  $TiC_{1-x}N_x$  and  $TaC_{1-x}N_x$  by Spark Plasma Sintering," *J. Mater. Sci.*, **39**, 1907-11 (2004).
- [17]. S.R. Bakshi, V. Musaramthota, D. Lahiri, V. Singh, S. Seal, and A. Agarwal, "Spark Plasma Sintered Tantalum Carbide: Effect of Pressure and Nano-Boron Carbide Addition on Microstructure and Mechanical Properties," *Mater. Sci. Eng. A*, **528**, 1287-95 (2011).
- [18]. I.G. Talmy, J.A. Zaykoski, and M.M. Opeka, "Synthesis, Processing and Properties of TaC-TaB<sub>2</sub>-C Ceramics," *J. Eur. Ceram. Soc.*, **30**, 2253-63 (2010).
- [19]. X. Zhang, G.E. Hilmas, and W.G. Fahrenholtz, "Densification and Mechanical Properties of TaC-Based Ceramics," *Mater. Sci. Eng. A*, **501**, 37-43 (2009).
- [20]. X. Zhang, G.E. Hilmas, and W.G. Fahrenholtz, "Hot Pressing of Tantalum Carbide With and Without Sintering Additives," *J. Am. Ceram. Soc.*, **90** [2] 393-401 (2007).
- [21]. D. Ghosh, G. Subhash, and G.R. Bourne, "Room-Temperature Dislocation Activity During Mechanical Deformation of Polycrystalline Ultra-High-Temperature Ceramics," *Scripta Materialia*, **61**, 1075-8 (2009).
- [22]. D. Ghosh, G. Subhash, and G.R. Bourne, "Inelastic Deformation Under Indentation and Scratch Loads in a ZrB<sub>2</sub>-SiC Composite," *J. Eur. Ceram. Soc.*, **29**, 3053-61 (2009).
- [23]. S.K. Mishra, S. Das, and L.C. Pathak, "Defect Structures in Zirconium Diboride Powders Prepared by Self-Propagating High-Temperature Synthesis," *Mater. Sci. Eng. A*, **364** [1-2] 249-55 (2004).
- [24]. M.M. Opeka, I.G. Talmy, E.J. Wuchina, J.A. Zaykoski, and S.J. Causey, "Mechanical, Thermal, and Oxidation Properties of Refractory Hafnium and Zirconium Compounds," *J. Eur. Ceram. Soc.*, **19** [13-14] 2405-14 (1999).

- [25]. M. Gasch, D. Ellerby, E. Irby, S. Beckman, M. Gusman, and S. Johnson, "Processing, Properties and Arc Jet Oxidation of Hafnium Diboride/Silicon Carbide Ultra-High Temperature Ceramics," *J. Mater. Sci.*, **39** [19] 5925-37 (2004).
- [26]. W.-W. Wu, G.-J. Zhang, Y.-M. Kan, and P.-L. Wang, "Reactive Hot Pressing of ZrB<sub>2</sub>-SiC-ZrC Ultra High-Temperature Ceramics at 1800°C," *J. Am. Ceram. Soc.*, **89** [9] 2967-9 (2006).
- [27]. M. Gasch, S. Johnson, and J. Marschall, "Thermal Conductivity Characterization of Hafnium Diboride-Based Ultra-High-Temperature Ceramics," *J. Am. Ceram. Soc.*, **91** [5] 1423-32 (2008).
- [28]. F. Monteverde, A. Bellosi, and L. Scatteia, "Processing and Properties of Ultra-High Temperature Ceramics for Space Applications," *Mater. Sci. Eng. A*, **485**, 415-21 (2008).
- [29]. F. Monteverde, A. Bellosi, and S. Guicciardi, "Processing and Properties of Zirconium Diboride-Based Composites," *J. Eur. Ceram. Soc.*, **22**, 279-88 (2002).
- [30]. S.A. Shvab and F.F. Egorov, "Theory and Technology of Sintering, Thermal, and Chemothermal Treatment Processes," *Poroshk. Metall.*, **244** [4] 22-6 (1983).
- [32]. C. Allison, M. Hoffman, and W.S. Williams, "Electron Energy Loss Spectroscopy of Carbon in Dissociated Dislocations in Tantalum Carbide," *J. Appl. Phys.*, **53** [10] 6757-61 (1982).
- [33]. E.A. Levashov, V.V. Kurbatkina, A.S. Rogachev, N.A. Kochetov, E.I. Patsera, and N.V. Sachkova, "Characteristic Properties of Combustion and Structure Formation in the Ti-Ta-C System," *Russ. J. Non-Ferrous Metals*, **49** [5] 404-13 (2008).
- [34]. R. Yu, Q. Zhan, L.L. He, Y.C. Zhou, and H.Q. Ye, "Si-Induced Twinning of TiC and Formation of Ti<sub>3</sub>SiC<sub>2</sub> Platelets," *Acta Materialia*, **50**, 4127-35 (2002).
- [35]. M.W. Barsoum, "The MAX Phases and Their Properties," *Ceramics Science and Technology, Vol 2: Properties*, Chapter 7, p. 299 Eds. R. Riedel & I.-W. Chen, Wiley-VCH Verlag GmbH & Co (2010).
- [36]. M.W. Barsoum and T. El-Raghy, "The MAX Phases: Unique New Carbide and Nitride Materials," *Amer. Sci.*, **89**, 334-43 (2001).
- [37]. N.J. Lane, M. Naguib, J. Lu, L. Hultman, and M.W. Barsoum, "Structure of a New Bulk Ti<sub>5</sub>Al<sub>2</sub>C<sub>3</sub> MAX Phase Produced by the Topotactic Transformation of Ti<sub>2</sub>AlC," *J. Eur. Ceram. Soc.*, **32**, 3485-91 (2012).